Elasticity and Viscoelasticity of Solid SiO_2 as a Function of Frequency and Temperature

Zur Erlangung des akademischen Grades eines

DOKTORS DER NATURWISSENSCHAFTEN

von der Fakultät für

Bauingenieur-, Geo- und Umweltwissenschaften

des Karlsruher Instituts für Technologie (KIT)

genehmigte

DISSERTATION

von

M. Sc. Geol. Steffen Klumbach

aus Heilbronn

Tag der mündlichen

Prüfung: 12.11.2015

Referent: Prof. Dr. Frank R. Schilling

Korreferent: Prof. Dr. Jörg-Detlef Eckhardt

Karlsruhe (2015)

“Since the *Principia*[*] is one of those works everyone talks of but no one reads, anything said about it other than the usual honey-sauced eulogy must stand up against righteous indignation from all sides. But it is a work of science, not a bible. It should be studied and weighed - admired, indeed, but not sworn upon. It has its novelties and its repetitions, its elegant perfections and its errors, its lightning abbreviations and its needless detours, its extraordinary standards of rigor and its logical gaps, its elimination of stated hypotheses and its introduction of unstated ones”.
(Truesdell 1968)

„Die *Principia*[*] ist ein wissenschaftliches Werk und keine Bibel. Man sollte es studieren und abwägen, bewundern - ja! - , aber nicht darauf schwören. Man findet in ihm Neuigkeiten und Wiederholungen, eine elegante Vollendung, aber auch Irrtümer, erleuchtende Kürze und überflüssige Umwege, außerordentliche Ansprüche und Strenge, aber auch Lückenhaftigkeit der Logik, das Aufräumen mit früher aufgestellten Hypothesen und die Einführung unerklärter neuer Annahmen“.
(Truesdell 1968, Simonyi 2012)

---

[*] *Philosophiae Naturalis Principia Mathematica*: fundamental natural scientific treatise by Isaac Newton from 1687 (Brewster 1840).

[*] *Philosophiae Naturalis Principia Mathematica*: grundlegende naturwissenschaftliche Abhandlung Isaac Newtons von 1687 (Brewster 1840).

Abstract

Quartz is one of the most abundant rock-forming minerals within the Earth´s crust and used in numerous modern technical applications. A profound knowledge of its physical properties, especially the complex elastic behaviour, decisively influences our understanding of the subsurface, which is mainly based on the interpretation of seismic waves. To quantify and to better understand the complex elastic properties of quartz and quartz-bearing rocks dynamic mechanical laboratory experiments are performed in the frequency range of seismic waves. In consequence to this, quartz shows a unique complex elastic behaviour in the vicinity of its α-β phase transition. This may help to estimate temperatures underground and to clearly distinguish between a fully crystallised and a partly molten crust.

The laboratory experiments of this study comprise the determination of the complex Young's moduli of synthetic and natural quartz crystals, quartz-bearing rocks as well as fused silica as a function of frequency and temperature in symmetrical three-point bending set-ups with support spacings of 20 and 40 mm. Plate-like specimens are loaded sinusoidally between 0.1 and 20 Hz. Dynamic stresses and strains as well as their phase lags are recorded isothermally from ambient temperature across the α-β transition in quartz to temperatures > 600 °C. For the interpretation of the observed mechanical behaviours, the samples are additionally investigated by differential thermal analysis, X-ray diffraction, X-ray fluorescence, ultrasonic velocity measurements as well as by uniaxial and triaxial compression tests.

Dynamic mechanical analyses between ambient temperature and ≈ 500 °C reveal that the complex Young's modulus of single-crystal α-quartz is anisotropic and frequency-independent, within the experimental uncertainties. An increasing frequency dependence of the complex Young's modulus of quartz is observed at higher temperatures towards the α-β transition. The storage modulus (real part) increases sigmoidally with frequency, while the dissipation modulus (imaginary part) reaches a maximum at ≈ 1 Hz. The dispersion of the storage modulus and the dissipation maximum are low (40 mm support spacing: ≈ 7.6 and ≈ 2.6 GPa, respectively) parallel to the *c*-axis of the crystal and comparably high (40 mm support spacing: ≈ 15.1 and ≈ 7.1 GPa, respectively) perpendicular to it. The frequency dependence of the complex Young's modulus for β-quartz vanishes just a few degrees centigrade above the phase transition.

For the entire temperature range, the observed mechanical behaviour can be described by the Poynting-Thomson model within the experimental uncertainties. This model is composed of two mechanical springs (E_1 and E_2) and one dashpot (η). Compliance coefficients (S_{ij}) modelled by

$$S_{\mathrm{ij}}^{-1}(\omega) = \frac{\frac{E_1 E_2}{E_1 + E_2} + \frac{E_2\, \eta^2\, \omega^2}{(E_1 + E_2)^2}}{1 + \omega^2 \left(\frac{\eta}{E_1 + E_2}\right)^2} + i\,\omega\, \frac{\frac{E_2\, \eta}{E_1 + E_2} - \frac{E_1 E_2\, \eta}{(E_1 + E_2)^2}}{1 + \omega^2 \left(\frac{\eta}{E_1 + E_2}\right)^2}$$

are used to determine the complex Young's modulus as a function of frequency and temperature for all crystallographic directions. At the α-β transition, model parameters of the compliance coefficients for quartz, which is investigated with 40 mm support spacing, are: (S_{11}) E_1 = 572 GPa, E_2 = 70.0 GPa, η = 64.6 GPa s, (S_{33}) E_1 = 127 GPa, E_2 = 52.1 GPa, η = 22.9 GPa s, (S_{44}) E_1 = 204 GPa, E_2 = 37.5 GPa, η = 26.4 GPa s, (S_{12}) E_1 = 612 GPa, E_2 = 106.7 GPa, η = 78.5 GPa s, (S_{13}) E_1 = 1,546 GPa, E_2 = 284 GPa, η = 200 GPa s; S_{14} is nearly constant and ≈ - 0.0024 GPa^{-1}.

It is suggested that the mechanical observations are related to the formation and variation of Dauphiné twin domains due to dynamic reorientations of the crystal lattice in the vicinity of the α-β transition. The reorganisation of twin domains is promoted by low-frequency loading and relaxation, while it is impeded by high-frequency loading and stress accumulation within the crystal lattice. The time constant of the relaxation process is ≈ 0.1 s. It is approximately isotropic and independent of temperature.

Modelling of the compressional wave velocity using the frequency-dependent stiffness coefficients at the α-β transition (20 mm support spacing) yields a dispersion of ≈ 0.38 km/s within seismic frequencies for an isotropic quartz polycrystal. This is in agreement with observations for an elastically isotropic quartzite, which also holds for the dissipation behaviour. Both frequency-dependent seismic wave velocities and their dissipation behaviour may be used to estimate temperatures and physical states of the Earth's crust, in places where it is thick and hot enough for the occurrence of the α-β transition in quartz-rich rocks. Moreover, the significance of the frequency-dependent elastic properties of crystalline SiO_2 is supported by the absence of this effect in fused silica.

Zusammenfassung

Quarz ist eines der häufigsten gesteinsbildenden Minerale innerhalb der Erdkruste und wird in zahlreichen modernen technischen Anwendungen genutzt. Eine fundierte Kenntnis seiner physikalischen Eigenschaften, insbesondere des komplexen elastischen Verhaltens, beeinflusst maßgeblich unser Verständnis des Untergrundes, welches vorwiegend auf der Interpretation seismischer Wellen beruht. Um die komplexen elastischen Eigenschaften von Quarz und quarzhaltigen Gesteinen zu quantifizieren und besser zu verstehen werden dynamisch mechanische Laboruntersuchungen im Frequenzbereich seismischer Wellen durchgeführt. Infolgedessen zeigt Quarz ein unverwechselbares komplexes elastisches Verhalten im Bereich seiner α-β Phasenumwandlung. Dies könnte dabei helfen die Temperatur untertage abzuschätzen und klar zwischen einer vollständig kristallisierten oder einer teilweise aufgeschmolzenen Kruste zu unterscheiden.

Die Laboruntersuchungen dieser Studie beinhalten die Bestimmung der komplexen Elastizitätsmoduln von synthetischen und natürlichen Quarzkristallen, quarzhaltigen Gesteinen sowie Silikatglas als Funktion der Frequenz und Temperatur in symmetrischen Dreipunktbiegezuganordnungen mit Auflageabständen von 20 und 40 mm. Plättchenförmige Probenkörper werden sinusoidal zwischen 0,1 und 20 Hz belastet. Dynamisch mechanische Spannungen und Verformungen sowie deren Phasenverschiebungen werden ausgehend von Raumtemperatur über den α-β Übergang in Quarz hinweg bis zu Temperaturen > 600 °C isothermal aufgezeichnet. Zur Interpretation der beobachteten mechanischen Verhaltensweisen wird das Probenmaterial zusätzlich mittels Differential-Thermoanalyse, Röntgenbeugung, Röntgenfluoreszenz, Ultraschallmessungen sowie uniaxialen und triaxialen Kompressionsversuchen untersucht.

Dynamisch mechanische Analysen zwischen Raumtemperatur und ≈ 500 °C zeigen, dass der komplexe Elastizitätsmodul von α-Quarzeinkristallen anisotrop und innerhalb der experimentellen Unsicherheiten frequenzunabhängig ist. Bei höheren Temperaturen, hin zum α-β Übergang, wird eine zunehmende Frequenzabhängigkeit des komplexen Elastizitätsmoduls von Quarz beobachtet. Der Speichermodul (Realteil) nimmt in sigmoidaler Form mit der Frequenz zu, während der Verlustmodul (Imaginärteil) ein Maximum bei ≈ 1 Hz aufweist. Die Dispersion des Speichermoduls und das Verlustmaximum sind parallel zur *c*-Achse des Kristalls gering (jeweils ≈ 7,6 und ≈ 2,6 GPa) und senkrecht dazu vergleichsweise groß (jeweils ≈ 15,1 und ≈ 7,1 GPa). Die Frequenzabhängigkeit des komplexen Elastizitätsmoduls für β-Quarz verschwindet nur wenige Grad Celsius oberhalb des Phasenübergangs.

Das beobachtete mechanische Verhalten kann für den gesamten Temperaturbereich innerhalb der experimentellen Unsicherheiten mit dem Poynting-Thomson Modell beschrieben werden. Dieses Modell besteht aus zwei mechanischen Federn (E_1 und E_2) und einem Stoßdämpfer (η). Elastizitätskonstanten (S_{ij}) modelliert nach

$$S_{\mathrm{ij}}^{-1}(\omega) = \frac{\frac{E_1 E_2}{E_1 + E_2} + \frac{E_2 \eta^2 \omega^2}{(E_1 + E_2)^2}}{1 + \omega^2 \left(\frac{\eta}{E_1 + E_2}\right)^2} + i\,\omega \frac{\frac{E_2\,\eta}{E_1 + E_2} - \frac{E_1 E_2 \eta}{(E_1 + E_2)^2}}{1 + \omega^2 \left(\frac{\eta}{E_1 + E_2}\right)^2}$$

werden genutzt um den komplexen Elastizitätsmodul als Funktion der Frequenz und Temperatur für alle kristallographischen Richtungen zu bestimmen. Am α-β Übergang sind die Modellierungsparameter der Elastizitätskonstanten für Quarz, welcher mit 40 mm Auflageabstand untersucht wird: (S_{11})

E_1 = 572 GPa, E_2 = 70,0 GPa, η = 64,6 GPa s, (S_{33}) E_1 = 127 GPa, E_2 = 52,1 GPa, η = 22,9 GPa s, (S_{44}) E_1 = 204 GPa, E_2 = 37,5 GPa, η = 26,4 GPa s, (S_{12}) E_1 = 612 GPa, E_2 = 106,7 GPa, η = 78,5 GPa s, (S_{13}) E_1 = 1.546 GPa, E_2 = 284 GPa, η = 200 GPa s; S_{14} ist nahezu konstant und beträgt ≈ - 0,0024 GPa^{-1}.

Es wird angenommen, dass die mechanischen Beobachtungen mit der Bildung und der Veränderung von Domänen aus Dauphiné-Zwillingen aufgrund dynamischer Umorientierungen des Kristallgitters in der Nähe des α-β Übergangs einhergehen. Die Umordnung von Zwillingsdomänen wird durch eine niederfrequente Belastung und Relaxation begünstigt, während sie durch eine hochfrequente Belastung und den Aufbau mechanischer Spannungen im Kristallgitter behindert wird. Die Zeitkonstante des Relaxationsprozesses ist ≈ 0.1 s. Sie ist näherungsweise isotrop und temperaturunabhängig.

Eine Modellierung der Kompressionswellengeschwindigkeit aus den frequenzabhängigen Elastizitätskonstanten am α-β Übergang (20 mm Auflageabstand) ergibt eine Dispersion von ≈ 0.38 km/s innerhalb seismischer Frequenzen für einen isotropen Quarzpolykristall. Dies steht im Einklang mit Beobachtungen an einem elastisch isotropen Quarziten, was auch für das Dämpfungsverhalten gilt. Sowohl frequenzabhängige Geschwindigkeiten seismischer Wellen als auch deren Dämpfungsverhalten könnten genutzt werden um Temperaturen und physikalische Zustände der Erdkruste abzuschätzen, an Stellen wo diese ausreichend dick oder heiß für das Auftreten des α-β Übergangs in quarzreichen Gesteinen ist. Darüber hinaus wird die Bedeutsamkeit der frequenzabhängigen elastischen Eigenschaften in kristallinem SiO_2 durch die Abwesenheit dieses Effekts in Silikatglas untermauert.

Table of contents

List of figures

List of tables

1. Introduction

Motivation

Quartz is an important mineral for technical applications due to its piezoelectric and optical properties (*e.g.* Götze 2009). It is also one of the most abundant rock-forming minerals within the Earth's crust (*e.g.* Ronov & Yaroshevsky 1969, Taylor 1964, 1967) and the basic component of many artificial silica compounds (*e.g.* Okrusch & Matthes 2010). A profound understanding of its physical properties (*e.g.* Höfer & Schilling 2002, Ogi *et al.* 2006), especially of its mechanical behaviour and underlying structural features (*e.g.* Tucker *et al.* 2001), is essential to model geodynamic processes of the Earth's interior (*e.g.* Schmidt *et al.* 2003).

The Earth's interior is commonly described by a shell model, consisting of oceanic and continental crust as well as several layers beneath with a total depth of ≈ 6370 km (*e.g.* Press & Siever 2000). This model is based on direct and indirect information on the subsurface. Direct information is obtained from observations in open and underground pits, caverns, tunnels, and wells. The lowermost well is the Russian Kola Superdeep Borehole with a vertical depth of ≈ 12,260 m (*e.g.* Okrusch & Matthes 2005). Information on greater depth is concluded indirectly from investigations of formerly deep-seated rocks that were brought to the surface by tectonic uplift and erosion or volcanic eruptions. Apart from crustal material, such rocks include mantle xenoliths and high-pressure mineral inclusions. Another major source of indirect information is the interpretation of geophysical recordings, with naturally triggered seismicity as well as reflection and refraction seismics being most important (*e.g.* Heier 1974). This means that travel times and attenuation characteristics of elastic waves in rocks and melt are evaluated, typically in the frequency range from ≈ 0.0003 to > 30 Hz (Lay 2002). Physical and mineralogical interpretation of such field data, however, requires reference values of elastic rock properties determined at the laboratory (*e.g.* Belikov 1962, Birch 1955, Kern 1990, 2011, Mainprice *et al.* 1990).

Based on seismic recordings, Gutenberg (1951) attributes a decrease of the compressional wave velocity with increasing depth in continental crust to the temperature dependence of the anisotropic Young's modulus observed for quartz in laboratory experiments (Perrier & De Mandrot 1923). This dependence is caused by a displacive reorientation of the quartz crystal lattice, known as α-β phase transition. Beyond this, the stabilisation of the high-temperature phase causes a rapid re-increase of the Young's modulus (Perrier & De Mandrot 1923). Key features to better understand the Earth's crust in this way are the modelling of isotropic elastic properties for quartz polycrystals from anisotropic single-crystal data and measurements of quartz-bearing rocks (*e.g.* Anderson *et al.* 1968). Fielitz (1971, 1976) and Kern (1979), for instance, present high-pressure elasticity data of quartz and quartz-rich rocks across the α-β transition. Their observations can be used as an *in-situ* thermal detector to estimate the temperature in the Earth's continental crust that is assumed to be rich in quartz (*e.g.* Mechie *et al.* 2004).

Numerous seismic studies already consider the α-β transition in quartz as a potential reason of an abnormally low Poisson's ratio in the Earth's continental crust (*e.g.* Kuo-Chen *et al.* 2012, Marini & Manzella 2005, Mechie *et al.* 2004, Sheehan *et al.* 2014, Shillington *et al.* 2013, Zandt *et al.* 1994, 1996). Mechie *et al.* (2004), for instance, describe the presence of the α-β transition in the Tibetan crust (Fig. 1). It is most likely due to the occurrence of felsic rocks (*e.g.* Sharma & Gupta 2012, Sharma *et al.* 2011).

Zandt *et al.* (1994, 1996) assume the α-β transition to be present in the Altiplano lower crust of the Bolivian Andes. Swenson *et al.* (2000) offer, however, various reasons that might explain the observations of Zandt *et al.* (1994, 1996). One of them is partial melting that is subject of a petrophysical investigation by Schmitz *et al.* (1997).

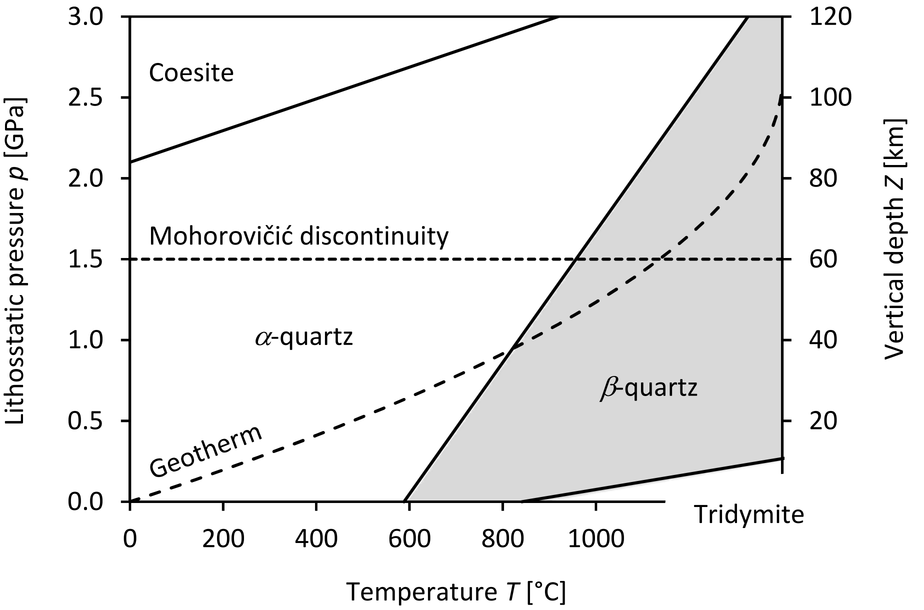

Fig. 1: Phase diagram of crystalline silica polymorphs, focusing on the phase boundary between the stability fields of the two quartz modifications (modified according to Schreyer 1976). The Mohorovičić discontinuity and geotherm (Appendix 1) are modelled for Tibetan crust (data from Herman *et al.* 2010, Mechie *et al.* 2004, Rudnick *et al.* 1998).

The complex Young's moduli of quartz and quartz-bearing rocks are determined by dynamic mechanical experiments as a function of frequency and temperature. Knowledge about these complex Young's moduli may contribute to a clear interpretation of the α-β transition in seismic recordings, apart from other reasons such as partial melting (*e.g.* Gordon & Davis 1968). The observed Young's modulus of quartz is therefore converted into the elasticity tensor and elastic wave velocities that are relevant for seismic interpretations. Particularly the compressional wave velocity is supposed to also exhibit a frequency-dependent behaviour due to its attenuation by viscoelastic effects in the quartz crystal lattice that are associated with the α-β transition (Klumbach & Schilling 2012, 2014). The attenuation of compressional waves is described by the inversed seismic quality factor Q^{-1}

$$Q^{-1}(\omega) = \frac{E''(\omega)}{E'(\omega)} \tag{1}$$

and can be related to different intra- and intercrystalline viscoelastic processes (*e.g.* Jackson & Anderson 1970, Karato & Spetzler 1990). The quality factor itself is defined by the ratio of stored and dissipated energy during one oscillation period of the wave (*e.g.* Anderson 1967). In terms of the complex Young's modulus, the seismic quality factor is expressed by the quotient of the storage modulus *E'* and dissipation modulus *E''*, respectively equal to the real and the imaginary part of the complex number (*e.g.* Mavko 2009). A high quality factor corresponds to a largely elastic behaviour of the material under investigation, while a low quality factor indicates viscoelastic effects (*e.g.* Mitchell 1995). Intracrystalline attenuation is generated by phase transformations, such as the α-β transition in quartz, for instance (*e.g.* Carpenter & Zhang 2011). Intercrystalline attenuation can be caused by grain boundary sliding, different pore space fillings, and the development of micro-cracks.

Structural properties of quartz

Pure single-crystal quartz (Fig. 2) exclusively consists of silicon Si and oxygen O_2 ions that build a three-dimensional framework silicate of interconnected SiO_4 tetrahedra (*e.g.* Press & Siever 2001). The tetrahedra are linked to each other by sharing all of their oxygen ions, resulting in an overall composition of SiO_2. Quartz is enantiomorphic, since right- or left-handed helices can be formed along the main axis of the crystal (Fig. 3, right). Under ambient conditions (20 °C, 0.1 MPa), the Si-O bond lengths within the tetrahedra vary between ≈ 1.60 and ≈ 1.64 Å (*e.g.* Putnis 1992), while the Si-O bond angles range from ≈ 108 to ≈ 111° (Kihara 1990, 1993). The Si-O-Si angle θ basically varies from 120 to 180° between two tetrahedra (*e.g.* Putnis 1992). It is ≈ 143.6° (Kihara 1990, 1993), whereas the tetrahedra exhibit a tilt angle φ of ≈ 16.3° (Heaney & Veblen 1991) under ambient conditions (Fig. 3, left).

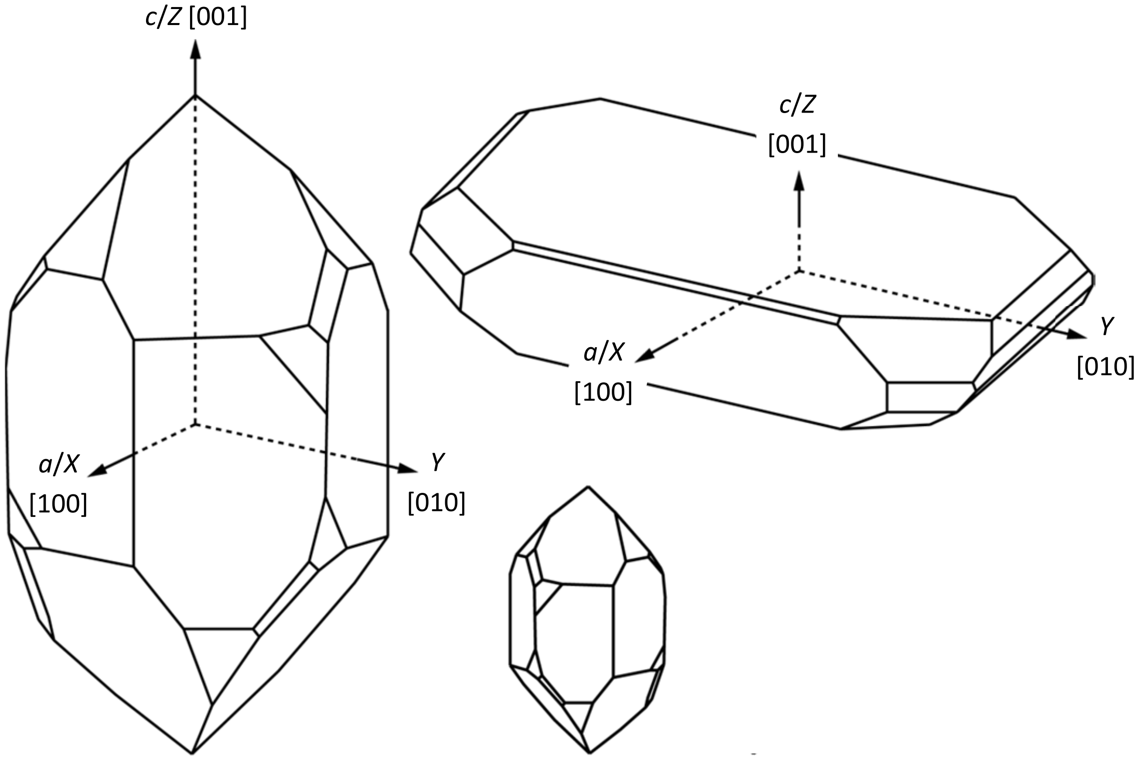

Fig. 2: Habitus of natural right- (left) and left-handed (lower right) α-quartz single crystals as well as of a synthetic α-quartz single crystal (upper right, modified according to Borchardt-Ott 2009, Götze 2009).

Under ambient conditions, the stable phase of crystalline SiO_2 is defined as α- or low quartz. It has a trigonal crystal structure with a three-fold *c*-axis (main axis) as well as three two-fold axes parallel to the *a*-axes (Bragg & Gibbs 1925), which is equivalent to point group 32 (Fig. 4, left). The *a*-axes are oriented perpendicular to the *c*-axis and form angles of 120°. Compared to the Cartesian coordinate system, the *Z*-axis is oriented parallel to the *c*-axis and the *X*-axis is located parallel to an *a*-axis (Fig. 2). The unit cell comprises three formula units. Its length is ≈ 4.904 Å along the *a*-axes and ≈ 5.393 Å along the *c*-axis of the crystal (Saha *et al.* 1979). This yields an axial ratio of ≈ 1.1. Hence, the density of quartz is ≈ 2.65 g/cm³ (*e.g.* Okrusch & Matthes 2005).

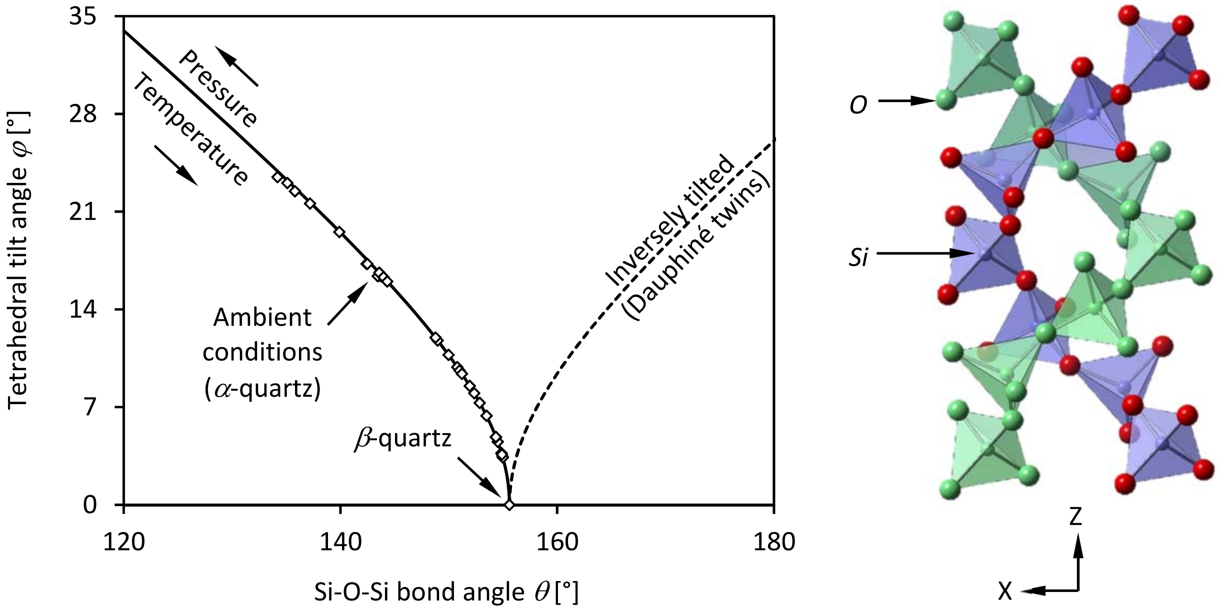

Fig. 3: Tetrahedral tilt versus Si-O-Si bond angle in quartz (left, modelled with data from Grimm & Dorner 1975, Heaney & Veblen 1991, Kihara 1990, Lager *et al.* 1982, Levien *et al.* 1980, Müser & Binder 2001, Thompson *et al.* 2011). Three-dimensional double helix of interconnected silica tetrahedra in right-handed α-quartz under ambient conditions (right, modelled with CrystalViewer, data taken from Kihara 1990).

Synthetic quartz crystals (Fig. 2, right) are several decimetres in size and hydrothermally grown from a seed at high pressure and high temperature (*e.g.* Brice 1985, Brown *et al.* 1952, Moriya & Ogawa 1982a). The elongation of a crystal corresponds to the *Y*-axis. Synthetic quartz contains lattice defects (*e.g.* Lang & Miuscov 1967, Moriya & Ogawa 1978, 1980, 1982b), but exhibits significantly less irregularities than natural crystals (*e.g.* Brown & Thomas 1960, Guzzo *et al.* 2004). The amount of water incorporated in the crystals lattice may vary during the growth of the mineral (*e.g.* Aines *et al.* 1984).

Natural quartz is idiomorphic and transparent and known as berg crystal, mountain crystal, and rock crystal. Lattice imperfections and impurities lead to numerous varieties (*e.g.* Rösler 1988). These include, for instance, smoky quartz of brownish colour due to point defects caused by radiation and trace amounts of aluminium incorporations. Structural defects, also caused by radiation, and incorporated iron typically form yellow-coloured citrine (*e.g.* Nesse 2000). Inclusions of ferric iron produce a purple colour found in amethyst, while titanium and manganese ions lead to pink-coloured rose quartz (*e.g.* Okrusch & Matthes 2005). This study is exclusively based on transparent samples of synthetic single-crystal quartz without macroscopically visible fluid inclusions and natural crystals of gem quality (Chapter 3).

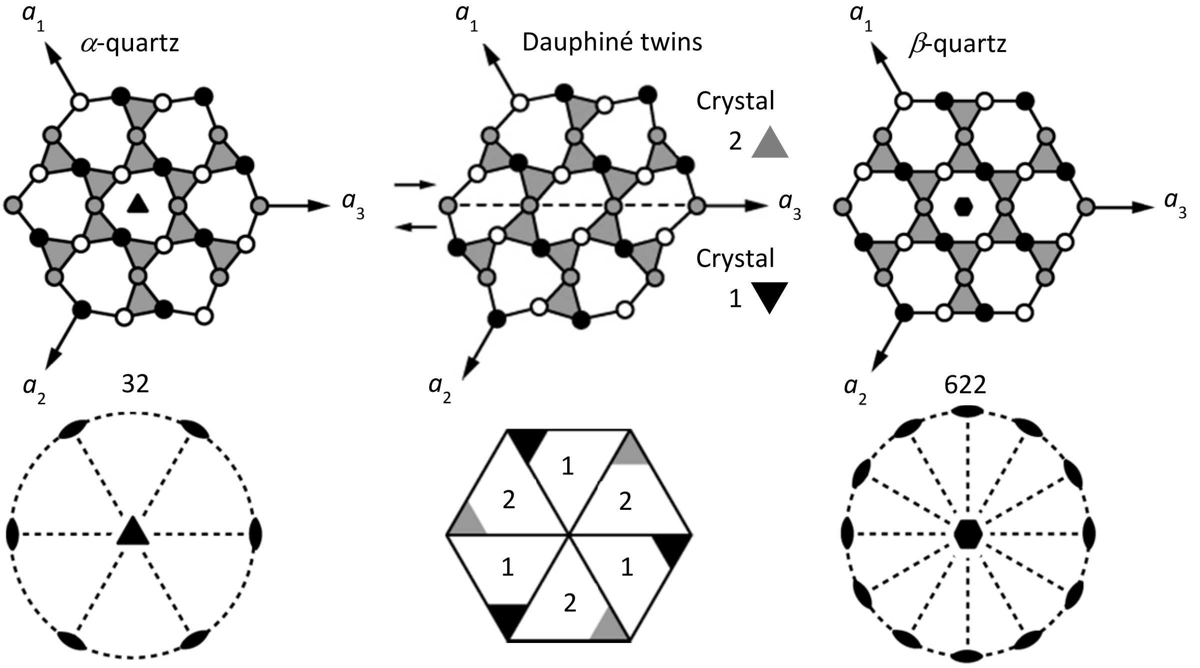

Fig. 4: *C*-cut representation (top) and symmetry elements (bottom) of untwinned α-quartz (left), Dauphiné twinned α-quartz (middle) and β-quartz (right). Silicon ions are located at three different *Z*-levels, without oxygen (modified according to Okrusch & Matthes 2005, Wenk *et al.* 2003).

Untwinned α-quartz is piezoelectric. This means that an elastic deformation of the crystal lattice by an external force leads to an electric potential. Vice versa this is known as indirect piezoelectric effect (Curie & Curie 1880, 1881). Comprehensive scientific work is performed on natural and synthetic single crystals already, since quartz is used as oscillator in a large variety of modern technical applications (*e.g.* Bechmann 1958, Cambon *et al.* 2005, Cook & Weissler 1950, Engel & Krempl 1982, Haines *et al.* 2002, Koga *et al.* 1958, Mullen 1969, Ohno 1990, Ogi *et al.* 2006, Uno & Noge 1999, Tarumi *et al.* 2007).

At ≈ 573 °C and ambient pressure, α-quartz transforms into β- or high quartz by an enantiotropic displacive phase transition as the result of a reorientation of its SiO_4 tetrahedra (*e.g.* Dove 1997, Dove *et al.* 1999, Ericksen 2001, Grimm & Dorner 1975, Müser & Binder 2001, Narayanaswamy 1948, Scott 1974, Shen *et al.* 1993, Venkataraman 1979). Heating of α-quartz, the tetrahedral tilt angle φ decreases by

$$\cos(\varphi) = \sqrt{\frac{3}{4} - \cos(\theta)} - \frac{1}{2\sqrt{3}} \tag{2}$$

and the Si-O-Si bond angle θ increases by

$$\cos(\theta) = \frac{3}{4}\left(\cos(\varphi) + \frac{1}{2\sqrt{3}}\right)^2 \tag{3}$$

with temperature (Fig. 3, left). Furthermore, the tilt angle increases and the Si-O-Si bond angle decreases at elevated pressure (*e.g.* Hazen *et al.* 1989). The trigonal crystal structure gradually becomes unstable due to the formation of Dauphiné twin domains below the transition temperature (*e.g.* Drebushchak & Dementiev 1996, Heaney & Veblen 1991, Thompson *et al.* 2011). The Dauphiné twins both exhibit the same chirality, rotated by 180° around the *c*-axis of the original crystal (Fig. 4, middle). Towards the transition temperature, the number of twin domains increases with a decrease of their size. The transition is additionally characterised by the appearance of an incommensurate phase between ≈ 573 and ≈ 574.3 °C, where the twin domains vanish (*e.g.* Jacob & Cordier 2010, Kato 1986, Putnis 1992, Spearing *et al.* 1992, Yamamoto *et al.* 1988). The transition from α-quartz to the incommensurate phase is ranked as a first-order transformation (*e.g.* Höchli 1970, Höchli & Scott 1971), whereas the transition between the incommensurate phase and β-quartz is of second order, according to a discontinuity in the derivative function for an observed physical property (*e.g.* Bachheimer 1980, Bachheimer & Dolino 1975, Dolino 1990, Heaney & Veblen 1991, Salje 1992). The incommensurate phase is studied intensively already (*e.g.* Aslanyan & Levanyuk 1979, Aslanyan *et al.* 1983, 1998, Dolino *et al.* 1983, 1984a, Walker 1983, 1985). However, it cannot be subject of this study, as the temperature uncertainty of the experimental set-up is with > ± 1 K too large to focus on the comparably narrow temperature range of 1.3 K (Chapter 2).

The β-phase has a hexagonal crystal symmetry (Fig. 4, right) that is represented by point group 622 (Bragg & Gibbs 1925, Kihara 1993). This symmetry is higher than for the trigonal crystal system. It is characterised by a six-fold *c*-axis (main axis) and six two-fold axes perpendicular to it. These correspond to the three *a*-axes. The silica tetrahedra are still coiled (Fig. 3, left). If the β-phase is considered to be of static nature, the tetrahedra are not tilted anymore, while the Si-O-Si angle is ≈ 155.6° (Thompson *et al.* 2011). Otherwise, the tetrahedra are supposed to vibrate around their state of equilibrium (Heaney & Veblen 1991). At 600 °C, for instance, Saha *et al.* (1979) observe ≈ 5.01 and ≈ 5.47 Å for the length of the *a*- and *c*-axes of the unit cell, respectively. Its axial ratio is lower than at ambient temperature, whereas increasing pressure leads to an elongation of the unit cell (Fig. 5). Consequently, the subsurface occurrence of the β-modification is limited to an abnormally thick and hot crust. Its geotherm needs to exceed the transition temperature of quartz above the Mohorovičić discontinuity (Fig. 1), since the presence of quartz is usually excluded by the mineralogy of the Earth's mantle.

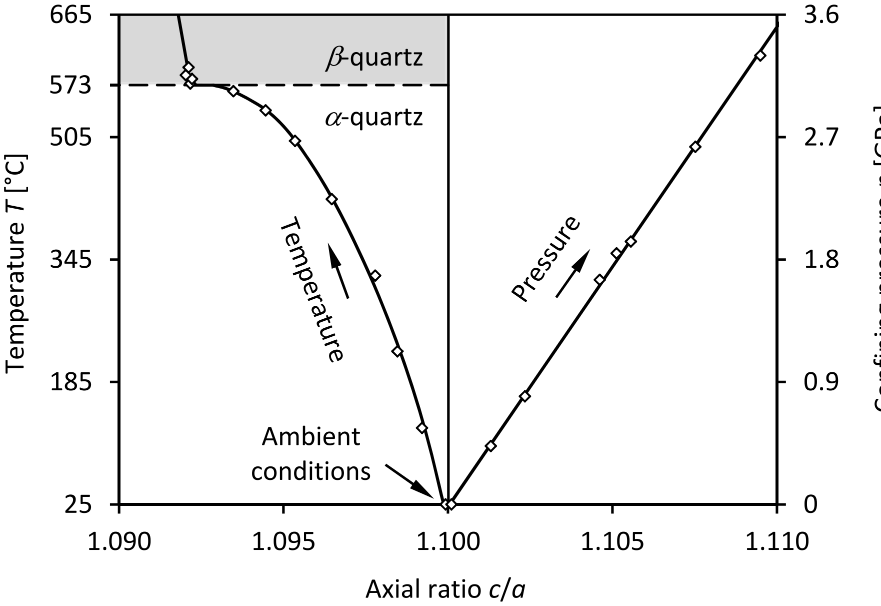

Fig. 5: Variation of the axial ratio for the quartz unit cell due to temperature and pressure variations (modified according to Kihara 1990, Angel *et al.* 1997).

Anisotropic elastic properties of quartz

Hooke's law (Hooke 1679), the basis of most considerations relating to mineral elasticity, is named after the English polymath Robert Hooke, who lived from 1635 to 1703 (*e.g.* Andrade 1960). According to Hooke's law a mechanical stress σ, which is the average force F per unit area A, is proportional to a resultant strain ε under consideration of a material-related isotropic or anisotropic modulus of elasticity E (*e.g.* Rösler *et al.* 2008)[1]. Hooke's law, however, only holds for infinitesimally small strains (*e.g.* Wang & Li 2009), excluding plasticity (*e.g.* Thurston *et al.* 1966). The modulus of elasticity is called Young's modulus after the English polymath Thomas Young, who lived from 1773 to 1829 (*e.g.* Peacock 1855).

Anisotropic elastic properties are expressed as a fourth-rank stiffness c_{ijkl} or compliance tensor s_{ijkl}

$$\sigma_{ij} = c_{ijkl}\,\varepsilon_{kl} = \frac{\varepsilon_{kl}}{s_{ijkl}} \tag{4}$$

that are inverse to each other (Appendix 6, *e.g.* Angel *et al.* 2009, Sadd 2005). A fourth-rank tensor basically consists of 81 coefficients, whereas the number of its independent coefficients is reduced due to symmetrical second-rank stress and strain tensors. The elasticity in any crystallographic direction also equals the value in the opposite direction according to Neumann's principle by

$$c_{ijkl} = c_{jikl} = c_{ijlk}. \tag{5}$$

Hence, the elasticity tensor of a triclinic crystal simplifies to 21 independent coefficients (*e.g.* Chung & Buessem 1967, Hearmon 1946, 1956).

The elasticity tensor of an α-quartz single crystal has six independent coefficients

$$C_{ij} = \begin{bmatrix} C_{11} & C_{12} & C_{13} & C_{14} & 0 & 0 \\ C_{12} & C_{11} & C_{13} & -C_{14} & 0 & 0 \\ C_{13} & C_{13} & C_{33} & 0 & 0 & 0 \\ C_{14} & -C_{14} & 0 & C_{44} & 0 & 0 \\ 0 & 0 & 0 & 0 & C_{44} & C_{14} \\ 0 & 0 & 0 & 0 & C_{14} & C_{66} \end{bmatrix} \tag{6}$$

due to its trigonal symmetry, while the elasticity tensor of β-quartz is described by five independent coefficients, as C_{14} and S_{14} vanish in the hexagonal crystal lattice (*e.g.* Nye 1992). For both modifications, C_{66} results from C_{11} and C_{12} (Appendix 5). The representation of the stiffness tensor by two indices as shown here is based on a commonly used notation introduced by Voigt (1966). A simplified conversion between stiffness and compliance for crystals of trigonal and hexagonal symmetry is presented by Mason (1943, Appendix 7).

The anisotropic Young's modulus of quartz is determined by a rotation of the compliance tensor

$$s'_{ijkl} = a_{im}\,a_{jn}\,a_{ko}\,a_{lp}\,s_{mnop} \tag{7}$$

in matrix notation. The rotation matrix a_{ij} results from rotations around two perpendicular axes in the Cartesian coordinate system (Appendix 2) and has to be applied four times. The inverse of the coefficient s'_{iiii} then equals the anisotropic Young's modulus E'_i

---

[1] Even though the correlation is called "Hooke's law", it is only a simplification, since it neglects higher-order elastic behaviour, like it is described by the Birch-Murnaghan equation of state, for instance.

$$E_{\mathrm{i}}^{'} = \frac{1}{s_{\mathrm{iiii}}^{'}}. \tag{8}$$

Further anisotropic mechanical properties, such as the shear modulus and Poisson's ratio, also can be determined in this way (*e.g.* Li 1976, Li & Chung 1978).

A simplification for the equations (7) and (8) for trigonal minerals by

$$E^{-1} = \left(1 - n_3^2\right)^2 S_{11} + n_3^4 \, S_{33} + n_3^2 \left(1 - n_3^2\right) \left(2\, S_{13} + S_{44}\right) + 2\, n_2 n_3 \left(3\, n_1^2 - n_2^2\right) S_{14} \tag{9}$$

reveals that the anisotropic Young's modulus of α-quartz depends on S_{11}, S_{33}, S_{13}, S_{44}, and S_{14}. The term including S_{14} is omitted for β-quartz (*e.g.* Cazzani & Rovati 2003). The anisotropic Young's modulus of quartz is independent of S_{12} and S_{66} (*e.g.* Chou & Sha 1971, Ting 2005). In this context the unity vector n_{i} describes any crystallographic direction and depends on the azimuth ϕ and the polar distance ψ (Appendix 3). The anisotropic Young's modulus of quartz can be determined completely by examining its elastic properties in four independent crystallographic directions according to individual and combined stiffness coefficients of the equation. The simplification by equation (9) is based on Savart's (1829) work, the first study of the anisotropic elastic behaviour of quartz in resonance experiments, and the interpretation of his results by Voigt (1966). Parallel

$$E_{\parallel c} = \frac{C_{33}\left(C_{11} + C_{12}\right) - 2\, C_{13}^2}{C_{11} + C_{12}} = \frac{1}{S_{33}} \tag{10}$$

and perpendicular

$$E_{\perp c} = \frac{2}{\dfrac{C_{33}}{C_{33}\left(C_{11} + C_{12}\right) - 2\, C_{13}^2} + \dfrac{C_{44}}{C_{44}\left(C_{11} - C_{12}\right) - 2\, C_{14}^2}} = \frac{1}{S_{11}} \tag{11}$$

to the *c*-axis of the quartz crystal, the anisotropic Young's modulus is given by the inverse of S_{33} and S_{11}, respectively. Both cases are independent of the azimuth.

Static elastic properties of quartz

Perrier & De Mandrot (1923) are the first to investigate the static anisotropic Young's modulus of quartz as a function of temperature across the α-β transition (Fig. 6) in symmetrical four-point bending experiments using plate-like specimens cut parallel and perpendicular to the *c*-axis of a single crystal. Perrier & De Mandrot (1923) also measure two specimens cut with azimuthal angles of 90 and 270°, respectively, and a polar distance of 50°.

Under ambient conditions, quartz shows a higher stiffness parallel to the *c*-axis of the crystal than parallel to the *a*-axis. The Young's moduli obtained for the two specimens with off-axis orientations correspond to the overall minimum and maximum stiffness of quartz for all crystallographic directions. Increasing temperature leads to a linear decrease of the anisotropic Young's modulus, which is less pronounced in the direction perpendicular to the *c*-axis of the crystal than in other orientations. Further heating causes a strong non-linear development of Young's modulus in the vicinity of the α-β transition. It minimises at ≈ 573°C and rapidly increases again for higher temperatures. The stiffness maximum of the β-phase is found parallel to the *a*-axis of the crystal, while the minimum is recorded parallel to the *c*-axis, contrary to observations at ambient temperature. The two specimens with off-axis crystallographic orientations exhibit the same stiffness. Such elastic anomalies can be described in terms of Landau's theory for phase transformations according to the order of the transition, for instance (*e.g.* Carpenter & Salje 1998, Carpenter *et al.* 1998, Cowley 1980, 2012, Landau & Lifshitz 1959, Liakos & Saunders 1982).

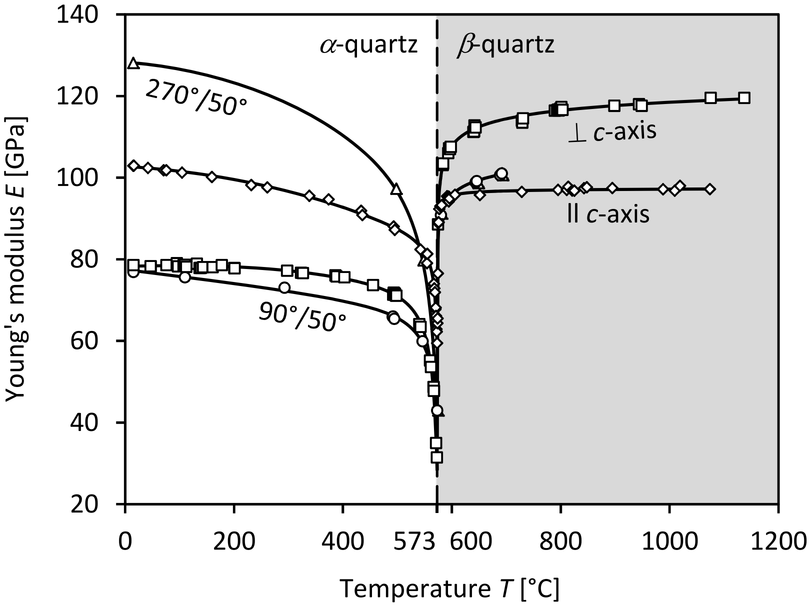

Fig. 6: Temperature dependence of the anisotropic Young's modulus of quartz across the α-β transition (modified according to Perrier & De Mandrot 1923, Appendix 10). Minima due to the α-β transition are calibrated to 573 °C. Off-axis crystallographic orientations are referred to as "azimuth/polar distance".

Dynamic elastic properties of quartz

The relationship between the stiffness tensor c_{ijkl} and different types of elastic wave velocities in a solid is given by Christoffel's equation

$$\left| c_{ijkl}\, g_j\, g_l - \rho v^2 \delta_{ik} \right| = 0, \tag{12}$$

where ρ represents the density of the material and δ_{ik} is the Kronecker delta (Appendix 4). Furthermore, the unit vector g corresponds to the propagation direction of the wave (*e.g.* Haussühl 1983, 2007). The determinant of Christoffel's equation has three solutions corresponding to the compressional wave velocity v_p as well as the respective vertical and horizontal shear wave velocities v_{sv} and v_{sh}. Parallel to the *c*-axis of a quartz crystal, the compressional wave velocity depends on the density as well as on C_{33} by

$$v_p\,[001] = \sqrt{\frac{C_{33}}{\rho}}, \tag{13}$$

while it is related to C_{11} parallel to the *a*-axis by

$$v_p\,[100] = \sqrt{\frac{C_{11}}{\rho}}. \tag{14}$$

Parallel to the *c*-axis of the crystal, the two different shear waves exhibit the same velocity, which is coupled to C_{44} by

$$v_s\,[001] = \sqrt{\frac{c_{44}}{\rho}}\,. \tag{15}$$

A crystallographic orientation showing such an effect is denoted principal direction. Equations (13) to (15) represent the simplest solutions of Christoffel's equation. Vice versa, the stiffness coefficients can be modelled from the elastic wave velocities (*e.g.* Mayer & Parker 1961).

A general review on the elastic properties of crystalline silica polymorphs and fused silica is made by Pabst & Gregorová (2013). Under ambient conditions, elastic properties of natural and synthetic quartz single crystals are presented by Heyliger *et al.* (2003), Hill & Burgess (1973) and Ohno *et al.* (1986), for instance. High-temperature data are given by Atanasoff & Hart (1941), Kammer & Atanasoff (1942), Kammer *et al.* (1948), Koga *et al.* (1958), Lakshtanov *et al.* (2007), Nakamura *et al.* (2012), Ohno *et al.* (1995, 2006), Pelous & Vacher (1976) Smirnov & Mirgorodsky (1997), Tsuneyuki (1990), and Uno & Noge (1999), among others. Lakshtanov *et al.* (2007), for instance, determine compressional and shear wave velocities along the *X*-, *Y*-, and *Z*-axes in single-crystal quartz as a function of temperature by Brillouin spectroscopy (Fig. 7) and obtain the stiffness tensor by solving Christoffel's equation (12).

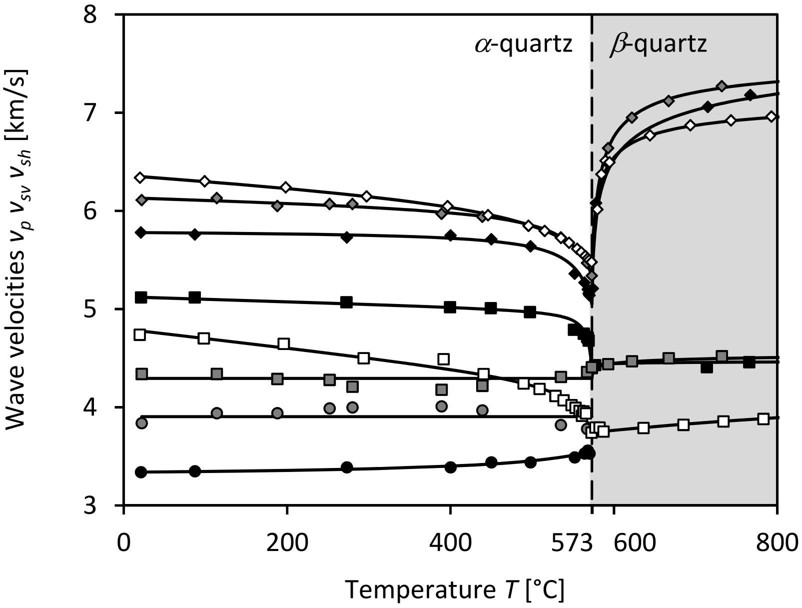

Fig. 7: Temperature dependence of different types of elastic wave velocities in single-crystal quartz (modified according to Lakshtanov *et al.* 2007, Appendix 10): compressional waves (diamonds), vertical (squares) and horizontal shear waves (circles) for [100] (black), [010] (grey), and [001] (white). Minima due to the α-β transition are calibrated to 573 °C.

Single-crystal elasticity data of quartz at low to ambient temperature are provided by Tarumi *et al.* (2007), for example. Results of elasticity measurements at low temperature and high pressure are published for instance by Mc Skimin (1962), Mc Skimin *et al.* (1965), and Wang *et al.* (1992). High-pressure data at ambient temperature are presented by Calderon *et al.* (2007), Gregoryanz *et al.* (2000), Kimizuka *et al.* (2007), Purton *et al.* (1992), Tse & Klug (1991), and Wang *et al.* (2011). Soga (1968) describes derivatives for the velocities of the different elastic waves in isotropic α-quartz polycrystals for both high temperature and high pressure. Fielitz (1971, 1976) and Kern (1978, 1982) are the first to experimentally determine the elastic properties of quartz-bearing rocks and quartz crystals (Kern 1979) across the α-β transition at high pressure. Sato *et al.* (2004), however, recognise the need of combined velocity and attenuation measurements at high temperature and simultaneously high pressure.

Wiedemann (1991) investigates the dynamic Young's modulus of quartz in symmetrical three-point-bending tests at ≈ 0.08 Hz sinusoidal loading as a function of temperature with a heating rate of 1 K/min across the α-β transition. Moreover, higher attenuation relating to the α-β transition are reported by Nikitin *et al.* (2007). This is confirmed by Beck (2010) and Beck & Schilling (2010), who carry out a dynamic mechanical thermal analysis of the complex Young's modulus of Dalsland quartzite. As a part of this study, Klumbach & Schilling (2012) present the first isothermal frequency-dependent data of quartz for various temperatures below and above the α-β transition. Peng *et al.* (2012) publish complex elastic data of quartz loaded at 1 Hz for temperature changes of 2 and 0.1 K/min across the α-β transition. Peng & Redfern (2013) also present data for quartz stressed at 2, 5, and 10 Hz as a function of temperature across the α-β transition as well as for novaculite and sandstone.

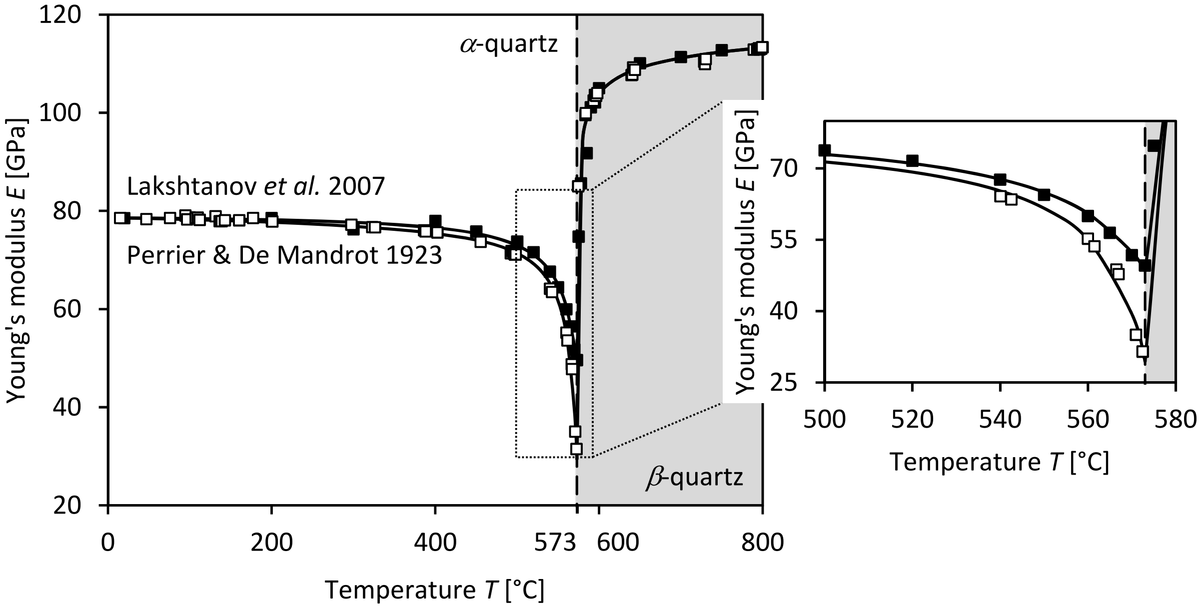

Fig. 8: Temperature dependence of the Young's modulus of quartz perpendicular to the *c*-axis of the crystal: modified according to Lakshtanov *et al.* (2007, black symbols) as well as Perrier & De Mandrot (1923, white symbols). A potential frequency dependence of the elasticity of α-quartz is observed close to the α-β transition (lines, Appendix 10). The moduli of the β-phase are normalised to the measured value at ≈ 900 °C.

According to equation (11) the stiffness coefficients from Lakshtanov *et al.* (2007) are used to model the temperature dependence of Young's modulus perpendicular to the *c*-axis of the crystal (Fig. 8). The results are compared with the static bending observations made by Perrier & De Mandrot (1923). Both data sets are consistent under ambient conditions and at high temperature in the stability field of the β-phase. Significant differences between the two data sets are found in the vicinity of the α-β transition. These differences might be explained by enhanced measurement precision during the 20th century. However, they might also be related to an viscoelastic behaviour linked to the phase transformation (*e.g.*

Grimm & Dorner 1975, Dove 1997, Dove *et al.* 1999, Ericksen 2001, Müser & Binder 2001, Scott 1974, Venkataraman 1979). Isothermal frequency-dependent measurements in the vicinity of the α-β transition are supposed to prove whether this assumption is correct or not (Klumbach & Schilling 2014).

Thermal properties of quartz

The α-β quartz transition at ≈ 573 °C is first observed by Le Chatelier (1889), who assumes an anisotropic thermal expansion of single crystals to be the reason of predominantly developing macroscopic cracks in silica ceramics during sintering. In dilatation experiments Le Chatelier (1889) discovers a higher expansion coefficient of α-quartz parallel to the *a*-axis of the crystal than parallel to its *c*-axis (Fig. 9). This effect significantly increases with temperature and reaches its maximum at ≈ 573 °C. The phase transformation is characterised by a discontinuity. Above the α-β transition, the expansion of β-quartz is found to be nearly independent of temperature.

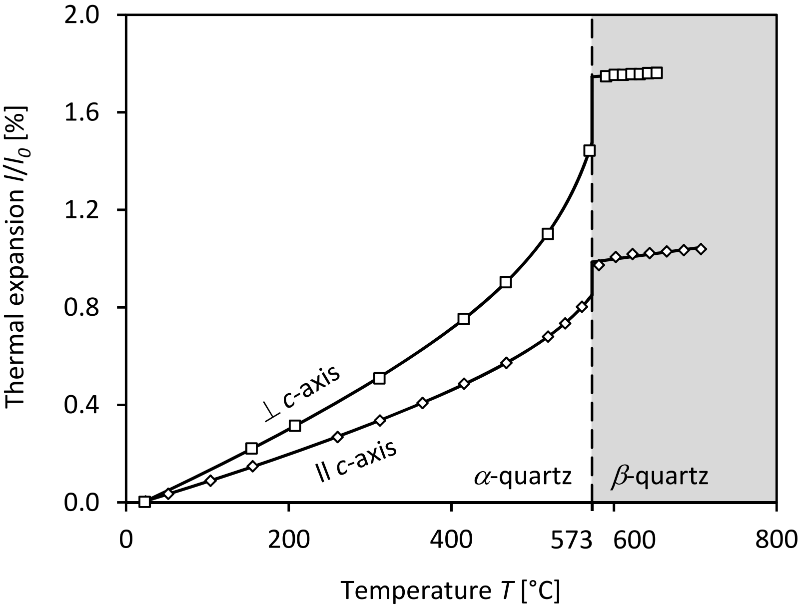

Fig. 9: Anisotropic thermal expansion of a quartz single crystal with temperature across the α-β transition at ambient pressure (modified according to Raz *et al.* 2002). Modelled data (lines) are used in this study (Appendix 10).

The thermal expansion of natural and synthetic quartz is studied intensively already (*e.g.* Amatuni & Shevchenko 1966, Banda *et al.* 1975, Gaskell 1966b, Jay 1933, Klement & Cohen 1968, Rosenholtz & Smith 1941, Smirnov 1999). Raz *et al.* (2002) recently publish ambient and high-pressure data. Additionally, Glover (1995) confirm the formation and propagation of micro-cracks caused by the α-β transition by means of acoustic emission recordings. The development of macroscopic cracks can be prevented by low heating rates, particularly in the vicinity of the phase transition.

In dynamic mechanical investigations as a function of temperature the thermal expansion of quartz or any quartz-bearing specimen has to be taken into account. In contrast to this, the thermal conductivity and heat capacity of quartz are not considered in this study, as adiabatic moduli are determined.

Elastic properties of isotropic silica polycrystals

Due to its abundance, quartz is one of the most important rock-forming minerals within the Earth's crust (*e.g.* Press & Siever 2001). When knowing its anisotropic single-crystal properties, the behaviour of isotropic quartz polycrystals and quartz-bearing rocks can be determined. The initial step from a single crystal to a polycrystalline aggregate is made by twinning, which is described as the constitutional combination by contact or penetration of two or more crystals from the same point group, leading to a reduction of the overall symmetry (*e.g.* Kleber *et al.* 1985). Different types of twins exist for quartz according to the Dauphiné, Brazilian, and Japanese laws (*e.g.* Okrusch & Matthes 2005). Twinning can occur during crystal growth or at phase transitions as well as by thermal treatment or mechanical deformation (*e.g.* Nesse 2000). The elastic properties of isotropic polycrystals are usually estimated from averaged anisotropic single-crystal data, for instance, according to the Voigt-Reuss-Hill approximation (*e.g.* den Toonder *et al.* 1999, Doncieux *et al.* 2008, Hill 1952, Man & Huang 2011, Reuss 1929, Voigt 1889) or the Hashin-Shtrikman approximation (*e.g.* Hashin & Shtrikman 1962, 1963, Peselnick & Meister 1965, Watt 1979, 1980, Watt *et al.* 1976, Watt & Peselnick 1980).

Under ambient conditions, the Young's modulus E_{VRH} of an isotropic α-quartz polycrystal is ≈ 95.6 GPa (Fig. 10). The Young's modulus of an isotropic β-quartz polycrystal is ≈ 99.1 GPa at 600 °C, while the density reduces from ≈ 2.65 to ≈ 2.53 g/cm^3 (*e.g.* Pabst & Gregorová 2013). Beyond these, other silica modifications exist at high pressure and high temperature that are metastable under ambient conditions.

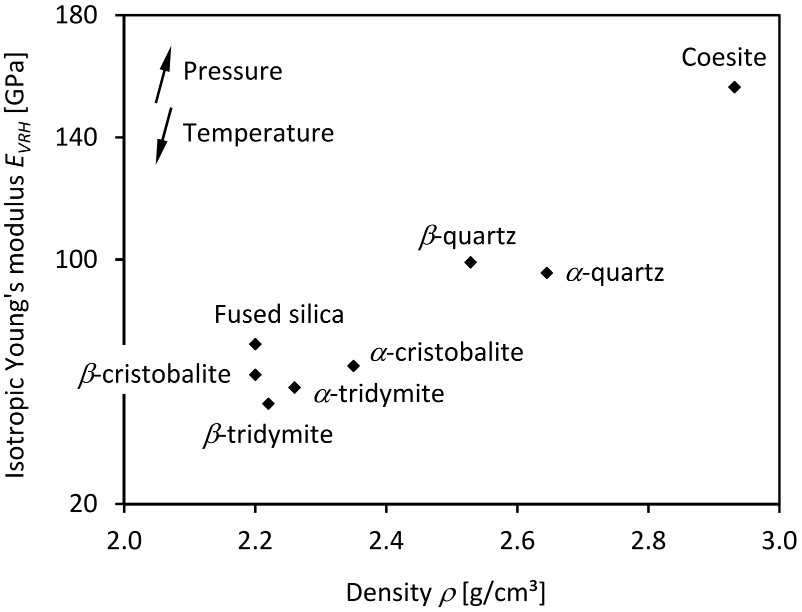

Fig. 10: Young's moduli of isotropic silica polycrystals with tetrahedral coordination (Appendix 8) and fused silica based on experimental and simulation data collected by Pabst & Gregorová (2013).

Increasing pressure leads to lattice compaction and transformation of quartz into coesite and stishovite, both with higher packing density and stiffness (*e.g.* Angel 1997, Fenner 1913, Kim-Zajonz 1999, Levien *et al.* 1980, Saika-Voivod *et al.* 2004, Stevens *et al.* 1997, Swamy *et al.* 1994). Coesite exhibits tetrahedrally coordinated silicon ions and a monoclinic crystal symmetry (*e.g.* Okrusch & Matthes

2005). Under ambient conditions, its density is ≈ 2.93 g/cm³ and the Young's modulus of an isotropic polycrystal equals ≈ 156.5 GPa (Weidner & Carleton 1977). Stishovite has a tetragonal crystal symmetry, whereas the silicon ions are octahedrally coordinated (*e.g.* Akaogi *et al.* 1995, Angel *et al.* 2001, Bourova *et al.* 2004, Dean *et al.* 2000). Its density is ≈ 4.3 g/cm³ and the Young's modulus of an isotropic polycrystal reaches ≈ 536.2 GPa under ambient conditions (Weidner *et al.* 1982).

Increasing temperature, by contrast, leads to an expansion of the crystal lattice and the formation of other silica phases. At ≈ 870 and ≈ 1470 °C, β-quartz transforms into β-tridymite and β-cristobalite (*e.g.* Okrusch & Matthes 2005). The exact transition temperatures depend on the purity of the material. This also holds for the α-β quartz transition (*e.g.* Ghiorso *et al.* 1979, Holmquist 1961, Kihara 1990). Metastable α-modifications exist as well (*e.g.* Pabst *et al.* 2014). Pabst & Gregorová (2013) model the Young's modulus of an isotropic α- or low-tridymite polycrystal for ambient conditions with ≈ 58.1 GPa, using a density of ≈ 2.26 g/cm³. Pabst & Gregorová (2013) also find a Young's modulus of ≈ 52.8 GPa for an isotropic polycrystal of β- or high-tridymite with a density of ≈ 2.22 g/cm³.

A tetragonal crystal symmetry and an ambient temperature density of ≈ 2.35 g/cm³ is found for α- or low-cristobalite. The stiffness of α-cristobalite is determined experimentally and by molecular dynamic simulations (Kimizuka *et al.* 2005, Yeganeh-Haeri *et al.* 1992), while the Young's modulus of an isotropic polycrystal is ≈ 65.2 GPa under ambient conditions (*e.g.* Pabst & Gregorová 2013). Increasing temperature leads to a displacive phase transition due to tetrahedral rotation and the formation of β- or high-cristobalite. It is comparable to the transition from α- to β-quartz. β-cristobalite is of cubic crystal symmetry with a density of ≈ 2.20 gm/cm³. Its isotropic high-temperature Young's modulus is ≈ 62.3 GPa. This value is determined by molecular dynamic simulations (Kimizuka *et al.* 2000, Swainson & Dove 1995). The isotropic Young's modulus is ≈ 27 GPa at the phase transition close to ≈ 776 °C (Kimizuka *et al.* 2003). A study of the high-temperature complex elastic behaviour of cristobalite is recommended.

Quartzite and sandstone

Rocks, including mono- and polycrystalline grains of quartz, are formed by magmatic, sedimentary or metamorphic processes (*e.g.* Emmons *et al.* 1955). Elastic properties of those rocks are based on the properties of quartz and other associated minerals. Size, shape, orientation, aspect ratio, and cementation of the grains as well as pore space and micro-cracks need to be taken into account as well (*e.g.* Schön 1983). Usually, the experimentally observed elastic moduli of rocks are lower than expected from polycrystalline models based on single-crystal data, which is due to micro-cracks and pores. This also holds for the thermal expansion of rocks or their thermal transport properties (*e.g.* de Wit 2008, Van der Molen 1981). By way of example a quartzite and a sandstone are investigated in this study (Chapter 3).

Quartzite serves as raw material for the silica industry. It is a nearly monomineralic metamorphic rock made of quartz (*e.g.* Emmons *et al.* 1955). Common accessories are sheet silicates, aluminium silicates or iron-bearing minerals (*e.g.* Okrusch & Matthes 2005). Consequently, the density of quartzite can be higher than that of pure quartz. Moreover, quartzite is a medium- to fine-grained and non-porous rock due to grain margin dissolution and re-crystallisation during its genesis out of a siliceous sandstone (*e.g.* Sebastian 2009). Potentially isotropic or anisotropic physical properties of quartzite are linked to the burial history and metamorphism. Quartzites of regional metamorphism at high pressure and low temperature likely exhibit a foliation with anisotropic physical properties. Highly impure sandstones would form shists under these conditions (*e.g.* Emmons *et al.* 1955). In contrast to that, contact metamorphism at high temperature and low pressure typically leads to the formation of physically isotropic quartzites without any foliation. Compressional and shear wave velocities of quartzite are ≈ 5.5 and ≈ 3.9 km/s, respectively (*e.g.* Gupta & Sharma 2012).

Sandstone is a clastic sedimentary rock with grain sizes between 0.062 and 2 mm (*e.g.* Press & Siever 2001). It is formed by physical erosion of a source rock followed by aqueous, aeolian or glacial transport and sedimentation (*e.g.* Leeder 2006). Its mineral content, particle shape, grain sorting, and bedding structures depend on the transportation distance and the deposition environment (*e.g.* Sebastian 2009). Due to its chemical resistance, quartz usually represents the main component in a sand deposit. Subsidence of the loose sediment leads to its diagenesis, which is the consolidation of the material by compaction, drainage, grain margin dissolution, and cementation. The cement of a sandstone can be made of calcite, dolomite, clay, iron oxides, or re-crystallised quartz (*e.g.* Emmons *et al.* 1955). Accessory minerals that are often found in sandstones are sheet silicates and clays from feldspar degradation (*e.g.* Okrusch & Matthes 2005). Besides the mineralogical composition and cementation, the porosity and incorporated pore fluids affect the physical properties of sandstone. The porosity of sandstone is < 26 % because of hexagonal grain packing as well as the previously mentioned properties of grains and cement. It is often associated with high permeability, compared to unfractured quartzite. Whenever the pore space is filled with oil and gas or even water, sandstone formations are of high interest to industry. Schön (1983), for instance, collects a wide range of elastic data with compressional wave velocities of up to ≈ 5 km/s and a ratio between shear and compressional waves of ≈ 0.5. In laboratory experiments, velocities observed perpendicular to the bedding are generally smaller than parallel to it (Schön 1983).

Fused silica

Fused silica is also called vitreous silica and silica glass or casually named quartz glass, which obviously is an oxymoron. It is the amorphous solid of super-cooled SiO_2 melt (*e.g.* Bell & Dean 1972). Thus, it is chemically identical with quartz, but structurally different. It is also used for a large scope of industrial applications (*e.g.* Brückner 1970). A review of its physical properties is published for instance by Ojovan (2008). The elastic properties of fused silica are well-known (*e.g.* Babcock *et al.* 1954, Fukuhara & Sanpei 1994, Fukuhara *et al.* 1997, Marx & Sivertsen 1953). Fused silica is elastically isotropic. Its stiffness tensor is composed of two independent coefficients, C_{11} and C_{12} (*e.g.* Levy *et al.* 2001). Its Young's modulus is ≈ 73 GPa (Fig. 10) under ambient conditions (Spinner 1954) and increases with temperature (Spinner 1956). Contrary to quartz, a phase transition at ≈ 573 °C does not exist, whereas Huang & Kieffer (2004a, 2004b) claim to recognize similarities to the α-β transition in cristobalite at high pressure and high temperature. The maximum stiffness of fused silica is recorded at ≈ 1100 °C (Spinner 1962), while it is stable at least up to ≈ 1200 °C (*e.g.* Pine 1969, Spinner & Cleek 1960). At ≈ 300 °C (Levelut *et al.* 2006) and close to ≈ - 273 °C (*e.g.* Anderson & Bömmel 1955, Bartell & Hunklinger 1982, Jäckle 1972, Piché *et al.* 1974), fused silica exhibits viscoelastic effects. In addition, its stiffness coefficients decrease for pressures < 2 GPa (Kondo *et al.* 1981) and re-increase above ≈ 2 GPa (Suito *et al.* 1992). With $\approx 0.55 \cdot 10^{-6}$ K^{-1}, the coefficient for the linear thermal expansion of fused silica is small in comparison to quartz and most other materials (*e.g.* Gaskell 1966a, Otto & Thomas 1963, Smyth 1955).

Summary and hypothesis

It is shown in terms of the Young's modulus (*e.g.* Perrier & De Mandrot 1923) and the compressional wave velocity (*e.g.* Lakshtanov *et al.* 2007) that the stiffness of single-crystal α-quartz anisotropically decreases with increasing temperature towards a minimum at the α-β transition. The values recover again in the stability field of the β-phase. Various authors also find this effect in quartz-bearing rocks at ambient (*e.g.* Beck 2010, Doncieux *et al.* 2008, Peng & Redfern 2013) and high pressure (*e.g.* Fielitz 1976, Kern 1978), while it is lacking in fused silica (*e.g.* Spinner 1956).

High- (*e.g.* Lakshtanov *et al.* 2007) and low-frequency (*e.g.* Perrier & De Mandrot 1923) elastic data of quartz differ significantly in the vicinity of the α-β transition. The Young's modulus recorded by static experiments is lower than values modelled from high-frequency stiffness coefficients at the same temperature. Furthermore, the α-β transition is associated with intensified attenuation due to intra- (*e.g.* Klumbach & Schilling 2012, Nikitin *et al.* 2007, Peng *et al.* 2012) and intercrystalline viscoelasticity.

This could have implications for the interpretation of seismic data from the Earth's crust (*e.g.* Kuo-Chen *et al.* 2012, Marini & Manzella 2005, Mechie *et al.* 2004, Sheehan *et al.* 2014, Shillington *et al.* 2013, Zandt *et al.* 1996). Isothermal frequency-dependent differences of the compressional wave velocity and the seismic quality factor derived from the complex Young's modulus could be used to estimate subsurface temperatures and distinguish between fully crystallised or partly molten crust. This gives rise to the following hypothesis: the Young's modulus of quartz becomes systematically frequency-dependent in the vicinity of the α-β transition. The primary tool to test this hypothesis is a dynamic mechanical thermal analysis.

2. Experimental methods

Dynamic mechanical thermal analysis (DMTA)

Dynamic mechanical thermal analysis (DMTA) serves to determine elastic and viscoelastic material properties at variable frequencies and temperatures[2]. This study uses the *Eplexor* DMTA system by *Gabo Qualimeter*, which is equipped with a special furnace for temperatures from - 100 to 1500 °C. The specimen holder of the experimental set-up is therefore made of polycrystalline $MoSi_2$ (*e.g.* Chu *et al.* 1999). The system also uses a 150 N load cell with a precision of $1.5 \cdot 10^{-3}$ N. It covers a frequency range of 0.01 to 100 Hz for dynamic loading, whereas this study uses 0.1 to 20 Hz.

Prior to dynamic loading, the position of a specimen is fixed by a static force. In this study the maximum dynamic force is set to half the amount of the static force. While a sinusoidal stress σ

$$\sigma(t) = \sigma_0 \ \sin(\omega t), \tag{16}$$

is applied on the specimen, its time-dependent bulk deformation ε

$$\varepsilon(t) = \varepsilon_0 \ \cos(\omega t - \delta) \tag{17}$$

is measured as a function of frequency in terms of the angular rate ω. Stress and strain maxima are denoted as σ_0 and ε_0, respectively (Fig. 11, left). The dynamic strain of the specimen is measured by a displacement transducer that has a precision of $1 \cdot 10^{-7}$ m. All three parameters - stress, strain, and their phase lag - are used to determine the complex Young's modulus E^*

$$E^*(\omega) = E'(\omega) + \mathrm{i}\, E''(\omega). \tag{18}$$

The complex Young's modulus consists of the storage modulus E' and the dissipation modulus E'', which correspond to the real part and the imaginary part of the complex number (Fig. 11, right), respectively. In the Gaussian representation the moduli form a rectangular triangle. Thus, they can be converted by

$$\tan(\delta) = \frac{E''(\omega)}{E'(\omega)}. \tag{19}$$

The two components also correlate to the amount of elastically stored and dissipated energy (*e.g.* Ferry 1961, Flügge 1975, Lakes 2009, Menard 1999, Shaw & Mac Knight 2005). Furthermore, an intrinsic attenuation of the apparatus causes an offset of the observed phase lag. This has to be taken into account for the evaluation of the moduli. Thus, a calibration is made with a specimen of corundum ceramics yielding a phase lag of ≈ 0.02, which has to be subtracted from the observed data.

This study uses two specimen holders, both with a symmetrical three-point bending geometry, consisting of an indenter from above and two supports from below with a spacing *d* of 20 and 40 mm (Fig. 12). The flexure of an elongated plate-like specimen leads to compressional stresses in its upper part and extensional stresses in its lower part. For the outer fibre in the lowermost part of the specimen, the stress is determined by

$$\sigma(\omega) = \frac{3\,F(\omega)\,d}{2\,w\,h^2} \tag{20}$$

---

[2] Here the term "viscoelastic" stands for the non-plastic deformation of a loaded specimen including energy dissipation.

and the strain equals

$$\varepsilon(\omega) = \frac{6\,h\,D(\omega)}{d^2}, \tag{21}$$

whereas the thickness and the width of the specimen are defined as *h* and *w*, respectively. The parameters *F* and *D* accordingly represent the dynamic force and the equivalent bulk deflection. The complex Young's modulus is derived from the frequency-depending notation of Hooke's law

$$E^*(\omega) = \frac{\sigma(\omega)}{\varepsilon(\omega)} \tag{22}$$

using equations (20) and (21)

$$E^*(\omega) = \frac{F(\omega)\,d^3}{4\,D(\omega)\,w\,h^3} \tag{23}$$

according to the experimental geometry.

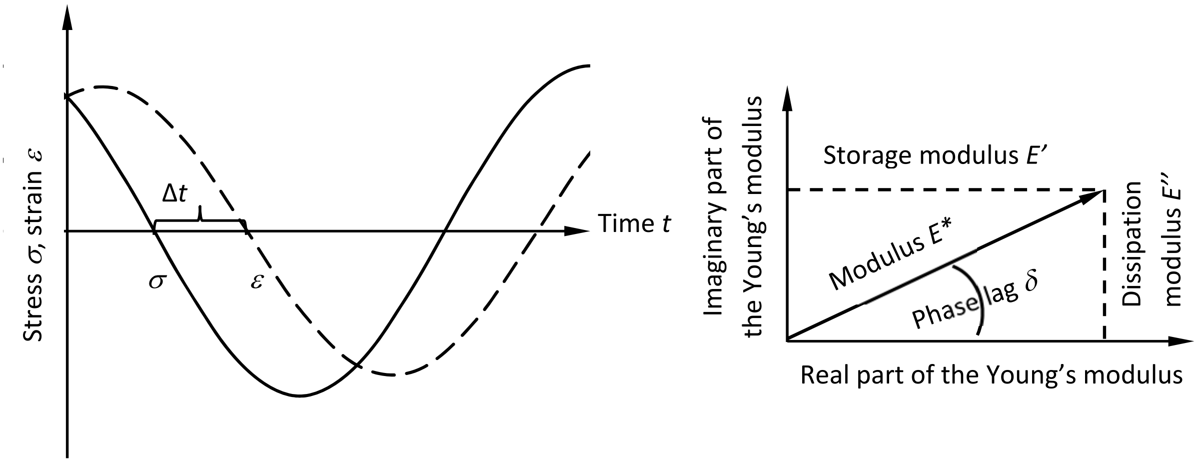

Fig. 11: Forced sinusoidal variation of stress and response in strain with a certain phase lag due to viscoelastic effects (left). Complex Young's modulus in the Gaussian representation (right).

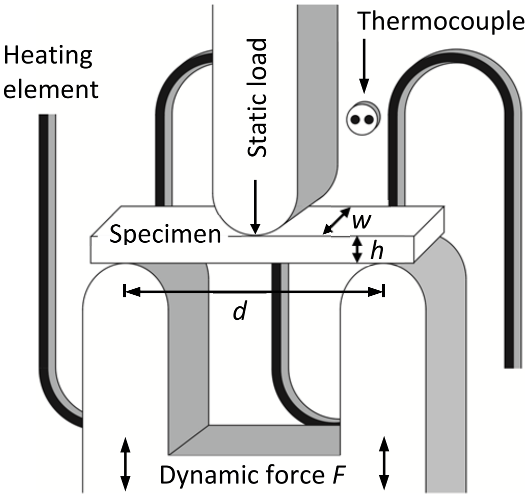

Fig. 12: Schematic view of a specimen in the symmetrical three-point bending experimental set-up.

Calibration of DMTA temperature readings

During a DMTA measurement the experimental temperature T is not determined on the specimen surface, since the contact with a thermocouple might affect its the bending. A Pt13%Rh-Pt thermocouple is located near the heating element of the furnace (Fig. 12) and used to control and record the temperature. The temperature where the complex Young's modulus reaches its minimum is abbreviated by $T_{\alpha\beta}$ and found to be lower than the α-β transition temperature given in literature at ≈ 573°C. For synthetic quartz, the α-β transition is recorded at ≈ 560 and ≈ 538 °C for 20 and 40 mm support spacings, respectively. Thus, the temperature readings need to be corrected with a linear temperature calibration according to

$$T = T\,\frac{573\,°\mathrm{C} - T_0}{T_{\alpha\beta} - T_0}, \tag{24}$$

where T_0 corresponds to ambient temperature.

Cohen & Klement (1967), for instance, evaluate the temperature and pressure dependence of the α-β transition in quartz by differential thermal analysis. Thereby temperature differences between a powder specimen and a reference (corundum) are recorded. This study includes recordings from differential thermal analysis and thermal gravimetric analysis (mass changes) of synthetic quartz and Dalsland quartzite (Chapter 3) at ambient pressure, while the onset of the α-β transition is determined to take place at ≈ 573 °C in both cases (Appendix 11, Appendix 12). The experiments are performed with a *Netzsch STA 409 PC/PG* system, which is equipped with a special furnace for temperatures up to 1650 °C. A powder mass of ≈ 64.80 mg is taken from synthetic quartz and of ≈ 103.94 mg from the quartzite. The masses of the powder references of corundum are ≈ 100.35 mg and ≈ 100.14 mg, respectively. Observed minima in quartz and quartzite correspond to endothermic reactions, while an exothermic reaction would exhibit a maximum. Mass changes in association with the α-β transition are determined neither for quartz nor for quartzite. Natural quartz, Lahr sandstone and fused silica (Chapter 3) are not examined with the differential thermal analysis system, since their observed α-β transition temperatures in DMTA are consistent with quartz. The occurrence of the incommensurate phase is neglected, as it is beyond the experimental precision of DMTA (Chapter 1).

Correction of results from DMTA by thermal expansion

The Young's moduli obtained from DMTA are basically affected by the thermal expansion u of the width and the thickness of a specimen. For this reason, all moduli observed at elevated temperature are overestimated. The storage and dissipation moduli as a function of temperature are corrected on the basis of thermal expansion data published by Raz *et al.* (2002, Fig. 9, Tab. 1) with

$$u_\alpha = \frac{a_\alpha}{T_\alpha - T} + b_\alpha\left(T_\alpha - T\right)^2 + c_\alpha\left(T_\alpha - T\right) + d_\alpha \tag{25}$$

and

$$u_\beta = a_\beta T + b_\beta \tag{26}$$

for α- (25) and β-quartz (26), respectively. In this context T is the calibrated temperature, while a_α, b_α, c_α, d_α, T_α, a_β, and b_β are the modelling parameters of the anisotropic fits for the two quartz phases.

Tab. 1: Modelling parameters for the thermal expansion of quartz as a function of temperature across the α-β transition at ambient pressure according to Fig. 9.

u_{ij} [%]	a_α [°C]	b_α [°C^2]	c_α [°C^{-1}]	d_α [%]	T_α [°C]	a_β [%/°C^{-1}]	b_β [%]
u_{11}	55.5	$2.7\cdot10^{-7}$	$-1.8\cdot10^{-3}$	0.93	653	$2.1\cdot10^{-4}$	1.63
u_{33}	21.4	$3.1\cdot10^{-7}$	$-1.4\cdot10^{-3}$	0.70	656	$4.5\cdot10^{-4}$	0.73

The anisotropic thermal expansion of a triclinic material is described by a second-rank tensor u_{ij} that has six independent coefficients (*e.g.* Nye 1992). For trigonal and hexagonal crystal symmetries, the tensor is simplified and three coefficients remain. These are u_{33} and u_{11} that are oriented parallel and perpendicular to the *c*-axis of the crystal, respectively, while u_{22} equals u_{11}. Thus, the inverse of the square root of the thermal expansion is three-dimensionally represented by a rotationally symmetrical ellipsoid. For any crystallographic direction it is

$$u_{\phi\psi} = u_{11}\,n_1^2 + u_{11}\,n_2^2 + u_{33}\,n_3^2, \tag{27}$$

where n_1 to n_3 are the directional cosines. The thickness of an elongated plate-like DMTA specimen at elevated temperature is corrected by the thermal expansion that is oriented at an angle of 90° to the polar distance along which the specimen was formerly cut. Hence, the thickness of the specimen is corrected by u_{11}, for a quartz specimen cut parallel to the *c*-axis of the crystal. The thickness is corrected by u_{33}, for quartz cut perpendicular to the *c*-axis. The width of a specimen is always corrected using u_{11}. The correction of the moduli is made by

$$E^* = E^* \left(\frac{h}{h + h\,u_{\phi\psi}}\right)^3 \left(\frac{w}{w + w\,u_{\phi\psi}}\right) \tag{28}$$

with reference to the experimental geometry.

Theoretically, the thermal expansion of the support spacing and the elongation of the indenter need to be corrected as well. Regarding single-crystal $MoSi_2$ with a tetragonal symmetry, the anisotropic thermal expansion is found to be significantly lower than that of quartz (*e.g.* Clark 1966, Zhao *et al.* 2004, Zhu *et al.* 2009). Thus, the expansion of the support spacing can be neglected, since its influence on the results is beyond the precision of the experiments.

DMTA experimental parameters

Both static and dynamic forces of the DMTA experiments are removed, while the specimen is heated to a certain temperature in order to minimise the residual stress and to better control the development of micro-cracks (Tab. 2). Temperature steps of up to 25 K are used. In the vicinity of the α-β transition, the steps are reduced to 5 to 3 K. The dynamic measurements are made under isothermal conditions. Prior to the recordings, between 180 and 300 s are allowed for temperature equilibration of the specimen and the experimental set-up. Usually, the data points for different loading frequencies are distributed logarithmically. In addition, some experiments are performed with a constant heating rate of 3 K/min using sinusoidal stress with a constant frequency of 10 Hz.

The force applied to a specimen should not exceed the elastic limit of the material from which it is made of. Hence, several specimens of quartz with the same crystallographic orientation are tested by

DMTA at different loads. Test are also carried out for three different crystallographic directions and it is found that the dynamic stresses and strains correctly exhibit linear relations according to the anisotropic Young's modulus, respectively (Appendix 13).

Tab. 2: DMTA experimental parameters. Abbreviations used for the specimen names are: *s* = synthetic, *n* = natural, *f* = fused, *c* = ceramic, *L-Sst* = Lahr sandstone, *D-Qtz* = Dalsland quartzite. The number of frequency and temperature data points is given in parentheses.

Measure-ment	**Specimen name**	**Spacing [mm]**	**Static force range [N]**	**Dynamic force range [N]**	**Frequency range [Hz]**	**Temperature range [°C]**
1	*s*-SiO_2-01	20	3.9 - 4.1	2.0 - 2.0	0.5 - 20 (10)	29 - 615 (52)
2	*s*-SiO_2-02	20	3.8 - 4.1	1.9 - 2.0	0.5 - 20 (10)	27 - 615 (52)
3	*s*-SiO_2-03	20	3.9 - 4.1	1.9 - 2.0	0.5 - 20 (10)	29 - 615 (52)
4	*s*-SiO_2-04	20	5.9 - 6.1	2.9 - 3.0	0.5 - 20 (10)	23 - 615 (52)
5	*s*-SiO_2-05$_b$	20	4.9 - 5.2	2.9 - 3.1	0.1 - 20 (14)	534 - 587 (18)
6	*s*-SiO_2-05$_b$	20	4.9 - 5.2	2.9 - 3.1	0.1 - 20 (14)	535 - 586 (18)
7	*s*-SiO_2-06	40	3.3 - 4.3	0.7 - 1.1	1.0 - 20 (5)	53 - 577 (39)
8	*s*-SiO_2-07	40	3.1 - 3.8	0.6 - 0.8	1.0 - 20 (5)	53 - 567 (37)
9	*s*-SiO_2-08	40	4.5 - 6.5	1.5 - 2.2	1.0 - 20 (5)	53 - 621 (47)
10	*s*-SiO_2-09	40	4.9 - 7.0	1.7 - 2.5	1.0 - 20 (5)	53 - 572 (38)
11	*s*-SiO_2-10	40	4.4 - 7.7	1.6 - 2.9	1.0 - 20 (5)	53 - 572 (27)
12	*s*-SiO_2-11	40	4.0 - 6.7	1.4 - 2.4	1.0 - 20 (5)	53 - 572 (26)
13	*s*-SiO_2-12	40	4.2 - 8.1	1.4 - 3.6	1.0 - 20 (5)	53 - 609 (33)
14	*s*-SiO_2-13	40	4.2 - 5.9	1.2 - 2.0	1.0 - 20 (5)	53 - 610 (45)
15	*s*-SiO_2-14	40	4.4 - 6.3	1.3 - 2.1	1.0 - 20 (5)	53 - 573 (38)
16	*s*-SiO_2-15	40	3.9 - 5.7	1.2 - 1.9	1.0 - 20 (5)	53 - 577 (39)
17	*s*-SiO_2-16	40	4.4 - 6.4	1.4 - 2.2	0.5 - 20 (5)	53 - 577 (39)
18	*n*-SiO_2-01	20	5.8 - 6.0	3.0 - 3.1	10 (1)	33 - 669 (121)
19	*n*-SiO_2-02	20	5.8 - 6.0	3.0 - 3.0	0.5 - 20 (10)	35 - 575 (35)
20	*D-Qtz*-01$_a$	20	59.7 - 60.2	30.0 - 30.0	10 (1)	34 - 663 (121)
21	*D-Qtz*-01$_a$	20	59.8 - 60.1	29.9 - 30.0	10 (1)	648 - 32 (121)
22	*D-Qtz*-01$_a$	20	59.7 - 60.2	29.9 - 30.0	10 (1)	420 - 639 (71)
23	*D-Qtz*-01$_a$	20	59.9 - 60.2	29.9 - 30.0	10 (1)	628 - 412 (71)
24	*D-Qtz*-01$_b$	20	5.0 - 5.1	2.9 - 3.1	0.1 - 20 (14)	533 - 576 (15)
25	*D-Qtz*-01$_b$	20	5.0 - 5.2	2.9 - 3.0	0.1 - 20 (14)	534 - 571 (13)
26	*D-Qtz*-01$_b$	20	4.9 - 6.0	2.9 - 3.0	0.1 - 20 (14)	534 - 586 (18)
27	*L-Sst*-01	20	19.9 - 20.2	14.5 - 15.0	10 (1)	131 - 630 (51)
28	*f*-SiO_2-01	20	5.0 - 5.1	2.9 - 3.0	1.0 - 21 (9)[1]	41 - 718 (34)
29	*f*-SiO_2-02	20	5.9 - 6.0	2.9 - 3.0	0.5 - 20 (10)	25 - 615 (52)
30	*c*-Al_2O_3-1	20	3.6 - 4.1	2.0 - 2.0	0.5 - 20 (10)	51 - 616 (52)

[1] linear distribution of data points

Ultrasonic experiments

Ultrasonic frequencies range between 20 kHz and 10 GHz, out of the human acoustic spectrum (*e.g.* Blumenauer 1994). Investigations with ultrasonic waves are non-destructive and commonly applied for quality control purposes (*e.g.* Deutsch *et al.* 1999). Ultrasonic waves also can be used to evaluate the elastic properties of minerals and rocks, which usually increase with density and pressure (*e.g.* Brocher 2005, Christensen 1996, Kanamori & Mizutani 1965) and decrease with temperature (*e.g.* Fig. 7). The determination of elastic material properties is based on logging the travel times of ultrasonic waves (*e.g.* Borgnis 1955, Brugger 1965, Castagnède *et al.* 1990). The compressional wave velocity v_p is fastest, followed by the slower velocities v_{sv} and v_{sh} of shear waves oscillating "parallel" and "perpendicular" to their propagation direction, respectively. In the principal directions of an anisotropic crystal as well for isotropic materials, only one shear wave is observed. In porous rocks different types of stored fluids significantly affect the elastic wave velocities and their attenuation properties (*e.g.* Castagna *et al.* 1985). Most ultrasonic studies of quartz-bearing rocks are limited to temperatures far below the α-β transition (*e.g.* Hughes & Cross 1951, Hughes & Maurette 1956).

Ultrasonic testing is carried out using piezoelectric sensors. There are two fundamental modes of operation, the transmission of signals and reflection of signals, which is also called impulse-echo method. The transmission method requires two identical transducers, one acting as a pulser and one as a sensor to receive the signal. These are connected to the specimen by a couplant and adjusted opposite to the polished specimen faces in consideration of a parallel alignment. The velocity v of an elastic wave is determined from its travel time t_{tra} over a distance s by

$$v = \frac{s}{t_{tra} - t_{sys}}, \tag{29}$$

taking into account the reaction time of the system t_{sys}. The reaction time depends on the ultrasonic device and the installed sensors. It is determined for all sensors used in this study (Appendix 17) by travel time recordings for several distances (Appendix 15) in an aluminium specimen (Appendix 14) using the linear regression method (Appendix 16).

In contrast to this, the impulse-echo method is based on the simultaneous emission and the detection of a signal with a single transducer by interface wave reflection. The wave velocity is given by

$$v = \frac{2\,s}{t_{tra} - t_{sys}}. \tag{30}$$

The reaction time for ultrasonic transmission measurements is equal to the reaction time of recordings form the impulse-echo method. Due to wave refraction and interference, the impulse-echo method is less suitable for shear wave investigations (*e.g.* Kushibiki *et al.* 2002, Liu *et al.* 2002).

The full determination of the elastic properties of any anisotropic material requires measurements along different crystallographic orientations (*e.g.* Alshits & Lothe 2006, Bechmann 1934, Huntington 1947, Mayer & Parker 1961, Naumenko 1996, Waterman 1959). The square sum R_{ij} of the different wave velocities in a particular direction is given by

$$v_p^2 + v_{sv}^2 + v_{sh}^2 = R_{\mathrm{ij}} \tag{31}$$

and simplifies - concerning the shear wave velocity in principal directions - to

$$2\,v_s = \sqrt{R_{\mathrm{ij}} - v_p^2}\,. \tag{32}$$

It is described by a second-rank tensor. The anisotropic Young's modulus is determined from ultrasonic measurements by solving Christoffel's equation (12) and using the resultant elasticity coefficients for the tensor rotation (7). The Young's modulus of an isotropic solid can be obtained from a simplification that uses the velocities two of the two different wave types and the density of the material (*e.g.* Zisman 1933) in the way of

$$E_{VRH} = \frac{\rho v_{s\,VRH}^2 (3 v_{p\,VRH}^2 - 4 v_{s\,VRH}^2)}{v_{p\,VRH}^2 - v_{s\,VRH}^2}. \tag{33}$$

This study uses an *Olympus PR5058* ultrasonic pulser-receiver system that is connected to a *DSO-X 3024 A* digital storage oscilloscope made by *Agilent Technologies* and transducers by *Panametrics NDT* in the transmission mode. The compressional wave velocities of a synthetic quartz single crystal and a specimen made of Dalsland quartzite (Chapter 3) are examined with a pair of *V125* transducers (0.375” diameter, 2.25 MHz frequency maximum, 1 MHz high-pass filter, 3 MHz low-pass filter, ≈ 0.28 μs reaction time). Specimens of Lahr sandstone (Chapter 3) are investigated with *V102* transducers for their compressional wave velocities (1” diameter, 1 MHz frequency maximum, 0.3 MHz high-pass filter, 3 MHz low-pass filter, ≈ 0.13 μs reaction time). The shear wave velocities in quartz are determined with *V153* transducers (0.5” diameter, 1 MHz frequency maximum, 0.3 MHz high-pass filter, 3 MHz low-pass filter, ≈ 0.39 μs reaction time). *V154* transducers are used to evaluate the shear wave velocities in quartzite (0.5” diameter, 2.25 MHz frequency maximum, 1 MHz high-pass filter, 3 MHz low-pass filter, ≈ 0.27 μs reaction time). The shear wave velocities in the sandstone specimens are measured with *V152* transducers (1” diameter, 1 MHz frequency maximum, 0.3 MHz high-pass filter, 3 MHz low-pass filter, ≈ 0.1 μs reaction time).

Coupling of the sensors to synthetic quartz and quartzite is accomplished with a gel-type couplant and a shear gel, both of which are provided by *Sonotech*. A thin layer of humid potter’s clay is used as couplant to determine the elastic wave velocities in sandstone. The maximum amplitude of the signal observed in every measurement is adjusted to the full screen of the oscilloscope by regulation of the voltage for the initial pulse and the attenuation of the signal. The travel times of the elastic waves are measured at the flank of the signal’s first arrival.

Uniaxial and triaxial compression tests

In contrast to ultrasonic testing, the mechanical properties of synthetic and natural rocks (*e.g.* Brace & Jones 1971, Hallbauer *et al.* 1973) as well as of polycrystals and single crystals (*e.g.* Coe & Paterson 1969, Scholz 1972) can be investigated destructively with compression tests (*e.g.* Jaeger *et al.* 2008). Usually, cube-shaped or cylindrical specimens are loaded via two coplanar plates. This leads to axial shortening and lateral widening of the specimen (DIN EN 1926) as long as the Poisson’s ratio of the material is positive (*e.g.* Gercek 2007, Lethbridge *et al.* 2010). The strength of a material σ_u is determined from the maximum force F_{max} on the specimen face A prior to macroscopic failure by

$$\sigma_u = \frac{F_{max}}{A}. \tag{34}$$

The Young’s modulus and Poisson’s ratio of a specimen can be determined using displacement transducers to observe the axial shortening and the lateral widening of a specimen (*e.g.* Hirsch 2006, Klumbach 2008, 2010). In this study Lahr sandstone (Chapter 3) is examined. Only the axial deformation of the specimens is recorded. On this basis the Young’s modulus and the rock strength could be identified. The Young’s modulus is obtained between ≈ 40 to ≈ 60 % of the maximum stress. Differences between statically and dynamically determined Young's moduli might be expected - even under ambient conditions (Ide 1936).

Besides uniaxial compression tests, a triaxial experiment is performed with a cylindrical specimen of Lahr sandstone. A confining pressure on such a cylindrical specimen corresponds to a biaxial rather than to a triaxial state of stress (DIN 18137-2). Generally, the lateral widening of a specimen is restrained, while both the Young's modulus and the strength of the material increase. Triaxial experiments also yield the internal friction angle and the cohesion of the material (*e.g.* Stüwe 2000). Furthermore, the residual strength and the tensile strength of the material are determined.

In uniaxial and triaxial compression tests, a specimen is usually loaded and unloaded cyclically with a stepwise increase of the axial stress and the confining pressure. First loading leads to the closure of laterally oriented micro-cracks and the reduction of pore space within the specimen. This results in a non-linear shape of the deformation curve during loading and a residual strain is observed after unloading. At the end of each loading or unloading phase, the stress is kept constant temporarily, as creeping might occur within the material. If the stress exceeds the elastic limit of the material axial micro-cracks are formed. This is again associated with a non-linear development of the loading curve (*e.g.* Blumenauer 1994) and the emissions of acoustic signals, which is known as the Kaiser effect (*e.g.* Mayr *et al.* 2011).

Results from the uniaxial compression of natural rocks vary quite often. Consequently, a minimum of five specimens should be examined, in order to determine reliable mean values of the previously introduced parameters. Since the basal faces of a specimen cylinder are affected by shear forces due to the contacting loading plates, the axial ratio of a specimen should be at least 2.5:1 in order to guarantee uniaxial stress inside (*e.g.* Wittke 1984). For smaller ratios, the compressional strength needs to be corrected (*e.g.* Obert & Duval 1967) according to

$$\sigma_{red} = \frac{8\,\sigma_u}{7 + \frac{5\,d}{2\,l}}. \tag{35}$$

This also holds for the specimens that are investigated in this study (Tab. 8). Analogously, a correction of the Young's modulus is recommended.

3. Specimen description

Properties and preparation of quartz

Synthetic quartz single crystals are bought from *Maicom Quarz*. The amounts of impurities and lattice defects are not examined, as these are in agreement with the industrial standard for technical applications (DIN EN 60758). To figure out crystallographic orientations, the elastic properties of quartz are examined by the transmission of ultrasonic waves. A cube-shaped specimen with polished faces is used, including a seed from the hydrothermal growth of the crystal (Tab. 3, Appendix 18 - Appendix 21).

The complex elastic properties of quartz as a function of temperature across the α-β transition are obtained by DMTA for differently oriented specimens (Tab. 2, Tab. 7). For this purpose, elongated plate-like specimens are ground and polished to a thickness < 1 mm. Furthermore, natural quartz crystals of gem quality are prepared for DMTA and examined in the same way as synthetic quartz.

Tab. 3: Relative to the main axes of synthetic single-crystal quartz and under ambient conditions, travel times of compressional and shear waves along the mean distances s_m are given as t_p, t_{sv}, and t_{sh}, respectively. Wave velocities with uncertainties are v_p, v_{sv}, and v_{sh} (Appendix 9).

Orientation	$s_m \pm \Delta s_m$ **[mm]**	$t_p \pm \Delta t_p$ **[µs]**	$v_p \pm \Delta v_p$ **[km/s]**	$t_{sv} \pm \Delta t_{sv}$ **[µs]**	$v_{sv} \pm \Delta v_{sv}$ **[µs]**	$t_{sh} \pm \Delta t_{sh}$ **[km/s]**	$v_{sh} \pm \Delta v_{sh}$ **[km/s]**	$R_{ij} \pm \Delta R_{ij}$ **[km²/s²]**
ll *c*-axis	20.68	3.25	6.36	4.35	4.754	4.35	4.754	86*
	± 0.07	± 0.02	± 0.05	± 0.02	± 0.025	± 0.02	± 0.025	± 4
ll *a*-axis	22.10	3.82	5.79	4.32	5.116	6.68	3.31	71*
	± 0.10				± 0.028		± 0.04	
ll *Y*-axis	20.723	3.46	5.99		04.486*	5.35	3.873	71*
	± 0.028		± 0.04		± 0.025		± 0.022	

* according to (31)

Properties and preparation of quartzite and sandstone

The quartzite examined in this study is from the Åmål province in southwestern Sweden and known as Dalsland quartzite. It is flesh-coloured, homogeneous, fine-grained, and ≈ 1.000 Ma old (Johansson 1985). According to Beck (2010), it has an extremely weak texture and a bimodal grain size distribution between ≈ 5 µm and ≈ 1 mm (Fig. 13, A - C). This indicates its genesis might be related to contact metamorphism. The composition of Dalsland quartzite is examined by X-ray powder diffraction (Fig. 14), with an X-ray beam being refracted by the crystal lattice (*e.g.* Nesse 2000), and X-ray fluorescence (Tab. 4), where X-rays are triggered by electron excitement due to radiation (*e.g.* Tertian & Claisse 1982).

The sandstone investigated in this study is from Lahr in southwestern Germany. It is classified as part of the Triassic Bausandstein formation *sus* (Fig. 13, 6 - 8). A detailed characterisation is presented by Hirsch (2008). Results of three out of four specimens from that study are in agreement with the observations made in this study. The rock is red-coloured due to an iron-bearing cement, homogeneous, well-sorted, and well-rounded with medium- to coarse-grained quartz sand. Bedding is weakly developed. Thin section countings by Hirsch (2008) yield ≈ 90 % of mono- and polycrystalline quartz grains. X-ray fluorescence (Tab. 4) and X-ray diffraction data (Fig. 15) are collected by Mühlbach *et al*. (2013). In addition, Rietveld refinements are performed with fullprof using ICSD and COD data (Allmann & Hinek 2007, Belsky *et al.* 2002, Brown & Mc Mahon 2002, Downs & Hall-Wallace 2003, Downs *et al.* 1994, Gražulis *et al.* 2009, 2012, Kaduk 2002, Le Page & Donnay 1976, Mc Cusker *et al.* 1999, Toby 2006).

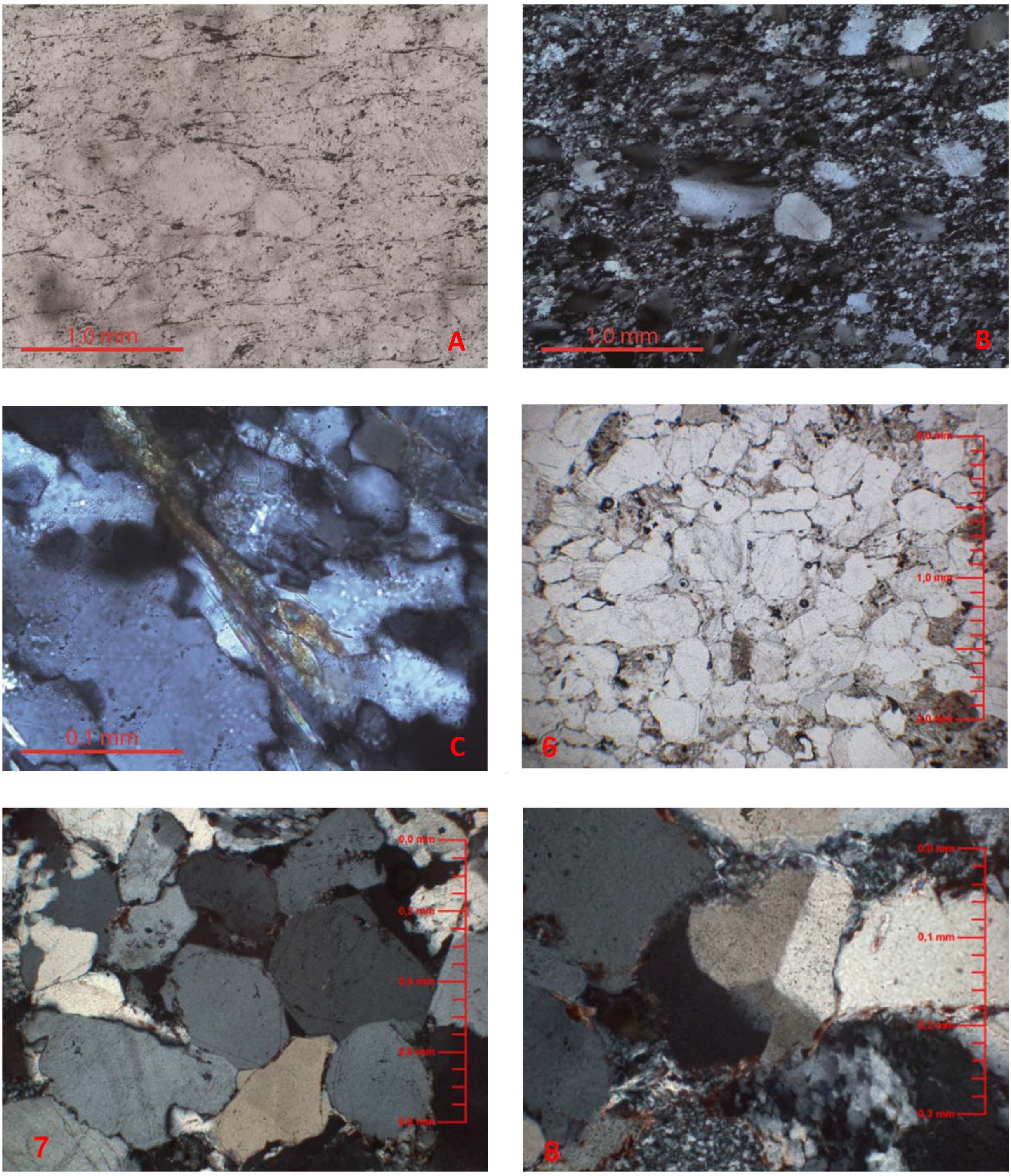

Fig. 13: Thin sections of Dalsland quartzite (A-C, Beck 2010) and Lahr sandstone (6-8, Hirsch 2008) under parallel (6, A) and crossed polarisers (7-8, B-C).

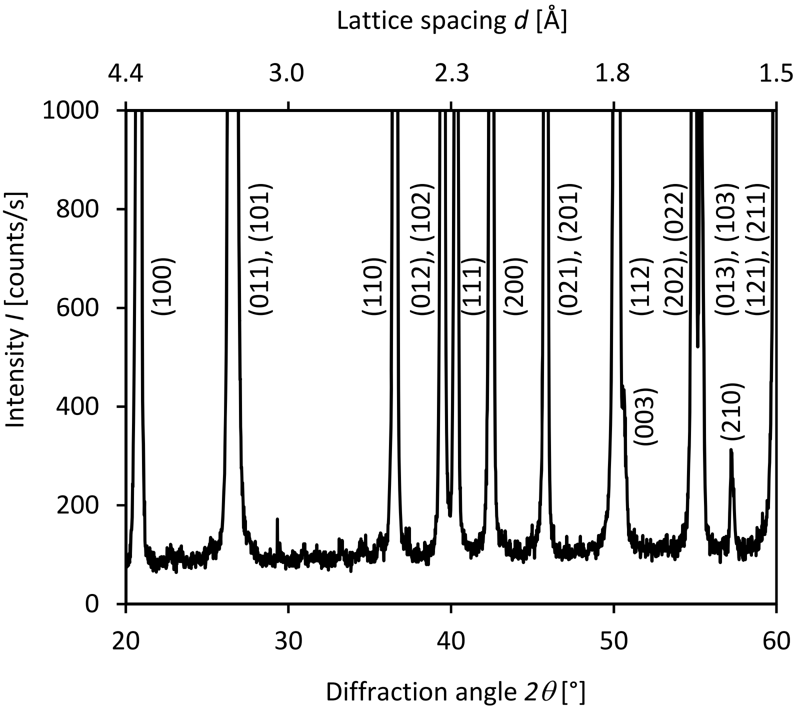

Fig. 14: Diffraction pattern of Dalsland quartzite with (*hkl*) for quartz (wave length = 1.54051, maximum intensity ≈ 56,700 cts/s, speed = 0.25, time step = 4.8, width = 0.02, fixed slit, 10 % uncertainty).

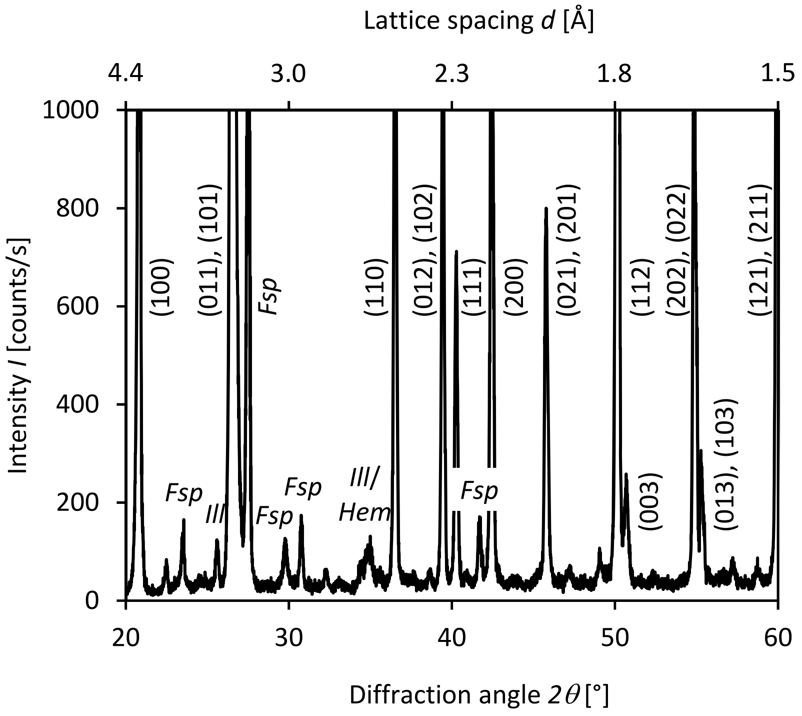

Fig. 15: Diffraction pattern of Lahr sandstone with (*hkl*) for quartz (wave length = 1.54051, maximum intensity ≈ 20,000 cts/s, speed = 0.5, time step = 1.2, width = 0.01, variable slit, 10 % uncertainty). Mineral abbreviations according to Whitney & Evans (2010).

While the interpretation of X-ray diffraction data confirms that quartz is the main component of both Dalsland quartzite and Lahr sandstone, normative X-ray fluorescence data are used to estimate the amount of secondary minerals. Dalsland quartzite consists of ≈ 99 % quartz and a minor amount of accessory sheet silicates. These are composed of ≈ 70 % muscovite[3]/illite and ≈ 30 % biotite. Beck (2010) also observes partial degradation of the biotite.

Tab. 4: Normative main oxides in quartzite, sandstone, and fused silica, determined from observations by powder X-ray fluorescence (± 1 to 5 % uncertainty).

Material	SiO_2 [wt%]	Al_2O_3 [wt%]	Fe_2O_3 [wt%]	K_2O [wt%]	TiO_2 [wt%]	Na_2O [wt%]	CaO [wt%]	MgO [wt%]	Ignition [wt%]
Quartzite†	98.70	0.39	0.31	0.17	0.02	0.02	0.01		0.37
Sandstone††	94.75	2.55	0.45	1.73	0.03	0.07	0.07	0.03	0.29
Sandstone‡	94.60	2.88	0.25	1.62	0.03	0.07	0.05	0.05	0.38
Fused silica‡‡	99.98								unkn.

† Beck (2010) †† Mühlbach *et al.* (2013) ‡ mean data from Hirsch (2006) ‡‡ GVB (2014)

In contrast to that, the X-ray fluorescence data of Lahr sandstone reveals that it consists of > 93 % quartz, with minor amounts of feldspar, plagioclase, and various accessory minerals. ≈ 70 % of muscovite/illite and ≈ 30 % of biotite are identified (Tab. 5). The X-ray diffraction pattern of Lahr sandstone (Fig. 15) also exhibits secondary illite and kaolinite, which most likely result from the degradation of mica and feldspar, respectively. Hirsch (2008) notes a bulk density of ≈ 2.63 g/cm^3, which is close to that of pure quartz.

Tab. 5: Normative mineral content in Dalsland quartzite and Lahr sandstone as obtained from the previously presented X-ray fluorescence data (Tab. 4). Mineral abbreviations according to Whitney & Evans (2010): Qtz = Quartz SiO_2, Or = Orthoclase $K[AlSi_3O_8]$, Ab = Albite $Na[AlSi_3O_8]$, An = Anorthite $CaAl_2Si_2O_8$, Kln = Kaolinite $Al_4[Si_4O_{10}(OH)_8]$, Ms = Muscovite $KAl_2[AlSi_3O_{10}(OH,F)_2]$, Mrg = Margarite $CaAl_2(Al_2Si_2)O_{10}(OH)_2$, Pg = Paragonite $NaAl_2[AlSi_3O_{10}(OH)_2]$, Bt = Biotite $K(Mg,Fe^{2+},Mn^{2+})_3[(Al,Fe^{3+},Ti^{3+})Si_3O_{10}(OH,F)_2]$, Hem = Hematite Fe_2O_3 (± 0.1 wt% uncertainty).

Material	*Qtz* [wt%]	*Or* [wt%]	*Ab* [wt%]	*An* [wt%]	*Kln* [wt%]	*Ms* [wt%]	*Mrg* [wt%]	*Pg* [wt%]	*Bt* [wt%]	*Hem* [wt%]
Quartzite¥	99.0	-	-	-	-	0.4	0.1	0.1	0.3	
Sandstone¥¥	93.1	5.0	0.3	0.3	0.2	0.6	-	-	0.2	0.2

¥ potential chloritisation of mica ¥¥ contains accessory apatite and dolomite

Elastic properties of quartzite, sandstone and fused silica

Cube-shaped specimens are prepared both from Dalsland quartzite and Lahr sandstone to investigate their elastic properties by ultrasonic wave transmission with compressional and shear waves under ambient conditions. Approximately isotropic velocities of both compressional and shear waves are observed within the experimental uncertainties (Tab. 6). Elongated plate-like specimens for DMTA are prepared

---

[3] Muscovite is used here as a collective term for all transparent micas.

analogously to quartz. However, the thickness of the specimens is larger in case of the two rock types, especially for Lahr sandstone (Tab. 7).

Fused silica is bought from *Glasvertrieb Braun*. Its quality meets industrial standards (DIN EN ISO 9001). A list of its physical and chemical (Tab. 4) properties is published in the Internet (latest download from www.g-v-b.de/File/quarzplatten_d(1).pdf on 02 October, 2014, abbreviated as "GVB 2014" in Tab. 4 and in the following text).

Tab. 6: Observed travel times of the compressional and shear waves t_p and t_s over the distance s as well as the wave velocities v_p and v_s of quartzite, sandstone, and fused silica under ambient conditions and with experimental uncertainties, respectively (*e.g.* Kuchling 2004, Appendix 9). Measurements are made in three orthogonal orientations for the quartz-bearing rocks.

Material (direction)	$s \pm \Delta s$ **[mm]**	$t_p \pm \Delta t_p$ **[μs]**	$v_p \pm \Delta v_p$ **[km/s]**	$t_s \pm \Delta t_s$ **[μs]**	$v_s \pm \Delta v_s$ **[km/s]**	$v_p/v_s \pm \Delta v_p/v_s$ **[-]**
Quartzite (1)	31.16 ± 0.05	5.34 ± 0.04	5.84 ± 0.05	7.80 ± 0.04	3.995 ± 0.022	1.466 ± 0.013
Quartzite (2 ⊥ 1)	31.95	5.42	5.89			
Quartzite (3 ⊥ 2 ⊥ 1)	42.76	7.32	5.84 ± 0.04			
Sandstone (1)	212 ± 3	73.3 ± 0.5	2.89 ± 0.05	110.6 ± 0.5	1.917 ± 0.029	1.508 ± 0.013
Sandstone (2 ⊥ 1)	192	63.9	3.00 ± 0.06	102.0	1.88 ± 0.04	1.596 ± 0.015
Sandstone (3 ⊥ 2 ⊥ 1)	273	89.6	3.05 ± 0.04	137.2	1.990 ± 0.024	1.533 ± 0.011
Fused silica			5.93		3.74	1.586

Fused silica is elastically isotropic and well-known. Under ambient conditions, the Young's modulus equals ≈ 72 GPa, while Poisson's ratio is ≈ 0.17 (GVB 2014). Elastic wave velocities are derived from these data (Tab. 6) for a density of 2.2 g/cm^3 (*e.g.* Schön 1983). The compressional strength is specified to be > 1.1 GPa and the tensile strength is measured to be ≈ 48 MPa. This is approximately one order of magnitude higher than for natural rocks.

Again, elongated plate-like specimens of fused silica are prepared for DMTA. Their dimensions are comparable to those of the quartz specimens (Tab. 7). The temperature readings from DTMA are calibrated analogously to quartz, assuming a hypothetical occurrence of the α-β transition. The observed Young's moduli are corrected by the thermal expansion coefficient, which is $\approx 0.55 \cdot 10^{-6}$ K^{-1} between 25 and 300 °C (GVB 2014). These corrections are also made for Dalsland quartzite and Lahr sandstone with the same temperatures that are used for quartz and the isotropic thermal expansion of quartz.

Geometrical properties of specimens for DMTA

Elongated plate-like specimens with parallel planes are required for the measurements in the symmetrical three-point bending experimental set-up of the DMTA apparatus (Chapter 2). The thicknesses and the widths of the specimens are measured with a digital calliper gauge and a precision of ± 0.01 mm. However, variations due to the preparation process are usually larger (Tab. 7).

Tab. 7: Geometrical properties of specimens for DMTA. Abbreviated specimen names according to Tab. 2. Orientations of the off-axis specimens are referred to as azimuth ϕ and polar distance ψ. Uncertainties of the specimen width and thickness are ± (0.02 + 0.01) mm according to preparation and the precision of the calliper gauge, respectively.

Specimen name	**Orientation (ϕ/ ψ)**	**Length *l* > [mm]**	**Thickness *h* [mm]**	**Width *w* [mm]**
s-SiO$_2$-01	ll *c*-axis	20	0.63	10.35
s-SiO$_2$-02	ll *a*-axis	20	0.62	10.61
s-SiO$_2$-03	90°/40°	20	0.63	10.13
s-SiO$_2$-04	90°/30°	20	0.63	10.00
s-SiO$_2$-05	ll *a*-axis	20	0.79	12.61
s-SiO$_2$-06	ll *c*-axis	40	0.64	12.48
s-SiO$_2$-07	ll *c*-axis	40	0.59	12.54
s-SiO$_2$-08	ll *c*-axis	40	0.79	12.76
s-SiO$_2$-09	ll *c*-axis	40	0.59	12.54
s-SiO$_2$-10	ll *a*-axis	40	0.82	12.83
s-SiO$_2$-11	ll *a*-axis	40	0.83	12.74
s-SiO$_2$-12	ll *a*-axis	40	0.84	12.53
s-SiO$_2$-13	90°/30°	40	0.78	12.49
s-SiO$_2$-14	90°/30°	40	0.79	12.38
s-SiO$_2$-15	90°/30°	40	0.77	12.45
s-SiO$_2$-16	ll *c*-axis	40	0.78	12.45
n-SiO$_2$-01$_b$	ll *c*-axis	20	0.80	12.63
n-SiO$_2$-02$_b$	ll *c*-axis	20	0.68	12.62
L-Sst-01	random	20	6.05	9.63
D-Qtz-01$_a$	random	20	4.16	9.06
D-Qtz-01$_b$	random	20	1.04	9.02
f-SiO$_2$-01	random	20	0.75	11.10
f-SiO$_2$-01	random	20	0.77	11.17
c-Al$_2$O$_3$-1	random	20	6.03	11.91

4. Experimental results

Results obtained from synthetic quartz

The complex Young's modulus of synthetic quartz is determined as a function of frequency and temperature across the α-β transition with 20 mm (Fig. 16) and 40 mm (Fig. 17, Fig. 18, Klumbach & Schilling 2012, 2014) support spacings in symmetrical three-point bending. The temperature readings are calibrated to 573 °C using the minimum of the observed storage modulus (Chapter 2). Temperature uncertainties are assumed to be < ± 2 K. The observed storage and dissipation moduli are corrected for an anisotropic expansion of each specimen based on the previously calibrated temperature.

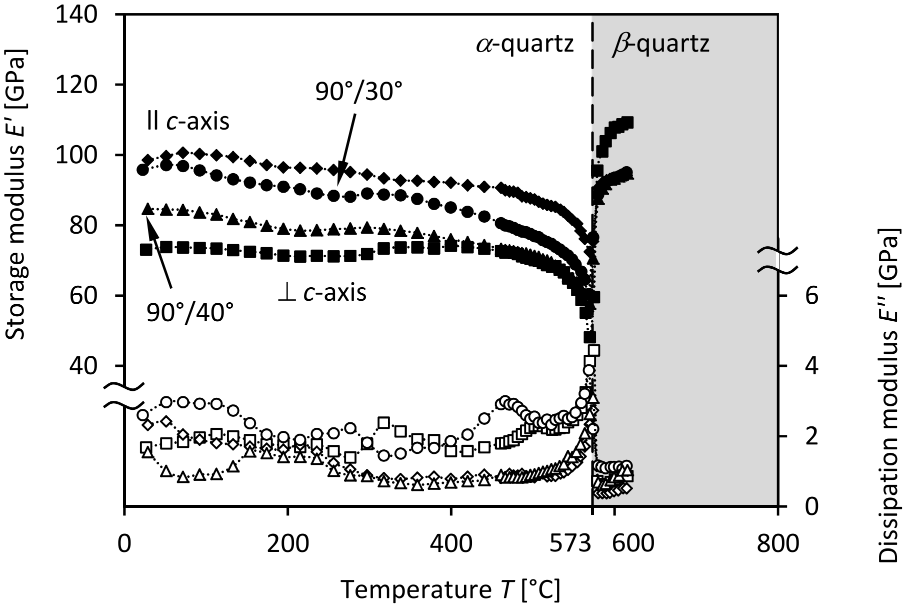

Fig. 16: Calibrated temperature dependence of the corrected anisotropic storage (black symbols) and dissipation moduli (white symbols) based on the observations for synthetic quartz crystals at 2.57 Hz across the α-β transition with 20 mm support spacing in symmetrical three-point bending. Off-axis crystallographic orientations are referred to as "azimuth/polar distance".

Under ambient conditions, the storage modulus parallel to the *c*-axis of the crystal is ≈ 20 % larger than that perpendicular to it (Fig. 16, Fig. 17). A potential frequency dependence of the complex Young's modulus is not observed (Fig. 18), whereas it might exist below the detection limit of the experimental set-up. The dissipation moduli are ≈ 1 to 3 % of the corresponding storage moduli, which is indeed close to the detection limit of the experimental set-up (Chapter 2).

At elevated temperature, minor deviations from the expected literature trends (*e.g.* Kimizuka *et al.* 2003, Lakshtanov *et al.* 2007, Ohno *et al.* 2006, Perrier & De Mandrot 1923, Zubov & Firsova 1962) are observed. The complex Young's modulus becomes frequency-dependent at ≈ 500 °C for recordings with a support spacing of 40 mm and at ≈ 550 °C for 20 mm. This frequency dependence gradually increases with temperature towards the α-β transition. At ≈ 573 °C, the minimum of the storage modulus is accompanied by a maximum of the dissipation modulus.

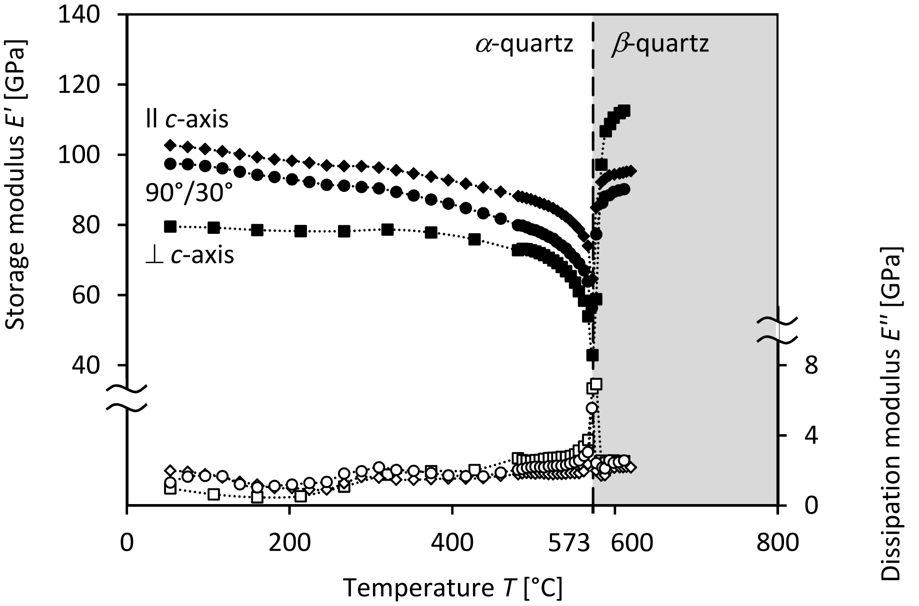

Fig. 17: Temperature dependence of the anisotropic storage (black symbols) and dissipation moduli (white symbols) of synthetic quartz crystals at 1 Hz across the α-β transition with 40 mm support spacing. Mean data from several specimens are shown. Off-axis crystallographic orientations are referred to as “azimuth/polar distance”.

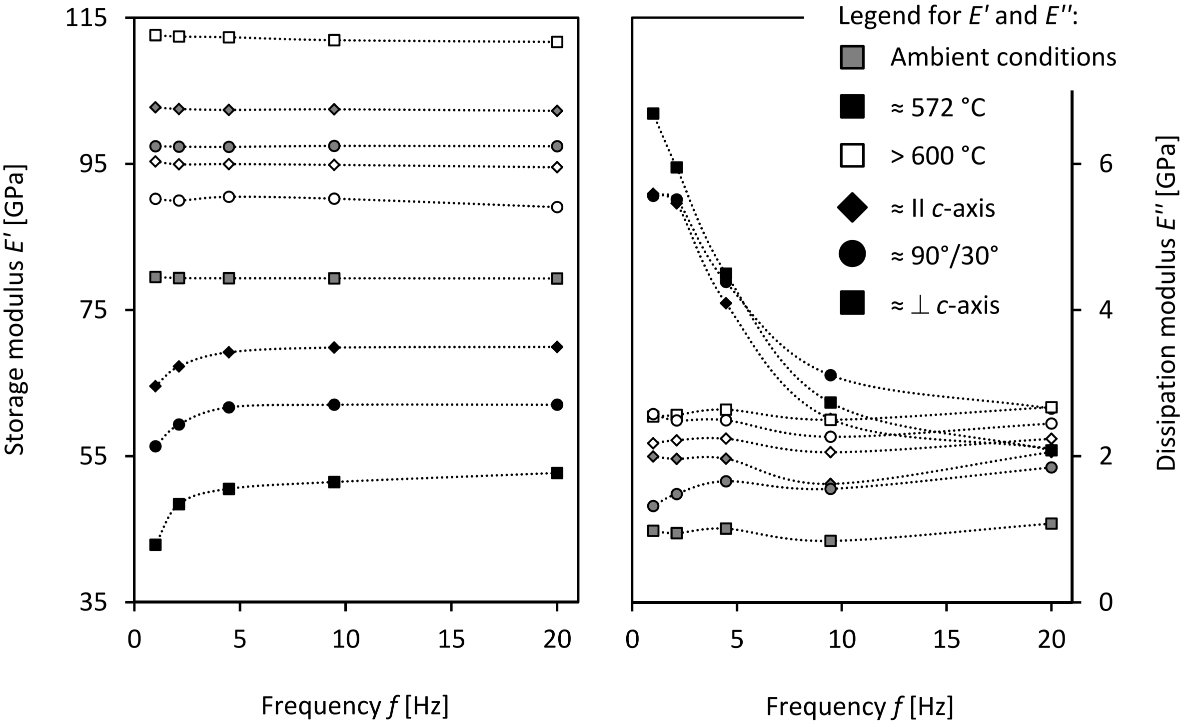

Fig. 18: Isothermal frequency dependence of the anisotropic storage (left) and dissipation moduli (right) of synthetic quartz across the α-β transition at 40 mm support spacing. Mean data are presented. Off-axis crystallographic orientations are referred to as “azimuth/polar distance”.

Isothermal frequency-dependent recordings in the vicinity of the α-β transition show low-frequency loading correlating with low storage moduli and low dissipation moduli, while high-frequency loading corresponds to high storage moduli and low dissipation moduli (Fig. 18). A maximum of the dissipation modulus is observed at ≈ 1 Hz, linked to a strongly increasing storage modulus. The dispersion of the storage modulus and the maximum of the dissipation modulus are low parallel to the *c*-axis of the crystal (≈ 7.6 and ≈ 2.6 GPa, respectively) and high perpendicular to it (≈ 15.1 and ≈ 7.1 GPa, respectively).

Above the α-β transition, the storage modulus increases anisotropically, as expected from the literature data presented (*e.g.* Perrier & De Mandrot 1923), while the dissipation modulus decreases. The complex Young's modulus loses its frequency dependence within a temperature range of < 10 K. Since the α-β transition is described as enantiotropic transformation (Chapter 1), repeated frequency- and temperature-dependent measurements with the same specimen lead to similar results (Tab. 2).

Results obtained from natural quartz

The complex Young's modulus of natural quartz is investigated as a function of frequency and temperature across the α-β transition in dynamic symmetrical three-point bending experiments with 20 mm support spacing. Both the temperature readings and the specimen expansion with increasing temperature are corrected analogously to the results of synthetic quartz (Chapter 2).

The high-temperature development of the storage modulus of natural quartz at 10 Hz cyclic loading is in agreement with the observations made for synthetic quartz. Under ambient conditions, however, the storage modulus of natural quartz is lower and its decrease with rising temperature is apparently stronger than one might expect. A pronounced increase of the storage modulus is observed between ≈ 250 and ≈ 350 °C, probably linked to a decrease of the dissipation modulus between ≈ 300 and ≈ 400 °C (Fig. 19).

At the α-β transition, a minimum of the storage modulus and a maximum of the dissipation modulus are observed as well although the dissipation modulus is merely as large as for temperatures < 300°C. Both the storage modulus and the dissipation modulus of the β-phase also meet the expectations based on the observations made for synthetic quartz. The dissipation modulus of natural β-quartz corresponds to the value observed below its α-β transition, between ≈ 400 to ≈ 500 °C, according to a combination of the intrinsic attenuation of the apparatus and quartz itself. The storage and dissipation moduli found below ≈ 400 °C might be due to crystal twining. Results of isothermal dynamic loadings of natural quartz show that the complex Young's modulus becomes frequency-dependent at ≈ 550 °C, while ≈ 559 °C seems to be the highest temperature, where the complex Young's modulus is recorded for the α-phase (Fig. 20). The data measured at ≈ 575 °C, which is the temperature closest to the α-β transition in this case, potentially corresponds to the β-phase already.

It is further observed that the first data point of the isothermally recorded storage moduli is always higher than expected. This is an artefact because of the combination of the temperature intervals and the time available for the thermal equilibration of the apparatus prior to specimen loading (Chapter 2). The equilibration time is supposed to be too short to compensate an ongoing thermal expansion of the loading axis of the machine. Theoretically, this effect is also influenced by the time needed for the dynamic measurement, which corresponds to the inverse loading frequency. The effect is observed for data of synthetic quartz at 20 mm support spacing as well.

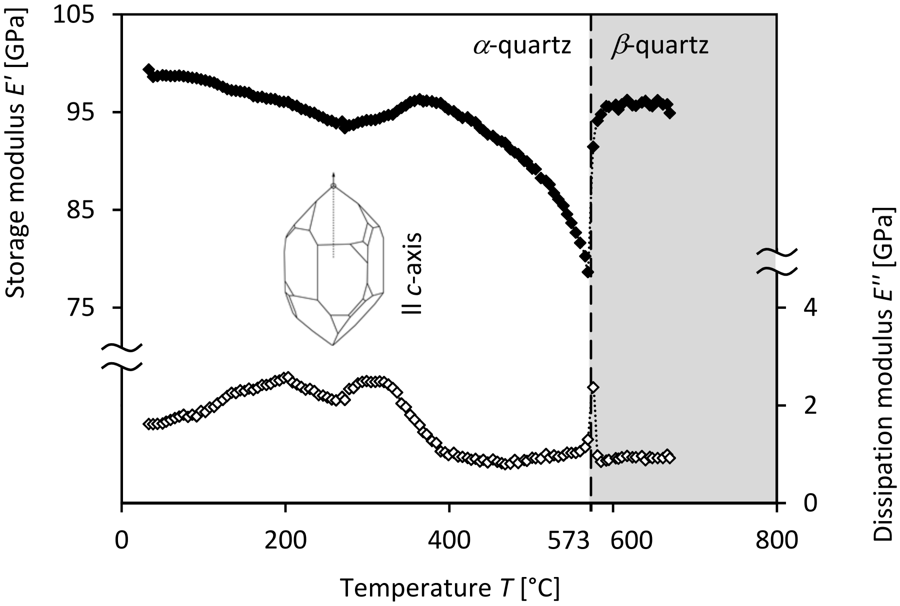

Fig. 19: Temperature dependence of the storage (black symbols) and dissipation moduli (white symbols) of natural quartz at 10 Hz loading across the α-β transition, with 20 mm support spacing.

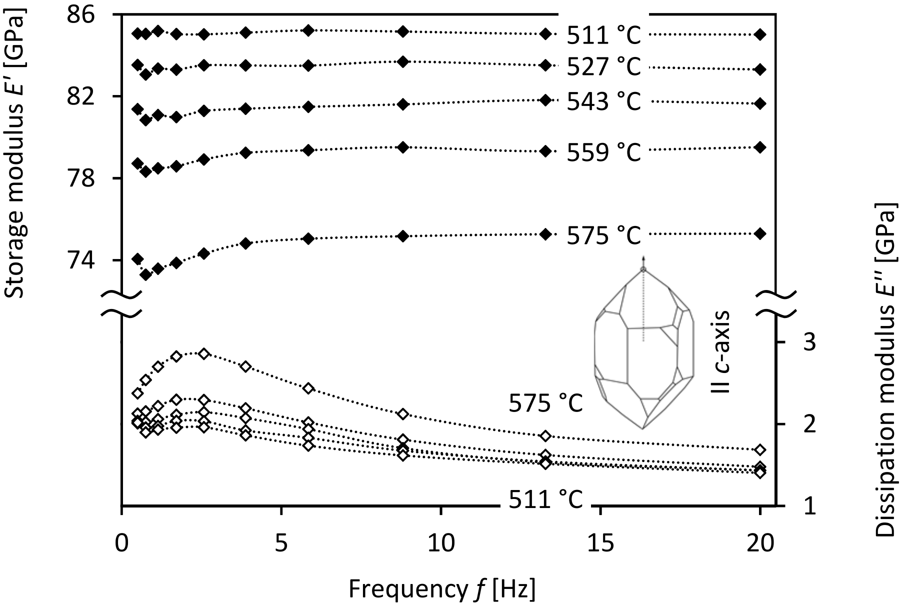

Fig. 20: Isothermal frequency dependence of the storage (black symbols) and dissipation moduli (white symbols) of natural quartz across the α-β transition, at 20 mm support spacing.

Results obtained from Dalsland quartzite

The complex Young's modulus of a specimen of Dalsland quartzite is investigated as a function of temperature across the α-β quartz transition at 10 Hz cyclic loading and 20 mm support spacing. Temperature readings are calibrated analogously to synthetic quartz (Chapter 2). Thermal changes of the specimen width and thickness are corrected by the volume expansion of quartz, as Dalsland quartzite can be considered an isotropic rock (Chapter 3). Hence, its storage and dissipation modulus may be expected to meet the averaged elastic data of quartz for an isotropic polycrystal.

Under ambient conditions, the storage modulus of Dalsland quartzite is ≈ 85.1 GPa. When a frequency dependence of the elastic properties is excluded, this storage modulus nearly is identical to a Young's modulus of ≈ 90.2 ± 1.2 GPa, which is derived from ultrasonic measurements (Tab. 6) and a density of 2.65 g/cm³ for an isotropic solid (33). For comparison, the average Young's modulus of an isotropic quartz polycrystal is ≈ 95.6 GPa according to the Voigt-Reuss-Hill approximation (Chapter 1). It is supposed to be different from the storage modulus of Dalsland quartzite due to grain boundaries and the intercrystalline presence of micro-cracks. This assumption seems to be supported by a single stepwise change of the storage modulus to ≈ 80.0 GPa due to heating and micro-crack development.

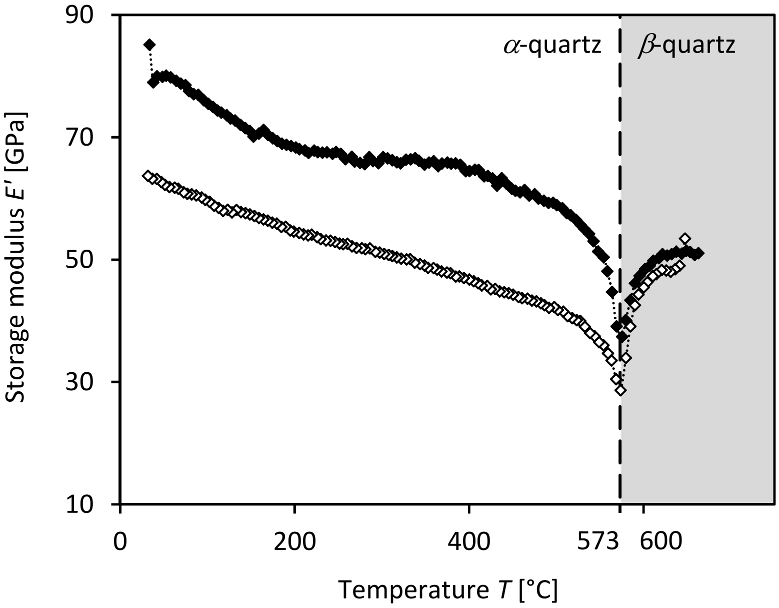

Fig. 21: Temperature dependence of the storage modulus of Dalsland quartzite across the α-β quartz transition at a testing frequency of 10 Hz: heating (black symbols) and cooling (white symbols).

During heating, the temperature dependence of the storage modulus of Dalsland quartzite qualitatively agrees with the observations made for quartz (Fig. 21). It also exhibits a minimum at the α-β transition. The storage modulus of the β-phase is consistent for both heating to ≈ 650 °C and cooling to ambient temperature at the rate of 3 K/min. Below the α-β transition the storage modulus recorded during cooling is ≈ 20 to 30 % lower than during heating. This difference is attributed to the formation and propagation of micro-cracks in the specimen, particularly in the vicinity of the α-β transition, where a strong and highly anisotropic thermal expansion occurs (Chapter 1). A dissipation maximum related to the α-β transition is not observed, as the testing frequency is 10 Hz.

However, the specimen of Dalsland quartzite is found to be macroscopically intact after the experiment. It is once more heated and cooled across the α-β transition in the same temperature range. Results from this correlate with the data from the first cooling cycle, since further micro-crack development does not take place until the temperature is > 650 °C. Again, no increasing dissipation is measured at the α-β transition and the specimen is found to be macroscopically intact afterwards.

The thickness of this used specimen made of Dalsland quartzite is reduced (Tab. 7) and it is subjected to isothermal sinusoidal loading at different frequencies and temperatures in the vicinity of the α-β quartz transition. The frequency range is chosen to be equal to that of quartz (Tab. 2). Storage and dissipation moduli are determined for temperatures > 520 °C across the α-β transition (Fig. 22). As observed for quartz, the complex Young's modulus of Dalsland quartzite shows a frequency dependence in the vicinity of the α-β transition. The dispersion of the storage modulus starts at ≈ 520 °C and maximises at ≈ 573 °C. Simultaneously, the dissipation modulus also maximises at the α-β transition, as one might already expect from the previously presented quartz data.

Isothermal frequency-dependent measurements at ≈ 571 °C show that the dispersion of the storage modulus between 0.1 and 20 Hz reaches ≈ 16.4% according to high-frequency observations. The dissipation modulus maximises at ≈ 0.8 Hz, which is slightly lower than in quartz, where it is found around ≈ 1Hz. It is ≈ 2.95 GPa, which is ≈ 11.6 % of the storage modulus at the same frequency.

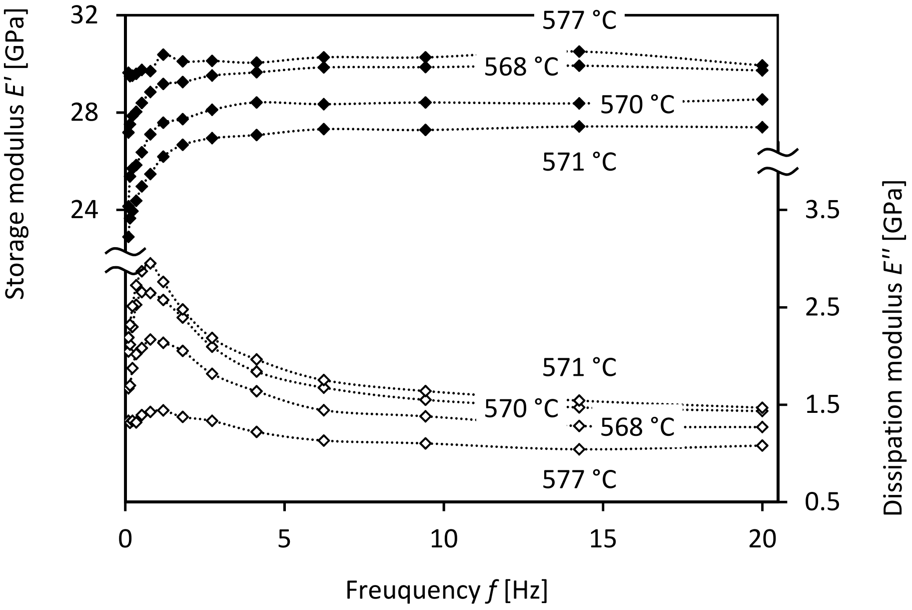

Fig. 22: Isothermal frequency dependence of the storage (black symbols) and dissipation moduli (white symbols) of Dalsland quartzite across the α-β transition, with 20 mm support spacing.

Results obtained from Lahr sandstone

Lahr sandstone is found to be elastically isotropic by ultrasonic measurements (Tab. 6). A Young's modulus E_{dyn} of ≈ 19.6 GPa is derived from equation (33) using the travel times of elastic waves and the density ρ of ≈ 2.2 g/cm^3 (Tab. 8). Uniaxial compression tests yield a static Young's modulus E_{sta} of ≈ 20.4 GPa (Appendix 22 - Appendix 30). Both results are in agreement within the experimental uncertainties, as it is known from quartz that a frequency dependence of the elastic properties is lacking at ambient temperature. Hence, the mean Young's modulus of Lahr sandstone equals ≈ 19.8 GPa.

The mean uniaxial compressional strength σ_{uc} of Lahr sandstone is ≈ 64 MPa (Tab. 8). It is corrected according to equation (35), because the cylindrical specimens exhibit a length:diameter ratio of < 2.5:1 (Chapter 2). However, a reduction of the uniaxial compressional strength is supposed to affect the corresponding Young's modulus derived from the observed strain. The Young's moduli obtained from uniaxial compression is modified analogously to the rock strength by introducing the correction factor n_{cor} (Tab. 8).

Measurements at 10 Hz dynamic loading and 20 mm support spacing yield a complex Young's modulus < 5 GPa, which is clearly different from the results of the other two methods. This difference results from the fact that the deformation in symmetrical three-point bending is impeded by a large specimen thickness compared to quartz and quartzite (Tab. 7). However, the chosen thickness is necessary as the sandstone grains are bound weakly in contrast to quartzite. Furthermore, the tensile rock strength is ≈ 7.1 MPa (Appendix 30). Since symmetrical three-point bending results in tensile stress in the lower part of the specimen (Chapter 2), the sandstone is prone to fail.

Temperature readings from investigations of Lahr sandstone with DMTA are calibrated analogously to quartz. The storage modulus exhibits decreasing values towards the α-β quartz transition. A re-increasing stiffness above 573 °C is interrupted by failure of the specimen at ≈ 600 °C (Fig. 23). It is evident that the dynamic symmetrical three-point bending data of this sandstone poorly reflect the observations made for quartz and quartzite. In the vicinity of the α-β transition no isothermal frequency-dependent elastic data are collected for Lahr sandstone.

In addition, a voluntary water absorption of ≈ 4.2 wt% is measured. Both the density and the voluntary water absorption found in this study are consistent with data presented by Hirsch (2008), who also determines an average porosity of ≈ 16.2 %.

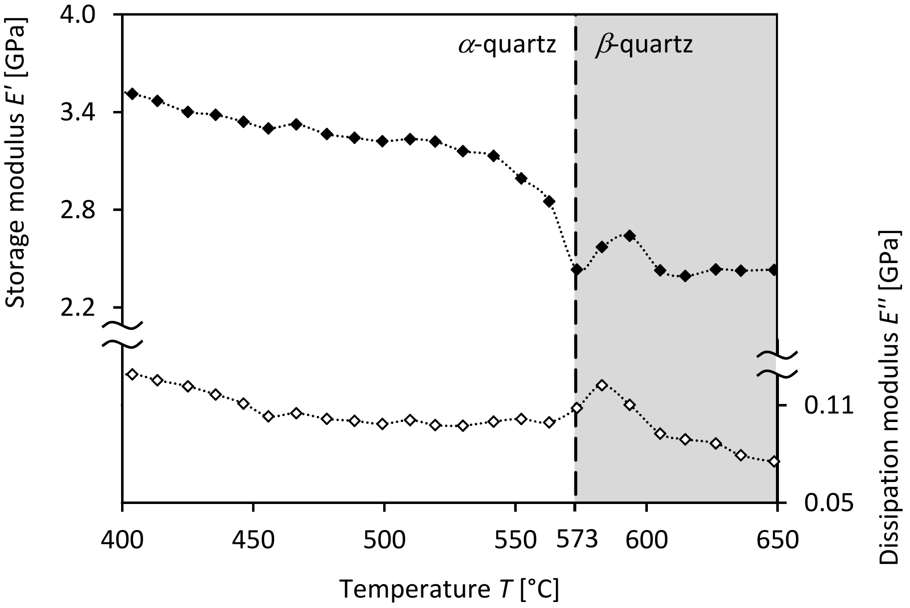

Fig. 23: Temperature dependence of the storage (black symbols) and dissipation moduli (white symbols) of Lahr sandstone across the α-β transition at 10 Hz loading frequency, with 20 mm support spacing.

Tab. 8: Physical properties of cylindrical specimens of Lahr sandstone (drilled perpendicular to bedding) with uncertainties (Appendix 9).

Specimen name	$\bar{l} \pm \Delta\bar{l}$ **[mm]**	$\bar{d} \pm \Delta\bar{d}$ **[mm]**	$\bar{l}/\bar{d} \pm \Delta\,\bar{l}/\bar{d}$ **[-]**	$\rho \pm \Delta\rho$ **[g/cm³]**	$t_p \pm \Delta t_p$ **[μs]**	$v_p \pm \Delta v_p$ **[km/s]**	$t_s \pm \Delta t_s$ **[μs]**	$v_s \pm \Delta v_s$ **[km/s]**	$v_p/v_s \pm \Delta v_p/v_s$ **[-]**	$E_{dyn} \pm \Delta E_{dyn}$ **[GPa]**	$E_{sta} \pm \Delta E_{sta}$ **[GPa]**	$\sigma_{uc} \pm \Delta\sigma_{uc}$ **[MPa]**	n_{cor} **[-]**
MKC-021	100.89 ± 0.12	50.07 ± 0.03	2.0150 ± 0.0027	2.212 ± 0.005	32.7 ± 0.5	3.09 ± 0.06	51.1 ± 0.5	1.974 ± 0.022	1.57 ± 0.04	19.9 ± 1.2			
MKC-022	101.96 ± 0.03	50.10 ± 0.04	2.0351 ± 0.0018	2.207	33.4	3.05 ± 0.05	51.0	1.999 ± 0.021	1.53	19.8 ± 1.0	19.7 ± 0.5	60.0 ± 0.8	0.973
MKC-023	102.45 ± 0.09	50.083 ± 0.017	2.0456 ± 0.0020	2.2053 ± 0.0026	33.6	3.05	52.0	1.970	1.55	19.5			
MKC-024	103.18 ± 0.07	50.08 ± 0.03	2.0603 ± 0.0019	2.204 ± 0.004	33.8	3.05	52.0	1.984	1.54	19.7			
MKC-025	99.64 ± 0.18	50.08	1.990 ± 0.004	2.192 ± 0.006	33.0	3.02 ± 0.06	52.1	1.912 ± 0.022	1.58	18.7 ± 1.2	20.3	66.6 ± 0.9	0.969
MKC-026	103.83 ± 0.12	50.08	2.0733 ± 0.0027	2.213 ± 0.005	33.9	3.06 ± 0.05	51.5	2.016	1.52	20.1 ± 1.0	21.2	69.2	0.975
MKC-027	103.54 ± 0.10	50.095 ± 0.024	2.0661 ± 0.0023	2.211 ± 0.004	33.8	3.06	53.1	1.949 ± 0.021	1.57	19.5 ± 1.1	20.8	66.2	0.975
MKC-028	101.23 ± 0.11	50.08 ± 0.05	2.021 ± 0.003	2.210 ± 0.006	33.1	3.06	51.5	1.966 ± 0.022	1.56	19.6	19.8	59.8	0.971
MKC-029	101.22 ± 0.07	50.068 ± 0.024	2.0217 ± 0.0018	2.2159 ± 0.0028	33.1	3.06	51.1	1.981 ± 0.021	1.54	19.8 ± 1.0			
MKC-030	102.54 ± 0.09	50.063 ± 0.017	2.0482 ± 0.0020	2.2017 ± 0.0026	33.6	3.05	51.6	1.987 ± 0.022	1.53	19.7			
MKC-031	100.53 ± 0.07	50.11 ± 0.06	2.0062 ± 0.0028	2.215 ± 0.006	31.8	3.16 ± 0.06	53.0	1.897 ± 0.020	1.66 ± 0.05	19.5 ± 1.3			
MKC-032	101.19 ± 0.16	50.11 ± 0.08	2.019 ± 0.005	2.204 ± 0.009	32.5	3.11	51.4	1.969 ± 0.023	1.58 ± 0.04	19.9			
MKC-033	101.28 ± 0.03	50.078 ± 0.017	2.0224 ± 0.0010	2.2067 ± 0.0018	33.0	3.07 ± 0.05	53.1	1.907 ± 0.019	1.61	19.0 ± 1.1			
MKC-038	100.12 ± 0.04	50.17 ± 0.04	1.9956 ± 0.0018	2.196 ± 0.005	32.1	3.12	50.0	2.002 ± 0.021	1.56	20.2			
Mean ± $2\bar{\sigma}$				2.207 ± 0.004		3.072 ± 0.021		1.965 ± 0.021	1.564 ± 0.022	19.64 ± 0.23	20.4 ± 0.8	64 ± 5	

Results obtained from fused silica

The complex Young's modulus of fused silica is investigated as a function of temperature across 573 °C at 10 Hz cyclic loading and 20 mm support spacing by symmetrical three-point bending. The temperature readings are calibrated analogously to quartz (Chapter 2). Observed storage and dissipation moduli are corrected according to a comparably low isotropic thermal expansion of the material (Chapter 3). Under ambient conditions, the storage modulus of fused silica is found to be independent of the loading frequency, consistent with the literature data (Chapter 1). The storage modulus is determined to be ≈ 76.1 GPa, while the equivalent dissipation modulus is ≈ 3.7 % of this value.

The temperature dependence of the 10 Hz complex Young's modulus of fused silica clearly differs from the results previously obtained for quartz and quartz-bearing rocks. Literature data published by Spinner (1956), for instance suggest a linearly increasing Young's modulus with temperature (Chapter 1). A gain in stiffness as a function of temperature is generally in agreement with the observations of this study. Below ≈ 250 °C, however, the storage modulus of fused silica appears to be nearly independent of temperature (Fig. 24).

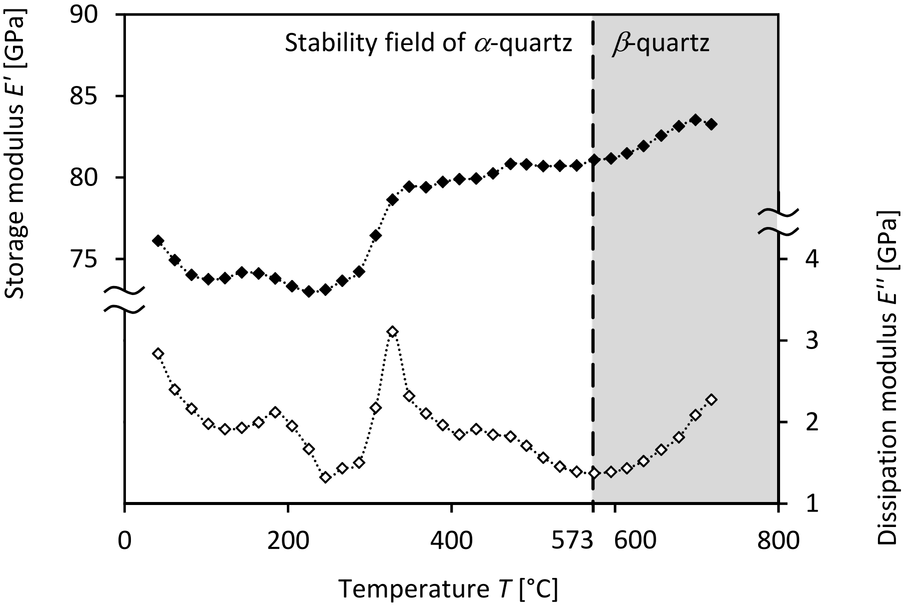

Fig. 24: Temperature dependence of the storage (black symbols) and dissipation moduli (white symbols) of fused silica at 3 K/min heating rate and 1 Hz loading frequency.

Around ≈ 300 °C, the storage modulus increases by ≈ 5 GPa, which is associated with a maximum of the dissipation modulus of ≈ 3.1 GPa. This seems to be comparable to viscoelastic effects in quartz that are described at ≈ 300 °C (*e.g.* Cook & Breckenridge 1953, Dodd & Fraser 1965) and at - 223 °C (*e.g.* Bömmel *et al.* 1956) and attributed to lattice defects (*e.g.* King 1959) and impurities (*e.g.* Fraser 1964, Lewis & Patterson 1967, Maris 1963). The behaviour around ≈ 300 °C may also result from structural relaxation of *in-situ* stresses due to the reorientation of SiO_4 tetrahedra.

For temperatures > 350 °C, the storage modulus increases approximately linearly. At ≈ 700 °C, it amounts to ≈ 83.5 GPa. Neither a minimum of the storage modulus nor a maximum of the dissipation modulus is detected around 573 °C. The dissipation modulus potentially increases at temperatures > 600 °C, whereas the observed values are close to the detection limit of the experimental set-up (Chapter 2).

From the clearly different 10 Hz temperature dependence of the storage and dissipation moduli in comparison to quartz, it is expected that the complex Young's modulus of fused silica does not exhibit any frequency dependence in the vicinity of the α-β transition temperature for quartz. This is confirmed by isothermal dynamic data of fused silica recorded in the same frequency range as for quartz and quartzite (Fig. 25). However, a minor frequency dependence seems to exist between ≈ 200 and ≈ 400 °C, which would be in agreement with the potential material effects mentioned above.

Beyond that the thermal expansion of the loading axis of the apparatus continues during the dynamic measurement and especially affects the moduli recorded at low frequency, which is also observed for quartz. This effect interferes with a potential frequency dependence of the complex Young's modulus.

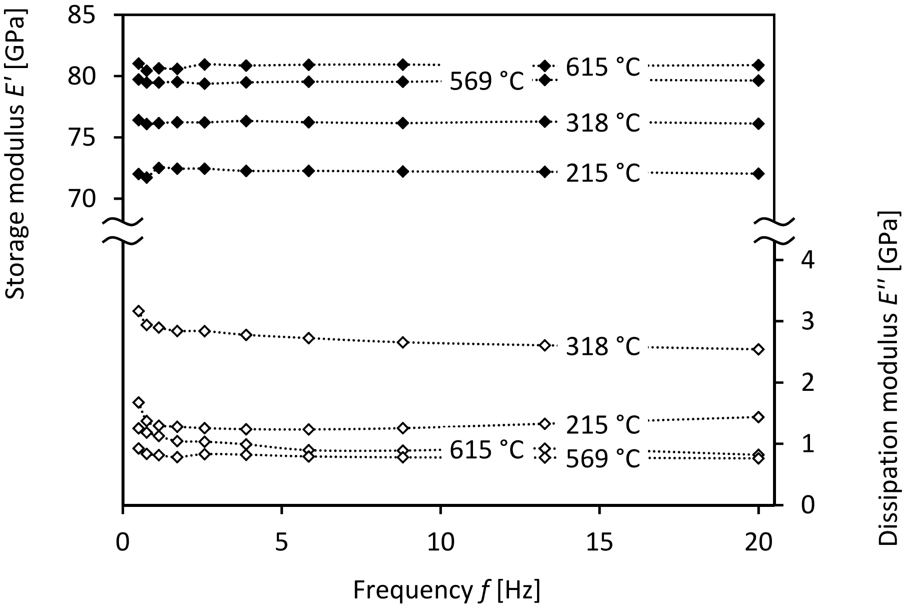

Fig. 25: Isothermal storage (black symbols) and dissipation moduli (white symbols) of fused silica at different frequencies and various elevated temperatures.

5. Discussion

Frequency-dependent elastic behaviour

At ambient temperature, no frequency dependence of the complex Young's modulus between 0.1 and 20 Hz is found for quartz and quartz-bearing rocks (Chapter 4). This also holds for the β-phase at temperatures above ≈ 600 °C. In both cases, a potential viscoelasticity of the material is below the detection limit of the experimental set-up (Chapter 2). Hence, the mechanical properties of quartz are approximated well to be linear elastic, comparable to the behaviour of a mechanical spring with a spring constant equal to the anisotropic Young's modulus (*e.g.* Courtney 2000).

The anisotropic complex Young's modulus of quartz and quartz-bearing rocks becomes significantly frequency-dependent in the vicinity of the α-β phase transition (Chapter 4) because of the occurrence of elastic and viscoelastic mechanical effects. Combined elastic and viscoelastic material properties are usually approximated by networks of elastic and viscous elements or springs and dashpots, respectively (*e.g.* Schiessel *et al.* 1995). The simplest combination of springs and dashpots, which may explain the experimental data of this study, is presented below.

Elementary networks consist of one spring with a Young's modulus E and one dashpot that is defined by a viscosity η. Two combinations result from either parallel or serial arrangement of these elements (*e.g.* Casula & Carcoine 1992). The parallel layout is known as Kelvin-Voigt model (Appendix 31a, *e.g.* Grau *et al.* 1983). It is characterised by a storage modulus

$$E'(\omega) = E \tag{36}$$

that is independent of frequency and a dissipation modulus

$$E''(\omega) = \eta\,\omega \tag{37}$$

that increases linearly with frequency. A least squares approximation shows that the Kelvin-Voigt model fits neither the storage modulus nor the dissipation modulus observed for quartz (Fig. 26) and quartz-bearing rocks.

In contrast to this, the serial arrangement of a spring and a dashpot, which is known as Maxwell model (Appendix 31b), exhibits an increasing storage modulus

$$E'(\omega) = \frac{E\,\eta^2\,\omega^2}{E^2 + \eta^2\,\omega^2} \tag{38}$$

with frequency until a constant value is reached, while the dissipation modulus decreases by

$$E''(\omega) = \frac{E^2\,\eta\,\omega}{E^2 + \eta^2\,\omega^2}. \tag{39}$$

The modelled behaviour of the storage modulus roughly approximates the experimental data, but the dissipation modulus is clearly in disagreement at low frequencies. Hence, the Maxwell model also is inappropriate to describe the results of the complex Young's modulus for quartz (Fig. 26) and quartz-bearing rocks.

Adding a second spring parallel to a Maxwell element yields the Zener model (Appendix 31d, Zener 1948). The serial arrangement of a Kelvin-Voigt element and a spring is known as Poynting-Thomson model (Appendix 31c, *e.g.* Qaisar 1989). These two models are equivalent to each other and also widely known as standard linear solid model (*e.g.* Meidav 1964). Their parameters can be converted into each other (Appendix 31e). The Poynting-Thomson model is used in this study. Modelling by Poynting-Thomson fits to the observed storage and dissipation moduli of quartz and quartzite over the entire temperature and frequency range investigated in this study.

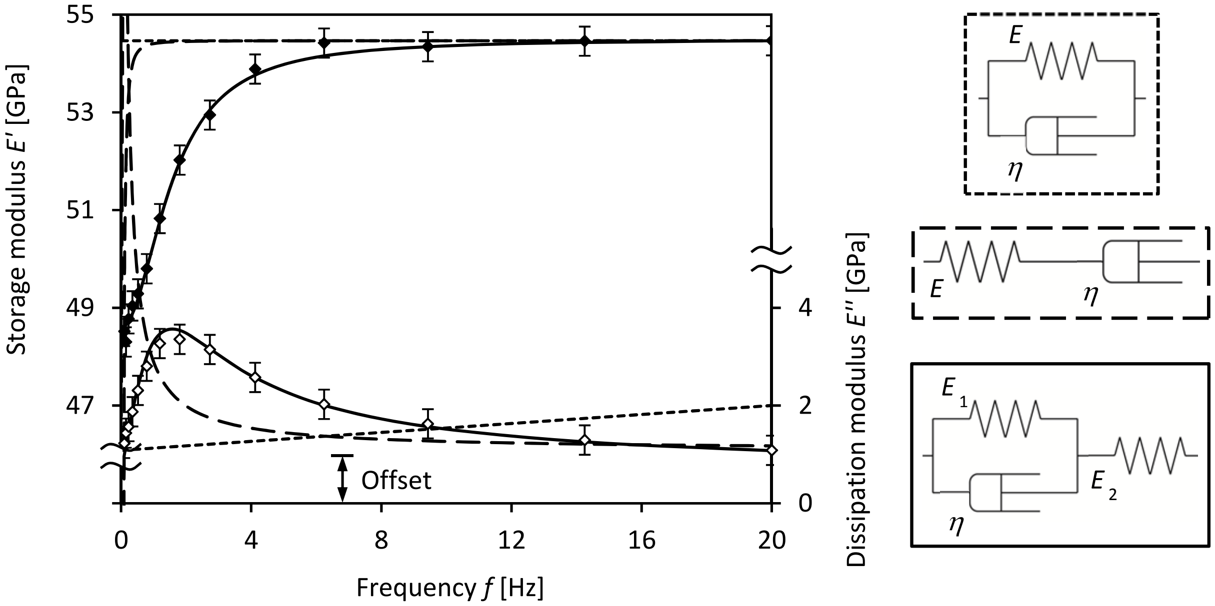

Fig. 26: Frequency dependence of the storage modulus *E′* (black symbols) and dissipation modulus *E″* (white symbols) for a specimen of synthetic quartz at ≈ 570 °C, cut parallel to the *a*-axis of the crystal. Least squares fits according to models of Kelvin-Voigt (fine dashed lines), Maxwell (coarse dashed lines), and Poynting-Thomson (solid lines, $2\sigma \approx 0.3$ GPa).

In the Poynting-Thomson model, the storage modulus exhibits a sigmoidal shape with increasing frequency (Fig. 26). The storage modulus *E′*

$$E'(\omega) = \frac{\frac{E_1 E_2}{E_1 + E_2} + E_2 (\omega\tau)^2}{1 + (\omega\tau)^2} \tag{40}$$

shows a steep slope at ≈ 1 Hz, while the dissipation modulus *E″* (41)

$$E''(\omega) = \frac{\omega\left(E_2 \tau - \frac{E_1 E_2 \tau}{E_1 + E_2}\right)}{1 + (\omega\tau)^2} \tag{41}$$

exhibits a maximum. The spring constant E_2 equals the high-frequency limit of the storage modulus. Moreover, the inverse of the sum of the inverse spring constants E_1 and E_2 represents its low-frequency limit. Dividing the viscosity of the dashpot by the sum of the two spring constants yields the time constant τ of the relaxation process:

$$\tau = \frac{\eta}{E_1 + E_2}. \tag{42}$$

In comparison to that, the spring constant E_2^* equals the lower limit of the storage modulus *E′*

$$E'(\omega) = \frac{E_2^* + (E_1^* + E_2^*)(\omega\tau)^2}{1 + (\omega\tau)^2} \tag{43}$$

under static conditions or low-frequency loading, while the spring constant E_1^* corresponds to its dispersion $\Delta E'$ in the Zener model. Thus, the sum of both spring constants is correlated with the upper limit of the storage modulus at high-frequency loading. The dissipation modulus E'' is then given by

$$E''(\omega) = \frac{E_1^* \omega \tau}{1 + (\omega \tau)^2} \tag{44}$$

and the time constant τ by

$$\tau = \frac{\eta}{E_1^*}. \tag{45}$$

α-β transition: structural explanation of the observations

When heating quartz to the temperature of its α-β transition, multiple domains of Dauphiné twins are produced (*e.g.* Van Tendeloo *et al.* 1976). Dauphiné twins are basically developed by the rotation of domains of silica tetrahedra without breaking the atomic bonds of the structure (*e.g.* Putnis 1992). Instead, the α-β transition is a displacive phase transformation (Chapter 1). All Dauphiné twin domains are oriented parallel to the *c*-axis of the crystal (Fig. 4).

When approaching the α-β transition from temperatures lower than 573 °C, the number of Dauphiné twin domains increases continuously, while their size decreases (Fig. 27). This modification of the crystal lattice culminates in the occurrence of the incommensurate phase, when a structural assignment to neither α-quartz nor the β-phase is possible (Chapter 1), as the size of individual Dauphiné twin domains cannot be resolved anymore (*e.g.* Armstrong 1946, Berge *et al.* 1984, 1986, Bethke *et al.* 1987, Dolino *et al.* 1984b, Van Landuyt *et al.* 1985). The Dauphiné twin domains are finally lost, as soon as the hexagonal symmetry of the β-phase is fully established.

Single-crystal α-quartz shows piezoelectricity (Chapter 1). However, natural quartz is often twinned and, hence, not piezoelectric. Sometimes, this is also true for synthetic crystals. In order to make them usable for industrial purposes, the Dauphiné twin domains are removed from the crystal lattice by heating the quartz across its α-β transition and controlling the cooling rate. Since twinning is a time-depending process, it is promoted by slow cooling and suppressed by fast cooling. Fast cooling generates stress in the crystal lattice and the formation of cracks becomes more likely (*e.g.* Frondel 1945).

Dauphiné twin domains can be formed at ≈ 500 °C by temperature differences of 15 to 25 K (Iliescu & Chirila 1995). Such temperature gradients are observed in this study as well (Chapter 2). In addition, twinning is also possible at low temperatures, when a laser beam is applied to a quartz specimen in order to produce temperature differences (Noge & Uno 2000). The formation of Dauphiné twin domains is known to be stress-induced (*e.g.* Markgraaff 1986, Moore 1986, Thomas & Wooster 1951), especially in symmetrical three-point bending (Wooster *et al.* 1947).

Based on the published elastic properties (Chapter 1) and the complex Young's modulus determined in this study, a structural model is presented in this chapter to explain the temperature- and frequency-dependent behaviour of quartz. At high-temperature, particularly when approaching the α-β transition, the Young's modulus of quartz decreases and the crystal lattice becomes unstable (*e.g.* Dolino & Bachheimer 1982). When a specimen of α-quartz is stressed at low frequency and temperatures close to the α-β transition, Dauphiné twins evolve due to the temperature differences in the experimental geometries. The observed storage modulus is low, since twinning is associated with intracrystalline deformation, which is related to the elastic energy that is necessary to produce the Dauphiné twin domains.

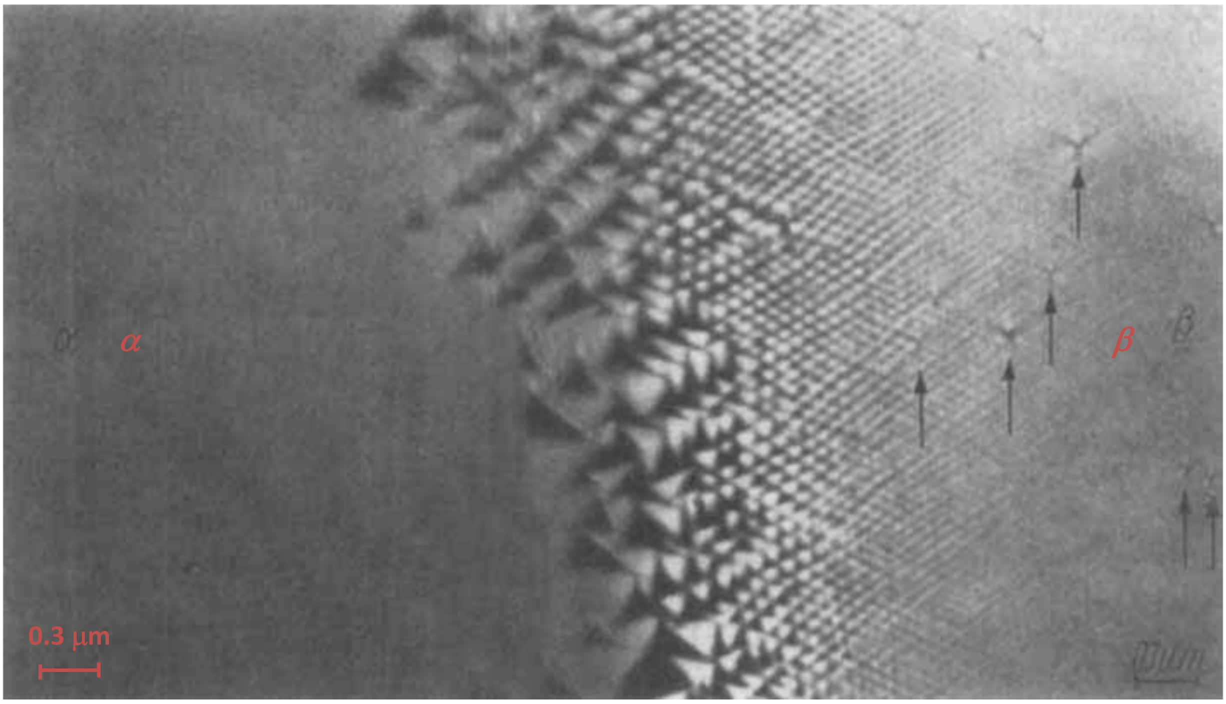

Fig. 27: Fine-scale array of Dauphiné twin domains (central part of the photograph) in quartz at the α-β transition observed by electron microscopy. Arrows indicate star patterns, which are centres of strain linked to lattice defects (Van Tendeloo *et al.* 1976).

In contrast to this, twinning is retained, when the relaxation time of the deformation process described by (42) or (45) for the time constant is larger than the inverse applied frequency. Hence, there is not sufficient time at high frequency to develop the Dauphiné twin domains and the measured storage modulus is comparably higher. Therefore, the frequency-dependent loading of quartz leads to a dispersion of its storage modulus, as observed in this study. Furthermore, the maximum of the dissipation modulus represents the disequilibrium between those two states and reflects the dynamic instability of the Dauphiné twin domains. The dissipation modulus is strongly influenced by the dashpot viscosity of the Poynting-Thomson model (Fig. 28).

The dashpot viscosity of the Poynting-Thomson model is found to be anisotropic. A higher viscosity is observed parallel to the *c*-axis of the crystal, than perpendicular to it. At ≈ 572 °C and 40 mm support spacing the viscosities are for instance ≈ 65 and ≈ 23 GPa s, respectively. Interpolations between 500 and 573 °C suggest a linear decrease of the viscosity towards the α-β transition, which is seen most clearly perpendicular to the *c*-axis ($a_{\parallel c} = -12.33$ GPa s K^{-1}, $b_{\parallel c} = 7131$ GPa s, $a_{\perp c} = -4.76$ GPa s K^{-1}, $b_{\perp c} = 2732$ GPa s). Theoretically, the viscosity would be correctly described by a fourth-rank tensor as well. Within the experimental uncertainties, however, it is sufficiently represented by a second-rank tensor. The time constant of the relaxation process is ≈ 0.11 ± 0.02 s (2σ). It is nearly isotropic and almost independent of temperature, since the spring constants of the model also decrease with increasing temperature. When this time constant is taken for the evaluation of all isothermal frequency-dependent data sets with different crystallographic orientations, an approximation of similar quality is reached within the experimental uncertainties.

The complex elastic behaviour of quartz can be regarded an interplay of its coiled structure and the tetrahedra stiffness. In a first approximation, the latter might be estimated from the Young's modulus of an isotropic coesite polycrystal (Chapter 1). As a consequence, another serial spring would have to be added to the Poynting-Thomson model. However, this cannot be measured with the experimental set-up used in this study. Moreover, no significant improvement of the fits is achieved by adding further model elements (*e.g.* Akyildiz *et al.* 1990, Casula & Carcoine 1992, Du & Tscheuschner 1986, Liu *et al.* 1976).

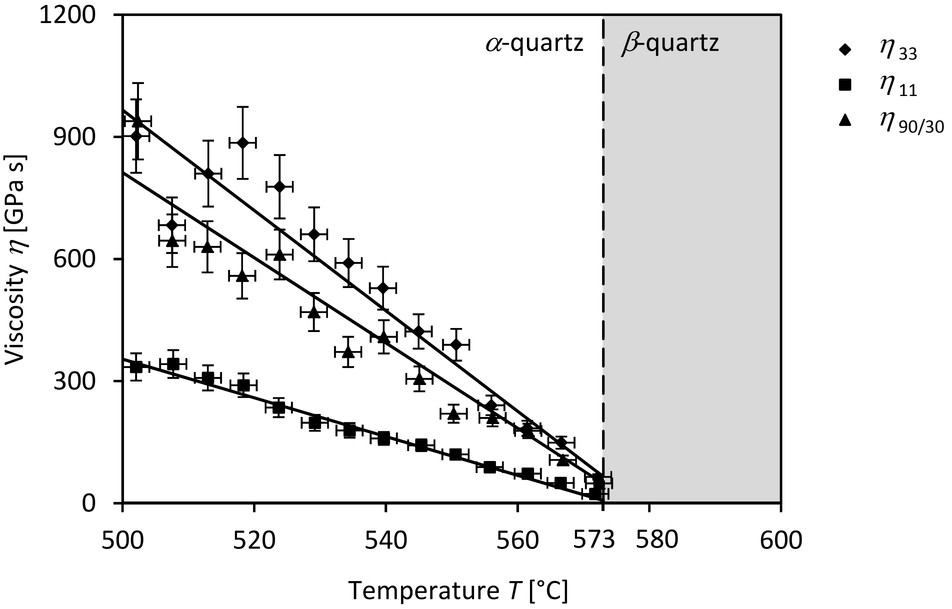

Fig. 28: Temperature dependence of the anisotropic dashpot viscosity obtained from isothermal frequency-dependent fits (symbols) and modelled data according to a second-rank tensor (lines) derived from equations (40) to (42). Error bars equal ± 10 % and ± 2 K.

Temperature-dependent elastic behaviour

The temperature dependence of the complex Young's modulus of quartz at temperatures > 500 °C and across the α-β transition is modelled using both high- and low-frequency data from the isothermal fits. The development of the storage modulus with temperature can be described by

$$E_\alpha = \frac{a}{T_\alpha - T} + b\left(T_\alpha - T\right)^2 + c\left(T_\alpha - T\right) + d \tag{46}$$

for the α-phase, while a to d and T_α are fit parameters, and by

$$E_\beta = e\left|T - T_\beta\right|^f + E_0 \tag{47}$$

for β-quartz with the fit parameters e, f, and T_β.

The high-frequency storage modulus is normalised to data from Lakshtanov *et al.* (2007) and Zubov & Firsova (1962). The frequency-dependent dispersion, increasing as a function of temperature towards the α-β transition, is taken from this study (Fig. 29, Fig. 30). The low-frequency storage modulus is found to be in agreement with the static Young's modulus presented by (Perrier & De Mandrot (1923). Within the experimental uncertainties, this effect can be explained by the occurrence of Dauphiné twin domains rather than by an enhanced measurement precision in the 20th century (Chapter 1).

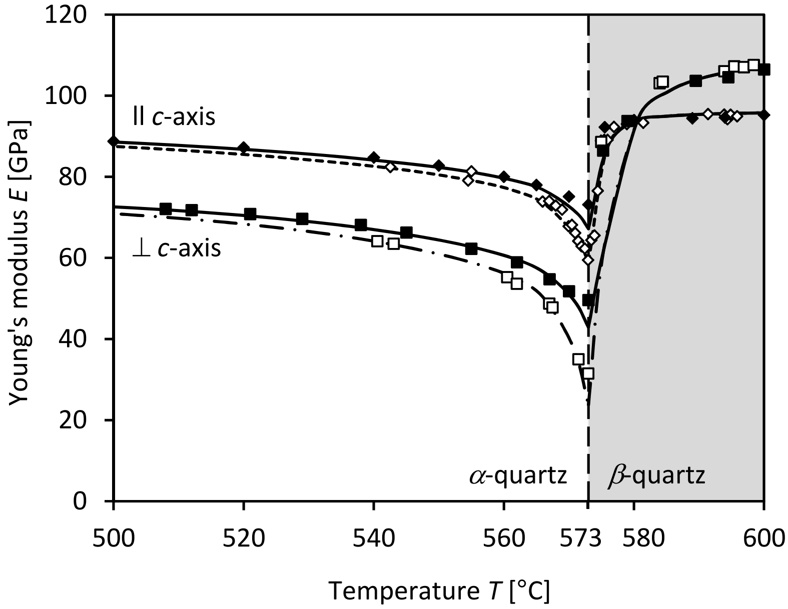

Fig. 29: Temperature dependence of the static (white symbols, Perrier & De Mandrot 1923) and dynamic Young's modulus (black symbols, Lakshtanov *et al.* 2007), against high- (solid lines) and low-frequency data (dashed lines) with 40 mm support spacing (Klumbach & Schilling 2014).

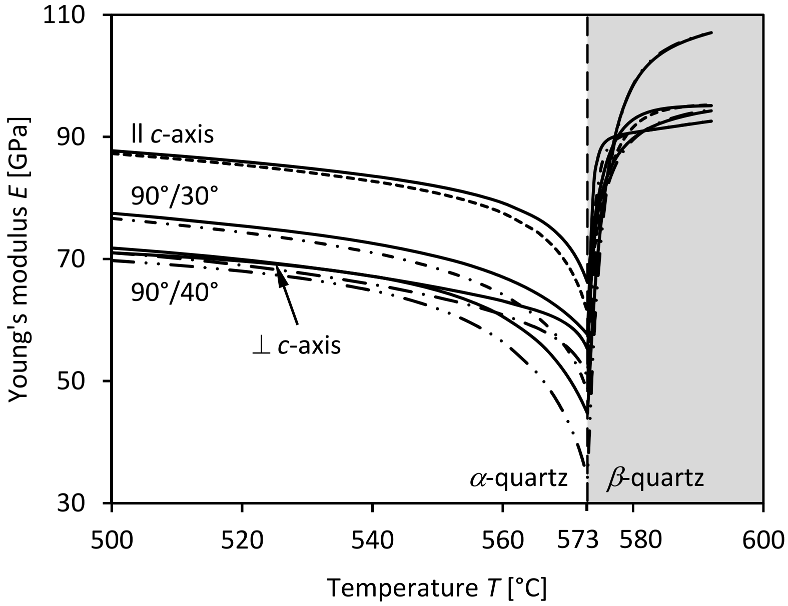

Fig. 30: High- (solid lines) and low-frequency (dashed lines) temperature dependence of the Young's modulus of quartz across the α-β transition with 20 mm support spacing. According to Fig. 16.

The temperature dependence of both high- and low-frequency compliance coefficients is modelled with a least squares fit using equation (9). Contrary to the Young's modulus, the compliance coefficients reach a maximum at the α-β transition and exhibit high values at low frequency and low values at high frequency (Fig. 31). A starting value for S_{14} is taken from Zubov & Firsova (1962) and refined during the modelling. It is found that in this case a frequency-dependent discrimination can be neglected. For frequency-dependent modelling of S_{11}, S_{33}, and the combination of S_{13} and S_{44}, only three differently oriented data sets are required. Hereinafter, data obtained with 40 mm support spacing are used.

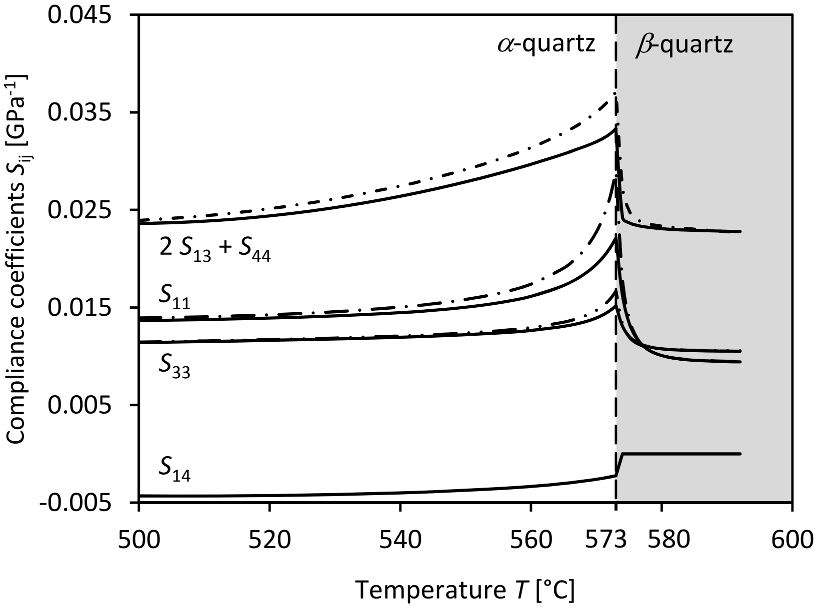

Fig. 31: High- (solid lines) and low-frequency (dashed lines) temperature dependence of the compliance coefficients derived from data presented in Fig. 30.

Anisotropy of the Young's modulus

Three-dimensional diagrams of the anisotropic Young's modulus of quartz are produced with an in-house python script that is based on equation (7) and a systematical variation of the azimuth and polar distance. Various published data sets can be used as input parameters for the elasticity tensor (*e.g.* Lakshtanov *et al.* 2007, Ohno *et al.* 2006, Perrier & De Mandrot 1923, Zubov & Firsova 1962). The Young's modulus of quartz is modelled for both the α-phase under ambient conditions (Fig. 32, left, S_{11} = 0.01273 GPa^{-1}, S_{13} = - 0.00123 GPa^{-1}, S_{14} = - 0.00436 GPa^{-1}, S_{33} = 0.00968 GPa^{-1}, S_{44} = 0.01941 GPa^{-1}) and the β-phase at 600 °C (Fig. 32, right, S_{11} = 0.00952 GPa^{-1}, S_{13} = - 0.00285 GPa^{-1}, S_{14} = 0, S_{33} = 0.01109 GPa^{-1}, S_{44} = 0.02801 GPa^{-1}). Each of the figures indicates the crystal symmetry of the respective quartz phase with identical moduli in opposing crystallographic directions according to Neumann's principle (Chapter 1).

Under ambient conditions, a maximum of the Young's modulus is found at a polar distance of ≈ 48° and an azimuth of 90° (Fig. 33). Two further maxima occur at the same polar distance for 120° azimuthal rotation around the *Z*-axis [001]. This is equivalent to the three-fold *c*-axis of the crystal (Fig. 4, lower left). The maximum modulus is ≈ 131.2 GPa (Fig. 33). Three minima of the Young's modulus are located in-between the maxima at a polar distance of ≈ 70°, they each amount to ≈ 70.0 GPa. The largest change of the Young's modulus by variation of the azimuth is ≈ 53.4 GPa and observed at a polar distance of ≈ 54°. Moreover, the Young's modulus is ≈ 103.3 GPa parallel to the *c*-axis of the crystal, while it is ≈ 78.6 GPa perpendicular to *c*-axis, where it is also invariant.

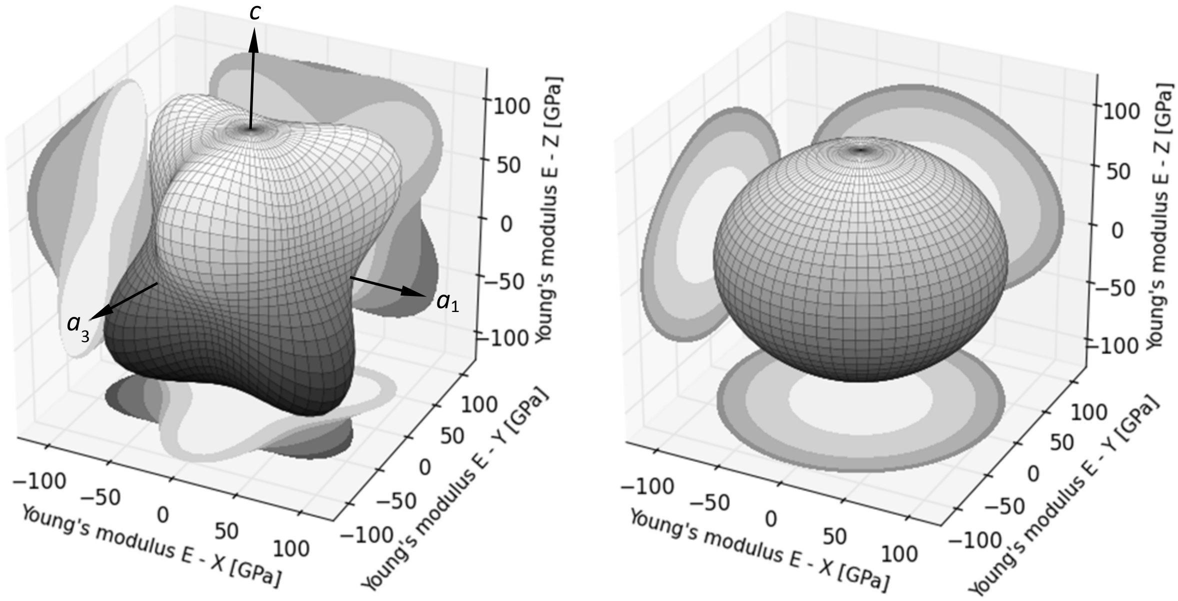

Fig. 32: Three-dimensional diagram of the anisotropic Young's modulus for α-quartz at 20 °C (left) and β-quartz at 600 °C (right). Grid increment = 5° (modified according to Lakshtanov *et al.* 2007).

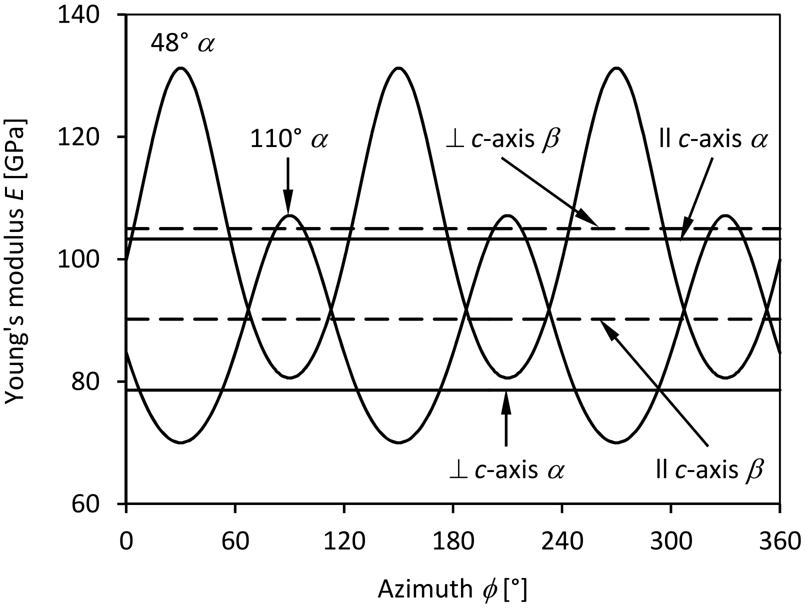

Fig. 33: Azimuthal variation of the anisotropic Young's modulus for α- (solid lines) and β-quartz (dashed lines). Selected polar distances. According to Fig. 32.

Since Fig. 32 is point symmetrical, the moduli observed for polar distances < 90° are found for polar distances > 90° again. The maxima of the α-phase occur at ≈ 132° polar distance, the minima at ≈ 110° (Fig. 33). Their respective azimuth is rotated by 60° compared to polar distances < 90°. For a fixed azimuth, each maximum at a polar distance < 90° corresponds to a minimum at a polar distance > 90° (Fig. 34) because of the two-fold axes perpendicular to the *c*-axis of the crystal (Fig. 4, lower left).

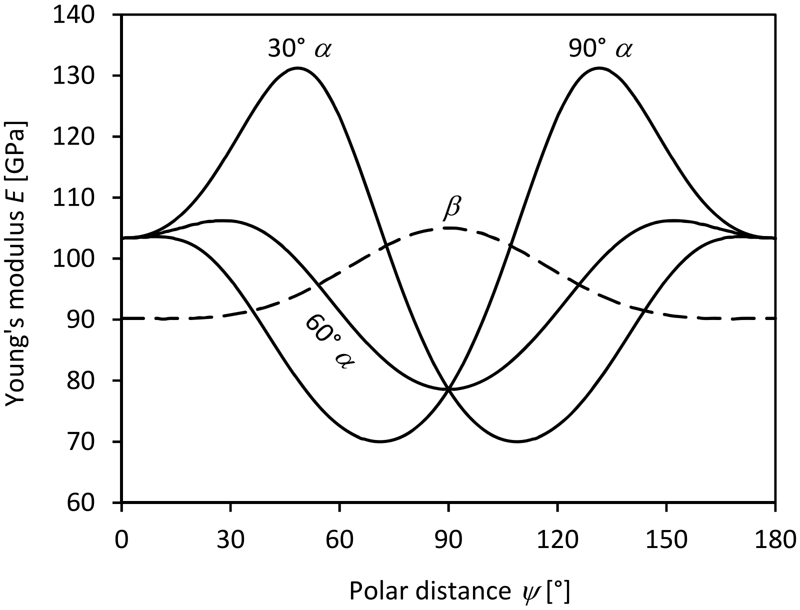

Fig. 34: Variation of the anisotropic Young's modulus for α- (solid lines) and β-quartz (dashed line) with polar distance. Selected azimuthal angles. According to Fig. 32.

Based on the increase of the crystal symmetry through the α-β transition, the three-dimensional diagram of the anisotropic Young's modulus for β-quartz at 600 °C is less complex than for the α-phase (Fig. 32, right). Alternating maxima and minima as present in α-quartz do not exist for β-quartz, since $C_{14} = 0$ (Fig. 33). Hence, the anisotropic Young's modulus depends on the polar distance only (Fig. 34). In contrast to ambient temperature, the Young's modulus parallel to the *c*-axis of the crystal at 600 °C is smaller than perpendicular to it, it reaches ≈ 90.2 and ≈ 105.0 GPa, respectively.

α-β transition: the complex Young's modulus

Equation (9) is transferred into a python script, which provides three-dimensional diagrams of the anisotropic complex Young's modulus of α-quartz, for instance, at ≈ 572 °C. The script uses data from this study, which is collected at 1 Hz and with 40 mm support spacing (Fig. 18). Generally, the storage modulus (40) and dissipation modulus (41) for a particular crystallographic orientation and a distinct frequency are given by the same set of Poynting-Thomson elements. However, real and imaginary compliance coefficients are necessary to describe the three-dimensional distribution of the storage modulus (Fig. 35, left, $S_{11} = 0.02218\ \mathrm{GPa}^{-1}$, $S_{33} = 0.01549\ \mathrm{GPa}^{-1}$, $2S_{13} + S_{44} = 0.03841\ \mathrm{GPa}^{-1}$, $S_{14} = -\ 0.00212\ \mathrm{GPa}^{-1}$) and the dissipation modulus at a certain frequency (Fig. 35, right, $\mathrm{i}S_{11} = 0.14135\ \mathrm{GPa}^{-1}$, $\mathrm{i}S_{33} = 0.38389\ \mathrm{GPa}^{-1}$, $2\mathrm{i}S_{13} + \mathrm{i}S_{44} = 0.50631\ \mathrm{GPa}^{-1}$, $\mathrm{i}S_{14} = -\ 0.00097\ \mathrm{GPa}^{-1}$).

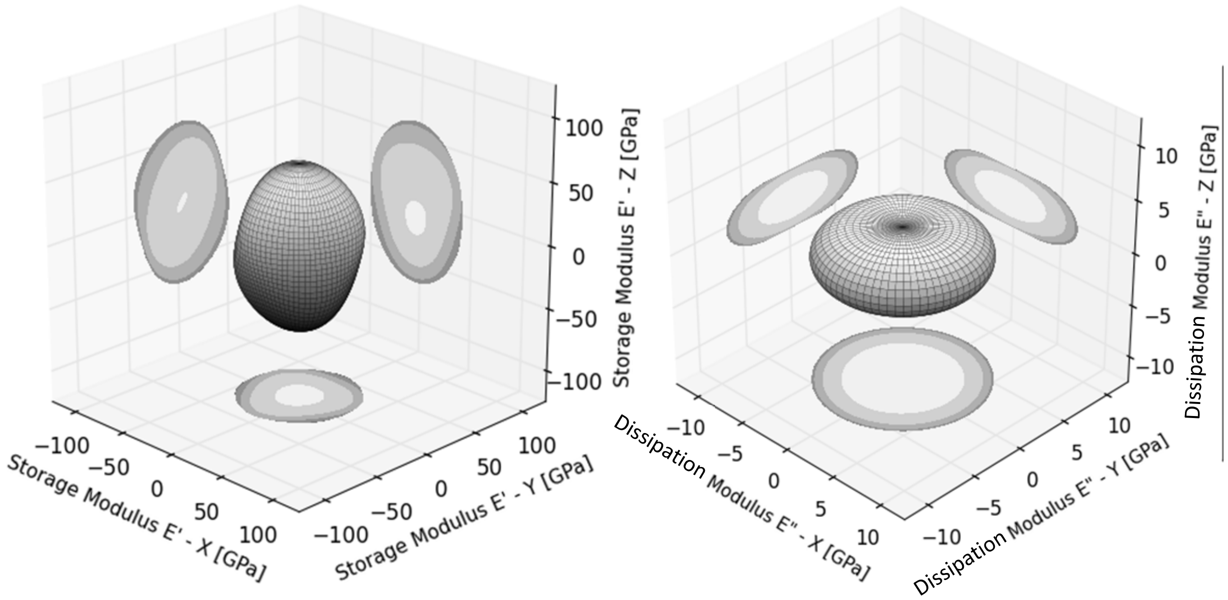

Fig. 35: Three-dimensional diagram of the anisotropic storage (left) and dissipation modulus (right) for α-quartz at ≈ 572 °C and 1 Hz. Grid increment = 5°.

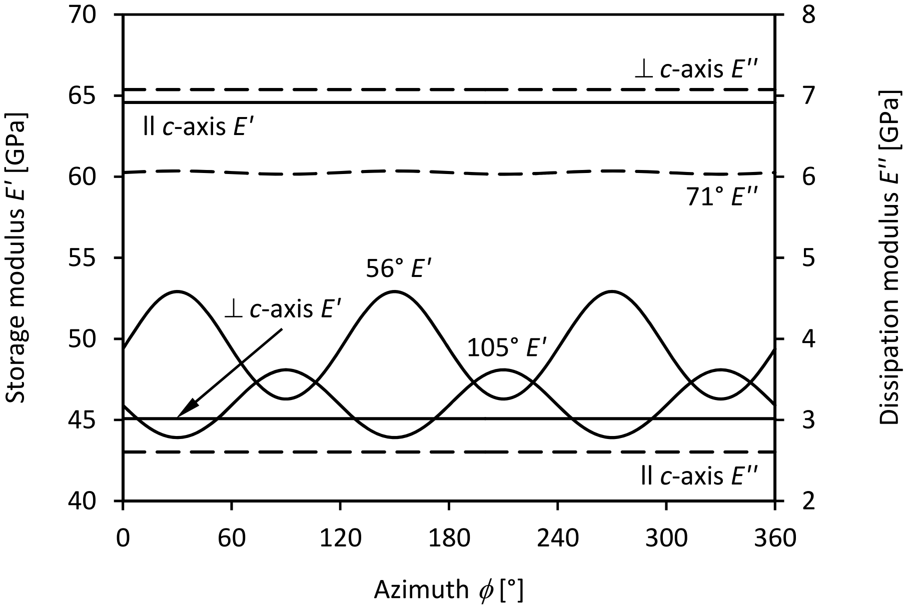

Fig. 36: Azimuthal variation of the anisotropic storage (solid lines) and dissipation modulus (dashed lines). Selected polar distances. According to Fig. 35.

At the α-β transition, the anisotropic storage modulus of α-quartz exhibits significantly lower values (Fig. 35, left) than under ambient conditions (Fig. 32, left). Even though the trigonal symmetry of α-quartz is less pronounced at ≈ 572 °C, it can still be identified (Fig. 35, left). Secondary maxima and primary minima of the storage modulus are shifted by 60° azimuthal rotation for polar distances < 90 and > 90°, while a circular section is found at 90°. The primary minima amount to ≈ 43.9 GPa at polar distances of ≈ 75 and ≈ 105 °C. The primary maximum of ≈ 64.6 GPa is located parallel to the *c*-axis of the crystal (Fig. 36). Perpendicular to that axis, the storage modulus is ≈ 45.1 GPa. Largest changes of the storage modulus by variation of the azimuth reach ≈ 6.6 GPa. This is observed at a polar distance close to ≈ 56°. Variations with polar distance for fixed azimuthal angles show that the storage modulus has a mirror symmetry perpendicular to the *c*-axis at an azimuth of 0° according to the two-fold axes of the crystal (Fig. 37). Hence, this symmetry is repeated by an azimuthal rotation of 60° between the mentioned maxima and minima.

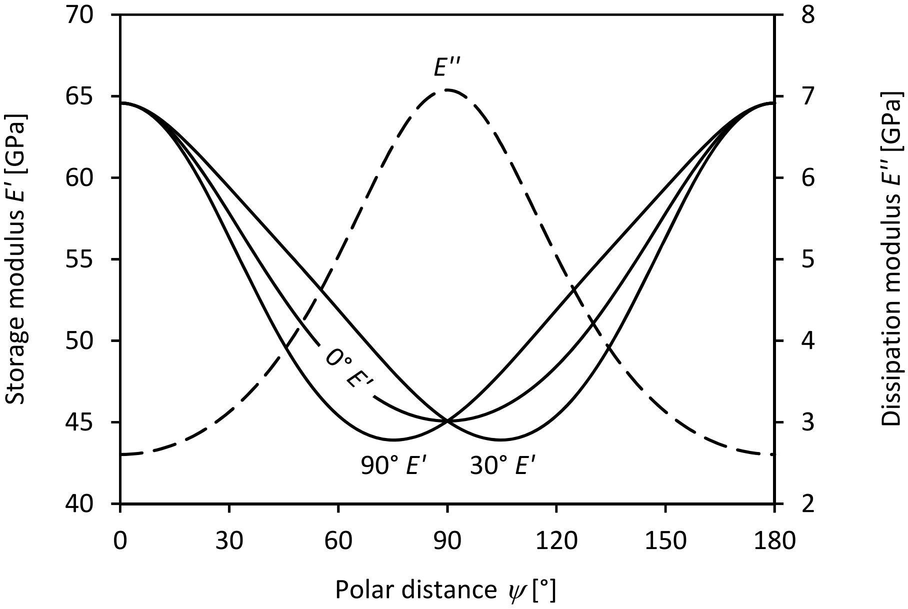

Fig. 37: Variation of the anisotropic storage (solid lines) and dissipation modulus (dashed line) with polar distance. Selected azimuthal angles. According to Fig. 35.

The three-dimensional diagram of the dissipation modulus is clearly different from the storage modulus (Fig. 35, right). Parallel to the *c*-axis of the crystal, where the storage modulus of quartz is relatively high, the dissipation modulus is with ≈ 2.6 GPa comparably low (Fig. 36). Perpendicular to the *c*-axis, the dissipation modulus is high, where the storage modulus of quartz is low. In this case, the dissipation modulus reaches ≈ 7.1 GPa (Fig. 37). Moreover, the dissipation modulus is nearly independent of the azimuth, as its changes are found to be < 0.1 GPa.

α-*β* transition: dispersion of the storage modulus

The difference between the storage modulus loaded at high frequency and the storage modulus loaded at low frequency is referred to as its dispersion. This dispersion is found to be anisotropic and is modelled in three dimensions for 573 °C, whereas the temperature is interpolated from data recorded at 20 mm support spacing (Fig. 38, left, high-frequency parameters: S_{11} = 0.02216 GPa^{-1}, S_{33} = 0.01517 GPa^{-1}, $2S_{13} + S_{44}$ = 0.03370 GPa^{-1}, S_{14} = - 0.00213 GPa^{-1}, low-frequency parameters: S_{11} = 0.02893 GPa^{-1}, S_{33} = 0.01667 GPa^{-1}, $2S_{13} + S_{44}$ = 0.03717 GPa^{-1}, S_{14} = - 0.00213 GPa^{-1}). It is also modelled from data determined at ≈ 572 °C and 40 mm support spacing (Fig. 38, right, high-frequency parameters: S_{11} =

0.01920 GPa^{-1}, S_{33} = 0.01428 GPa^{-1}, 2 S_{13} + S_{44} = 0.03374 GPa^{-1}, S_{14} = - 0.00240 GPa^{-1}, low-frequency parameters: S_{11} = 0.02705 GPa^{-1}, S_{33} = 0.01603 GPa^{-1}, 2 S_{13} + S_{44} = 0.03988 GPa^{-1}, S_{14} = - 0.00240 GPa^{-1}). The two three-dimensional diagrams are qualitatively equal and minor differences can be seen in the contour plots only. However, the dispersion resulting from 40 mm recordings is clearly larger than from 20 mm. Hence, a size effect of the observed behaviour might be assumed.

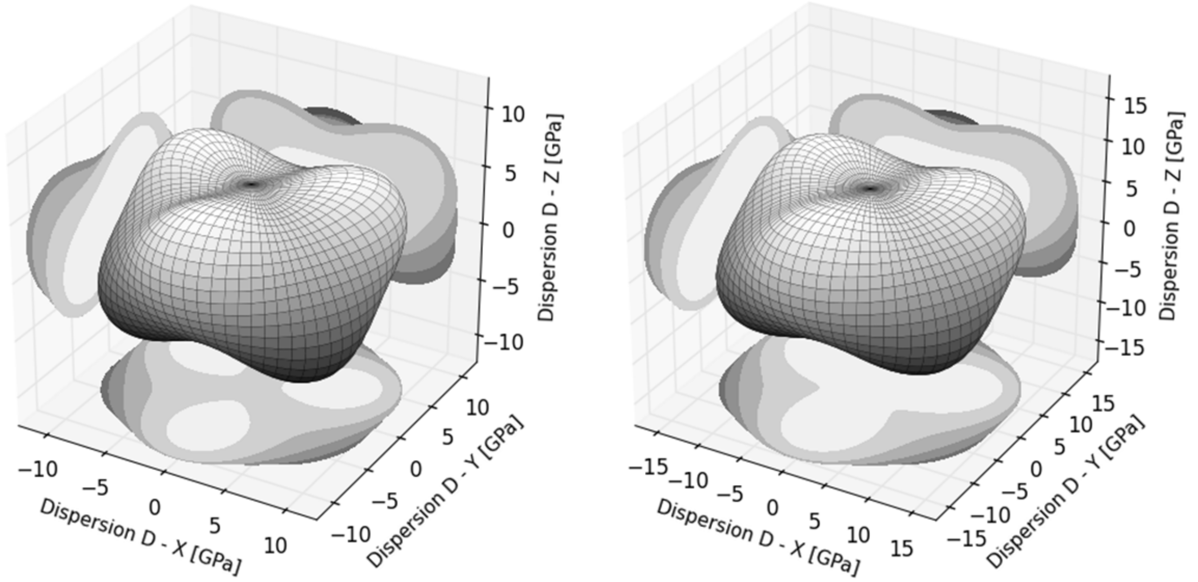

Fig. 38: Three-dimensional diagram of the storage modulus dispersion for quartz: data at 573 °C and 20 mm support spacing (left), data at ≈ 572 °C and 40 mm spacing (right). Grid increment = 5°.

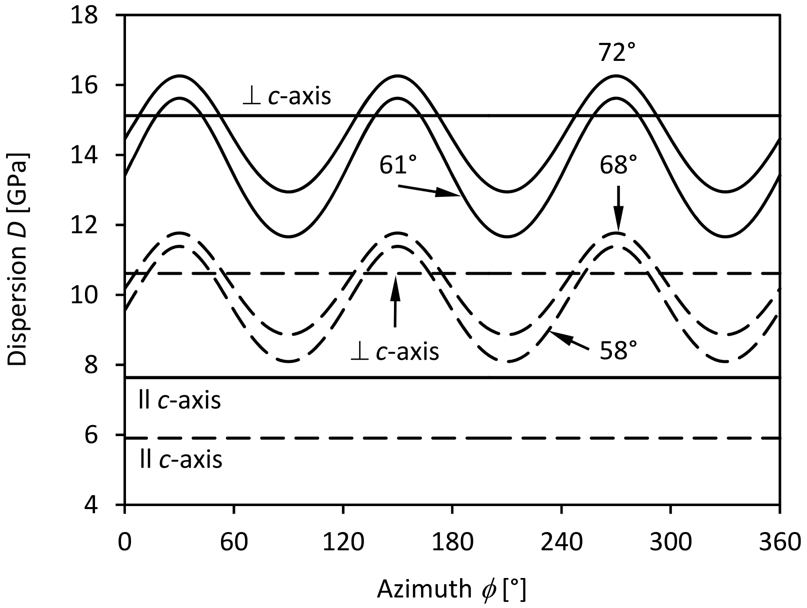

Fig. 39: Azimuthal variation of the storage modulus dispersion for data with 20 mm (dashed lines) and 40 mm (solid lines) support spacing. Selected polar distances. According to Fig. 38.

Perpendicular to the *c*-axis of the crystal, the dispersion of the storage modulus is high, while the storage modulus itself is low. The dispersion modelled from data measured at 20 and 40 mm support spacing is ≈ 10.6 and ≈ 15.1 GPa, respectively (Fig. 39, Fig. 40). The primary dispersion maximum occurs at polar distances close to ≈ 68 and ≈ 72° and amounts to ≈ 11.8 and ≈ 16.3 GPa, respectively. Largest changes of the dispersion by variation of the azimuth are ≈ 3.3 and ≈ 4.0 GPa for polar distances of ≈ 58 and ≈ 61°, respectively. The dispersion minimum is located parallel to the *c*-axis of the crystal and amounts to ≈ 5.9 and ≈ 7.6 GPa, respectively.

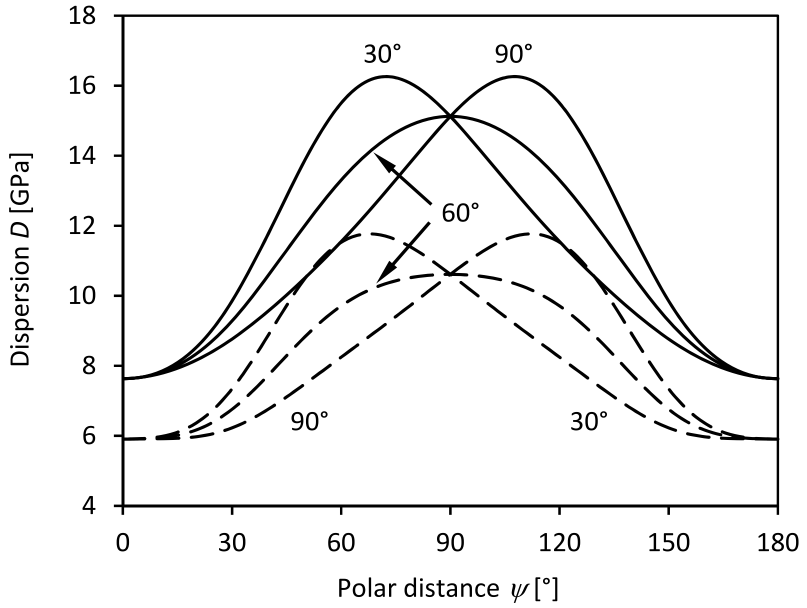

Fig. 40: Variation of the storage modulus dispersion with polar distance for data measured with 20 mm (dashed lines) and 40 mm (solid lines) support spacing. Selected azimuthal angles. According to Fig. 38.

α-β transition: frequency dependence of the elasticity tensor

The determination of the full elasticity tensor of quartz from the Young's modulus technically is not possible. This is shown by the inversion of data according to equation (9) and explained in chapter 1 already. A frequency-dependent assessment of the compliance coefficients for quartz and the equivalent stiffness coefficients at ≈ 572 °C and 40 mm support spacing as well as at ≈ 570 °C and 20 mm support spacing is, however, made on the basis of the observed storage modulus and a set of boundary conditions. The latter rely on data from Lakshtanov *et al.* (2007), whereas the following elasticity tensors are not normalised to this reference.

Contrary to the storage modulus (Fig. 18, left), the compliance coefficients exhibit high values at low frequencies and low values at high frequencies (Fig. 41). S_{11} equals the inverse of the storage modulus perpendicular to the *c*-axis of the crystal (11). Its frequency dependence is described by equation (43) of the Poynting-Thomson model (S_{11}^{-1} 40 mm: E_1 = 572 GPa, E_2 = 70.0 GPa, η = 64.6 GPa; S_{11}^{-1} 20 mm: E_1 = 314 GPa, E_2 = 52.4 GPa, η = 20.9 GPa s). S_{33} equals the inverse of the storage modulus parallel to the *c*-

axis (10). Its frequency dependence is described in the same way (S_{33}^{-1} 40 mm: E_1 = 127 GPa, E_2 = 52.1 GPa, η = 22.9 GPa s; S_{33}^{-1} 20 mm: E_1 = 1,627 GPa, E_2 = 73.7 GPa, η = 124 GPa s). S_{14} is relatively small compared to the other coefficients and can be considered approximately frequency-independent (40 mm: S_{14} = - 0.0024. 20 mm: S_{14} = - 0.0027 GPa^{-1}). At the α-β transition, the ratio between S_{13} and S_{44} is ≈ 0.132. If this ratio is assumed to be frequency-independent as well, the inverse of the corresponding coefficients can also be described by the Poynting-Thomson model. S_{13} (S_{13}^{-1} 40 mm: E_1 = 1,546 GPa, E_2 = 284 GPa, η = 200 GPa s; S_{13}^{-1} 20 mm: E_1 = 1,711 GPa, E_2 = 267 GPa, η = 273 GPa s) and S_{44} (S_{44}^{-1} 40 mm: E_1 = 204 GPa, E_2 = 37.5 GPa, η = 26.4 GPa s; S_{44}^{-1} 20 mm: E_1 = 223 GPa, E_2 = 35.2 GPa, η = 37.2 GPa s) are determined from "$2S_{13} + S_{44}$" (9). Since S_{12} does not contribute to the Young's modulus (Chapter 1), a potential frequency dependence cannot be determined with the experimental set-up. It is estimated from the mean values of the model parameters used for the other coefficients (S_{12}^{-1} 40 mm: E_1 = 612 GPa, E_2 = 106.7 GPa, η = 78.5 GPa s; S_{12}^{-1} 20 mm: E_1 = 969 GPa, E_2 = 107.1 GPa, η = 114 GPa s).

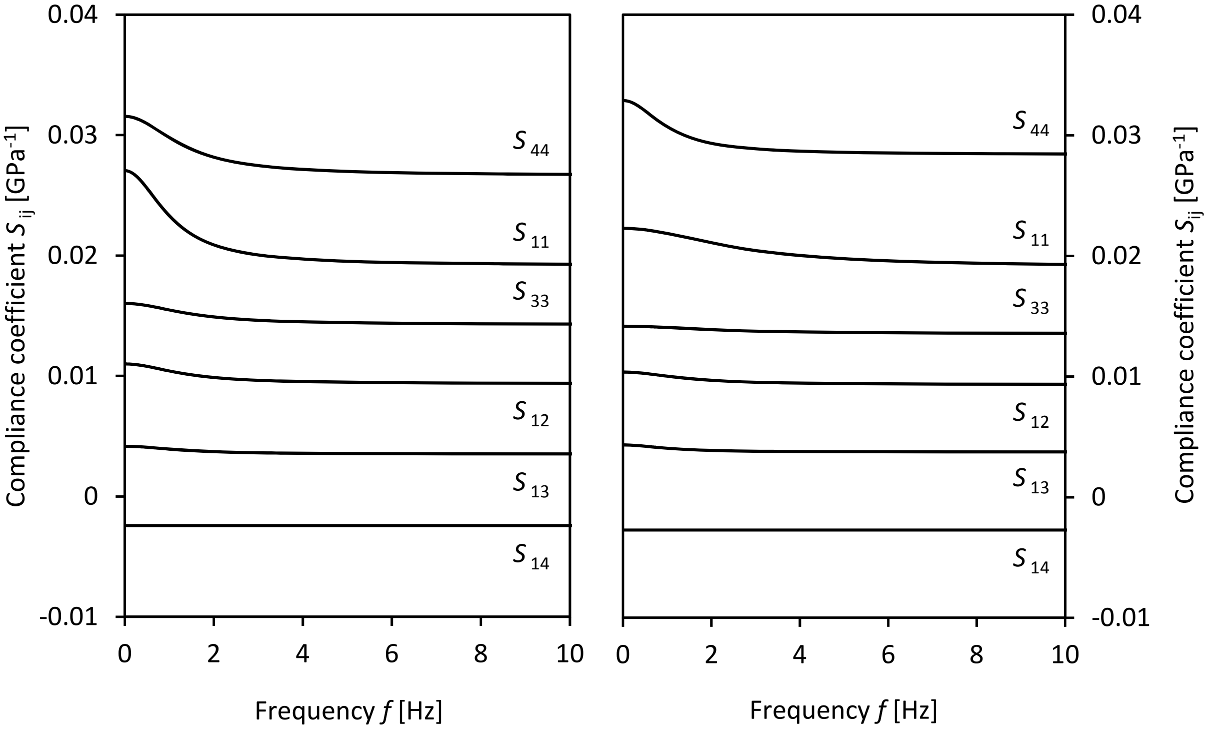

Fig. 41: Frequency dependence of the compliance coefficients for quartz at ≈ 572 °C with 40 mm support spacing (left) and at ≈ 570 °C with 20 mm support spacing (right).

As a result, strong frequency dependences are observed for S_{11} and S_{44}. S_{33} as well as the off-axis coefficients S_{12} and S_{13} are less frequency-dependent. The stiffness tensor is given by the inversion of the compliance tensor (Fig. 42, Appendix 6, Appendix 7). Analogously to the storage modulus, its coefficients show low values at low frequency and high values at high frequency. C_{13} and particularly C_{12} exhibit opposite trends, while the inversion of the elasticity tensor might inherit large systematic errors depending on the C_{12}/C_{11} relationship (Ledbetter *et al.* 1981). Another experimental set-up is therefore recommended, for instance, the logging of travel times of infrasonic elastic waves. Moreover, the parameters could be used to model the frequency-dependent viscoelasticity tensor (44).

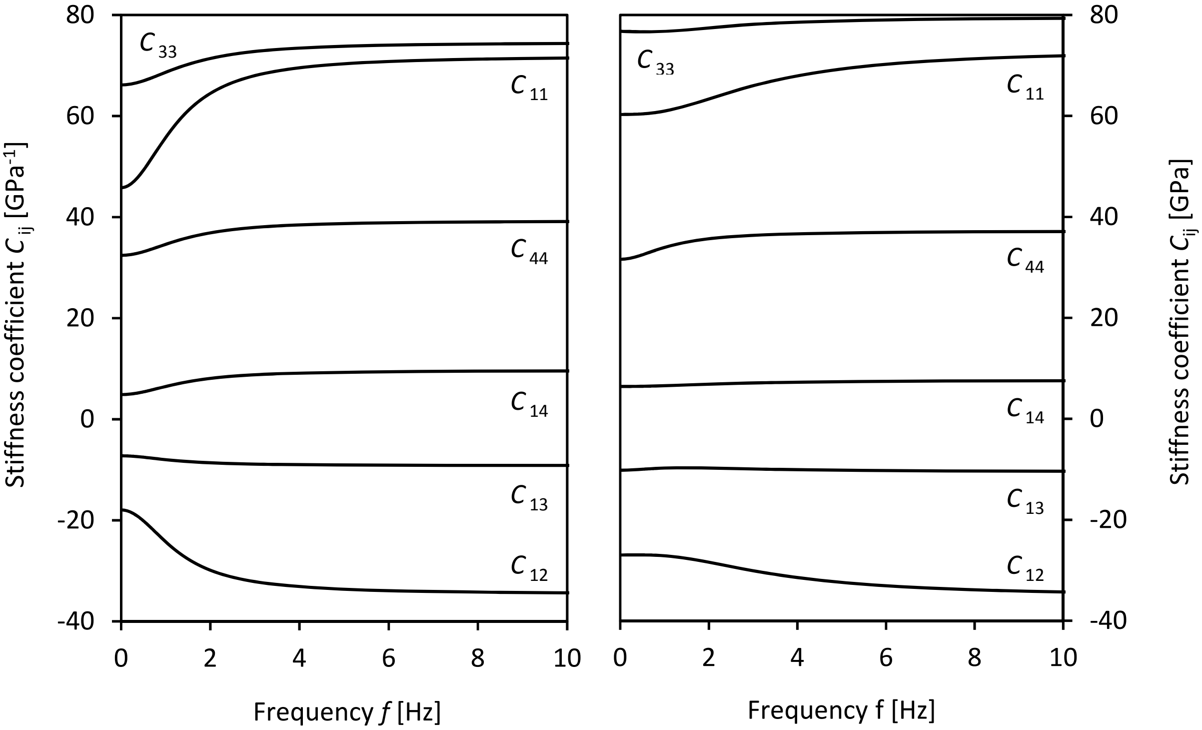

Fig. 42: Frequency dependence of the stiffness coefficients for quartz at ≈ 572 °C with 40 mm support spacing (left) and at ≈ 570 °C with 20 mm support spacing (right).

Frequency and temperature dependence of the elasticity tensor

It is demonstrated already that the Poynting-Thomson model is also valid for describing the elastic and viscoelastic properties of quartz between ≈ 500 °C and the α-β transition. Thus, the anisotropic complex elastic properties of quartz can be derived as a function of frequency for the entire temperature range, if the elements E_1 (Fig. 43), E_2 (Fig. 44), and η (Fig. 45) are expressed as "compliance coefficients".

The "compliance coefficients" in terms of the spring E_2 correspond to the elastic high-frequency limit, with the measured Young's moduli calibrated to data published by Lakshtanov *et al.* (2007) or Zubov & Firsova (1962), for instance. Again, "S_{11}" and "S_{33}" are inverted directly from the Young's modulus perpendicular and parallel to the *c*-axis of the crystal, respectively. Since the frequency dependence of the off-axis coefficients "S_{12}", "S_{13}" and "S_{14}" is found to be of minor importance at the α-β transition, "S_{44}" is now supposed to contain the residual amount of the observed viscoelasticity. The compliance coefficients in terms of the spring constant E_1 consequently are reduced to "S_{11}", "S_{33}", and "S_{44}" (Fig. 44). Values for "S_{12}", "S_{13}", and "S_{14}" are taken from Zubov & Firsova (1962). The dashpot viscosity η is described in sufficient approximation by a second-rank tensor composed of η_{11} and η_{33}. These are modelled from the equivalent complex Young's modulus perpendicular and parallel to the *c*-axis of the crystal, respectively (Fig. 45). The coefficients "S_{11}" and "S_{33}" are directly inverse to η_{11} and η_{33}.

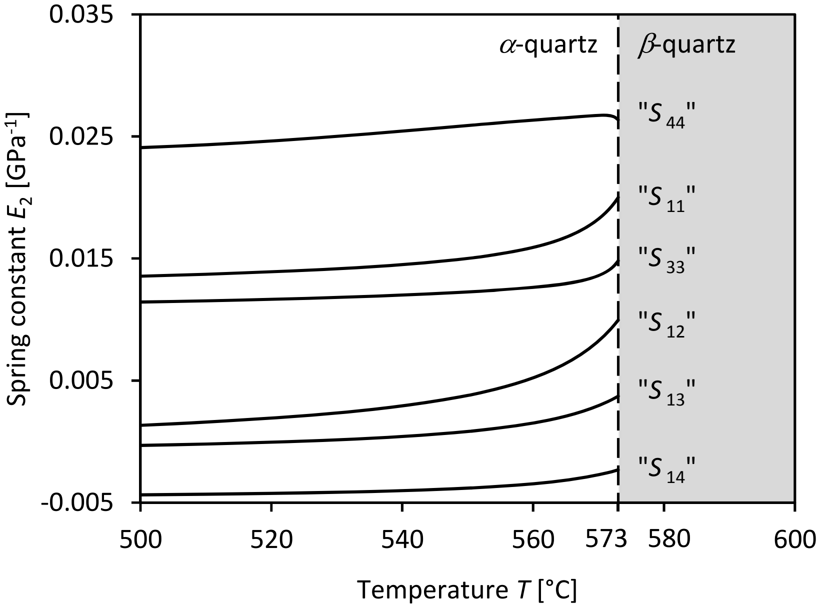

Fig. 43: Temperature dependence of the "compliance coefficients" for α-quartz at 40 mm support spacing between 500 °C and the α-β transition, expressed in terms of the spring constant E_2.

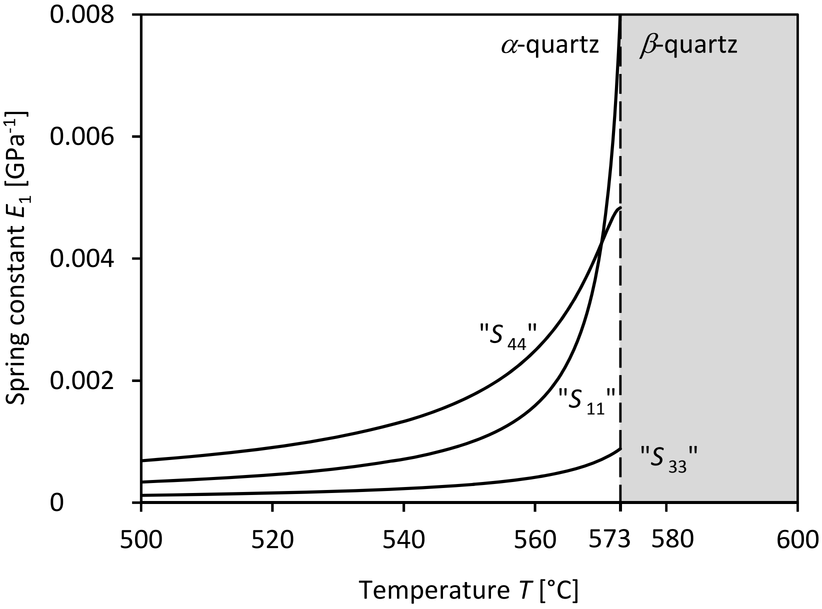

Fig. 44: Temperature dependence of the "compliance coefficients" for α-quartz at 40 mm support spacing between 500 °C and the α-β transition, expressed in terms of the spring constant E_1.

The determination of the "compliance coefficients" in terms of the model elements for the Poynting-Thomson layout is performed by a least squares fit according to equation (9) for data determined at 40 mm support spacing. Equations describing the respective temperature dependences do not exist, but the data can be approximated by equation (46), for instance. Instead, the complex elastic behaviour of quartz as a function of frequency and temperature can be approximated more elegantly using the Pointing-Thomson model with an isotropic time constant of ≈ 0.1 s for the relaxation process, which can be considered independent of temperature within the experimental uncertainties of this study.

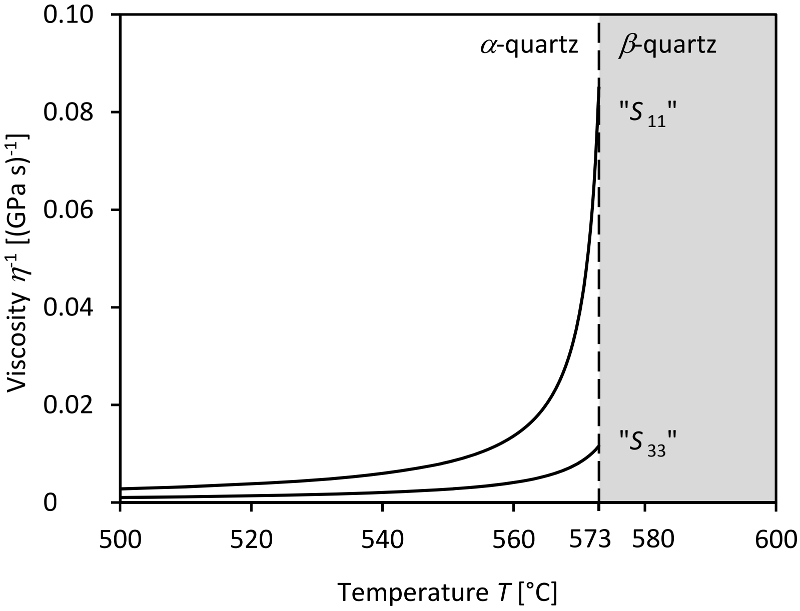

Fig. 45: Temperature dependence of "compliance coefficients" for α-quartz at 40 mm support spacing between 500 °C and the α-β transition, expressed in terms of the inverse dashpot viscosity η.

Anisotropy of the compressional wave velocity

The anisotropic elastic wave velocities of quartz are modelled three-dimensionally with the help of an in-house python script based on the solutions of Christoffel's equation (12). The stiffness coefficients published by Lakshtanov *et al.* (2007) are taken exemplarily as input parameters. Systematic variations of the azimuth and polar distance yield all three elastic wave velocities (Chapter 1), whereas the following considerations are limited to the compressional wave velocity.

The three-dimensional distribution of the compressional wave velocity (Fig. 46) is similar to the three-dimensional diagram of the anisotropic Young's modulus (Fig. 32) due to the trigonal crystal symmetry of α-quartz. Under ambient conditions (Fig. 46, left), for instance, three maxima and three minima shifted by an azimuthal rotation of 60° are observed for both polar distances < 90 and > 90°. This can also be found for high temperatures up to the α-β transition at 573°C (Fig. 46, right), whereas the velocity decreases as the Young's modulus (Fig. 35, left). For the β-phase, a lower compressional wave velocity is found parallel to the *c*-axis of the crystal than perpendicular to it, while the maxima and minima observed for the α-phase vanish as well. The compressional wave velocity is independent of the azimuth.

A significant difference of the three-dimensional diagrams for the compressional wave velocity and the Young's modulus, however, appears perpendicular to the *c*-axis of the crystal. In this case, the compressional wave velocity shows a six-fold symmetry instead of a circular section, which is due to a distortion between the direction of wave propagation and the direction of wave motion (Appendix 4). The maximum distortion perpendicular to the *c*-axis is ≈ 25.9°. It occurs at an azimuth of 30° and a rotation of

60° around the *c*-axis. The distortion vanishes in principal directions according to the crystallographic *a*- and *c*-axes (Fig. 47, right). A section of the *XZ*-plane also shows strong variation of the distortion (Fig. 48, right).

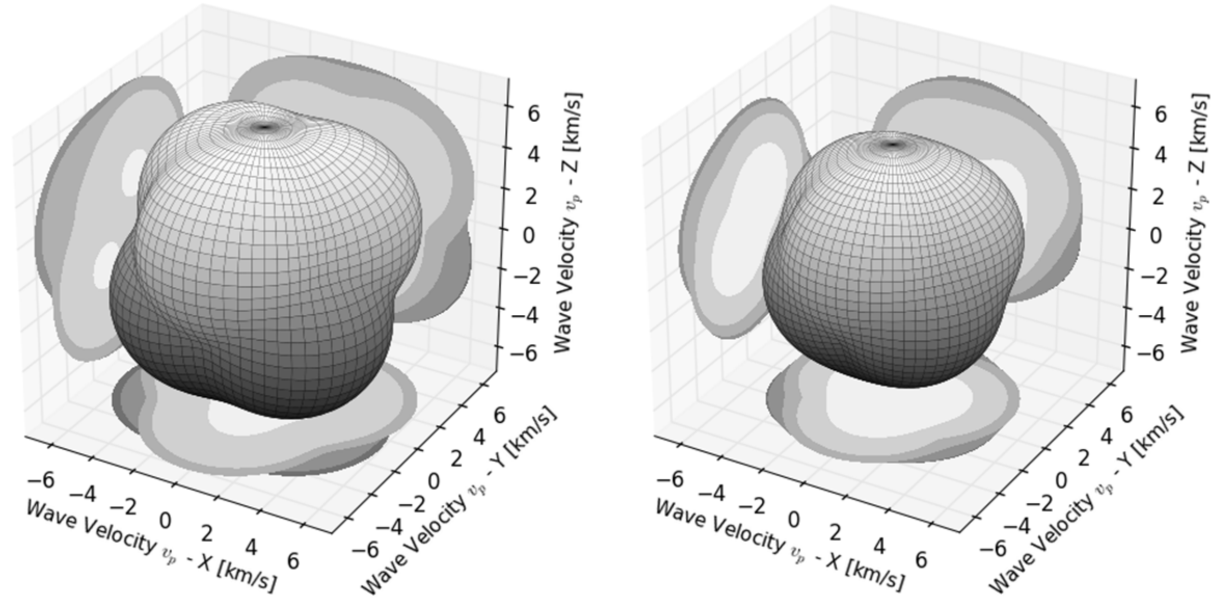

Fig. 46: Three-dimensional diagram of the compressional wave velocity for α-quartz at high frequency and ambient temperature (left) and 573 °C (right). Grid increment = 5° (modified according to Lakshtanov *et al.* 2007).

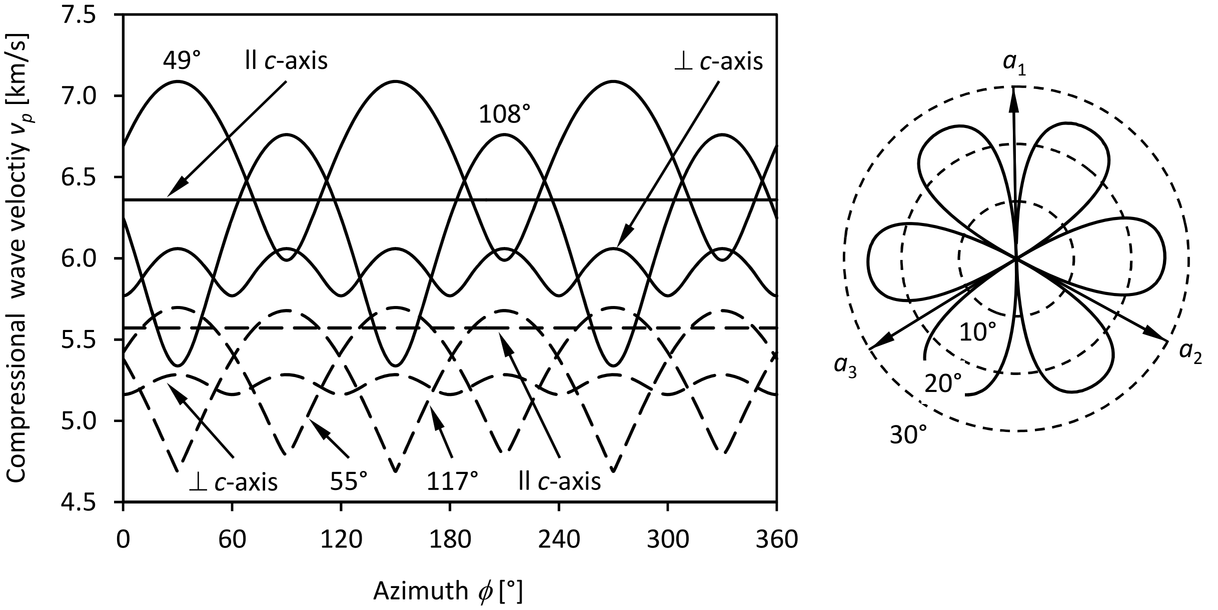

Fig. 47: Azimuthal variation of the compressional wave velocity (left) for selected polar distances at ambient temperature (solid lines) and 573 °C (dashed lines) according to Fig. 46. *C*-cut of the distortion between propagation and motion vectors of the wave under ambient conditions (right).

The compressional velocity parallel to the *c*-axis of the crystal is ≈ 6.36 km/s (Fig. 47, left, Fig. 48, left). Its primary maximum is ≈ 7.09 km/s and found at an azimuth of ≈ 29° and a polar distance of ≈ 49°. The minimum is ≈ 5.34 km/s and it is observed close to ≈ 108° polar distance. The largest change in the compressional wave velocity by variation of the azimuth occurs at polar distances of ≈ 68 and ≈ 112°. It amounts to ≈ 1.48 km/s. Perpendicular to the *c*-axis, the compressional wave velocity varies between ≈ 5.77 km/s parallel to the *X*-axis/*a*-axis and ≈ 6.06 km/s parallel to the *Y*-axis. These values are modelled for a density of 2.65 g/cm³ under ambient conditions (*e.g.* Okrusch & Matthes 2005).

In contrast, the density of quartz at the α-β transition is given by ≈ 2.53 g/cm³ (*e.g.* Ohno *et al.* 2006). The compressional wave velocity parallel to the *c*-axis of α-quartz is ≈ 5.52 km/s. The primary maximum of the compressional wave velocity is ≈ 5.70 km/s and found at polar distances of ≈ 55 and ≈ 125°. The minimum is ≈ 4.70 km/s, it is observed at polar distances at ≈ 63° and ≈ 117°. The largest change of the compressional wave velocity by variation of the azimuth amounts to ≈ 0.99 km/s at polar distances of ≈ 62° and ≈ 118°. Variations from ≈ 5.16 to ≈ 5.28 km/s are observed parallel to the *X*-axis/*a*-axis and *Y*-axis, respectively.

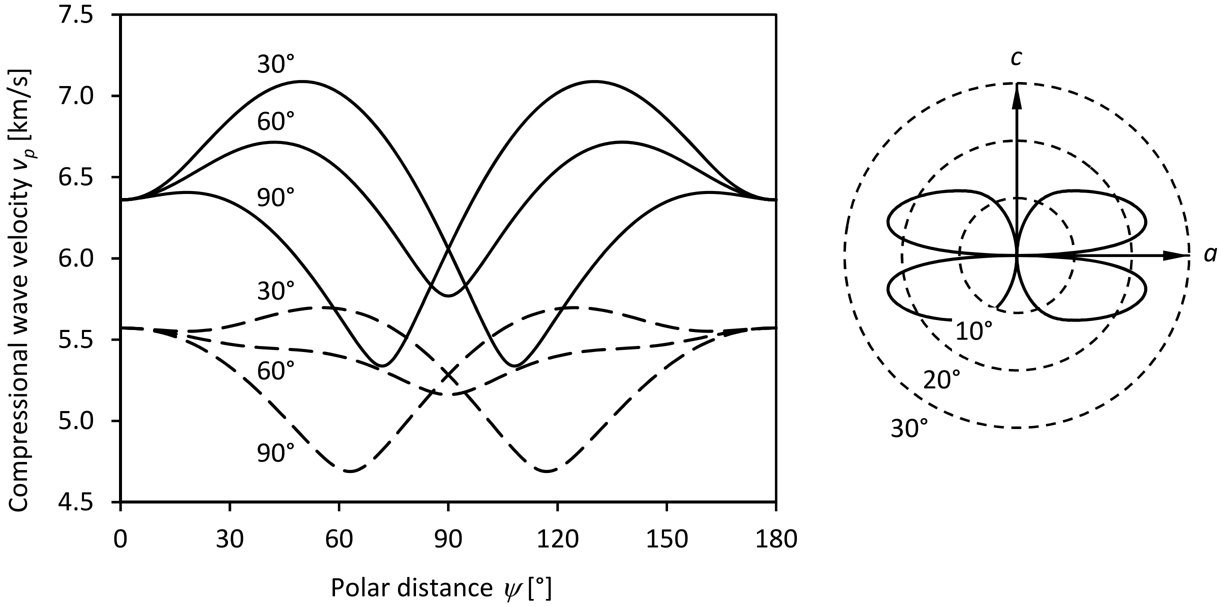

Fig. 48: Variation of the compressional wave velocity with polar distance for selected azimuthal angles (left) at ambient temperature (solid lines) and at 573°C (dashed lines) according to Fig. 46. *Y*-cut of the distortion between propagation and motion vectors of the wave under ambient conditions (right).

α-β transition: dispersion of the compressional wave velocity and the seismic quality factor

The anisotropic dispersion of the compressional wave velocity in α-quartz at the α-β transition is modelled parallel to the *c*-axis (13) and parallel to the *a*-axis of the crystal (14) on the basis of the previously presented frequency-dependent elasticity coefficients for 40 mm (Fig. 42, left) and 20 mm support spacing (Fig. 42, right). A density of 2.53 g/cm³ (Ohno *et al.* 2006) is used in both cases. The high-frequency compressional wave velocities are normalised to data published by Lakshtanov *et al.* (2007). At 40 mm support spacing, the dispersion of the anisotropic compressional wave velocity between 0 to 10 Hz is ≈ 0.31 km/s parallel to the *c*-axis of the crystal and ≈ 1.07 km/s parallel to the *a*-axis (Fig. 49, left). At 20 mm support spacing, it is ≈ 0.10 and 0.49 km/s, respectively (Fig. 49, right).

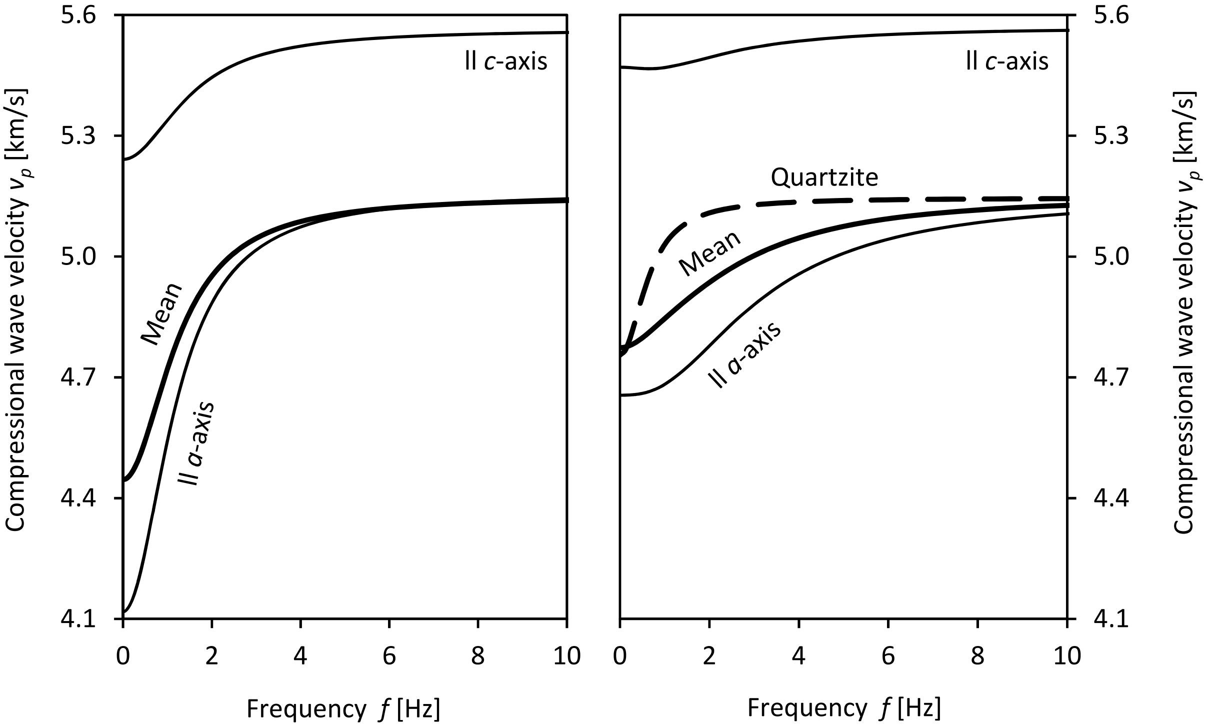

Fig. 49: Anisotropic frequency-dependent compressional wave velocities for quartz at ≈ 572 °C and 40 mm support spacing (left) as well as for quartz and quartzite at ≈ 570 °C and 20 mm support spacing (right). Mean values are Voigt-Reuss-Hill averages. See text for details.

The dispersion of the mean compressional wave velocity for an isotropic quartz polycrystal is modelled using the Voigt-Reuss-Hill approximation (Appendix 8) to derive the mean Young's modulus (E_{VRH} 40 mm: E_1 = 199 GPa, E_2 = 58.9 GPa, η = 31.4 GPa s; E_{VRH} 20 mm: E_1 = 429 GPa, E_2 = 58.9 GPa, η = 34.4 GPa s) from the frequency-dependent stiffness tensor (Fig. 42). Again, the high-frequency limit is normalised to the value published by Lakshtanov *et al.* (2007), which is very close to the compressional wave velocity parallel to the *a*-axis of a quartz crystal. The resultant mean dispersion is ≈ 0.72 km/s at 40 mm support spacing and ≈ 0.38 km/s at 20 mm support spacing.

The high-frequency storage modulus for Dalsland quartzite is normalised to the isotropic Young's modulus of quartz at the α-β transition, which is ≈ 57.7 GPa (Lakshtanov *et al.* (2007). A density of 2.53 g/cm^3 and a Poisson's ratio of - 0.3 are used to convert the Young's modulus into the compressional wave velocity (Appendix 8). A dispersion of ≈ 0.39 km/s resulted. This is in agreement with the expectations based on quartz. The time constant of the relaxation for Dalsland quartzite is ≈ 0.24 s, which is more than twice the observed relaxation time for quartz. Hence, the relaxation process is assumed to be dominated by intergranular effects, such as grain boundary sliding. When the intra- and intergranular complex elastic properties of Dalsland quartzite correspond to a serial layout of two Poynting-Thomson models, 51.7 and 43.2 GPa are the high- and low-frequency limits of the grain boundary effect, respectively.

The seismic quality factor equals the ratio between the storage modulus and the dissipation modulus according to equation (1). It is generally dimensionless and anisotropic in case of a trigonal crystal like α-quartz. The inverse of the seismic quality factor corresponds to the internal friction and is equivalent to the phase lag between sinusoidal stress and strain amplitudes (19). The seismic quality factor and internal friction are modelled both parallel and perpendicular to the *c*-axis of a quartz crystal from the complex Young's moduli observed at ≈ 572 °C and 40 mm support spacing (Fig. 50, left) as well as at ≈ 570 °C and 20 mm support spacing (Fig. 50, right).

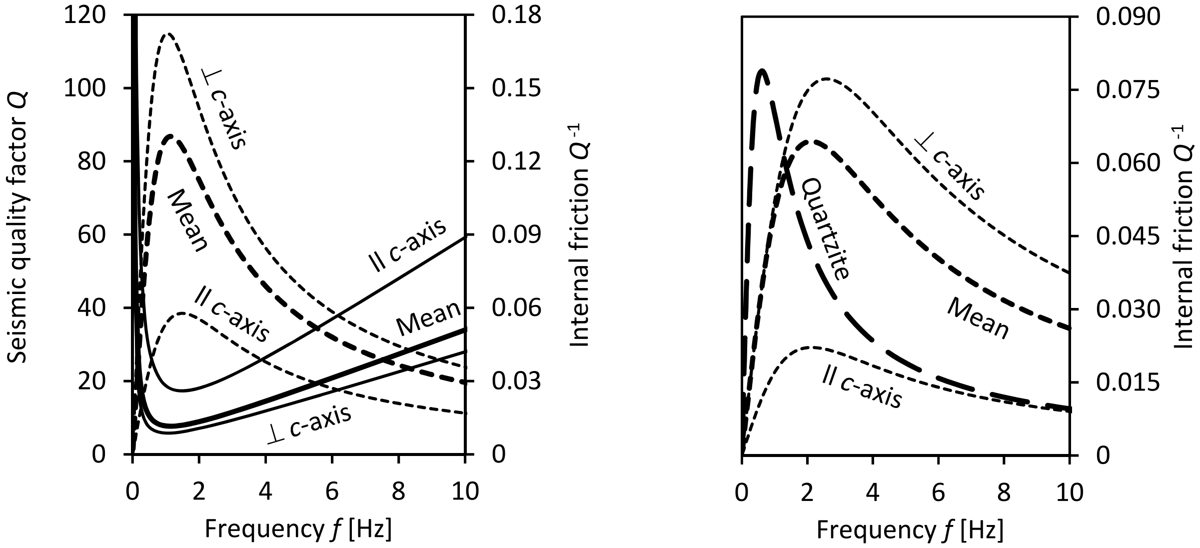

Fig. 50: Frequency dependence of the seismic quality factor (solid lines) and the internal friction (dashed lines) for quartz at ≈ 572 °C and 40 mm support spacing (left) as well as for quartz and quartzite (coarse dashed line) at ≈ 570 °C and 20 mm support spacing (right).

From 0 to 10 Hz, the seismic quality factor exhibits a minimum, while the internal friction exhibits a maximum at the same frequency. Both show stronger changes at frequencies below the extremes than above. The maxima recorded with 40 mm support spacing are ≈ 0.058 at ≈ 1.5 Hz and ≈ 0.172 at ≈ 1.0 Hz parallel and perpendicular to the c-axis of a quartz crystal, respectively. The maxima observed for 20 mm support spacing are ≈ 0.022 at ≈ 2.1 Hz and ≈ 0.077 at ≈ 2.1 Hz. The maximum of the mean internal friction in an isotropic quartz polycrystal is ≈ 0.130 at ≈ 1.1 Hz and ≈ 0.064 and ≈ 2.1 Hz for 40 and 20 mm support spacings, respectively. In comparison, a maximum internal friction of ≈ 0.079 is found for Dalsland quartzite at ≈ 0.6 Hz.

In consequence, it is proposed to use the frequency- and temperature-dependent elastic properties of quartz and quartzite, especially in the vicinity of its α-β transition, as an additional tool to estimate temperatures within the Earth's crust. This could help to better distinguish between a fully crystallised and a partly molten crust. This might be tested with high-resolution seismic methods in a hot, thick, rather dry, and quartz-rich continental crust. Strongly frequency-dependent seismic wave velocities related to a strong and frequency-dependent attenuation of the waves could be used. In a quartz-rich crust a maximum attenuation of seismic waves is expected at ≈ 1 Hz, whereas at lower and higher frequencies the attenuation should decrease. This would provide an independent proof of the crustal models proposed, for instance, by Mechie *et al.* (2004) and Marini & Manzella (2005), which assume a quartz-rich crust, *e.g.* beneath Tibet and the Tuscany.

Differences between quartz and quartzite

Approaching the α-β transition in a quartzite, cracks will form and propagate (*e.g.* Mc Knight 2008) as a results of the anisotropic thermal expansion of quartz (Chapter 1). For Dalsland quartzite, this is associated with a permanent reduction of the Young's modulus due to the development of micro-cracks (Chapter 4). In comparison to intact quartz, a so-called crack density (*e.g.* O'Connell & Budiansky 1974) or damage factor (*e.g.* Doncieux *et al.* 2008) can be assigned to the rock. Thus, close to the α-β transition at ≈ 570 °C, the high-frequency Young's modulus of Dalsland quartzite is ≈ 50 % lower than the Young's modulus of a modelled isotropic quartz polycrystal (Fig. 51). At ambient temperature, the crack density results in a lower Young's modulus of ≈ 33 % (Fig. 21).

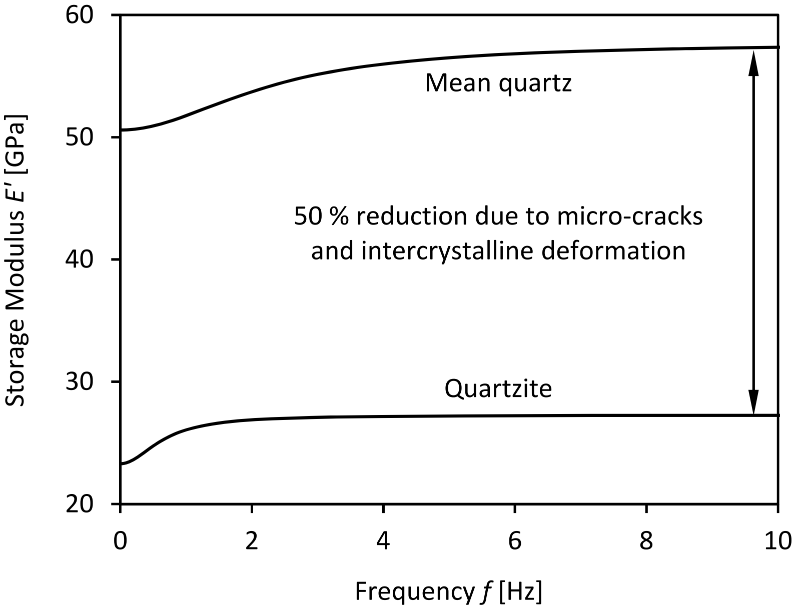

Fig. 51: Frequency dependence of the storage modulus for an isotropic quartz polycrystal compared to quartzite from measurements with 20 mm support spacing.

One might speculate that the lower relaxation time of Dalsland quartzite in comparison to a single crystal quartz specimen with a time constant of ≈ 0.24 s and ≈ 1 s, respectively, might be due to a temperature uncertainty of the experiment. Intercrystalline viscoelastic effects, however, need to be taken into account in polycrystals (Chapter 1). These are pores, which could be approximated as a spring low Young's modulus in an equivalent mechanical model, and grain boundary sliding that is often represented by a Kelvin-Voigt element (*e.g.* Mosher *et al.* 1976). In a model representation, these intercrystalline effects can be added in series to the Poynting-Thomson model describing the intracrystalline part, when the bulk deformation of the specimen is modelled. As Dalsland quartzite has a negligible porosity, mainly grain boundary sliding needs to be considered.

Pressure dependence of elasticity

Rising pressure leads to linearly increasing stiffness coefficients of α-quartz (*e.g.* Calderon *et al.* 2007) by compaction of the crystal lattice (Fig. 5) that is linked to an enlargement of the tetrahedral tilt (Fig. 3, left). Compared to ambient pressure, higher temperatures are necessary to rotate the tetrahedra from the given trigonal symmetry of the α-phase to the hexagonal configuration of the β-phase (Fig. 4). The combination of physical conditions meeting the α-β transition (Fig. 1, Appendix 1) is described by the Clausius-Clapeyron relation, which is verified experimentally by *e.g.* de Boer (1996). As a consequence, both the Young's modulus and compressional wave velocity also increase with pressure (*e.g.* Fielitz 1971, Kern 1979).

These intracrystalline considerations also hold for quartz-bearing rocks. Their stiffness first increases non-linearly due to the closure of pore space and micro-cracks. This is reflected by a triaxial compression of Lahr sandstone (Fig. 52). Its non-linear pressure-dependent elastic behaviour is approximated by

$$E(\sigma_3) = S - \left(S - E_0\right) e^{k\,\sigma_3}. \qquad (48)$$

This exponential function needs to be expanded by a linear term with a slope positive for even higher pressures, as they occur deep in the Earth's crust. In equation (48) σ_3 stands for the confining pressure, while E_0 and S represent the lower and upper limits of the relatively increasing Young's modulus, respectively.

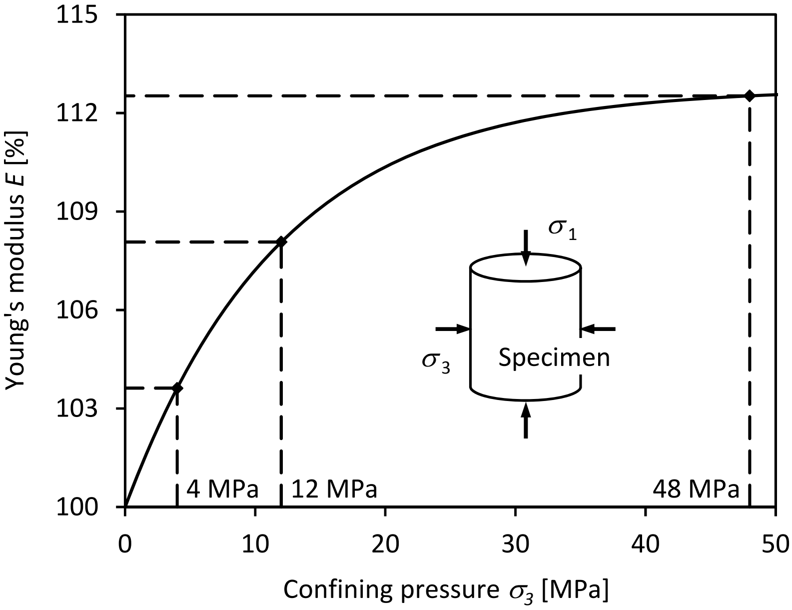

Fig. 52: Relative pressure dependence (line) of the static Young's modulus for Lahr sandstone. Data points (symbols) are from triaxial compression at ambient temperature.

Peng & Redfern (2013) show by dynamic torsion at ambient pressure that the shear modulus of novaculite is nearly frequency-independent at the α-β transition. This is in disagreement with a dispersion of ≈ 11.5 GPa for the isotropic shear modulus in this study. Dynamic forced torsion experiments at high temperature and high pressure by Lu & Jackson (1998) reveal intensified attenuation of the complex shear modulus of Cape Sorell quartzite and Delegate aplite at the α-β transition. The dissipation modulus at high pressure is approximately one order of magnitude lower than observed in this study. Lu & Jackson (1998) also do not determine a frequency dependence of the storage modulus. Hence, it may be speculated that the dynamic variation of Dauphiné twin domains could be largely inhibited at elevated pressure. Further considerations would require dynamic triaxial experiments, which is beyond the scope of this thesis.

6. Conclusions

Initially, the following hypothesis is made: the Young's modulus of quartz becomes systematically frequency-dependent in the vicinity of the α-β transition. The results obtained from dynamic mechanical thermal analysis of this study support this hypothesis. The frequency dependence of the elastic properties of quartz is caused by gradual softening of the crystal lattice in the vicinity of the α-β transition. In detail, the following conclusions are drawn:

- At a constant loading frequency, the storage modulus of quartz exhibits a minimum at the α-β transition, while the equivalent dissipation modulus shows a maximum at ≈ 1 Hz.
- Isothermal variations of the loading frequency lead to a frequency dependence of the complex Young's modulus of quartz, most clearly at 573 °C. It vanishes below ≈ 500 °C as well as above the transformation.
- The storage modulus of quartz sigmoidally increases with frequency. Including the dissipation maximum, the complex elastic behaviour can be fully described by the mechanical Poynting-Thomson model, within the experimental uncertainties.
- The frequency dependence of the complex Young's modulus for quartz is explained by the temporal formation of Dauphiné twin domains, whereas the high-temperature elastic data of fused silica are free from such a viscoelastic effect.
- Discrepancies for several published data sets of the high-temperature Young's modulus of quartz close to the α-β transition are in agreement with the observations in this study. These discrepancies can be explained as the result of a frequency dependence of the Young's modulus.
- The frequency dependence of the complex Young's modulus is found to be anisotropic. Perpendicular to the *c*-axis of the crystal, the dispersion of the storage modulus and the dissipation modulus are large, while both are comparably small parallel to the *c*-axis, respectively depending on the experimental geometry.
- The anisotropic viscosity resulting from the Poynting-Thomson model decreases linearly with increasing temperature towards the α-β transition. It can be fully described by a second-rank tensor, within the experimental uncertainties. Measurements close to ≈ 572 °C at 40 mm support spacing yield viscosities of ≈ 65 GPa s parallel to the *c*-axis of the crystal and ≈ 23 GPa s perpendicular to it. The isotropic temperature-independent time constant of the relaxation process is ≈ 0.1 s.
- A frequency-dependent elasticity tensor of quartz is determined. Its stiffness coefficients are used to model the dispersion of the compressional wave velocity of ≈ 6 % parallel to the *c*-axis of the crystal and ≈ 20 % parallel to the *a*-axis with 40 mm support spacing.
- Observations for synthetic quartz at 20 mm support spacing also hold for natural crystals and quartz-bearing rocks at the same experimental geometry. The dispersion of the mean compressional wave velocity of quartz is in agreement with the observations for isotropic Dalsland quartzite, it is ≈ 0.39 km/s. The internal friction of quartzite is slightly higher than for an isotropic quartz polycrystal due to grain boundary sliding, which also slows down the relaxation process.
- Pressure has the opposite effect on the elastic properties of brittle rocks, such as the quartz-rich Lahr sandstone, than temperature. The influence of pressure on the frequency dependence of the elastic properties of quartz and quartz-rich rocks remains an open question.

- A symmetrical three-point bending geometry is suited for the examination of crystals and fine-grained rocks, such as Dalsland quartzite. Medium- to coarse-grained rocks, such as Lahr sandstone, can be investigated more precisely by uniaxial loading.

It is proposed to use the frequency- and temperature-dependent elastic properties of quartz in the vicinity of its α-β transition as an additional tool to estimate temperatures within the Earth's crust and to distinguish between a fully crystallised and a partly molten crust.

7. Acknowledgement

First, I would like to thank my family and friends for their encouragement and support over many years! Second, this work was supported by many scientists, technicians and administrative staff, whom I want offer my sincere gratitude.

I thank my supervisor Prof. Dr. Frank R. Schilling (Chair in Technical Petrophysics at KIT) for his advice and patience. He gave me the opportunity to study the elastic properties of minerals and rocks under excellent conditions, based on funding by Dr. Martin Herrenknecht (Founder of Herrenknecht Tunneling Systems). This collaboration deeply contributed to the consolidation and broadening of my knowledge.

Special thanks go to my secondary supervisor PD Dr. Jörg-Detlef Eckhardt (Chair in Chemistry and Mineralogy of Building Materials at KIT) and the examination board, notably Prof. Dr. Thomas Kohl (Chair in Geothermics at KIT), Prof. Dr. Heinz-Günter Stosch (Chair in Mineralogy and Petrology at KIT), Prof. Dr. Thomas Neumann (Chair in Geochemistry at KIT), and Prof. Dr. Thomas Seelig (Chair in Mechanics at KIT).

I enjoyed profound scientific discussions with my scientific colleagues Dr. Birgit Müller, Dr. Christian Scheffzük, Dr. Alik Ismail-Zadeh, and Dr. Tobias Hergert as well as many students in geosciences. In addition, I appreciate the experimental support by Dr. Elisabeth Eiche.

I further acknowledge all technicians from the Institute of Applied Geosciences and from the Institute of Soil Mechanics and Rock Mechanics for their help with the preparation of the investigated specimen. I also thank the administrative staff at KIT, particularly in the division for Technical Petrophysics.

Additionally, I thank all members of the COBRA-team for the collaboration within the correspondent project throughout the past years, funded by a Geotechnologies grant (support code: 03G0763A) from the German Federal Ministry of Education and Research.

8. References

Aines, R.D., Kirby, S.H. & Rossman, G.R. Hydrogen specification in synthetic quartz. *Phys. Chem. Minerals* **11**, 204-212 (1984).

Akaogi, M., Yusa, H., Shiraishi, K. & Suzuki, T. Thermodynamic properties of α-quartz, coesite, and stishovite and equilibrium phase relations at high pressures and high temperatures. *J. Geophys. Res.* **100**, 22,337-22,347 (1995).

Akyildiz, F., Jones, R.S. & Walters, K. On the spring-dashpot representation of linear viscoelastic behaviour. *Rheol. Acta.* **29**, 482-484 (1990).

Allmann, R. & Hinek, R. The introduction of structure types into the Inorganic Crystal Structure Database ICSD. *Acta Cryst. A* **63**, 412-417 (2007).

Alshits, V.I. & Lothe, J. Acoustic axes in trigonal crystals. *Wave Motion* **43**, 177-192 (2006).

Amatuni, A.N. & Shevchenko, E.B. Linear thermal expansion of monocrystalline quartz and aluminium oxide. *Meas. Tech.* **9**, 1256-1260 (1966).

Anderson, D.L. The anelasticity of the mantle. *Geophys. J. R. Astr. Soc.* **14**, 135-164 (1967).

Anderson, O.L. & Bömmel, H.E. Ultrasonic absorption in fused silica at low temperatures and high frequencies. *J. Am. Ceram. Soc.* **38**, 125-131 (1955).

Anderson, O.L., Schreiber, E. & Liebermann, R.C. Some elastic constant data on minerals relevant to geophysics. *Rev. Geophys.* **6**, 491-524 (1968).

Andrade, E.N. da C. Robert Hooke, F.R.S. (1635-1703). *Notes Rec. R. Soc. Lond.* **15**, 137-145 (1960).

Angel, R.J., Allan, D.R., Miletich, R. & Finger, L.W. The use of quartz as an internal pressure standard in high-pressure crystallography. *J. Appl. Cryst.* **30**, 461-466 (1997).

Angel, R.J., Jackson, J.M., Reichmann, H.J. & Speziale, S. Elasticity measurements on minerals: a review. *Eur. J. Mineral.* **21**, 525-550 (2009).

Angel, R.J., Mosenfelder, J.L. & Shaw, C.S.J. Anomalous compression and equation of state of coesite. *Phys. Earth Planet. Inter.* **124**, 71-79 (2001).

Armstrong, E. Relation between secondary Dauphiné twinning and irradiation-coloring in quartz. *Am. Mineral.* **31**, 456-461 (1946).

Aslanyan, T.A. & Levanyuk, A.P. On the possibility of the incommensurate phase near α-β transition point in quartz. *Solid State Commun.* **31**, 547-550 (1979).

Aslanyan, T.A., Levanyuk, A.P., Vallade, M. & Lajzerowicz, J. Various possibilities for formation of incommensurate superstructure near the α-β transition in quartz. *J. Phys. C: Solid State Phys.* **16**, 6705-6712 (1983).

Aslanyan, T.A., Shigenari, T. & Abe, K. On the origin of the inhomogeneities and birefringence in the incommensurate phase of quartz. *J. Phys.: Condens. Matter* **10**, 4577-4586 (1998).

Atanasoff, J.V. & Hart, P.J. Dynamical determination of the elastic constants and their temperature coefficients for quartz. *Phys. Rev.* **59**, 85-96 (1941).

Babcock, C.L., Barber, S.W. & Fajans, K. Coexisting structures in vitreous silica. *Ind. Eng. Chem.* **46**, 161-166 (1954).

Bachheimer J.P. An anomaly in the β-phase near the α-β transition of quartz. *J. Physique Lett.* **41**, 559-561 (1980).

Bachheimer, J.P. & Dolino, G. Measurement of the order parameter of α-quartz be second-harmonic generation of light. *Phys. Rev. B* **11**, 3195-3205 (1975).

Banda, E.J.K.B., Crave, R.A., Parks, R.D., Horn, P.M. & Blume, M. α-β transition in quartz: classical versus critical behavior. *Solid State Commun.* **17**, 11-14 (1975).

Bartell, U. & Hunklinger, S. Pressure dependence of the low temperature acoustic anomalies in vitreous silica. *J. Phys.* **43**, 489-492 (1982).

Bechmann, R. Messung der Schallgeschwindigkeit in anisotropen Medien, insbesondere in Quarz mittels piezoelektrischer Erregung. *Z. Phys.* **91**, 670-678 (1934).

Bechmann, R. Elastic and piezoelectric constants of α-quartz. *Phys. Rev.* **110**, 1060-1061 (1958).

Beck, M.M. *Dynamisch-mechanische Analyse von Quarzit im Bereich des Tiefquarz-Hochquarz-Phasenübergangs*. Bachelor Thesis, Karlsruhe Institute of Technology (2010).

Beck, M.M. & Schilling, F.R. damping of elastic waves during low to high quartz transition. American Geophysical Union Fall Meeting (2010).

Belikov, B.P. Elastic properties of rocks. *Studia Geoph. Geod.* **6**, 75-85 (1962).

Bell, R.J. & Dean, P. The structure of vitreous silica: validity of the random network theory. *Philos. Mag.* **25**, 1381-1398 (1972).

Belsky, A., Hellenbrandt, M., Karen, L.V., Luksch, P. New developments in the Inorganic Crystal Structure Database (ICSD): accessibility in support of materials research and design. *Acta Cryst. B* **58**, 364-369 (2002).

Berge, B., Dolino, G., Vallade, M., Boissier, M. & Vacher, R. Incommensurate phase of quartz. II: Brillouin scattering studies. *J. Phys.* **45**, 715-724 (1984).

Berge, B., Bachheimer, J.P., Dolino, G., Vallade, M. & Zeyen, C.M.E. Inelastic neutron scattering study of quartz near the incommensurate phase transition. *Ferroelectr.* **66**, 73-84 (1986).

Bethke, J., Dolino, G., Eckhold, G., Berge, B., Vallade, M., Zeyen, C.M.E, Hahn, T., Arnold, H. & Moussa, F. Phonon dispersion and mode coupling in high-quartz near the incommensurate phase transition. *Europhys. Lett.* **3**, 207-212 (1987).

Birch, F. Physics of the crust. *Geol. Soc. Am. Special Pap.* **62**, 101-118 (1955).

Blumenauer, H. *Werkstoffprüfung* (Deutscher Verlag für Grundstoffindustrie, Leipzig, 1994).

Bömmel, H.E., Mason, W.P. & Warner, A.W. Dislocations, relaxations, and anelasticity of crystalline quartz. *Phys. Rev.* **102**, 64-71 (1956).

Borchardt-Ott, W. *Kristallographie - Eine Einführung für Naturwissenschaftler* (Springer-Verlag, Berlin, 2009).

Borgnis, F.E. Specific directions of longitudinal wave propagation in anisotropic media. *Phys. Rev.* **98**, 1000-1005 (1955).

Bourova, E., Parker, S.C. & Richet, P. High-temperature structure and dynamics of coesite (SiO_2) from numerical simulations. *Phys. Chem. Minerals* **31**, 569-579 (2004).

Brace, W.F. & Jones, A.H. Comparison of uniaxial deformation in shock and static loading of three rocks. *J. Geophys. Res.* **76**, 4913-4921 (1971).

Bragg, W.F.R.S. & Gibbs, R.E. The structure of α- and β-quartz. *Proc. R. Soc. Lond. A* **109**, 405-427 (1925).

Brewster D. *The Life of Sir Isaac Newton* (Harper & Brothers, New York, 1840).

Brice, J.C. Crystals for quartz resonators. *Rev. Mod. Phys.* **57**, 105-147 (1985).

Brocher, T.M. Empirical relations between elastic wavespeeds and density in the Earth's crust. *Bull. Seismol. Soc. Am.* **95**, 2081-2092 (2005).

Brown, C.S., Kell, R.C., Thomas, L.A., Wooster, N. & Wooster, W.A. The growth and properties of large crystals of synthetic quartz. , *Min. Mag.* **29**, 858-874 (1952).

Brown, C.S. & Thomas, L.A. The effect of impurities on the growth of synthetic quartz. *J. Phys. Chem. Solids* **13**, 337-343 (1960).

Brown, I.D. & Mc Mahon, B. CIF: the computer language of crystallography. *Acta Cyst. B* **58**, 317-324 (2002).

Brückner, R. Properties and structure of vitreous silica. I. *J. Non-Cryst. Solids* **5**, 123-175 (1970).

Brugger, K. Pure modes for elastic waves in crystals. *J. Appl. Phys.* **36**, 759-768 (1965).

Calderon, E., Gauthier, M., Decremps, F., Hamel, G., Syfosse, G. & Polian, A. Complete determination of the elastic moduli of α-quartz under hydrostatic pressure up to 1 GPa: an ultrasonic study. *J. Phys.: Condens. Matter* **19**, 436228-13 (2007).

Cambon, O., Haines, J., Fraysse, G., Keen, D.A. & Tucker, M.G. Piezoelectric properties at high temperature in α-quartz materials. *J. Phys.* **126**, 27-30 (2005).

Carpenter, M.A. & Salje, E.K.H. Elastic anomalies in minerals due to structural phase transitions. *Eur. J. Mineral.* **10**, 693-812 (1998).

Carpenter, M.A., Salje, E.K.H., Graeme-Barber, A., Wruck, B., Dove, M.T. & Knight, K.S. Calibration of excess thermodynamic properties and elastic constant variations associated with the α-β phase transition in quartz. *Am. Mineral.* **83**, 2-22 (1998).

Carpenter, M.A. & Zhang, Z. Anelasticity maps for acoustic dissipation associated with phase transitions in minerals. *Geophys. J. Int.* **186**, 279-295 (2011).

Castagna, J.P., Batzle, M.L. & Eastwood, R.L. Relationships between compressional-wave and shear-wave velocities. *Geophys.* **50**, 571-581 (1985).

Castagnède, B., Jenkins, J.T., Sachse, W. & Baste, S. Optimal determination of the elastic constants of composite materials from ultrasonic wavespeed measurements. *J. Appl. Phys.* **67**, 2753-2761 (1990).

Casula, G. & Carcoine, J.M. Generalized mechanical model analogues of linear viscoelastic behaviour. *B. Geofis. Teor. Appl.* **34**, 235-256 (1992).

Cazzani, A. & Rovati, M. Extrema of Young's modulus for cubic and transversely isotropic solids. *Int. J. Solids Struct.* **40**, 1713-1744 (2003).

Chou, Y.T. & Sha, G.T. Dislocation energies in anisotropic trigonal crystals. *Phys. Stat. Sol. (a)* **6**, 505-513 (1971).

Christensen, N.I. Poisson's ratio and crustal seismology. *J. Geophys. Res.* **101**, 3139-3156 (1996).

Chu, F., Thoma, D.J., Mc Clellan, K.J. & Peralta, P. Mo_5Si_3 single crystals: Physical properties and mechanical behavior. *Mater. Sci. Eng. A* **261**, 44-52 (1999).

Chung, D.H. & Buessem, W.R. The elastic anisotropy of crystals. *J. Appl. Phys.* **38**, 2010-2012 (1967).

Clark Jr., S.P. *Handbook of physical constants* (The Society of America, New York, 1966).

Coe, R.S. & Paterson, M.S. The α-β inversion in quartz: a coherent phase transition under nonhydrostatic stress. *J. Geophys. Res.* **74**, 4921-4948 (1969).

Cohen, L.H. & Klement Jr., W. High-low quartz inversion: determination to 35 kilobars. *J. Geophys. Res.* **72**, 4245-4251 (1967).

Cook, R.K. & Breckenridge, R.G. Anelasticity of quartz. *Phys. Rev.* **92**, 1419-1423 (1953).

Cook, R.K. & Weissler, P.G. Piezoelectric constants of α- and β-quartz at various temperature. *Phys. Rev.* **80**, 712-717 (1950).

Courtney, T.H. *Mechanical behavior of materials* (Mc Graw-Hill higher Education, Boston, 2000).

Cowley, R.A. Structural phase transitions I. Landau theory. *Adv. Phys.* **29**, 1-110 (1980).

Cowley, R.A. Soft modes and structural phase transitions. *Integr. Ferroelectr.* **133**, 109117 (2012).

Curie, J. & Curie, P. Développement par compression de l'électricité polaire dans les cristaux hémièdres à faces inclinées. *Bull. Soc. Mineral. Fr.* **3**, 90-93 (1880).

Curie, J. & Curie, P. Contractions et dilatations produites par des tensions électriques dans les cristaux hémièdres à faces inclinées. *C. R. Hebd. Seances Acad. Sci.* **93**, 1137-1140 (1881).

Dean, D.W., Wentzcovitch, R.M., Keskar, N., Chelikowsky, J.R. & Binggeli, N. Pressure-induced amorphization in crystalline silica: Soft phonon modes and shear instabilities in coesite. *Phys. Rev. B* **61**, 3303-3309 (2000).

De Boer, K., Jansen, A.P.J., Van Santen, R.A., Watson, G.W. & Parker, S.C. Free-energy calculations of thermodynamic, vibrational, elastic, and structural properties of α-quartz at variable pressures and temperatures. *Phys. Rev. B* **54**, 826-835 (1996).

Den Toonder, J.M.J., Van Dommelen, J.A.W. & Baaijens, F.P.T. The relation between single crystal elasticity and the effective elastic behaviour of polycrystalline materials: theory, measurement and computation. *Modell. Simul. Mater. Sci. Eng.* **7**, 909-928 (1999).

Deutsch, V., Platte, M. & Vogt, M. *Ultraschallprüfung: Grundlagen und industrielle Anwendungen* (Springer-Verlag, Berlin, 1999).

De Wit, R. Elastic constants and thermal expansion averages of a nontextured polycrystal. *J. Mech. Mater. Struct.* **3**, 195-212 (2008).

DIN 18137-2 Baugrund, Untersuchung von Bodenproben Bestimmung der Scherfestigkeit - Teil 2: Triaxialversuch (2011).

DIN EN 1926 Prüfverfahren für Naturstein - Bestimmung der einachsigen Druckfestigkeit (2007).

DIN EN 60758 Synthetischer Quarzkristall - Festlegung und Leitfaden für die Anwendung (2009).

DIN EN ISO 9001 Qualitätsmanagementsysteme - Anforderungen (2014).

Dodd, D.M. & Fraser, D.B. The 3000-3900 cm^{-1} absorption bands and anelasticity in crystalline α-quartz. *J. Phys. Chem. Solids* **26**, 673-686 (1965).

Dolino, G. The α-inc-β transitions of quartz: a century of research on displacive phase transitions. *Phase Transitions* **21**, 59-72 (1990).

Dolino, G. & Bachheimer, J.P. Effect of the α-β transition on mechanical properties of quartz. *Ferroelectr.* **43**, 77-86 (1982).

Dolino, G., Bachheimer, J.P., Berge, B. & Zeyen, C.M.E. Incommensurate phase of quartz: I. elastic neutron scattering. *J. Physique* **45**, 361-371 (1984a).

Dolino, G., Bachheimer, J.P., Berge, B., Zeyen, C.M.E., Van Tendeloo, G., Van Landuyt, J. & Amelinckx, S. Incommensurate phase of quartz: III. study of the coexistence state between the incommensurate and the α-phases by neutron scattering and electron microscopy. *J. Phys.* **45**, 901-912 (1984b).

Dolino, G., Bachheimer, J.P. & Zeyen, C.M.E. Observation of an intermediate phase near the α-β transition of quartz be heat capacity and neutron scattering measurements. *Solid State Commun.* **45**, 295-299 (1983).

Doncieux, A., Stagnol, D., Huger, M. Chotard, T., Gault, C., Ota, T. & Hashimoto, S. Thermo-elastic behaviour of a natural quartzite: Itacolumite. *J. Mater. Sci.* **43**, 4167-4174 (2008).

Dove, M.T. Theory of displacive phase transitions in minerals. *Am. Mineral.* **82**, 213-244 (1997).

Dove, M.T., Gambhir, M. & Heine, V. Anatomy of a structural phase transition: theoretical analysis of the displacive phase transition in quartz and other silicates. *Phys. Chem. Minerals* **26**, 344-353 (1999).

Downs, R.T. & Hall-Wallace, M. The American Mineralogist crystal structure database. *Am. Mineral.* **88**, 247-250 (2003).

Downs, R.T. & Palmer, D.C. The pressure behavior of α-cristobalite. *Am. Mineral.* **79**, 9-14 (1994).

Drebushchak V.A. & Dementiev, S.N. Fine structure of the thermoanalytical peak of the phase transition in quartz. *J. Struct. Chem.* **37**, 150-151 (1996).

Du, D. & Tscheuschner, H.-D. Mechanische Modelle zur Beschreibung des Deformationsverhaltens von Lebensmitteln und ihre Klassifizierung. *Tech. Mech.* **7**, 43-50 (1986).

Emmons, W.H., Thiel, G.A., Stauffer, C.R. & Allison, I.S. Geology - Principles and Processes (Mc Graw-Hill Book Company, New York, 1955).

Engel, G.F. and Krempl, P.W. The temperature dependence of piezoelectric constants of e_i μOF α-quartz. *Phys. Lett. A* **92**, 469-470 (1982).

Ericksen, J.L. On the theory of the α-β phase transition in quartz. *J. Elasticity* **63**, 61-86 (2001).

Fenner, C.N. The stability relations of the silica minerals. *Am. J. Sci.* **36**, 331-384 (1913).

Ferry, J.D. *Viscoelastic properties of polymers* (Wiley, New York, 1961).

Fielitz, K. Elastic wave velocities in different rocks at high pressure and temperature up to 750 °C. *Z. Geophys.* **37**, 943-956 (1971).

Fielitz, K. Compressional and shear wave velocities as a function of temperature in rocks at high pressure. In: Giese, P., Prodehl, C. & Stein, A. (eds.) *Explosion seismology in central Europe* (Springer-Verlag, Berlin, 1976).

Flügge, W. *Viscoelasticity* (Springer-Verlag, Berlin 1975).

Fraser, D.B. Anelastic effects of alkali ions in crystalline quartz. *J. Appl. Phys.* **35**, 2913-2918 (1964).

Frondel, C. Secondary Dauphiné twinning in quartz. *Am. Mineral.* **30**, 447-460 (1945).

Fukuhara, M. & Sanpei, A. High temperature-elastic moduli and internal dilational and shear frictions of fused quartz. *Jpn. J. Appl. Phys.* **33**, 2890-2893 (1994).

Fukuhara, M., Sanpei, A. & Shibuki, K. Low temperature-elastic moduli, Debye temperature and internal dilational and shear frictions and fused quartz. *J. Mater. Sci.* **32**, 1207-1211 (1997).

Gaskell, P.H. Thermal properties of silica. Part 1 - Effect of temperature on infra-red reflection spectra of quartz, cristobalite and vitreous silica. *Trans. Faraday Soc.* **62**, 1493-1504 (1966a).

Gaskell, P.H. Thermal properties of silica. Part 2 - Thermal expansion coefficient of vitreous silica. *Trans. Faraday Soc.* **62**, 1505-1510 (1966b).

Gercek, H. Poisson's ratio values for rocks. *Int. J. Rock Mech. Min. Sci.* **44**, 1-13 (2007).

Ghiorso, M.S., Carmichael, I.S.E. & Moret, L.K. Inverted high-temperature quartz - unit cell parameters and properties of the α-β inversion. *Contrib. Mineral. Petrol.* **68**, 307-323 (1979).

Glover, P.W.J., Baud, P., Darot, M., Meredith, P.G., Boon, S.A., le Ravalec, M., Zoussi, S. & Reuschlé, T. α-β phase transition in quartz monitored using acoustic emissions. *Geophys. J. Int.* **120**, 775-782 (1995).

Götze, J. Chemistry, textures and physical properties of quartz - geological interpretation and technical application. *Min. Mag.* **73**, 645-671 (2009).

Gordon, R.B. & Davis, L.A. Velocity and attenuation of seismic waves in imperfectly elastic rock. *J. Geophys. Res.* **73**, 3917-3935 (1968).

Grau, P., Berg, G. & Gießmann, E.-J. Rheologische Untersuchungen fester Stoffe mit Dehnungsratenwechselversuchen. *Tech. Mech.* **4**, 54-58 (1983).

Gražulis, S., Chateigner, D., Downs, R.T., Yokochi, A.F.T., Quirós, M., Lutterotti, L., Manakova, E., Butkus, J., Moeck, P. & le Bail, A. Crystallography Open Database – an open-access collection of crystal structures. *J. Appl. Cryst.* **42**, 726-729 (2009).

Gražulis, S., Daškevič, A., Merkys, A., Chateigner, D., Lutterotti, L., Quirós, M., Serebryanaya, N.R., Moeck, P., Downs, R.T. & le Bail, A. Crystallography Open Database (COD): an open-access collection of crystal structures and platform for world-wide collaboration. *Nucleic Acids Res.* **40**, 420-427 (2012).

Gregoryanz, E., Hemley, R.J., Mao, H. & Gillet, P. High-pressure elasticity of α-quartz: instability and ferroelastic transition. *Phys. Rev. Lett.* **84**, 3117-3120 (2000).

Grimm, H. & Dorner, B. On the mechanism of the α-β phase transformation of quartz. *J. Phys. Chem. Solids* **36**, 407-416 (1975).

Gupta, V. & Sharma, R. Relationship between textural, petrophysical and mechanical properties of quartzites: a case study from northwestern Himalaya. *Eng. Geol.* **135-136**, 1-9 (2012).

Gutenberg, B. Crustal Layers of the continents and oceans. *Bull. Geol. Soc. Am.* **62**, 427-440 (1951).

Guzzo, P.L., Shinohara, A.H., Costa, H.A.D., Raslan, A.A., Suzuki, C.K. & Azevedo, W.M. Characterization of growth sectors in synthetic quartz grown from cylindrical seed parallel to [0001] direction. *Mater. Res.* **7**, 285-291 (2004).

Haines, J., Cambon, O., Keen, D.A., Tucker, M.G. & Dove, M.T. Structural disorder and loss of piezoelectric properties in α-quartz at high temperature. *Appl. Phys. Lett.* **81**, 2968-2970 (2002).

Hallbauer, D.K., Wagner, H. & Cook, N.G.W. Some observations concerning the microscopic and mechanical behaviour of quartzite specimens in stiff, triaxial compression tests. *Int. J. Rock Mech. Min. Sci. & Geomech. Abstr.* **10**, 713-726 (1973).

Hashin, Z. & Shtrikman, S. A variational approach to the theory of the elastic behaviour of polycrystals. *J. Mech. Phys. Solids* **10**, 343-352 (1962).

Hashin, Z. & Shtrikman, S. A variational approach to the theory of the elastic behaviour of multiphase materials. *J. Mech. Phys. Solids* **11**, 127-140 (1963).

Haussühl, S. *Kristallphysik* (Physik Verlag, Weinheim, 1983).

Haussühl, S. *Physical properties of crystals - An introduction* (Wiley-VCH, Weinheim, 2007).

Hazen, R.M., Finger, L.W., Hemley, R.J. & Mao, H.-k. High-pressure crystal chemistry and amorphization of α-quartz. *Solid State Commun.* **72**, 507-511 (1989).

Heaney, P.J. & Veblen, D.R. Observations of the α-β phase transition in quartz: a review of imaging and diffraction studies and some new results. *Am. Mineral.* **76**, 1018-1032 (1991).

Hearmon, R.F.S. The elastic constants of anisotropic materials. *Rev. Mod. Phys.* **18**, 409-440 (1946).

Hearmon, R.F.S. The elastic constants of anisotropic materials - II. *Adv. Phys.* **5**, 323-382 (1956).

Heier, K.S. The contribution of geophysical investigations to our geological understanding of the deep crust. In: *Annales de la Société géologique de Belgique*, Publications spéciales, Géologie des domaines cristallins - Centenaire de la Société géologique de Belgique, 23-44 (1974).

Herman, F., Copeland, P., Avouac, J.-P., Bollinger, L., Mahéo, G., le Fort, P., Rai, S., Foster, D. Pêcher, A., Stüwe, K. & Henry, P. Exhumation, crustal deformation, and thermal structure of the Nepal Himalaya derived from the inversion of thermochronological and thermobarometric data and modeling of the topography. *J. Geophys. Res.* **115**, B06407-38 (2010).

Heyliger, P., Ledbetter, H. & Kim, S. Elastic constants of natural quartz. *J. Acoust. Soc. Am.* **114**, 644-650 (2003).

Hill, E.J. & Burgess, J.H. Velocity measurements of microwave ultrasonic waves in quartz. *J. Appl. Phys.* **44**, 5-6 (1973).

Hill, R. The elastic behaviour of a crystalline aggregate. *Proc. Phys. Soc.* **65**, 349-354 (1952).

Hirsch, A. *Felsmechanische und petrographische Untersuchungen an Werksteinen des Buntsandsteins im Nordschwarzwald*. Diploma Thesis, Albert-Ludwigs-University Freiburg (2006).

Hirsch, A. *Gesteinsuntersuchungen und Bausteinkartierung am Turmhelm des Freiburger Münsters*. Diploma Thesis, Albert-Ludwigs-University Freiburg (2008).

Höchli, U.T. Ultrasonic investigation of the first-order α-β phase transition in quartz. *Solid State Commun.* **8**, 1487-1490 (1970).

Höchli, U.T. & Scott, J.F. Displacement parameter, soft-mode frequency, and fluctuations in quartz below its α-β phase transition. *Phys. Rev. Lett.* **26**, 1627-1629 (1971).

Höfer, M. & Schilling, F.R. Heat transfer in quartz, orthoclase, and sanidine at elevated temperature. *Phys. Chem. Minerals* **29**, 571-584 (2002).

Holmquist, S.B. Conversion of quartz to tridymite. *Journal of the American Ceramic Society* **44**, 82-86 (1961).

Hooke, R. *Collection of lectures* (John Martyn, London, 1679).

Huang, L. & Kieffer, J. Amorphous-amorphous transitions in silica glass. I. Reversible transitions and thermomechanical anomalies. *Phys. Rev. B* **69**, 224203-11 (2004a).

Huang, L. & Kieffer, J. Amorphous-amorphous transitions in silica glass. II. Irreversible transitions and densification limit. *Phys. Rev. B* **69**, 224204-8 (2004b).

Hughes, D.S. & Cross, J.H. Elastic wave velocities in rocks at high pressures and temperatures. *Geophys.* **16**, 577-593 (1951).

Hughes, D.S. & Maurette, C. Variation of elastic wave velocities in granites with pressure and temperature. *Geophys.* **21**, 277-284 (1956).

Huntington, H.B. Ultrasonic measurements on single crystals. *Phys. Rev.* **72**, 321-331 (1947).

Ide, J.M. Comparison of statically and dynamically determined Young's modulus of rocks. *Proc. Natl. Acad. Sci. U.S.A.* **22**, 81-92 (1936).

Iliescu, B. & Chirila, R. Electric twinning in quartz by temperature gradient. *Cryst. Res. Technol.* **30**, 231-235 (1995).

Jackson, D.D. & Anderson, D.L. Physical mechanisms of seismic-wave attenuation. *Rev. Geophys. Space Phys.* **8**, 1-63 (1970).

Jacob, D. & Cordier, P. A precession electron diffraction study of α-,β-phases and Dauphiné twin in quartz. *Ultramicrosc.* **110**, 1166-1177 (2010).

Jäckle, J. On the ultrasonic attenuation in glasses at low temperatures. *Z. Phys.* **257**, 212-223 (1972).

Jaeger, J.C., Cook, N.G.W. & Zimmerman, R.W. *Fundamentals of Rock Mechanics* (Blackwell Publishing, Malden, 2008).

Jay, A.H. The thermal expansion of quartz by x-ray measurements. *Proc. R. Soc. Lond. A* **142**, 237-247 (1933).

Johansson, Å. The Dalslandian sulphide-bearing quartz veins of Dalsland and Värmskog southwest Sweden. *Sveriges Geol. Unders. C* **809**, 1-48 (1985).

Kaduk, J.A. Use of the Inorganic Crystal Structure Database as a problem solving tool. *Acta Cryst. B* **58**, 370-379 (2002).

Kammer, E.W. & Atanasoff, J.V. A determination of the elastic constants of β-quartz. *Phys. Rev.* **62**, 395-401 (1942).

Kammer, E.W., Pardue, T.E. & Frissel, H.F. A determination of the elastic constants for β-quartz. *J. Appl. Phys.* **19**, 265-270 (1948).

Kanamori, H. & Mizutani, H. Ultrasonic measurement of elastic constants of rocks under high pressures. *Bull. Earthquake Res. Inst.* **43**, 173-194 (1965).

Karato, S. & Spetzler, H.A. Defect microdynamics in minerals and solid-state mechanics of seismic wave attenuation and velocity dispersion in the mantle. *Rev. Geophys.* **28**, 399-421 (1990).

Kato, N. & Gouhara, K. Intermediate phase between the α-and β-phases of quartz. *Phys. Rev. B* **34**, 2001-2003 (1986).

Kern, H. The effect of high temperature and high confining pressure on compressional wave velocities in quartz-bearing and quartz-free igneous and metamorphic rocks. *Tectonophys.* **44**, 185-203 (1978).

Kern, H. Effect of high-low quartz transition on compressional and shear wave velocities in rocks under high pressure. *Phys. Chem. Minerals* **4**, 161-171 (1979).

Kern, H. Elastic-wave velocity in crustal and mantle rocks at high pressure and temperature: the role of the high-low quartz transition and of dehydration reactions. *Phys. Earth Planet. Inter.* **29**, 12-23 (1982).

Kern, H. Laboratory seismic measurements: an aid in the interpretation of seismic field data. *Terra Nova* **2**, 617-628 (1990).

Kern, H. Measuring and modeling of p- and s-wave velocities on crustal rocks: a key for the interpretation of seismic reflection and refraction data. *Int. J. Geophys.* **2011**, 530728-9 (2011).

Kihara, K. An X-ray study of the temperature dependence of the quartz structure. *Eur. J. Mineral.* **2**, 63-77 (1990).

Kihara, K. Lattice dynamical calculations of anisotropic temperature factors of atoms in quartz, and the structure of β-quartz. *Phys. Chem. Minerals* **19**, 492-501 (1993).

Kimizuka, H., Kaburaki, H. & Kogure, Y. Mechanism for negative Poisson ratio over the α-β transition of cristobalite, SiO_2: a molecular-dynamics study. *Phys. Rev. Lett.* **84**, 5548-5551 (2000).

Kimizuka, H., Kaburaki, H. & Kogure, Y. Molecular-dynamics study of the high-temperature elasticity of quartz above the α-β-phase transition. *Phys. Rev. B* **67**, 024105-7 (2003).

Kimizuka, H., Ogata, S. & Shibutani, Y. High-pressure elasticity and auxetic property of α-cristobalite. *Mater. Trans.* **46**, 1161-1166 (2005).

Kimizuka, H., Ogata, S., Li, J. & Shibutani, Y. Complete set of elastic constants of α-quartz at high pressure: a first-principles study. *Phys. Rev. B* **75**, 054109-6 (2007).

Kim-Zajonz, J., Werner, S. & Schulz, H. High pressure single crystal X-ray diffraction study on α-quartz. *Z. Kristallogr.* **214**, 324-330 (1999).

King, J.C. The anelasticity of natural and synthetic quartz at low temperatures. *Bell Syst. Tech. J.* **38**, 573-602 (1959).

Kleber, W., Bautsch, H.-J. & Bohm, J. *Einführung in die Kristallographie* (Verlag Technik, Berlin, 1998).

Klement Jr., W. & Cohen, L.H. High-low quartz inversion: thermodynamics of the lambda transition. *J. Geophys. Res.* **73**, 2249-2259 (1968).

Klumbach, S. *Photogrammetrische und felsmechanische Untersuchungen am Piesberger Karbon-Quarzit*. Bachelor Thesis, Albert-Ludwigs-University Freiburg (2008).

Klumbach, S. *Petrophysical properties of geothermal reservoir rocks in the Upper Rhine Graben from surface outcrops*. Master Thesis, Albert-Ludwigs-University Freiburg (2010).

Klumbach, S. & Schilling, F.R. Frequency-dependent viscoelastic properties of quartz. Conference Contribution, European Mineralogical Conference (2012).

Klumbach, S. & Schilling, F.R. Elastic and anelastic properties of α- and β-quartz single crystals. *Eur. J. Mineral.* **26**, 211-220 (2014). Supplementary material via www.scheizerbart.de.

Koga, I., Aruga, M. & Yoshinaka, Y. Theory of plane elastic waves in a piezoelectric crystalline medium and determination of elastic and piezoelectric constants of quartz. *Phys. Rev.* **109**, 1467-1473 (1958).

Kondo, K., Lio, S. & Sawaoka, A. Nonlinear pressure dependence of the elastic moduli of fused quartz up to 3 GPa. *J. Appl. Phys.* **52**, 2826-2831 (1981).

Kuo-Chen, H., Wu, F.T., Jenkins, D.M., Mechie, J., Roecker, S.W., Wang, C.-Y. & Huang, B.-S. Seismic evidence for the α-β quartz transition beneath Taiwan from vp/vs tomography. *Geophys. Res. Lett.* **39**, L22302-6 (2012).

Kuchling, H. *Taschenbuch der Physik* (Fachbuchverlag Leipzig im Carl Hanser Verlag, München, 2004).

Kushibiki, J., Takanaga, I. & Nishiyama, S. Accurate measurements of the acoustical physical constants of synthetic α-quartz for SAW devices. *IEEE Trans. Ultrason. Ferroelectr. Freq. Control* **49**, 125-135 (2002).

Lager, G.A., Jorgensen, J.D. & Rotella, F.J. Crystal structure and thermal expansion of α-quartz SiO_2 at low temperatures. *J. Appl. Phys.* **53**, 6751-6756 (1982).

Lakes, R. *Viscoelastic materials* (Cambridge University Press, New York, 2009).

Lakshtanov, D.L., Sinogeikin, S.V. & Bass, J.D. High-temperature phase transitions and elasticity of silica polymorphs. *Phys. Chem. Minerals* **34**, 11-22 (2007).

Landau, L.D. & Lifshitz, E.M. *Theory of elasticity* (Pergamon Press, Oxford, 1970).

Lang, A.R. & Miuscov, V.F. Dislocations and fault surfaces in synthetic quartz. *J. Appl. Phys.* **38**, 2477-2483 (1967).

Lay, T. The Earth's interior. *Int. Handb. Earthquake Eng. Seismolog.* **81**, 829-860 (2002).

Le Chatelier, H.L. Sur la dilatation du quartz. *C. R. Ac. Sci.* **108**, 1046-1049 (1889).

Ledbetter, H.M., la Brecque, J.F. & Dahnke, J.L. Propagation errors in elastic-constant inversion. *Phys. Stat. Sol. A* **67**, 643-647 (1981).

Leeder, M. Sedimentology and sedimentary basins - From turbulence to tectonics (Blackwell Publishing, Malden, 2006).

Lethbridge, Z.A.D., Walton, R.I., Marmier, A.S.H., Smith, C.W. & Evans, K.E. Elastic anisotropy and extreme Poisson's ratios in single crystals. *Acta Mater.* **58**, 6444-6451 (2010).

Le Page, Y. & Donnay, G. Refinement of the crystal structure of low-quartz. *Acta Cryst. B* **32**, 2456-2459 (1976).

Levelut, C., le Parc, R. & Pelous, J. Dynamic sound attenuation at hypersonic frequencies in silica glass. *Phys. Rev. B* **73**, 052202-4 (2006).

Levien, L., Prewitt, C.T. & Weidner, D.J. Structure and elastic properties of quartz at pressure. *Am. Mineral.* **65**, 920-930 (1980).

Levy, M., Bass, H.E. & Stern, R. *Modern acoustical techniques for the measurement of mechanical properties* (Academic Press, San Diego, 2001).

Lewis, M.F. & Patterson E. Microwave phonon-attenuation measurements in quartz. *Phys. Rev.* **159**, 703-711 (1967).

Li, Y. The anisotropic behavior of Poisson's ratio, Young's modulus, and shear modulus in hexagonal materials. *Phys. Stat. Sol. (a)* **38**, 171-175 (1976).

Li, Y. & Chung, D.Y. The anisotropic behavior of Poisson's ratio, Young's modulus, and shear modulus in crystals with different symmetries. *Phys. Stat. Sol. (a)* **46**, 603-608 (1978).

Liakos, J.K. & Saunders, G.A. Application of the Landau theory to elastic phase transition. *Philos. Mag.* **46**, 217-242 (1982).

Liu, H.P., Anderson, D.L. & Kanamori, H. Velocity dispersion due to anelasticity; implications for seismology and mantle composition. *Geophys. J. R. Astr. Soc.* **47**, 41-58 (1976).

Liu, Y., Xie, H., Zhou, W. & Guo, J. A method for experimental determination of compressional velocities in rocks and minerals at high pressure and high temperature. *J. Phys.: Condens. Matter* **14**, 11381-11384 (2002).

Lu, C. & Jackson, I. Seismic-frequency laboratory measurements of shear mode viscoelasticity in crustal rocks II: thermally stressed quartzite and granite. *Pure Appl. Geophys.* **153**, 441-473 (1998).

Mainprice, D., Humbert, M. & Wagner, F. Phase transformations and inherited lattice preferred orientations: implications for seismic properties. *Tectonophys.* **180**, 2013-228 (1990).

Man, C.-S. & Huang, M. A simple explicit formula for the Voigt-Reuss-Hill average of elastic polycrystals with arbitrary crystal and texture symmetries. *J. Elast.* **105**, 29-48 (2011).

Marini, L. & Manzella, A. Possible seismic signature of the α-β quartz transition in the lithosphere of southern Tuscany (Italy). *J. Volc. Geotherm. Res.* **148**, 81-97 (2005).

Maris, H.J. Attenuation of ultra-high-frequency acoustic waves in quartz at low temperature. Nature 198, 876-877 (1963).

Markgraaff, J. Elastic behavior of quartz during stress induced Dauphiné twinning. *Phys. Chem. Minerals* **13**, 102-112 (1986).

Marx, J.W. & Sivertsen, J.M. Temperature dependence of the elastic moduli and internal friction of silica and glass. *J. Appl. Phys.* **24**, 81-87 (1953).

Mason, W.P. Quartz crystal applications. *Bell Syst. Tech. J.* **22**, 178-223 (1943).

Mavko, G., Mukerji, T. & Dvorkin, J. *The rock physics handbook - Tools for analysis of porous media* (Cambridge University Press, New York, 2009).

Mayer, W.G. & Parker, P.M. Method for the determination of elastic constants of trigonal crystal systems. *Acta Cryst.* **14**, 725-726 (1961).

Mayr, S.I., Stanchits, S., Langenbruch, C., Dresen, G. & Shapiro, S.A. Acoustic emission induced by pore-pressure changes in sandstone samples. *Geophys.* **76**, MA21-MA32 (2011).

Mc Cusker, L.B., von Dreele, R.B., Cox, D.E., Louër, D. & Scardi, P. Rietveld refinement guidelines. *J. Appl. Cryst.* **32**, 36-50 (1999).

Mc Knight, R.E.A., Moxon, T., Buckley, A., Taylor, P.A., Darling, T.W. & Carpenter, M.A. Grain size dependence of elastic anomalies accompanying the α-β phase transition in polycrystalline quartz. *J. Phys.: Condens. Matter* **20**, 18 (2008).

Mc Skimin, H.J. Measurement of the 25 °C zero-field elastic moduli of quartz by high-frequency plane wave propagation. *J. Acoust. Soc. Am.* **34**, 1271-1274 (1962).

Mc Skimin, H.J., Andreatch, P. & Thurston, R.N. Elastic moduli of quartz versus hydrostatic pressure at 25 and -195.8 °C. *J. Appl. Phys.* **36**, 1624-1632 (1965).

Mechie, J., Sobolev, S.V., Ratschbacher, L., Babeyko, A.Y., Bock, G., Jones, A.G., Nelson, K.D., Solon, K.D., Brown, L.D. & Zhao, W. Precise temperature estimation in the Tibetan crust from seismic detection of the α-β quartz transition. *Geol.* **32**, 601-604 (2004).

Menard, K.P. *Dynamic mechanical analysis: a practical introduction* (CRC Press LLC, Boca Raton, 1999).

Meidav, T. Viscoelastic properties of the standard linear solid. *Geophys. Prospect.* **12**, 80-99 (1964).

Mitchell, B.J. Anelastic structure and evolution of the continental crust and upper mantle from seismic surface wave attenuation. *Rev. Geophys.* **33**, 441-462 (1995).

Moore, G.S.M. The α-β inversion in quartz and the effects of structural damage. *Phase Transitions* **7**, 25-40 (1986).

Moriya K. & Ogawa, T. Observation of growth defects in synthetic quartz crystals by light-scattering tomography. *J. Cryst. Growth* **44**, 53-60 (1978).

Moriya, K. & Ogawa, T. Observation of dislocations in a synthetic quartz crystal by light scattering tomography. *Philos. Mag. A* **41**, 191-200 (1980).

Moriya, K. & Ogawa, T. Growth history of a synthetic quartz crystal. *J. Cryst. Growth* **58**, 115-121 (1982a).

Moriya, K. & Ogawa, T. Plate-like defects in a synthetic quartz crystal. *J. Cryst. Growth* **60**, 1-8 (1982b).

Mosher, D.R., Raj, R. & Kossowsky, R. Measurement of viscosity of the grain-boundary phase in hot pressed-silicon nitride. *J. Mater. Sci.* **11**, 49-53 (1976).

Mühlbach, J., Klumbach, S., Hirsch, A. & Kromer, M. Physical and chemical properties of rocks and well cement for CO_2 storage applications in a full scale borehole simulator. Pau Sustainable Earth Science (2013).

Müser, M.H. & Binder, K. Molecular dynamics study of the α-β transition in quartz: elastic properties, finite size effects, and hysteresis in the local structure. *Phys. Chem. Minerals* **28**, 746-755 (2001).

Mullen, A.J. Temperature variation of the piezoelectric constant of quartz. *J. Appl. Phys.* **40**, 1693-1696 (1969).

Nakamura, M., Matsumoto, S. & Hirano, T. Elastic constants of $MoSi_2$ and WSi_2 single crystals. *J. Mater. Sci.* **25**, 3309-3313 (1990).

Nakamura, N., Sakamoto, M. & Hirao, M. Elastic constants of langasite and α-quartz at high temperatures measured by antenna transmission acoustic resonance. *Rev. Sci. Instr.* **83**, 073901-7 (2012).

Narayanaswamy, P.K. The α-β transformation in quartz. *Proc. Ind. Acad. Sci. A* **28**, 417-423 (1948). Naumenko, N.F. Application of exceptional wave theory to materials used in surface acoustic wave devices. *J. Appl. Phys.* **79**, 8936-8943 (1996).

Nesse, W.D. *Introduction to mineralogy* (Oxford University Press, New York, 2000).

Nikitin, A.N., Markova, G.V., Balagurov, A.M., Vasin, R.N. & Alekseeva, O.V. Investigation of the structure and properties of quartz in the α-β transition range by neutron diffraction and mechanical spectroscopy. *Crystallogr. Rep.* **52**, 428-435 (2007).

Noge, S. & Uno, T. Twinning of α quartz plate at low temperature using a laser beam. *Jpn. J. Appl. Phys.* **39**, 3056-3059 (2000).

Nye, J.F. *Physical properties of crystals - their representation by tensors and matrices* (Clarendon Press, Oxford, 1992).

Obert, L. & Duvall, W.I. *Rock mechanics and the design of structures in Rock* (Wiley, New York, 1967).

O'Connell, R.J. & Budiansky, B. Seismic velocities in dry and saturated cracked solids. *J. Geophys. Res.* **79**, 5412-5426 (1974).

Ogi, H., Ohmori, T., Nakamura, N. & Hirao, M. Elastic, anelastic, and piezoelectric coefficients of α-quartz determined by resonance ultrasound spectroscopy. *J. Appl. Phys.* **100**, 053511-7 (2006).

Ohno, I. Rectangular parallelepiped resonance method for piezoelectric crystals and elastic constants of α-quartz. *Phys. Chem. Minerals* **17**, 371-378 (1990).

Ohno, I. Temperature variation of elastic properties of α-quartz up to the α-β transition. *J. Phys. Earth* **43**, 157-169 (1995).

Ohno, I., Harada, K. & Yoshitomi, C. Temperature variation of elastic constants of quartz across the α-β transition. *Phys. Chem. Minerals* **33**, 1-9 (2006).

Ohno, I., Yamamoto, S., Anderson, O.L. & Noda, I. Determination of elastic constants of trigonal crystals by the rectangular parallelepiped resonance method. *J. Phys. Chem. Solids* **47**, 1103-1108 (1986).

Ojovan, M.I. Viscosity and glass transition in amorphous oxides. *Adv. Condens. Matter Phys.* **2008**, 817829-23 (2008).

Okrusch, M. & Matthes, S. *Mineralogie - Eine Einführung in die spezielle Mineralogie, Petrologie und Lagerstättenkunde* (Springer-Verlag, Berlin, 2005).

Otto, J. & Thomas, W. Die thermische Ausdehnung von Quarzglas im Temperaturbereich von 0 bis 1060 °C. *Z. Phys.* **175**, 337-344 (1963).

Pabst, W. & Gregorová, E. Elastic properties of silica polymorphs - a review. *Ceramics* **57**, 167-184 (2013).

Pabst, W., Gregorová, E. & Kutzendörfer, J. Elastic anomalies in tridymite- and cristobalite-based silica materials. *Ceram. Int.* **40**, 4207-4211 (2014).

Peacock, G. *Life of Thomas Young, M.D.* (John Murray, London, 1855).

Pelous, J. and Vacher, R. Thermal Brillouin scattering in crystalline and fused quartz from 20 to 1000 °C. *Solid State Commun.* **18**, 657-661 (1976).

Peng, Z., Chien, S.Y. & Redfern, S.A.T. Dynamic mechanical relaxation and loss in the incommensurate phase of quartz. *J. Phys.: Condens. Matter* **24**, 255403-6 (2012).

Peng, Z. & Redfern, S. A.T. Mechanical properties of quartz at the α-β phase transition: implications for tectonic and seismic anomalies. *Geochem. Geophys. Geosyst.* **14**, 18-28 (2013).

Perrier, A. & De Mandrot, R. Elasticité et symétrie du quartz aux températures élevées. *Mém. Soc. Vaud. Sci. Nat.* **7**, 333-363 (1923).

Peselnick, L. & Meister, R. Variational method of determining effective moduli of polycrystals: (A) hexagonal symmetry, (B) trigonal symmetry. *J. Appl. Phys.* **36**, 2879-2884 (1965).

Piché, L., Maynard, R., Hunklinger, S. & Jäckle, J. Anomalous sound velocity in vitreous silica at very low temperatures. *Phys. Rev. Lett.* **32**, 1426-1429 (1974).

Pine, A.S. Brillouin scattering study of acoustic attenuation in fused quartz. *Phys. Rev.* **185**, 1187-1193 (1969).

Press, F. & Siever, R. *Allgemeine Geologie - Einführung in das System Erde* (Spektrum Akademischer Verlag, München, 2001).

Purton, J., Jones, R., Catlow, C.R.A. & Leslie, M. Ab initio potentials for the calculation of the dynamical and elastic properties of α-quartz. *Phys. Chem. Minerals* **19**, 392-400 (1993).

Putnis, A. *Introduction to mineral sciences* (Cambridge University Press, Cambridge, 1992)

Qaisar, M. Attenuation properties of viscoelastic material. *Pageoph.* **131**, 703-713 (1989).

Raz, U., Girsperger, S. & Thompson, A.B. Thermal expansion, compressibility and volumetric changes of quartz obtained by single crystal dilatometry to 700 °C and 3.5 kilobars (0.35 GPa). ETH, Eidgenössische Technische Hochschule Zürich, Department of Earth Sciences, 2002.

Reuss, A. Berechnung der Fließgrenze von Mischkristallen auf Grund der Plastizitätbedingung für Einkristalle. *Z. Angew. Math. Mech.* **9**, 49-58 (1929).

Rösler, H.J. *Lehrbuch der Mineralogie* (Deutscher Verlag für Grundstoffindustrie, Leipzig, 1988).

Rösler, J., Harders, H. & Bäker, M. *Mechanisches Verhalten der Werkstoffe* (Vieweg + Teubner, Wiesbaden 2008).

Ronov, A.B. & Yaroshevsky, A.A. Chemical composition of the Earth's crust. *Geophys. Monogr. Ser.* **13**, 37-57 (1969).

Rosenholtz, J.L. & Smith, D.T. Linear thermal expansion and inversions of quartz, var. rock crystal. *Am. Mineral.* **26**, 103-109 (1941)

Rudnick, R.L., Mc Donough, W.F. & O'Connell, R.J. Thermal structure, thickness and composition of continental lithosphere. *Chem. Geol.* **145**, 395-411 (1998).

Sadd, M.H. *Elasticity: theory, applications and numerics* (Elsevier, Amsterdam, 2005).

Saha, P., Annamalai, N., Bandyopadhyay, T. α-Quartz 1. crystallography and crystal defects. *Mater. Sci. Bull.* **1**, 15-34 (1979).

Saika-Voivod, I., Sciortino, F., Grande, T. & Poole, P.H. Phase diagram of silica from computer simulation. *Phys. Rev. E* **70**, 061507-8 (2004).

Salje E.K.H. Application of Landau theory for the analysis of phase transitions in minerals. *Phys. Rep.* **215**, 49-99 (1992).

Sato, H., Ito, K. & Aizawa, Y. Simultaneous velocity and attenuation measurements applicable to various solids at high pressures and temperatures up to 1200 °C. *Meas. Sci. Technol.* **15**, 1787-1793 (2004).

Savart, M.F. Sur l'élasticité des corps qui cristallisent régulièrement. *Ann. Chim. Phys.* **40**, 5-30 (1829).

Schiessel, H., Metzler, R., Blumen, A. & Nonnenmacher, T.F. Generalized viscoelastic models: their fractional equations with solutions. *J. Phys. A: Math. Gen.* **28**, 6567-6584 (1995).

Schmidt, C., Bruhn, D. & Wirth, R. Experimental evidence of transformation plasticity in silicates: minimum of creep strength in quartz. *Earth Planet. Sci. Lett.* **205**, 273-280 (2003).

Schmitz, M., Heinsohn, W. & Schilling, F.R. Seismic gravity and petrophysical evidence for partial melt beneath the thickened Central Andean crust (21-23° S). *Tectonophys.* **270**, 313-326 (1997).

Schön, J. *Petrophysik* (Akademie-Verlag, Berlin, 1983).

Scholz, C.H. Static fatigue of quartz. *J. Geophys. Res.* **77**, 2104-2114 (1972).

Schreyer, W. *Hochdruckforschung in der modernen Gesteinskunde* (Westdeutscher Verlag, Opladen, 1976).

Scott, J.F. Soft-mode spectroscopy: experimental studies of structural phase transitions. *Rev. Mod. Phys.* **46**, 83-128 (1974).

Sebastian, U. *Gesteinskunde - Ein Leitfaden für Einsteiger und Anwender* (Spektrum, Heidelberg 2009).

Sharma, R., Gupta, V., Arora, B.R. & Sen, K. Petrophysical properties of the Himalayan granitoids: implication on composition and source. *Tectonophys.* **497**, 23-33 (2011).

Shaw, M.T. & Mac Knight, W.J. *Introduction to polymer viscosity* (Wiley-Interscience, Hoboken, 2005).

Sheehan, A.F., de la Torre, T., Monslave, G., Abers, G.A. & Hacker, B.R. Physical state of the Himalayan crust and uppermost mantle: constraints from seismic attenuation and velocity tomography. *J. Geophys. Res. Solid Earth* **119**, 567-580 (2014).

Shen, A.H., Bassett, W.A. & Chou, I.-M. The α-β quartz transition at high temperatures and pressures in a diamond-anvil cell by laser interferometry. *Am. Mineral.* **78**, 694-698 (1993).

Shillington, D.J., Van Avendonk, H.J.A., Behn, M.D., Kelen, P.B. & Jagoutz, O. Constraints on the composition of the Aleutian arc lower crust from v_p/v_s. *Geophys. Res. Lett* **40**, 2579-2584 (2013).

Simonyi, K. *Kulturgeschichte der Physik - Von den Anfängen bis heute* (Verlag Harri Deutsch, Frankfurt am Main, 2012).

Smirnov, M.B. Lattice dynamics and thermal expansion of quartz. *Phys. Rev. B* **59**, 4036-4043 (1999).

Smirnov, M.B. & Mirgorodsky, A.P. Lattice-dynamical study of the α-β phase transition of quartz: soft-mode behavior and elastic anomalies. *Phys. Rev. Lett.* **78**, 2413-2416 (1997).

Smyth, H.T. Thermal expansion of vitreous silica. *J. Am. Ceram. Soc.* **38**, 140-141 (1955).

Soga, N. Temperature and pressure derivatives of isotropic sound velocities of α quartz. *J. Geophys. Res.* **73**, 827-829 (1968).

Spearing, D.R., Farnan, I. & Stebbins, J.F. Dynamics of the α-β phase transitions in quartz and cristobalite as observed by in-situ high temperature ^{29}Si and ^{17}O NMR. *Phys. Chem. Minerals* **19**, 307-321 (1992).

Spinner, S. Elastic moduli of glasses by a dynamic method. *J. Am. Ceram. Soc.* **37**, 229-234 (1954).

Spinner, S. Elastic moduli of glasses at elevated temperatures by a dynamic method. *J. Am. Ceram. Soc.* **39**, 113-118 (1956).

Spinner, S. Temperature dependence of elastic constants of vitreous silica. *J. Am. Ceram. Soc.* **45**, 394-397 (1962).

Spinner, S. & Cleek, G.W. Temperature dependence of Young's modulus of vitreous germania and silica. *J. Appl. Phys.* **31**, 1407-1410 (1960).

Stevens, S.J., Hand, R.J. & Sharp, J.H. Polymorphism of silica. *J. Mater. Sci.* **32**, 2929-2935 (1997).

Stüwe, K. *Geodynamik der Lithosphäre* (Springer-Verlag, Berlin, 2000).

Suito, K., Miyoshi, M., Sasakura, T. & Fujisawa, H. Elastic properties of obsidian, vitreous SiO_2, and vitreous GeO_2 under high pressure up to 6 GPa. *Geophys. Monogr. Ser.* **67**, 219-225 (1992).

Swainson, I.P. & Dove, M.T. Molecular dynamics simulation of α- and β-cristobalite. *J. Phys.: Condens. Matter* **7**, 1771-1788 (1995).

Swamy, V., Saxena, S.K., Sundman, B. & Zhang, J. A thermodynamic assessment of silica phase diagram. *J. Geophys. Res.* **99**, 11787-11794 (1994).

Swenson, J.L., Beck, S.L. & Zandt, G. Crustal structure of the Altiplano from broadband regional wavefront modeling: implications for the composition of thick continental crust. *J. Geophys. Res.* **105**, 607-621 (2000).

Tarumi, R., Nakamura, K., Ogi, H. & Hirao, M. Complete set of elastic and piezoelectric coefficients of α-quartz at low temperatures. *J. Appl. Phys.* **102**, 113508-6 (2007).

Taylor, S.R. Abundance of chemical elements in the continental crust: a new table. *Geochim. Cosmochim. Acta* **28**, 1273-1285 (1964).

Taylor, S.R. The origin and growth of continents. *Tectonophys.* **4**, 17-34 (1967).

Tertian, R. & Claisse, F. *Principles of quantitative X-ray fluorescence analysis* (Heyden & Son Ltd, London 1982).

Thomas, L.A. & Wooster, W.A. Piezocrescence - The growth of Dauphiné twinning in quartz under stress. *Proc. R. Soc. London, Ser. A* **208**, 43-62 (1951).

Thompson, R.M., Downs, R.T. & Dera, P. The compression pathway of quartz. *Am. Mineral.* **96**, 1495-1502 (2011).

Thurston, R.N., Mc Skimin, H.J. & Andreatch, P. Third-order elastic coefficients of quartz. *J. Appl. Phys.* **37**, 267-275 (1966).

Ting, T.C.T. Explicit expression of the stationary values of Young's modulus and the shear modulus for anisotropic elastic materials. *J. Mech.* **21**, 255-266 (2005).

Truesdell, C. *Essays in the History of Mechanics* (Springer, New York, 1968).

Toby, B.H. R factors in Rietveld analysis: how good is good enough? *Powder Diffr.* **21**, 67-70 (2006).

Tse, J.S. & Klug, D.D. Mechanical instability of α-quartz: a molecular-dynamics study. *Phys. Rev. Lett.* **67**, 3559-3562 (1991).

Tsuneyuki, S., Aoki, H., Tsukada, M. & Matsui, Y. Molecular-dynamics study of the α to β structural phase transition of quartz. *Phys. Rev. Lett.* **64**, 776-779 (1990).

Tucker, M.G., Keen, D.A. & Dove, M.T. A detailed structural characterization of quartz on heating through the α-β phase transition. *Min. Mag.* **65**, 489-507 (2001).

Uno, T. & Noge, S. Piezoelectric and elastic properties of β-phase quartz. *Ferroelectr.* **224**, 63-70 (1999).

Van der Molen, I. The shift of the α-β transition temperature of quartz associated with the thermal expansion of granite at high pressure. *Tectonophys.* **73**, 323-342 (1981).

Van Landuyt, J., Van Tendeloo, G., Amelinckx, S. & Walker, M.B. Interpretation of Dauphiné-twin-domain configurations resulting from the α-β phase transition in quartz and aluminum phosphate. *Phys. Rev. B* **31**, 2986-2992 (1985).

Van Tendeloo, G., Van Landuyt, J. & Amelinckx, S. The α-β phase transition in quartz and $AlPO_4$ as studied by electron microscopy and diffraction. *Phys. Stat. Sol. A* **33**, 723-735 (1976).

Venkataraman, G. Soft modes and structural phase transitions. *Bull. Mater. Sci.* **1**, 129-170 (1979).

Voigt, W. Über die Beziehung zwischen den beiden Elastizitätsconstanten isotroper Körper. *Ann. Phys.* **38**, 573- 587 (1889).

Voigt, W. *Lehrbuch der Kristallphysik – mit Ausschluss der Kristalloptik* (Johnson Reprint Corporation, New York, 1966).

Walker, M.B. Theory of domain structures and associated defects in the incommensurable phase of quartz. *Phys. Rev. B* **28**, 6407-6410 (1983).

Walker, M.B. & Gooding, R.J. Theory of coupled phason and sound-wave normal modes in the incommensurate phase of quartz. *Phys. Rev. B* **32**, 7412-7416 (1985).

Wang, H. & Li, M. Ab initio calculations of second-, third-, and fourth-order elastic constants for single crystals. *Phys. Rev. B* **79**, 224102-10 (2009).

Wang, Q., Saunders, G.A., Lambson, E.F., Tschhaufeser, P., Parker, S.C. & James, B.J. Temperature dependence of the acoustic-mode vibrational anharmonicity of quartz from 243 to 393 K. *Phys. Rev. B* **45**, 10242-10254 (1992).

Wang, Z., Liu, Y. Song, W., Bi, Y. & Xie, H. A broadband spectroscopy method for ultrasonic wave velocity measurement under high pressure. *Rev. Sci. Instrum.* **82**, 014501-5 (2011).

Waterman, P.C. Orientation dependence of elastic waves in single crystals. *Phys. Rev.* **113**, 1240-1253 (1959).

Watt, J.P. Hashin-Shtrikman bounds on the effective elastic moduli of polycrystals with orthorhombic symmetry. *J. Appl. Phys.* **50**, 6290-6295 (1979).

Watt, J.P. Hashin-Shtrikman bounds on the effective elastic moduli of polycrystals with monoclinic symmetry. *J. Appl. Phys.* **51**, 1520-1524 (1980).

Watt, J.P., Davies, G.F. & O'Connell, R.J. The elastic properties of composite materials. *Rev. Geophys. Space Phys.* **14**, 541-563 (1976).

Watt, J.P. & Peselnick, L. Clarification of the HashinShtrikman bounds on the effective elastic moduli of polycrystals with hexagonal, trigonal, and tetragonal symmetries. *J. Appl. Phys.* **51**, 1525-1531 (1980).

Weidner, D.J., Bass, J.D., Ringwood, A.E. & Sinclair, W. The single-crystal elastic moduli of stishovite. *J. Geophys. Res.* **87**, 4740-4746 (1982).

Weidner, D.J. & Carleton H.R. Elasticity of coesite. *J. Geophys. Res.* **82**, 1334-1346 (1977).

Wenk, H.-R., Grigull, S., Pehl, J. & Williams, D.J. Texture changes during the quartz α-β phase transition studied by neutron diffraction. Los Alamos National Laboratory Report LALP-03-041 (2003).

Wiedemann, H.G. Thermomechanical analysis of quartz, glasses and woods. *J. Therm. Anal.* **37**, 1557-1567 (1991).

Whitney, D.L. & Evans, B.W. Abbreviations for names of rock-forming minerals. *Am. Mineral.* **95**, 185-187 (2010).

Wittke, W. *Felsmechanik: Grundlagen für wirtschaftliches Bauen im Fels* (Springer-Verlag, Berlin, 1984).

Wooster, W.A., Wooster, N., Rycroft, J.L. & Thomas, L.A. The control and elimination of electrical (Dauphiné) twinning in quartz. *J. Inst. Electr. Eng.* **94**, 927-938 (1947).

Yamamoto, N., Tsuda, K. & Yagi, K. High voltage electron microscope study of incommensurate phase in quartz. *J. Phys. Soc. Jpn.* **57**, 1352-1364 (1988).

Yeganeh-Haeri, A., Weidner, D.J. & Parise, J.B. Elasticity of α-cristobalite: a silicon dioxide with a negative Poisson's ratio. *Sci.* **257**, 650-652 (1992).

Zandt, G., Beck, S.L., Ruppert, S.R., Ammon, C.J., Rock, D., Minaya, E., Wallace, T.C. & Silver, P.G. Anomalous crust of the Bolivian Altiplano, Central Andes: constraints from broadband regional seismic waveforms. *Geophys. Res. Lett.* **23**, 1159-1162 (1996).

Zandt, G., Velasco, A.A. & Beck, S.L. Composition and thickness of the southern Altiplano crust, Bolivia. *Geology* **22**, 1003-1006 (1994).

Zener, C. Elasticity and anelasticity of metals (The University of Chicago Press, Chicago, 1948).

Zhao, H.L., Kramer, M.J. & Akinc, M. Thermal expansion behavior of intermetallic compounds in the Mo-Si-B system. *Intermet.* **12**, 493-498 (2004).

Zhu, Z.-L., Fu, H.-Z., Sun, J.-F., Liu, Y.-F., Shi, D.-H. & Xu, G.-L. First-principles calculations of elastic and thermal properties of molybdenum discilicide. *Chin. Phys. Lett.* **26**, 086203-4 (2009).

Zisman, W.A. Young's modulus and Poisson's ratio with reference to geophysical applications. *Geol.* **19**, 653-665 (1933).

Zubov, V.G. & Firsova, M.M. Elastic properties of quartz near the α-β transition. *Sov. Phys. Crystallogr.* **7**, 374-376 (1962).

9. Appendix

Appendix 1: Phase boundaries for silica phases at pressure p and temperature T (Fig. 1): α-β quartz transition (1), quartz-coesite transition (2) and quartz-tridymite transition (3). The geotherm (4) is modelled with a surface temperature T_0 of 0 °C, a surface heat flow q_s of 72.5 mWm^{-2}, a thermal conductivity of 2.5 $Wm^{-1}K^{-1}$, and a radiogenic heat production of 1 μWm^{-3}. A density of 2.8 g/cm^3 is used for the conversion between depth and lithostatic pressure in first approximation.

$$p = 0.0041\,T - 2.3887 \tag{1}$$

$$p = 0.0010\,T + 2.0992 \tag{2}$$

$$p = 0.0005\,T + 0.4015 \tag{3}$$

$$T_z = T_0 + \frac{q_s z}{K} - \frac{A z^2}{2K} \tag{4}$$

Appendix 2: Rotation matrices for rotations around the X- (1), Y- (2), and Z-axis (3) of a Cartesian coordinate system according to the azimuth ϕ and the polar distance ψ of any specimen orientation. In this study the rotation matrix from combined rotations as shown below is used (4).

$$a_X = \begin{bmatrix} 1 & 0 & 0 \\ 0 & \cos(\psi) & -\sin(\psi) \\ 0 & \sin(\psi) & \cos(\psi) \end{bmatrix} \tag{1}$$

$$a_Y = \begin{bmatrix} \cos(\psi) & 0 & \sin(\psi) \\ 0 & 1 & 0 \\ -\sin(\psi) & 0 & \cos(\psi) \end{bmatrix} \tag{2}$$

$$a_Z = \begin{bmatrix} \cos(\phi) & -\sin(\phi) & 0 \\ \sin(\phi) & \cos(\phi) & 0 \\ 0 & 0 & 1 \end{bmatrix} \tag{3}$$

$$a_{YZ} = \begin{bmatrix} \cos(\psi)\cos(\phi) & -\cos(\psi)\sin(\phi) & \sin(\psi) \\ \sin(\phi) & \cos(\phi) & 0 \\ -\sin(\psi)\cos(\phi) & \sin(\psi)\sin(\phi) & \cos(\psi) \end{bmatrix} \tag{4 from (2) \& (3)}$$

Appendix 3: Directional cosines n_1 to n_3 based on the azimuth ϕ and the polar distance ψ.

$$n_1 = \cos(\phi)\sin(\psi) \tag{1}$$

$$n_2 = \sin(\phi)\sin(\psi) \tag{2}$$

$$n_3 = \cos(\psi) \tag{3}$$

$$n_1^2 + n_2^2 + n_3^2 = 1 \tag{4}$$

Appendix 4: Derivation from Christoffel's equation: simplified determination of the elastic wave velocities v_p (19), v_{sv} (17), and v_{sh} (18) as well as the distortion vectors $\acute{\zeta}$ to ζ'''. See chapter 1 for the definition of further varibles. Also given: the angle γ between two vectors.

$$a_{ik} = \begin{vmatrix} a_{11} & a_{12} & a_{13} \\ a_{21} & a_{22} & a_{23} \\ a_{31} & a_{32} & a_{33} \end{vmatrix} = \begin{vmatrix} c_{1j1l}\, g_j\, g_l & c_{1j2l}\, g_j\, g_l & c_{1j3l}\, g_j\, g_l \\ c_{2j1l}\, g_j\, g_l & c_{2j2l}\, g_j\, g_l & c_{2j3l}\, g_j\, g_l \\ c_{3j1l}\, g_j\, g_l & c_{3j2l}\, g_j\, g_l & c_{3j3l}\, g_j\, g_l \end{vmatrix} = 0 \tag{1}$$

$$a_{11}\, a_{22}\, a_{33} + a_{12}\, a_{23}\, a_{31} + a_{31}\, a_{21}\, a_{32} - a_{13}\, a_{22}\, a_{31} - a_{11}\, a_{23}\, a_{32} - a_{12}\, a_{21}\, a_{33} = 0 \tag{2}$$

$$a_{11} = c_{1111}\, g_1\, g_1 + c_{1112}\, g_1\, g_2 + c_{1113}\, g_1\, g_3 + c_{1211}\, g_2\, g_1 + \ldots \tag{3}$$

$$a_{12} = c_{1121}\, g_1\, g_1 + c_{1122}\, g_1\, g_2 + \ldots \tag{4}$$

$$a_{13} = \ldots \tag{5) - (11}$$

$$K_1 = a_{11} + a_{22} + a_{33} \tag{12) from (1) - (11}$$

$$K_2 = a_{12}\, a_{21} + a_{23}\, a_{32} + a_{13}\, a_{31} - a_{11}\, a_{22} - a_{11}\, a_{33} - a_{22}\, a_{33} \tag{13}$$

$$K_3 = a_{31}\, a_{12}\, a_{23} - a_{11}\, a_{23}\, a_{32} - a_{31}\, a_{13}\, a_{22} - a_{21}\, a_{12}\, a_{33} + a_{11}\, a_{22}\, a_{33} + a_{21}\, a_{13}\, a_{32} \tag{14}$$

$$R_2 = 4\, K_1^3\, K_3 - K_1^2\, K_2^2 + 18\, K_1\, K_2\, K_3 - 4\, K_2^3 + 27\, K_3^2 \tag{15}$$

$$R_1 = \left(\frac{1}{9}\, \sqrt{3}\, \left(K_1^2 + 3\, K_2\right)^{1.5}\right) \left(2\, K_1^3 + 9\, K_1\, K_2 + 27\, K_3\right) \sqrt{\frac{-R_2}{\left(K_1^2 + 3\, K_2\right)^3}} \tag{16}$$

$$v_{sh} = \sqrt{\frac{\frac{2}{3}\sqrt{K_1^2 + 3\, K_2}\, \sin\left(\frac{\tan^{-1}\left(\frac{R_1}{R_2}\right)}{3}\right) + \frac{K_1}{3}}{\rho}} \tag{17}$$

$$v_{sv} = \sqrt{\frac{\frac{K_1}{3} - \frac{2}{3}\sqrt{K_1^2 + 3\, K_2}\, \sin\left(\frac{\tan^{-1}\left(\frac{R_1}{R_2}\right) + \pi}{3}\right)}{\rho}} \tag{18}$$

$$v_p = \sqrt{\frac{\frac{2}{3}\sqrt{K_1^2 + 3\, K_2}\, \cos\left(\frac{\tan^{-1}\left(\frac{R_1}{R_2}\right) + \frac{\pi}{2}}{3}\right) + \frac{K_1}{3}}{\rho}} \tag{19}$$

$$\xi_1''' = a_{13}\left(a_{22} - \rho\, v_p^2\right) - a_{23}\, a_{12} \tag{20}$$

$$\xi_2''' = a_{23}\left(a_{11} - \rho\, v_p^2\right) - a_{21}\, a_{13} \tag{21}$$

$$\xi_3''' = a_{21}\, a_{12} - \left(a_{22} - \rho\, v_p^2\right)\left(a_{11} - \rho\, v_p^2\right) \tag{22}$$

$$\xi''_1 = a_{12}\left(a_{33} - \rho v_{sv}^2\right) - a_{13}\,a_{32} \tag{23}$$

$$\xi''_2 = a_{13}\,a_{31} - \left(a_{11} - \rho v_{sv}^2\right)\left(a_{33} - \rho v_{sv}^2\right) \tag{24}$$

$$\xi''_3 = a_{32}\left(a_{11} - \rho v_{sv}^2\right) - a_{21}\,a_{31} \tag{25}$$

$$\xi'_1 = a_{32}\,a_{23} - \left(a_{33} - \rho v_{sh}^2\right)\left(a_{22} - \rho v_{sh}^2\right) \tag{26}$$

$$\xi'_2 = a_{21}\left(a_{33} - \rho v_{sh}^2\right) - a_{31}\,a_{23} \tag{27}$$

$$\xi'_3 = a_{31}\left(a_{22} - \rho v_{sh}^2\right) - a_{32}\,a_{21} \tag{28}$$

$$|\xi| = \sqrt{\xi_1^2 + \xi_2^2 + \xi_3^2} \tag{29}$$

$$\cos(\gamma) = \frac{\xi' + \xi''}{|\xi'|\,|\xi''|} \tag{30}$$

Appendix 5: Simplification of a second-rank tensor T_{ij}, *e.g.* the thermal expansion, a third-rank tensor P_{ij}, *e.g.* the direct piezoelectric effect, and a fourth-rank tensor, *e.g.* the stiffness C_{ij} and compliance tensor S_{ij}, in Voigt notation (except for T_{ij} and the first index of P_{ij}) and for different crystal symmetries. The representation of P_{ij} is equivalent to S_{ij} and for P_{i6} factor 2 reduces to 1 if the tensor of the converse piezoelectric effect is considered (*e.g.* Nye 1992).

a) Triclinic crystal system (crystal classes: 1, $\bar{1}$, represents the general case for all crystal classes):

$$T_{ij} = \begin{bmatrix} T_{11} & T_{12} & T_{13} \\ T_{12} & T_{22} & T_{23} \\ T_{13} & T_{23} & T_{33} \end{bmatrix} \tag{1}$$

$$P_{ij} = \begin{bmatrix} P_{11} & P_{12} & P_{13} & P_{14} & P_{15} & P_{16} \\ P_{21} & P_{22} & P_{23} & P_{24} & P_{25} & P_{26} \\ P_{31} & P_{32} & P_{33} & P_{34} & P_{35} & P_{36} \end{bmatrix} \tag{2}$$

$$C_{ij} = \begin{bmatrix} C_{11} & C_{12} & C_{13} & C_{14} & C_{15} & C_{16} \\ C_{12} & C_{22} & C_{23} & C_{24} & C_{25} & C_{26} \\ C_{13} & C_{23} & C_{33} & C_{34} & C_{35} & C_{36} \\ C_{14} & C_{24} & C_{34} & C_{44} & C_{45} & C_{46} \\ C_{15} & C_{25} & C_{35} & C_{45} & C_{55} & C_{56} \\ C_{16} & C_{26} & C_{36} & C_{46} & C_{56} & C_{66} \end{bmatrix} \tag{3}$$

$$S_{ij} = \begin{bmatrix} S_{11} & S_{12} & S_{13} & S_{14} & S_{15} & S_{16} \\ S_{12} & S_{22} & S_{23} & S_{24} & S_{25} & S_{26} \\ S_{13} & S_{23} & S_{33} & S_{34} & S_{35} & S_{36} \\ S_{14} & S_{24} & S_{34} & S_{44} & S_{45} & S_{46} \\ S_{15} & S_{25} & S_{35} & S_{45} & S_{55} & S_{56} \\ S_{16} & S_{26} & S_{36} & S_{46} & S_{56} & S_{66} \end{bmatrix} \tag{4}$$

b) Monoclinic crystal system (crystal classes: 2 (6) & (7), m (8) & (9), $\frac{2}{m}$, *e.g.* coesite, α-tridymite):

$$T_{ij} = \begin{bmatrix} T_{11} & 0 & T_{13} \\ 0 & T_{22} & 0 \\ T_{13} & 0 & T_{33} \end{bmatrix} \tag{5}$$

$$P_{ij} = \begin{bmatrix} 0 & 0 & 0 & P_{14} & 0 & P_{16} \\ P_{21} & P_{22} & \mathrm{P}_{23} & 0 & P_{25} & 0 \\ 0 & 0 & 0 & P_{34} & 0 & P_{36} \end{bmatrix} \tag{6}$$

$$P_{ij} = \begin{bmatrix} 0 & 0 & 0 & P_{14} & P_{15} & 0 \\ 0 & 0 & 0 & P_{24} & P_{25} & 0 \\ P_{31} & P_{32} & P_{33} & 0 & 0 & P_{36} \end{bmatrix} \tag{7}$$

$$P_{ij} = \begin{bmatrix} P_{11} & P_{12} & P_{13} & 0 & P_{15} & 0 \\ 0 & 0 & 0 & P_{14} & 0 & P_{16} \\ P_{31} & P_{32} & P_{33} & 0 & P_{35} & 0 \end{bmatrix} \tag{8}$$

$$P_{ij} = \begin{bmatrix} P_{11} & P_{12} & P_{13} & 0 & 0 & P_{16} \\ P_{21} & P_{22} & P_{23} & 0 & 0 & P_{26} \\ 0 & 0 & 0 & P_{34} & P_{35} & 0 \end{bmatrix} \tag{9}$$

$$C_{ij} = \begin{bmatrix} C_{11} & C_{12} & C_{13} & 0 & C_{15} & 0 \\ C_{12} & C_{22} & C_{23} & 0 & C_{25} & 0 \\ C_{13} & C_{23} & C_{33} & 0 & C_{35} & 0 \\ 0 & 0 & 0 & C_{44} & 0 & C_{46} \\ C_{15} & C_{25} & C_{35} & 0 & C_{55} & 0 \\ 0 & 0 & 0 & C_{46} & 0 & C_{66} \end{bmatrix} \tag{10}$$

$$S_{ij} = \begin{bmatrix} S_{11} & S_{12} & S_{13} & 0 & S_{15} & 0 \\ S_{12} & S_{22} & S_{23} & 0 & S_{25} & 0 \\ S_{13} & S_{23} & S_{33} & 0 & S_{35} & 0 \\ 0 & 0 & 0 & S_{44} & 0 & S_{46} \\ S_{15} & S_{25} & S_{35} & S_{45} & S_{55} & 0 \\ 0 & 0 & 0 & S_{46} & 0 & S_{66} \end{bmatrix} \tag{11}$$

c) Orthorhombic crystal system (crystal classes: 222 (13), mm2 (14), mmm, *e.g.* rocks):

$$T_{ij} = \begin{bmatrix} T_{11} & 0 & 0 \\ 0 & T_{22} & 0 \\ 0 & 0 & T_{33} \end{bmatrix} \tag{12}$$

$$P_{ij} = \begin{bmatrix} 0 & 0 & 0 & P_{14} & 0 & 0 \\ 0 & 0 & 0 & 0 & P_{25} & 0 \\ 0 & 0 & 0 & 0 & 0 & P_{36} \end{bmatrix} \tag{13}$$

$$P_{ij} = \begin{bmatrix} 0 & 0 & 0 & 0 & P_{15} & 0 \\ 0 & 0 & 0 & P_{24} & 0 & 0 \\ P_{31} & P_{32} & P_{33} & 0 & 0 & 0 \end{bmatrix} \tag{14}$$

$$C_{ij} = \begin{bmatrix} C_{11} & C_{12} & C_{13} & 0 & 0 & 0 \\ C_{12} & C_{22} & C_{23} & 0 & 0 & 0 \\ C_{13} & C_{23} & C_{33} & 0 & 0 & 0 \\ 0 & 0 & 0 & C_{44} & 0 & 0 \\ 0 & 0 & 0 & 0 & C_{55} & 0 \\ 0 & 0 & 0 & 0 & 0 & C_{66} \end{bmatrix} \tag{15}$$

$$S_{ij} = \begin{bmatrix} S_{11} & S_{12} & S_{13} & 0 & 0 & 0 \\ S_{12} & S_{22} & S_{23} & 0 & 0 & 0 \\ S_{13} & S_{23} & S_{33} & 0 & 0 & 0 \\ 0 & 0 & 0 & S_{44} & 0 & 0 \\ 0 & 0 & 0 & 0 & S_{55} & 0 \\ 0 & 0 & 0 & 0 & 0 & S_{66} \end{bmatrix} \tag{16}$$

d) Tetragonal crystal system (crystal classes: 4 (18), $\bar{4}$ (19), $\frac{4}{m}$):

$$T_{ij} = \begin{bmatrix} T_{11} & 0 & 0 \\ 0 & T_{11} & 0 \\ 0 & 0 & T_{33} \end{bmatrix} \tag{17}$$

$$P_{ij} = \begin{bmatrix} 0 & 0 & 0 & P_{14} & P_{15} & 0 \\ 0 & 0 & 0 & P_{15} & -P_{14} & 0 \\ P_{31} & P_{31} & P_{33} & 0 & 0 & 0 \end{bmatrix} \tag{18}$$

$$P_{ij} = \begin{bmatrix} 0 & 0 & 0 & P_{14} & P_{15} & 0 \\ 0 & 0 & 0 & -P_{15} & P_{14} & 0 \\ P_{31} & -P_{31} & 0 & 0 & 0 & P_{36} \end{bmatrix} \tag{19}$$

$$C_{ij} = \begin{bmatrix} C_{11} & C_{12} & C_{13} & 0 & 0 & C_{16} \\ C_{12} & C_{11} & C_{13} & 0 & 0 & -C_{16} \\ C_{13} & C_{13} & C_{33} & 0 & 0 & 0 \\ 0 & 0 & 0 & C_{44} & 0 & 0 \\ 0 & 0 & 0 & 0 & C_{44} & 0 \\ C_{16} & -C_{16} & 0 & 0 & 0 & C_{66} \end{bmatrix} \tag{20}$$

$$S_{ij} = \begin{bmatrix} S_{11} & S_{12} & S_{13} & 0 & 0 & S_{16} \\ S_{12} & S_{11} & S_{13} & 0 & 0 & -S_{16} \\ S_{13} & S_{13} & S_{33} & 0 & 0 & 0 \\ 0 & 0 & 0 & S_{44} & 0 & 0 \\ 0 & 0 & 0 & 0 & S_{44} & 0 \\ S_{16} & -S_{16} & 0 & 0 & 0 & S_{66} \end{bmatrix} \tag{21}$$

e) Tetragonal crystal system (crystal classes: 422 (22), 4mm (23), $\bar{4}$2m (24), $\frac{4}{m}$mm, *e.g.* α-cristobalite):

$$P_{ij} = \begin{bmatrix} 0 & 0 & 0 & P_{14} & 0 & 0 \\ 0 & 0 & 0 & 0 & -P_{14} & 0 \\ 0 & 0 & 0 & 0 & 0 & 0 \end{bmatrix} \tag{22}$$

$$P_{ij} = \begin{bmatrix} 0 & 0 & 0 & 0 & P_{15} & 0 \\ 0 & 0 & 0 & P_{15} & 0 & 0 \\ P_{31} & P_{31} & P_{33} & 0 & 0 & 0 \end{bmatrix} \qquad (23)$$

$$P_{ij} = \begin{bmatrix} 0 & 0 & 0 & P_{14} & 0 & 0 \\ 0 & 0 & 0 & 0 & P_{14} & 0 \\ 0 & 0 & 0 & 0 & 0 & P_{36} \end{bmatrix} \qquad (24)$$

$$C_{ij} = \begin{bmatrix} C_{11} & C_{12} & C_{13} & 0 & 0 & 0 \\ C_{12} & C_{11} & C_{13} & 0 & 0 & 0 \\ C_{13} & C_{13} & C_{33} & 0 & 0 & 0 \\ 0 & 0 & 0 & C_{44} & 0 & 0 \\ 0 & 0 & 0 & 0 & C_{44} & 0 \\ 0 & 0 & 0 & 0 & 0 & C_{66} \end{bmatrix} \qquad (25)$$

$$S_{ij} = \begin{bmatrix} S_{11} & S_{12} & S_{13} & 0 & 0 & 0 \\ S_{12} & S_{11} & S_{13} & 0 & 0 & 0 \\ S_{13} & S_{13} & S_{33} & 0 & 0 & 0 \\ 0 & 0 & 0 & S_{44} & 0 & 0 \\ 0 & 0 & 0 & 0 & S_{44} & 0 \\ 0 & 0 & 0 & 0 & 0 & S_{66} \end{bmatrix} \qquad (26)$$

f) Trigonal crystal system (crystal classes: 3, $\overline{3}$):

$$T_{ij} = \begin{bmatrix} T_{11} & 0 & 0 \\ 0 & T_{11} & 0 \\ 0 & 0 & T_{33} \end{bmatrix} \qquad (27)$$

$$P_{ij} = \begin{bmatrix} P_{11} & -P_{11} & 0 & P_{14} & P_{15} & -2\,P_{21} \\ -P_{21} & P_{21} & 0 & P_{15} & -P_{14} & -2\,P_{11} \\ P_{31} & P_{31} & P_{33} & 0 & 0 & 0 \end{bmatrix} \qquad (28)$$

$$C_{ij} = \begin{bmatrix} C_{11} & C_{12} & C_{13} & C_{14} & -C_{25} & 0 \\ C_{12} & C_{11} & C_{13} & -C_{14} & C_{25} & 0 \\ C_{13} & C_{13} & C_{33} & 0 & 0 & 0 \\ C_{14} & -C_{14} & 0 & C_{44} & 0 & C_{25} \\ -C_{25} & C_{25} & 0 & 0 & C_{44} & C_{14} \\ 0 & 0 & 0 & C_{25} & C_{14} & \frac{1}{2}\left(C_{11} - C_{12}\right) \end{bmatrix} \qquad (29)$$

$$S_{ij} = \begin{bmatrix} S_{11} & S_{12} & S_{13} & S_{14} & -S_{25} & 0 \\ S_{12} & S_{11} & S_{13} & -S_{14} & S_{25} & 0 \\ S_{13} & S_{13} & S_{33} & 0 & 0 & 0 \\ S_{14} & -S_{14} & 0 & S_{44} & 0 & 2\,S_{25} \\ -S_{25} & S_{25} & 0 & 0 & S_{44} & 2\,S_{14} \\ 0 & 0 & 0 & 2\,S_{25} & 2\,S_{14} & 2\left(S_{11} - S_{12}\right) \end{bmatrix} \qquad (30)$$

g) Trigonal crystal system (crystal classes: 32 (31), 3m (32) & (33), $\bar{3}$m, *e.g.* α-quartz):

$$P_{ij} = \begin{bmatrix} P_{11} & -P_{11} & 0 & P_{14} & 0 & 0 \\ 0 & 0 & 0 & 0 & -P_{14} & -2P_{11} \\ 0 & 0 & 0 & 0 & 0 & 0 \end{bmatrix} \tag{31}$$

$$P_{ij} = \begin{bmatrix} 0 & 0 & 0 & 0 & P_{15} & -2P_{21} \\ -P_{21} & P_{21} & 0 & P_{15} & 0 & 0 \\ P_{31} & P_{31} & P_{33} & 0 & 0 & 0 \end{bmatrix} \tag{32}$$

$$P_{ij} = \begin{bmatrix} P_{11} & -P_{11} & 0 & 0 & P_{15} & 0 \\ 0 & 0 & 0 & P_{15} & 0 & -2P_{11} \\ P_{31} & P_{31} & P_{33} & 0 & 0 & 0 \end{bmatrix} \tag{33}$$

$$C_{ij} = \begin{bmatrix} C_{11} & C_{12} & C_{13} & C_{14} & 0 & 0 \\ C_{12} & C_{11} & C_{13} & -C_{14} & 0 & 0 \\ C_{13} & C_{13} & C_{33} & 0 & 0 & 0 \\ C_{14} & -C_{14} & 0 & C_{44} & 0 & 0 \\ 0 & 0 & 0 & 0 & C_{44} & C_{14} \\ 0 & 0 & 0 & 0 & C_{14} & \frac{1}{2}\left(C_{11} - C_{12}\right) \end{bmatrix} \tag{34}$$

$$S_{ij} = \begin{bmatrix} S_{11} & S_{12} & S_{13} & S_{14} & 0 & 0 \\ S_{12} & S_{11} & S_{13} & -S_{14} & 0 & 0 \\ S_{13} & S_{13} & S_{33} & 0 & 0 & 0 \\ S_{14} & -S_{14} & 0 & S_{44} & 0 & 0 \\ 0 & 0 & 0 & 0 & S_{44} & 2S_{14} \\ 0 & 0 & 0 & 0 & 2S_{14} & 2\left(S_{11} - S_{12}\right) \end{bmatrix} \tag{35}$$

h) Hexagonal crystal system (crystal classes: 6 (37), $\bar{6}$ (40), $\frac{6}{m}$, $\frac{6}{m}$mm, 622 (39), 6mm (38), $\bar{6}$m2 (41) & (42), *e.g.* β-quartz):

$$T_{ij} = \begin{bmatrix} T_{11} & 0 & 0 \\ 0 & T_{11} & 0 \\ 0 & 0 & T_{33} \end{bmatrix} \tag{36}$$

$$P_{ij} = \begin{bmatrix} 0 & 0 & 0 & P_{14} & P_{15} & 0 \\ 0 & 0 & 0 & P_{15} & -P_{14} & 0 \\ P_{31} & P_{31} & P_{33} & 0 & 0 & 0 \end{bmatrix} \tag{37}$$

$$P_{ij} = \begin{bmatrix} 0 & 0 & 0 & 0 & P_{15} & 0 \\ 0 & 0 & 0 & P_{15} & 0 & 0 \\ P_{31} & P_{31} & P_{33} & 0 & 0 & 0 \end{bmatrix} \tag{38}$$

$$P_{ij} = \begin{bmatrix} 0 & 0 & 0 & P_{14} & 0 & 0 \\ 0 & 0 & 0 & 0 & -P_{14} & 0 \\ 0 & 0 & 0 & 0 & 0 & 0 \end{bmatrix} \tag{39}$$

$$P_{ij} = \begin{bmatrix} P_{11} & -P_{11} & 0 & 0 & 0 & -2P_{21} \\ -P_{21} & P_{21} & 0 & 0 & 0 & -2P_{11} \\ 0 & 0 & 0 & 0 & 0 & 0 \end{bmatrix} \tag{40}$$

$$P_{ij} = \begin{bmatrix} 0 & 0 & 0 & 0 & 0 & -2P_{21} \\ -P_{21} & P_{21} & 0 & 0 & 0 & 0 \\ 0 & 0 & 0 & 0 & 0 & 0 \end{bmatrix} \tag{41}$$

$$P_{ij} = \begin{bmatrix} P_{11} & -P_{11} & 0 & 0 & 0 & 0 \\ 0 & 0 & 0 & 0 & 0 & -2P_{11} \\ 0 & 0 & 0 & 0 & 0 & 0 \end{bmatrix} \tag{42}$$

$$C_{ij} = \begin{bmatrix} C_{11} & C_{12} & C_{13} & 0 & 0 & 0 \\ C_{12} & C_{11} & C_{13} & 0 & 0 & 0 \\ C_{13} & C_{13} & C_{33} & 0 & 0 & 0 \\ 0 & 0 & 0 & C_{44} & 0 & 0 \\ 0 & 0 & 0 & 0 & C_{44} & 0 \\ 0 & 0 & 0 & 0 & 0 & \frac{1}{2}\left(C_{11}-C_{12}\right) \end{bmatrix} \tag{43}$$

$$S_{ij} = \begin{bmatrix} S_{11} & S_{12} & S_{13} & 0 & 0 & 0 \\ S_{12} & S_{11} & S_{13} & 0 & 0 & 0 \\ S_{13} & S_{13} & S_{33} & 0 & 0 & 0 \\ 0 & 0 & 0 & S_{44} & 0 & 0 \\ 0 & 0 & 0 & 0 & S_{44} & 0 \\ 0 & 0 & 0 & 0 & 0 & 2\left(S_{11}-S_{12}\right) \end{bmatrix} \tag{44}$$

h) Cubic crystal system (crystal classes: 23 (47), $\bar{4}$3m (47), m3, 432 (46), m3m, *e.g.* β-cristobalite):

$$T_{ij} = \begin{bmatrix} T_{11} & 0 & 0 \\ 0 & T_{11} & 0 \\ 0 & 0 & T_{11} \end{bmatrix} \tag{45}$$

$$P_{ij} = \begin{bmatrix} 0 & 0 & 0 & 0 & 0 & 0 \\ 0 & 0 & 0 & 0 & 0 & 0 \\ 0 & 0 & 0 & 0 & 0 & 0 \end{bmatrix} \tag{46}$$

$$P_{ij} = \begin{bmatrix} 0 & 0 & 0 & P_{14} & 0 & 0 \\ 0 & 0 & 0 & 0 & P_{14} & 0 \\ 0 & 0 & 0 & 0 & 0 & P_{14} \end{bmatrix} \tag{47}$$

$$C_{ij} = \begin{bmatrix} C_{11} & C_{12} & C_{12} & 0 & 0 & 0 \\ C_{12} & C_{11} & C_{12} & 0 & 0 & 0 \\ C_{12} & C_{12} & C_{11} & 0 & 0 & 0 \\ 0 & 0 & 0 & C_{44} & 0 & 0 \\ 0 & 0 & 0 & 0 & C_{44} & 0 \\ 0 & 0 & 0 & 0 & 0 & C_{44} \end{bmatrix} \tag{48}$$

$$S_{\text{ij}} = \begin{bmatrix} S_{11} & S_{12} & S_{12} & 0 & 0 & 0 \\ S_{12} & S_{11} & S_{12} & 0 & 0 & 0 \\ S_{12} & S_{12} & S_{11} & 0 & 0 & 0 \\ 0 & 0 & 0 & S_{44} & 0 & 0 \\ 0 & 0 & 0 & 0 & S_{44} & 0 \\ 0 & 0 & 0 & 0 & 0 & S_{44} \end{bmatrix} \tag{49}$$

i) Isotropic (*e.g.* polycrystals, rocks):

$$T_{\text{ij}} = \begin{bmatrix} T_{11} & 0 & 0 \\ 0 & T_{11} & 0 \\ 0 & 0 & T_{11} \end{bmatrix} \tag{50}$$

$$P_{\text{ij}} = \begin{bmatrix} 0 & 0 & 0 & 0 & 0 & 0 \\ 0 & 0 & 0 & 0 & 0 & 0 \\ 0 & 0 & 0 & 0 & 0 & 0 \end{bmatrix} \tag{51}$$

$$C_{\text{ij}} = \begin{bmatrix} C_{11} & C_{12} & C_{12} & 0 & 0 & 0 \\ C_{12} & C_{11} & C_{12} & 0 & 0 & 0 \\ C_{12} & C_{12} & C_{11} & 0 & 0 & 0 \\ 0 & 0 & 0 & \frac{1}{2}\left(C_{11} - C_{12}\right) & 0 & 0 \\ 0 & 0 & 0 & 0 & \frac{1}{2}\left(C_{11} - C_{12}\right) & 0 \\ 0 & 0 & 0 & 0 & 0 & \frac{1}{2}\left(C_{11} - C_{12}\right) \end{bmatrix} \tag{52}$$

$$S_{\text{ij}} = \begin{bmatrix} S_{11} & S_{12} & S_{12} & 0 & 0 & 0 \\ S_{12} & S_{11} & S_{12} & 0 & 0 & 0 \\ S_{12} & S_{12} & S_{11} & 0 & 0 & 0 \\ 0 & 0 & 0 & 2\left(S_{11} - S_{12}\right) & 0 & 0 \\ 0 & 0 & 0 & 0 & 2\left(S_{11} - S_{12}\right) & 0 \\ 0 & 0 & 0 & 0 & 0 & 2\left(S_{11} - S_{12}\right) \end{bmatrix} \tag{53}$$

j) Conversion between the Voigt notation and matrix notation.

$$11 = 1111 \tag{54}$$

$$22 = 2222 \tag{55}$$

$$33 = 3333 \tag{56}$$

$$44 = 2323 \tag{57}$$

$$55 = 1313 \tag{58}$$

$$66 = 1212 \tag{59}$$

$$12 = 1122 \tag{60}$$

...

Appendix 6: Matrix inversion explained for the stiffness C_{ij} and compliance tensor S_{ij} in Voigt notation and vise versa (Python command: “S = np.linalg.inv(C)”, Microsoft Excel command: “S = minv(C)”). M_{ii} equals the Kronecker delta.

$$C_{ij}\,S_{ij} = M_{ii} = \begin{bmatrix} 1 & 0 & 0 & 0 & 0 & 0 \\ 0 & 1 & 0 & 0 & 0 & 0 \\ 0 & 0 & 1 & 0 & 0 & 0 \\ 0 & 0 & 0 & 1 & 0 & 0 \\ 0 & 0 & 0 & 0 & 1 & 0 \\ 0 & 0 & 0 & 0 & 0 & 1 \end{bmatrix} \tag{1}$$

$$S_{ij} = C_{ij}\,M_{ii} = \left[\begin{array}{cccccc|cccccc} C_{11} & C_{12} & C_{13} & C_{14} & C_{15} & C_{16} & 1 & 0 & 0 & 0 & 0 & 0 \\ C_{21} & C_{22} & C_{23} & C_{24} & C_{25} & C_{26} & 0 & 1 & 0 & 0 & 0 & 0 \\ C_{31} & C_{32} & C_{33} & C_{34} & C_{35} & C_{36} & 0 & 0 & 1 & 0 & 0 & 0 \\ C_{41} & C_{42} & C_{43} & C_{44} & C_{45} & C_{46} & 0 & 0 & 0 & 1 & 0 & 0 \\ C_{51} & C_{52} & C_{53} & C_{54} & C_{55} & C_{56} & 0 & 0 & 0 & 0 & 1 & 0 \\ C_{61} & C_{62} & C_{63} & C_{64} & C_{65} & C_{66} & 0 & 0 & 0 & 0 & 0 & 1 \end{array}\right] = \begin{bmatrix} R_1 \\ R_2 \\ R_3 \\ R_4 \\ R_5 \\ R_6 \end{bmatrix} \tag{2}$$

$$R'_1 = \frac{R_1}{C_{11}} \tag{3}$$

$$R'_2 = R_2 - R'_1\,C_{21} \tag{4}$$

$$R'_3 = R_3 - R'_1\,C_{31} \tag{5}$$

$$R'_4 = \ldots \tag{6}$$

$$R''_2 = \frac{R'_2}{C'_{22}} \tag{7}$$

$$R''_1 = R'_1 - R''_2\,C'_{12} \tag{8}$$

$$R''_3 = R'_3 - R''_2\,C'_{32} \tag{9}$$

$$R''_4 = \ldots \tag{10}$$

…

$$C_{ij} = S_{ij}\,M_{ii} = \left[\begin{array}{cccccc|cccccc} 1 & 0 & 0 & 0 & 0 & 0 & S_{11} & S_{12} & S_{13} & S_{14} & S_{15} & S_{16} \\ 0 & 1 & 0 & 0 & 0 & 0 & S_{21} & S_{22} & S_{23} & S_{24} & S_{25} & S_{26} \\ 0 & 0 & 1 & 0 & 0 & 0 & S_{31} & S_{32} & S_{33} & S_{34} & S_{35} & S_{36} \\ 0 & 0 & 0 & 1 & 0 & 0 & S_{41} & S_{42} & S_{43} & S_{44} & S_{45} & S_{46} \\ 0 & 0 & 0 & 0 & 1 & 0 & S_{51} & S_{52} & S_{53} & S_{54} & S_{55} & S_{56} \\ 0 & 0 & 0 & 0 & 0 & 1 & S_{61} & S_{62} & S_{63} & S_{64} & S_{65} & S_{66} \end{array}\right] = \begin{bmatrix} R_1 \\ R_2 \\ R_3 \\ R_4 \\ R_5 \\ R_6 \end{bmatrix} \tag{39}$$

$$R'_1 = \frac{R_1}{S_{11}} \tag{40}$$

$$R'_2 = R_2 - R'_1\,S_{21} \tag{41}$$

$$R'_3 = R_3 - R'_1\,S_{31} \tag{42}$$

$$R'_4 = \ldots \tag{43}$$

$$R''_2 = \frac{R'_2}{S'_{22}} \tag{44}$$

$$R''_1 = R'_1 - R''_2\, S'_{12} \tag{45}$$

$$R''_3 = R'_3 - R''_2\, S'_{32} \tag{46}$$

$$R''_4 = \ldots \tag{47}$$

…

Appendix 7: Simplification of the matrix inversion for the stiffness C_{ij} and compliance tensor S_{ij} with a trigonal (Appendix 5g) and a hexagonal symmetry in Voigt notation.

$$2\,C_{11} = \frac{S_{33}}{f} + \frac{S_{44}}{g} \tag{1}$$

$$2\,C_{12} = \frac{S_{33}}{f} - \frac{S_{44}}{g} \tag{2}$$

$$C_{13} = \frac{-\,S_{13}}{f} \tag{3}$$

$$C_{14} = \frac{-\,S_{14}}{g} \tag{4}$$

$$C_{33} = \frac{S_{11} + S_{12}}{f} \tag{5}$$

$$C_{44} = \frac{S_{11} - S_{12}}{g} \tag{6}$$

$$C_{66} = \frac{C_{11} - C_{12}}{2} = \frac{S_{44}}{2\,g} \tag{7}$$

$$f = S_{33}\,(S_{11} + S_{12}) - 2\,S_{13}^2 \tag{8}$$

$$g = S_{44}\,\left(S_{11} - S_{12}\right) - 2\,S_{14}^2 \tag{9}$$

$$2\,S_{11} = \frac{C_{33}}{f'} + \frac{C_{44}}{g'} \tag{10}$$

$$2\,S_{12} = \frac{C_{33}}{f'} - \frac{C_{44}}{g'} \tag{11}$$

$$S_{13} = \frac{-\,C_{13}}{f'} \tag{12}$$

$$S_{14} = \frac{-\,C_{14}}{g'} \tag{13}$$

$$S_{33} = \frac{C_{11} + C_{12}}{f'} \tag{14}$$

$$S_{44} = \frac{C_{11} - C_{12}}{g'} \tag{15}$$

$$S_{66} = 2\left(S_{11} - S_{12}\right) = \frac{2\,C_{44}}{g'} \tag{16}$$

$$f' = C_{33}\left(C_{11} + C_{12}\right) - 2\,C_{13}^{2} \tag{17}$$

$$g' = C_{44}\left(C_{11} - C_{12}\right) - 2\,C_{14}^{2} \tag{18}$$

Appendix 8: Determination of elastic mean values for an isotropic polycrystal or an isotropic rock after Voigt-Reuss-Hill. The bulk *K*, shear *G* and Young's moduli *E* are modelled from the stiffness C_{ij} and compliance coefficients S_{ij} in Voigt notation. λ, ν, v_p and v_s correspond to a Lamé constant, the Poisson's ratio, the compressional and shear wave velocities, respectively.

$$K_V = \frac{\left(C_{11} + C_{22} + C_{33}\right) + 2\left(C_{12} + C_{23} + C_{13}\right)}{9} \tag{1}$$

$$G_V = \frac{\left(C_{11} + C_{22} + C_{33}\right) - \left(C_{12} + C_{23} + C_{13}\right) + 3\left(C_{44} + C_{55} + C_{66}\right)}{15} \tag{2}$$

$$K_R = \frac{1}{\left(S_{11} + S_{22} + S_{33}\right) + 2\left(S_{12} + S_{23} + S_{13}\right)} \tag{3}$$

$$G_R = \frac{15}{4\left(S_{11} + S_{22} + S_{33}\right) - 4\left(S_{12} + S_{23} + S_{13}\right) + 3\left(S_{44} + S_{55} + S_{66}\right)} \tag{4}$$

$$K_{VRH} = \frac{K_V + K_R}{2} \qquad \text{(5) from (1) \& (3)}$$

$$G_{VRH} = \frac{G_V + G_R}{2} \qquad \text{(6) from (2) \& (4)}$$

$$E_{VRH} = \frac{G_{VRH}\left(3\,M - 4\,G_{VRH}\right)}{M - G_{VRH}} = \frac{G_{VRH}\left(3\,\lambda_{VRH} + 2\,G_{VRH}\right)}{\lambda_{VRH} + G_{VRH}} =$$

$$\frac{\lambda_{VRH}\left(1 + \nu_{VRH}\right)\left(1 - 2\,\nu_{VRH}\right)}{\nu_{VRH}} = 3\,K_{VRH}\left(1 - 2\,\nu_{VRH}\right) = \frac{9\,K_{VRH}\,G_{VRH}}{3\,K_{VRH} + G_{VRH}} \tag{7}$$

$$K_{VRH} = \mathrm{M} - \frac{4}{3}\,G_{VRH} = \lambda_{VRH} + \frac{2}{3}\,G_{VRH} = \frac{\lambda_{VRH}\left(1 + \nu_{VRH}\right)}{3\,\nu_{VRH}} =$$

$$\frac{E_{VRH}}{3\left(1 - 2\,\nu_{VRH}\right)} = \frac{E_{VRH}\,G_{VRH}}{3\left(3\,G_{VRH} - E_{VRH}\right)} \tag{8}$$

$$M = \lambda_{VRH} + 2\,G_{VRH} = \frac{\lambda_{VRH}\left(1 - \nu_{VRH}\right)}{\nu_{VRH}} = \frac{3\,K_{VRH}\left(1 - \nu_{VRH}\right)}{1 + \nu_{VRH}} =$$

$$K_{VRH} + \frac{4}{3}\,G_{VRH} = \frac{E_{VRH}\left(1 - \nu_{VRH}\right)}{\left(1 + \nu_{VRH}\right)\left(1 - 2\,\nu_{VRH}\right)} = \frac{G_{VRH}\left(4\,G_{VRH} - E_{VRH}\right)}{3\,G_{VRH} - E_{VRH}} \tag{9}$$

$$\lambda_{VRH} = M - 2\,G_{VRH} = \frac{3\,K_{VRH}\,\nu_{VRH}}{1 + \nu_{VRH}} = K_{VRH} - \frac{2}{3}\,G_{VRH} =$$

$$\frac{E_{VRH}\,\nu_{VRH}}{(1+\nu_{VRH})\left(1-2\,\nu_{VRH}\right)}=\frac{G_{VRH}\left(E_{VRH}-2\,G_{VRH}\right)}{3\,G_{VRH}-E_{VRH}} \tag{10}$$

$$G_{VRH}=\frac{\lambda_{VRH}\left(1-2\,\nu_{VRH}\right)}{2\,\nu_{VRH}}=\frac{3\,K_{VRH}\left(1-2\,\nu_{VRH}\right)}{2\,(1+\nu_{VRH})}=\frac{E_{VRH}}{2\,(1+\nu_{VRH})} \tag{11}$$

$$\nu_{VRH}=\frac{M-2\,G_{VRH}}{2\left(M-G_{VRH}\right)}=\frac{\lambda_{VRH}}{2\,(\lambda_{VRH}+G_{VRH})}=\frac{3\,K_{VRH}-2\,G_{VRH}}{2\,(3\,K_{VRH}+G_{VRH})}=\frac{E_{VRH}}{2\,G_{VRH}}-1 \tag{12}$$

$$v_{p\,VRH}=\sqrt{\frac{\lambda_{VRH}+2\,G_{VRH}}{\rho}}=\sqrt{\frac{E_{VRH}\left(1-\nu_{VRH}\right)}{\rho\,(1+\nu_{VRH})\left(1-2\,\nu_{VRH}\right)}}=\sqrt{\frac{M}{\rho}} \tag{13}$$

$$v_{s\,VRH}=\sqrt{\frac{G_{VRH}}{\rho}}=\sqrt{\frac{E_{VRH}}{2\,\rho\,(1+\nu_{VRH})}} \tag{14}$$

$$\frac{v_{p\,VRH}}{v_{s\,VRH}}=\sqrt{2\,\frac{1-\nu_{VRH}}{1-2\,\nu_{VRH}}} \tag{15}$$

$$\nu_{VRH}=\frac{v_{p\,VRH}^2-2\,v_{s\,VRH}^2}{2\left(v_{p\,VRH}^2-v_{s\,VRH}^2\right)}=\frac{\left(\frac{v_{p\,VRH}}{v_{s\,VRH}}\right)^2}{2\left(\frac{v_{p\,VRH}^2}{v_{s\,VRH}}-1\right)} \tag{16}$$

Appendix 9: General determination of the experimental uncertainty Δx of a directly measured parameter x from its systematic and random errors Δx_s and Δx_r, respectively. For any indirectly determined parameter F the uncertainty ΔF is determined by a linear and a quadratic propagation of the errors of the directly determined parameters, when either systematic or random errors dominate. n is the number of repeated measurements and t corresponds to a confidential interval of 95 % (2 σ).

$$\Delta x=|\Delta x_s|+|\Delta x_r|=|\Delta x_s|+s_{\bar{x}} \tag{1}$$

$$|\Delta x_s|>s_{\bar{x}} \tag{2}$$

$$\Delta F=\left|\frac{\partial F}{\partial x}\,\Delta x\right|+\ldots \tag{3}$$

$$|\Delta x_s|<s_{\bar{x}} \tag{4}$$

$$\Delta F=\sqrt{\left(\frac{\partial F}{\partial x}\,\Delta x\right)^2+\ldots} \tag{5}$$

$$s_x=\sqrt{\frac{1}{n-1}\,\sum_{i=1}^{n}\left(x_i-\bar{x}\right)^2} \tag{6}$$

$$s_{\bar{x}}=\frac{t}{\sqrt{n}}\,s_x=\Delta\bar{x} \tag{7}$$

n	1	2	3	4	5	6	7	8	9
t	12.70	4.30	3.18	2.78	2.57	2.45	2.36	2.31	2.26
n	10	12	14	16	18	20	30	50	100
t	2.23	2.18	2.14	2.12	2.10	2.09	2.04	2.01	001.98

Appendix 10: Initial modelling parameters for a least squares approximation of various figures presented in the text (Chapter 1).

Fig.	**Eq.**	**Parameter**	**Orientation**	a_α **[var.]**	b_α **[var.]**	c_α **[var.]**	d_α **[var.]**	T_α **[°C]**	a_β **[var.]**	b_β **[-]**	T_β **[°C]**	X_0 **[var.]**	**Reference**
7	32 (α), 37 (β)	E [GPa]	II *c*-axis	139	$4.0\cdot10^{-5}$	$5.0\cdot10^{-2}$	85	578	11	0.50		98	Perrier & De Mandrot 1923
			$\perp$ *c*-axis	443	$2.0\cdot10^{-5}$	$2.0\cdot10^{-2}$	75	583	49	0.20		135	
			90°/50°	460		$2.0\cdot10^{-2}$	69	59	62	0.10		145	
			270°/50°	1270	$7.0\cdot10^{-5}$	$9.0\cdot10^{-2}$	102	594	62	0.10		145	
8	32 (α), 37 (β)	v_p [km/s]	II *c*-axis	52		$5.0\cdot10^{-4}$	6	649	3	0.41	570	7	Lakshtanov *et al.* 2007
			II *a*-axis (0°/90°)	0017			6	995	4	0.13	572	9	
			$\perp$ *c*-axis (90°/90°)	23		$2.0\cdot10^{-4}$	6	605	5	0.48	569	8	
	32 (α), 33 (β)	v_{sv} [GPa]	II *c*-axis	0014		$9.0\cdot10^{-4}$	4	598	6	0.20	195	5	
			II *a*-axis	3		$2.0\cdot10^{-4}$	5	579	1	0.01	573	5	
	33 (α), 37 (β)		$\perp$ *c*-axis				4		2	0.02	573	6	
	32 (α), 37 (β)	v_{sh} [GPa]	II *a*-axis	6			3	711					
	33 (α), 37 (β)		$\perp$ *c*-axis				4						
9		E_{dyn} [GPa]	$\perp$ *c*-axis	661	$1.0\cdot10^{-6}$		80	594	53	0.40	573	120	Lakshtanov *et al.* 2007
		E_{sta} [GPa]	$\perp$ *c*-axis	0554	$4.0\cdot10^{-6}$	$6.0\cdot10^{-3}$	78	585	60	0.20	573	138	Perrier & De Mandrot 1923
10	32 (α), 33 (β)	u [%]	$\perp$ *c*-axis	55.5	$2.7\cdot10^{-7}$	$-1.8\cdot10^{-3}$	0.93	653	$2.1\cdot10^{-4}$	1.63			Raz *et al.* 2002
			II *c*-axis	0021.4	$3.1\cdot10^{-7}$	$-1.4\cdot10^{-3}$	0.70	656	$4.5\cdot10^{-4}$	0.73			

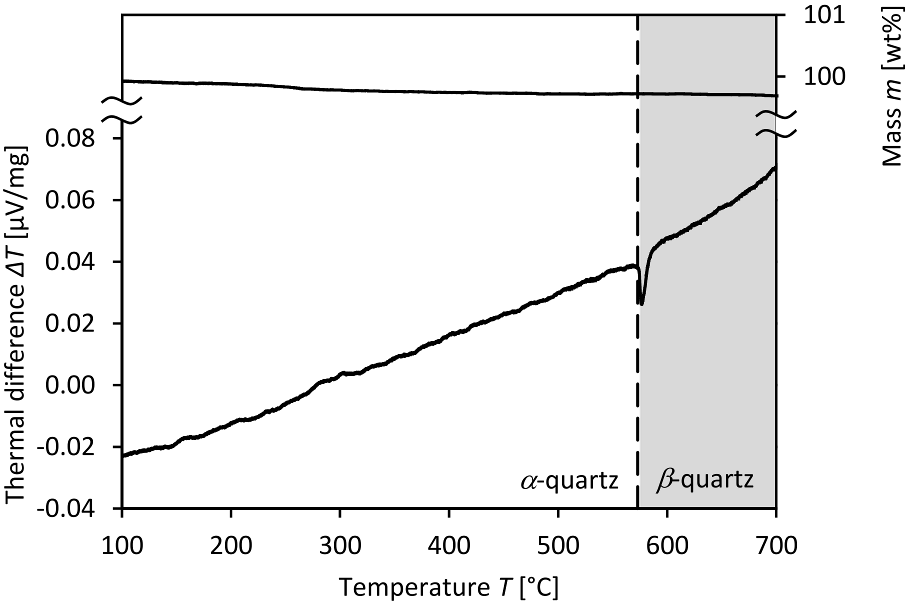

Appendix 11: Thermal and gravimetric differences of synthetic quartz across the α-β transition (3 K/min heating rate, with baseline correction, ± 1 K temperature uncertainty, ±2 µg uncertainty of the mass).

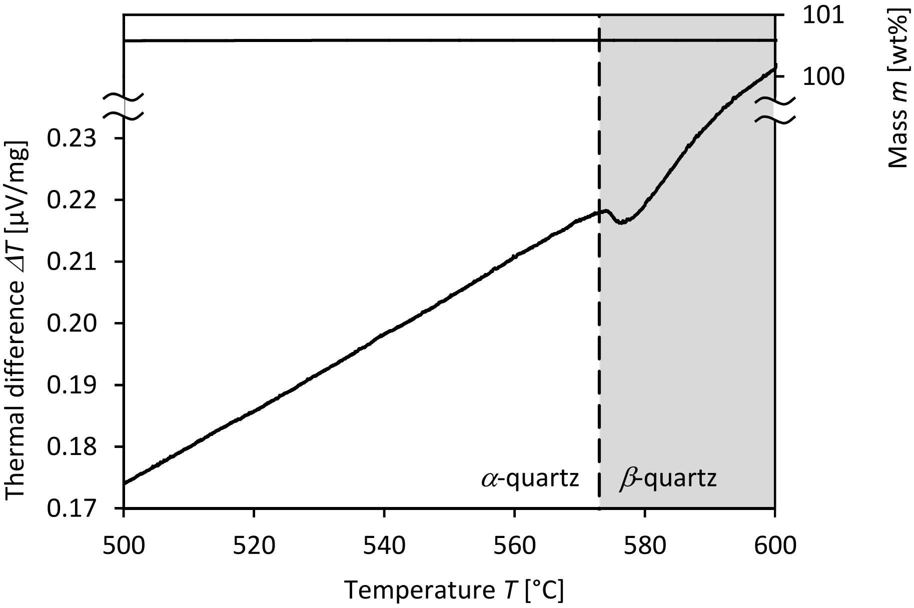

Appendix 12: Thermal and gravimetric differences of Dalsland quartzite across the α-β transition (3 K/min heating rate, without baseline correction, ± 1 K temperature uncertainty, ±2 µg uncertainty of the mass).

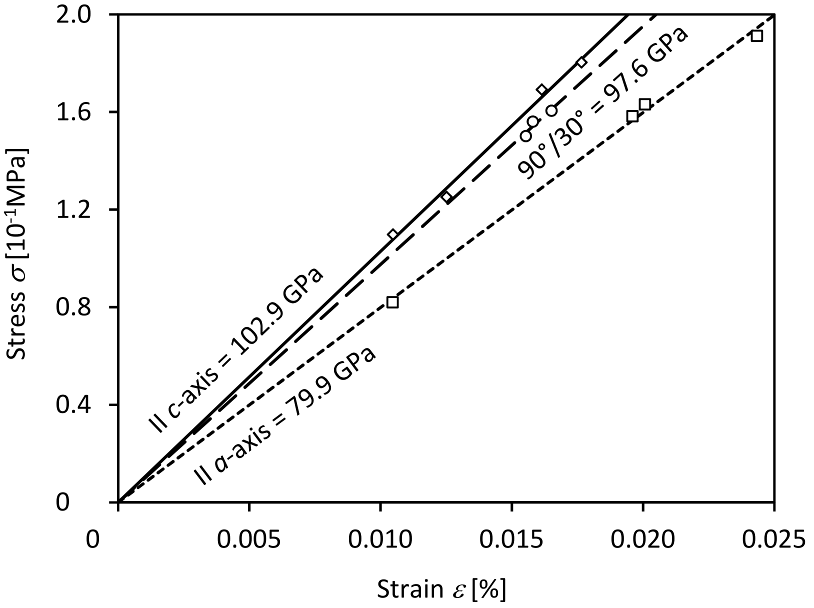

Appendix 13: Linear correlation of the elastic stress and strain. Averaged data from three-point bending at ≈ 53 °C and 40 mm support spacing is presented.

Appendix 14: Dimensions of a stair-shaped aluminium specimen (± 0.005 mm nonius error).

Measure-ment	**Step 1 [mm]**	**Step 2 [mm]**	**Step 3 [mm]**	**Step 4 [mm]**	**Step 5 [mm]**	**Step 6 [mm]**
1	30.000	25.050	20.060	15.075	10.055	5.055
2	30.010	25.045	20.060	15.070	10.065	5.040
3	30.000	25.045	20.055	15.065	10.070	5.030
4	30.010	25.045	20.050	15.075	10.055	5.050
5	30.010	25.050	20.060	15.070	10.065	5.045
6	30.000					
Mean	30.005	25.047	20.057	15.071	10.062	5.044
$\pm 2\overline{\sigma}$	± 0.006	± 0.004	± 0.006	± 0.005	± 0.008	± 0.012

Appendix 15: Travel times of the compressional wave in the aluminium specimen (Appendix 14) under ambient conditions from impulse-echo experiments with a *Panametrics V125* transducer.

Measure-ment	***t* [μs] Step 1**	***t* [μs] Step 2**	***t* [μs] Step 3**	***t* [μs] Step 4**	***t* [μs] Step 5**	***t* [μs] Step 6**
1	9.70	8.14	6.55	4.98	3.42	1.89
2	9.69	8.14	6.56	4.99	3.44	1.87
3	9.71	8.14	6.56	4.98	3.41	1.88
4	9.69	8.13	6.55	4.99	3.42	1.88
5	9.69	8.12	6.56	4.99	3.42	1.87
Mean	9.696	8.134	6.556	4.986	3.422	1.880
$\pm 2\overline{\sigma}$	± 0.011	± 0.011	± 0.007	± 0.007	± 0.013	± 0.010

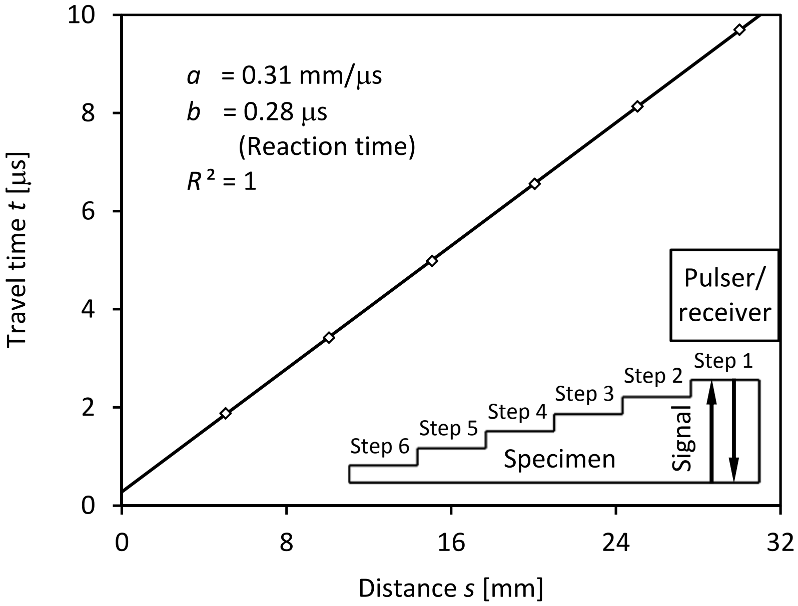

Appendix 16: Determination of the reaction time of the ultrasonic testing system (*V125*) by a linear correlation of the distance and the travel time of the wave (Appendix 14 & Appendix 15).

Appendix 17: Travel times of compressional and shear waves in the aluminium specimen (Appendix 14) under ambient conditions from impulse-echo experiments with various transducers.

Sensor	***t* [µs] Step 1**	***t* [µs] Step 2**	***t* [µs] Step 3**	***t* [µs] Step 4**	***t* [µs] Step 5**	***t* [µs] Step 6**
V102	9.54	7.98	6.42	4.86	3.29	1.71
V152	4.83	4.05	3.26	2.48	1.69	0.90
V153	5.12	4.33	3.55	2.79	1.98	1.17
V154	5.01	4.22	3.44	2.65	1.86	1.07

Appendix 18: Dimensions of a cube-shaped specimen from single-crystal synthetic quartz (± 0.01 mm uncertainty of the calliper gauge).

Measurement	**Direction 1 [mm]**	**Direction 2 [mm]**	**Direction 3 [mm]**
1	20.69	22.09	20.79
2	20.72	22.07	20.77
3	20.62	22.06	20.60
4	20.67	22.07	20.73
5			20.68
Mean ± $2\overline{\sigma}$	20.68 ± 0.06	22.073 ± 0.018	20.71 ± 0.09

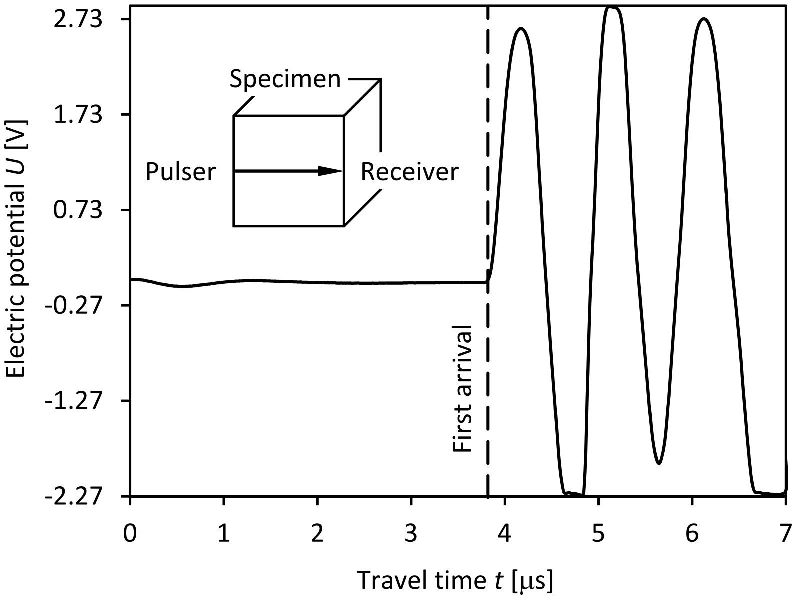

Appendix 19: Electric potential as a function of travel time of the compressional wave parallel to the *a*-axis of a synthetic quartz single crystal under ambient conditions.

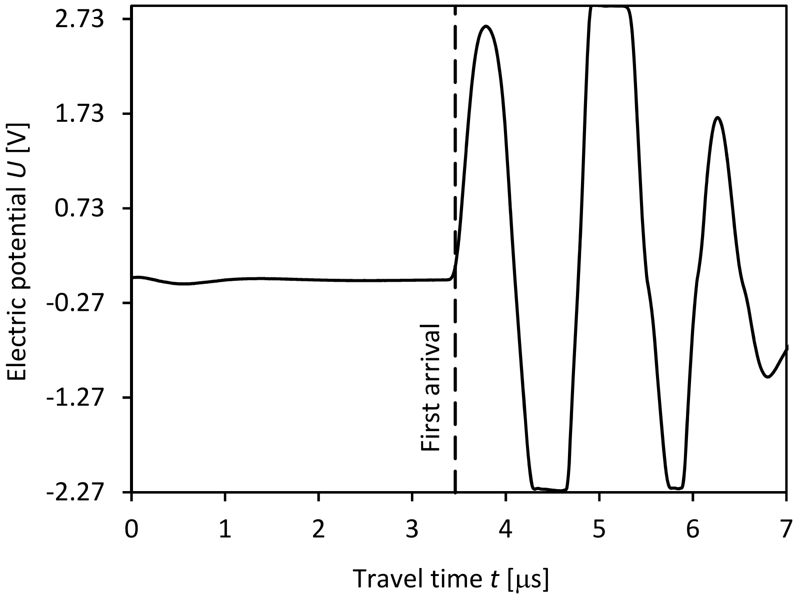

Appendix 20: Electric potential as a function of travel time of the compressional wave parallel to the *Y*-axis of a synthetic quartz single crystal under ambient conditions.

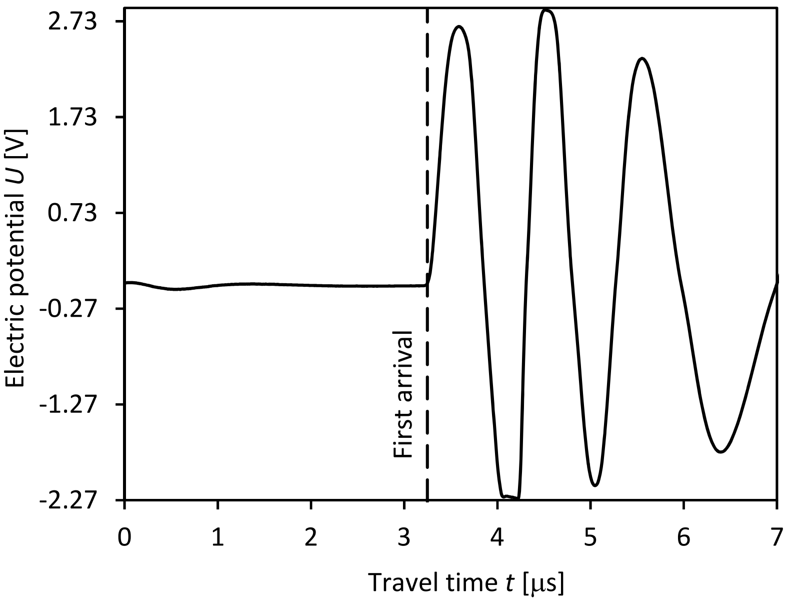

Appendix 21: Electric potential as a function of travel time of the compressional wave parallel to the *c*-axis of a synthetic quartz single crystal under ambient conditions.

Appendix 22: Dimensions of the cylindrical specimens of Lahr sandstone with random errors due to irregularities from specimen preparation. Moreover, systematic errors are: ± 0.01 mm for the used calliper gauge error, ± 0.1 g for the used scales.

Specimen name	l_1 **[mm]**	l_2 **[mm]**	l_3 **[mm]**	l_4 **[mm]**	$\bar{l} \pm s_{\bar{l}}$ § **[mm]**	d_1 **[mm]**	d_2 **[mm]**	d_3 **[mm]**	d_4 **[mm]**	$\bar{d} \pm s_{\bar{d}}$ § **[mm]**	m_1 **[g]**	m_2 **[g]**	m_3 **[g]**	m_4 **[g]**
MKC-021	100.93	100.98	100.83	100.83	100.89 ± 0.11	50.06	50.07	50.09	50.06	50.070 ± 0.020	439.8	439.5	439.4	439.5
MKC-022	101.96	101.95	101.98	101.95	101.96 ± 0.02	50.12	50.11	50.09	50.09	50.103 ± 0.021	444.1	443.7	443.7	443.7
MKC-023	102.38	102.48	102.43	102.49	102.45 ± 0.08	50.08	50.08	50.08	50.09	50.083 ± 0.007	445.6	445.1	445.0	445.1
MKC-024	103.18	103.21	103.21	103.13	103.18 ± 0.06	50.10	50.08	50.08	50.07	50.083 ± 0.018	448.9	448.1	448.0	448.0
MKC-025	99.56	99.54	99.80	99.67	99.64 ± 0.17	50.08	50.07	50.07	50.10	50.080 ± 0.020	431.5	430.5	430.4	430.3
MKC-026	103.73	103.89	103.88	103.80	103.83 ± 0.11	50.07	50.10	50.07	50.08	50.080	453.5	452.5	452.4	452.5
MKC-027	103.59	103.59	103.49	103.48	103.54 ± 0.09	50.09	50.09	50.11	50.09	50.095 ± 0.014	452.6	451.2	451.1	451.1
MKC-028	101.25	101.14	101.23	101.30	101.23 ± 0.10	50.07	50.11	50.05	50.08	50.08 ± 0.04	443.4	441.6	440.6	440.7
MKC-029	101.28	101.18	101.21	101.21	101.22 ± 0.06	50.06	50.06	50.07	50.08	50.068 ± 0.014	445.4	441.7	441.6	441.6
MKC-030	102.47	102.59	102.51	102.57	102.54 ± 0.08	50.06	50.06	50.06	50.07	50.063 ± 0.007	446.9	444.5	444.4	444.4
MKC-031	100.53	100.48	100.58	100.52	100.53 ± 0.06	50.11	50.13	50.12	50.06	50.11 ± 0.05	452.7			439.3
MKC-032	101.09	101.24	101.31	101.10	101.19 ± 0.15	50.08	50.18	50.11	50.07	50.11 ± 0.07				440.0
MKC-033	101.28	101.30	101.27	101.27	101.28 ± 0.02	50.08	50.07	50.08	50.08	50.078 ± 0.007	453.0			440.2
MKC-038	100.09	100.13	100.13	100.12	100.118 ± 0.027	50.16	50.15	50.19	50.17	50.168 ± 0.024				434.5

§ The standard deviation *s* of the mean values $\bar{l}$ and $\bar{d}$ is presented for a confidence level of 95 % (2σ). For the total error of both parameters the systematic error of the calliper gauge has to be added (Tab. 8).

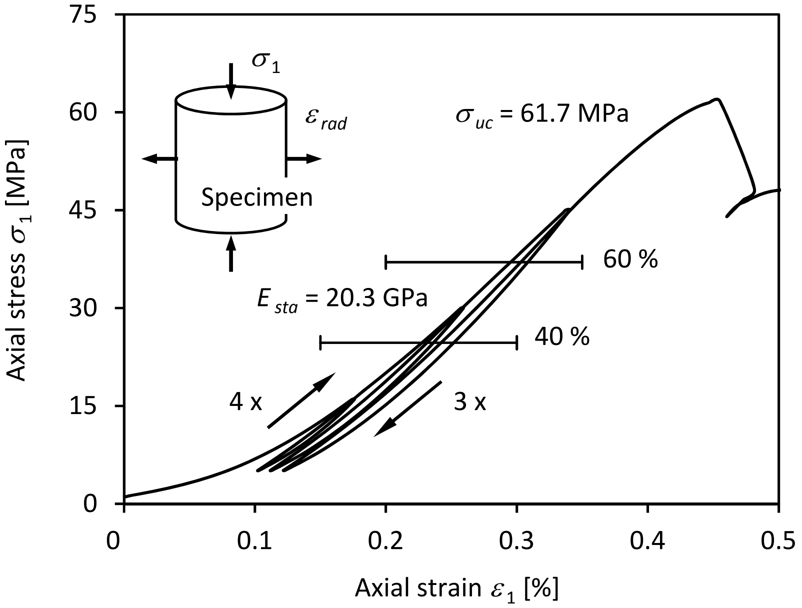

Appendix 23: Loading curve from the uniaxial compression test of the specimen MKC-022 (0.05 mm/min axial shortening, 120 s equilibration time, ambient temperature). See chapter 2 for the definition of further variables.

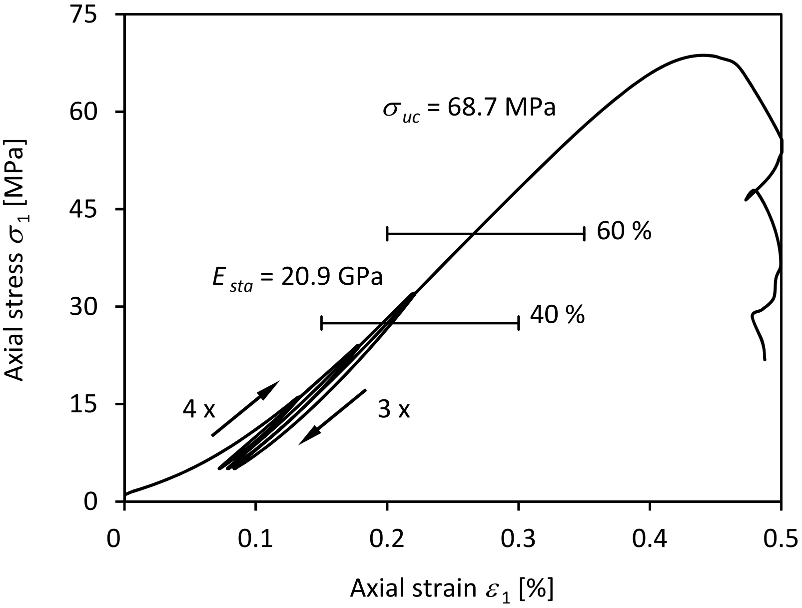

Appendix 24: Loading curve from the uniaxial compression test of the specimen MKC-025 (0.05 mm/min axial shortening, 120 s equilibration time, ambient temperature). See chapter 2 for the definition of further variables.

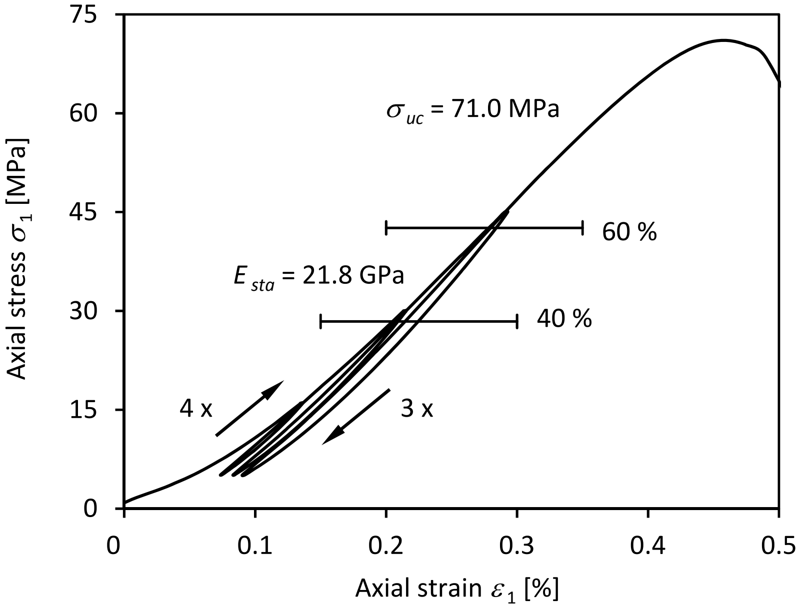

Appendix 25: Loading curve from the uniaxial compression test of the specimen MKC-026 (0.05 mm/min axial shortening, 120 s equilibration time, ambient temperature). See chapter 2 for the definition of further variables.

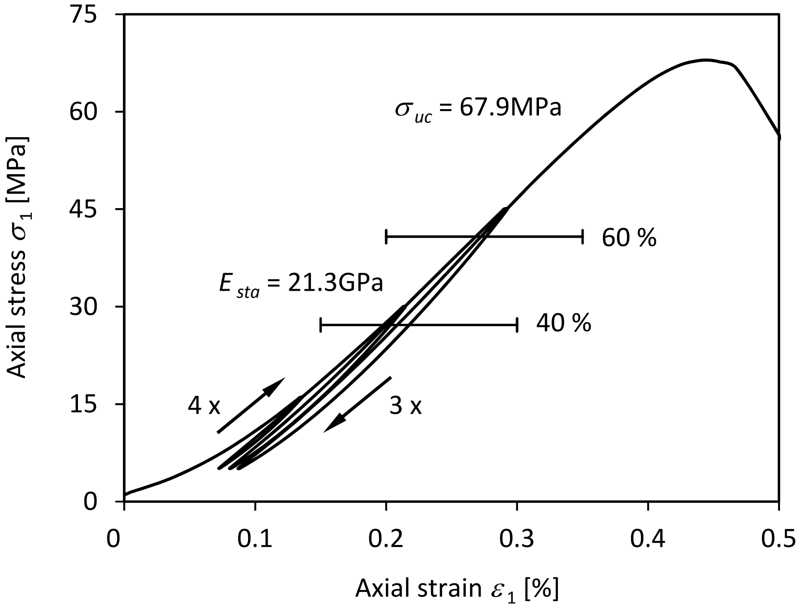

Appendix 26: Loading curve from the uniaxial compression test of the specimen MKC-027 (0.05 mm/min axial shortening, 120 s equilibration time, ambient temperature). See chapter 2 for the definition of further variables.

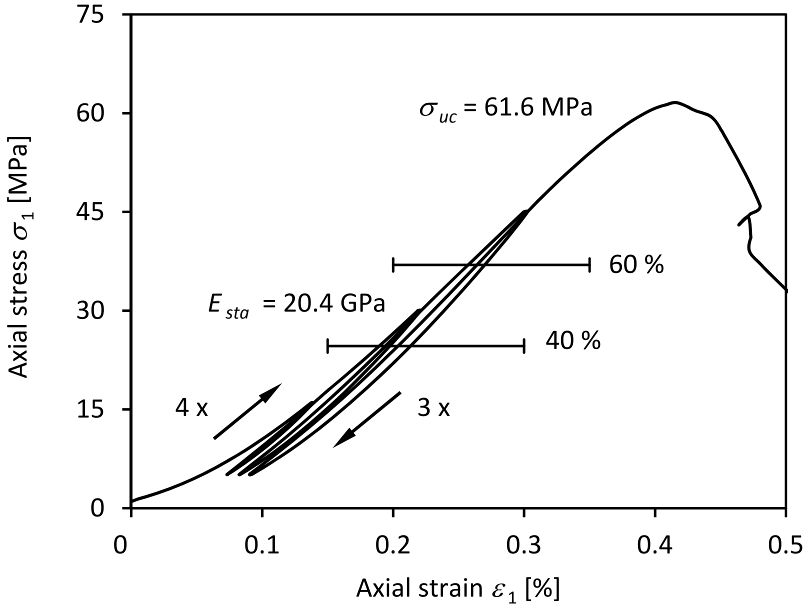

Appendix 27: Loading curve from the uniaxial compression test of the specimen MKC-028 (0.05 mm/min axial shortening, 120 s equilibration time, ambient temperature). See chapter 2 for the definition of further variables.

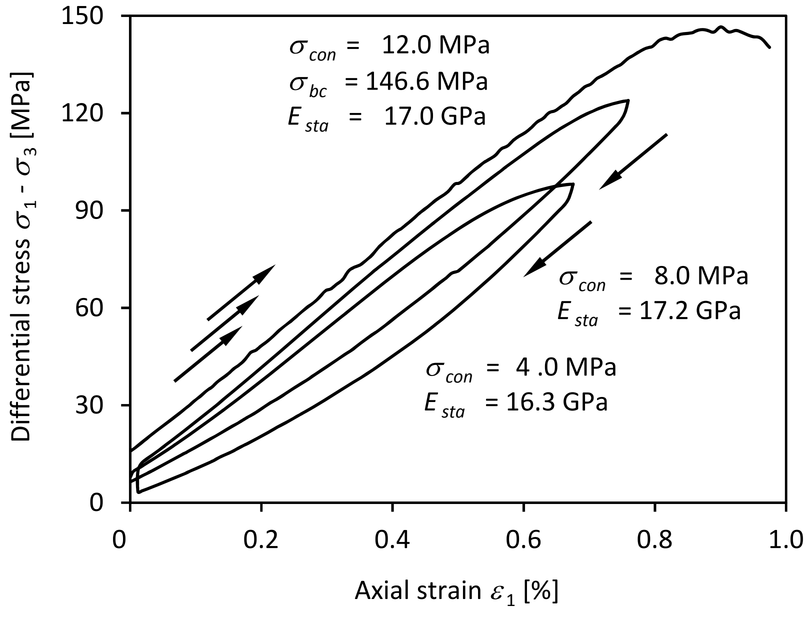

Appendix 28: Loading curve from the triaxial compression test of the specimen MKC-024 until failure (0.05 mm/min axial shortening, 120 s equilibration time, ambient temperature). σ_{con} and σ_{bc} correspond to the confining pressure and the maximum axial stress, respectively. See chapter 2 for the definition of further variables.

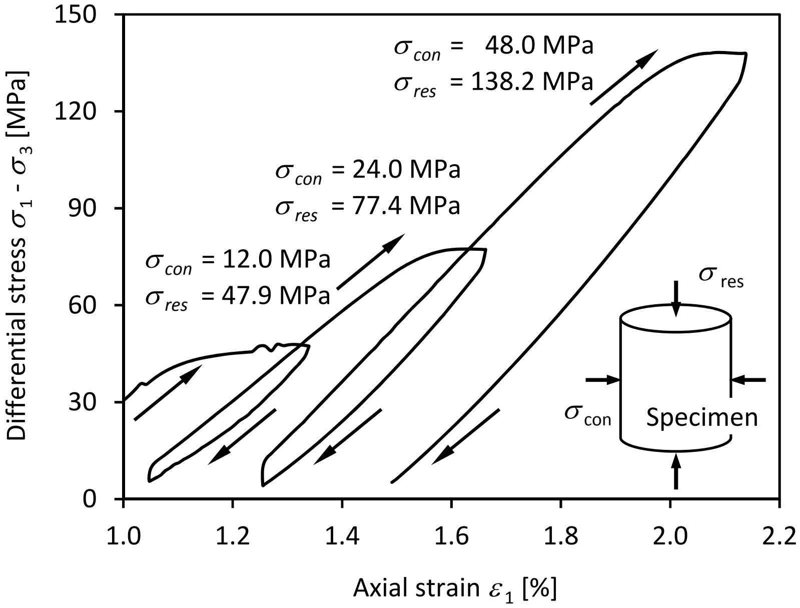

Appendix 29: Post-failure loading curve from the triaxial compression test of the specimen MKC-024 (0.05 mm/min axial shortening, 120 s equilibration time, ambient temperature).

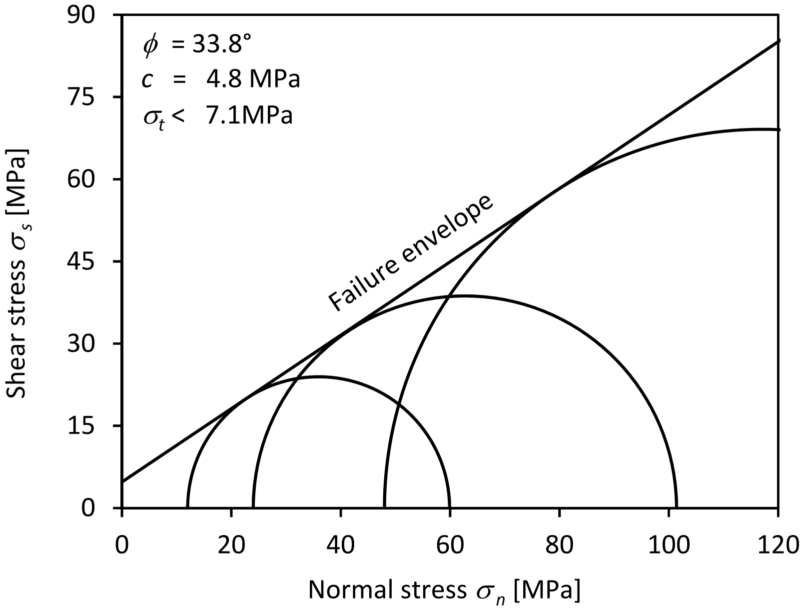

Appendix 30: Mohr-Coulomb criterion of the specimen MKC-024 from its post-failure triaxial compression (Appendix 28). See chapter 2 for the definition of further variables.

Appendix 31: Derivations of the tested mechanical models.

a) Kelvin-Voigt model:

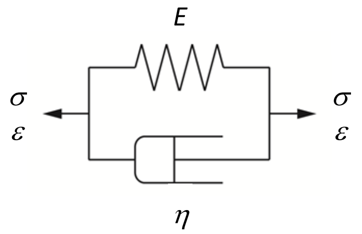

$$\sigma = \sigma_1 + \sigma_2 \tag*{(1)}$$

$$\varepsilon = \varepsilon_1 = \varepsilon_2 \tag*{(2)}$$

$$\sigma_1 = E\,\varepsilon \tag*{(3)}$$

$$\sigma_2 = \eta\,\dot{\varepsilon} \tag*{(4)}$$

$$\sigma = E\,\varepsilon + \eta\,\dot{\varepsilon} \tag*{(5) by (3) \& (4) in (1)}$$

$$\varepsilon(t) = \varepsilon_0 \cos(\omega t) \tag*{(6)}$$

$$\overline{\varepsilon} = \varepsilon_0\, e^{i\omega t} \tag*{(7)}$$

$$\dot{\varepsilon} = \varepsilon_0\, i\,\omega\, e^{i\omega t} \tag*{(8)}$$

$$\sigma(t) = \sigma_0 \cos(\omega t - \delta) \tag*{(9)}$$

$$\overline{\sigma}(t) = \sigma_0\, e^{i\delta} e^{i\omega t} \tag*{(10)}$$

$$\sigma_0\, e^{i\delta} = E\,\varepsilon_0 + \eta\,\varepsilon_0\, i\,\omega = \varepsilon_0\,(E + \eta\, i\,\omega) \tag*{(11) by (7), (8) \& (10) in (5)}$$

$$\tau = \frac{\eta}{E} \tag*{(12)}$$

$$\sigma_0\, e^{i\delta} = \varepsilon_0 \left(\frac{\eta}{\tau} + i\,\omega\,\tau E\right) \tag*{(13) by (12) in (11)}$$

$$E = \frac{\sigma}{\varepsilon} \tag*{(14)}$$

$$E^* = E' + i\,E'' \tag*{(15)}$$

$$E^* = \frac{\sigma_0\, e^{i\delta}}{\varepsilon_0} = \frac{\eta}{\tau} + i\,\omega\,\tau E \tag*{(16) by (12) in (14) \& (15)}$$

$$E'(\omega) = \frac{\eta}{\tau} \tag*{(17) from (16)}$$

$$E''(\omega) = \omega\,\tau E \tag*{(18 from (16)}$$

b) Maxwell model:

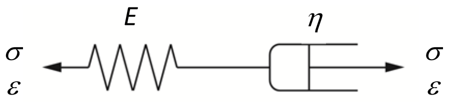

$$\sigma = \sigma_1 = \sigma_2 \tag{1}$$

$$\dot{\sigma} = \dot{\sigma}_1 = \dot{\sigma}_2 \tag{2}$$

$$\varepsilon = \varepsilon_1 + \varepsilon_2 \tag{3}$$

$$\dot{\varepsilon} = \dot{\varepsilon}_1 + \dot{\varepsilon}_2 \tag{4}$$

$$\varepsilon_1 = \frac{\sigma}{E} \tag{5}$$

$$\dot{\varepsilon}_1 = \frac{\dot{\sigma}}{E} \tag{6}$$

$$\dot{\varepsilon}_2 = \frac{\sigma}{\eta} \tag{7}$$

$$\dot{\varepsilon} = \frac{\sigma}{E} + \frac{\sigma}{\eta} \qquad \text{(8) by (6) \& (7) in (4)}$$

$$\dot{\sigma} + \frac{E}{\eta}\,\sigma = E\,\dot{\varepsilon} \qquad \text{(9) equivalent to (8)}$$

$$\varepsilon(t) = \varepsilon_0\ \cos(\omega t) \tag{10}$$

$$\overline{\varepsilon} = \varepsilon_0\, e^{i\,\omega t} \tag{11}$$

$$\dot{\varepsilon} = \varepsilon_0\, i\,\omega\, e^{i\,\omega t} \tag{12}$$

$$\sigma(t) = \sigma_0\ \cos(\omega t - \delta) \tag{13}$$

$$\overline{\sigma}(t) = \sigma_0\, e^{i\,\delta}\, e^{i\,\omega t} \tag{14}$$

$$\dot{\sigma} = \sigma_0\, i\,\omega\, e^{i\,\delta} e^{i\,\omega t} \tag{15}$$

$$\sigma_0\, i\,\omega\, e^{i\,\delta} + \frac{E}{\eta}\,\sigma_0\, e^{i\,\delta} = E\,\varepsilon_0\, i\,\omega \qquad \text{(16) by (12), (14) \& (15) in (9)}$$

$$\sigma_0\, e^{i\,\delta} = \varepsilon_0\ \frac{E\,i\,\omega}{\frac{E}{\eta} + i\,\omega} \qquad \text{(17) equivalent to (16)}$$

$$\sigma_0\, e^{i\,\delta} = \varepsilon_0\ \frac{E\,\omega^2 + i\,\omega \frac{E^2}{\eta}}{\frac{E^2}{\eta^2} + \omega^2} \qquad \text{(18) by (17), times } \frac{\frac{E}{\eta} - i\,\omega}{\frac{E}{\eta} - i\,\omega}$$

$$\tau = \frac{\eta}{E} \tag{19}$$

$$\sigma_0\, e^{i\,\delta} = \varepsilon_0 \frac{\frac{E}{\tau}\,\omega^2 + i\,\omega \frac{E}{\tau}}{\frac{1}{\tau^2} + \omega^2} \qquad \text{(20) by (19) in (18), times } \frac{\tau^2}{\tau^2}$$

$$\sigma_0\, e^{i\,\delta} = \varepsilon_0\, \frac{\tau\,\eta\,\omega^2 + i\,\eta\,\omega}{1 + (\omega\,\tau)^2} \qquad (21)$$

$$E = \frac{\sigma}{\varepsilon} \qquad (22)$$

$$E^* = E' + i\,E'' \qquad (23)$$

$$E^* = \frac{\sigma_0\, e^{i\,\delta}}{\varepsilon_0} = \frac{\tau\,\eta\,\omega^2 + i\,\eta\,\omega}{1 + (\omega\,\tau)^2} \qquad \text{(24) by (21) in (22) \& (23)}$$

$$E'(\omega) = \frac{\tau\,\eta\,\omega^2}{1 + (\omega\,\tau)^2} \qquad \text{(25) from (24)}$$

$$E''(\omega) = \frac{\eta\,\omega}{1 + (\omega\,\tau)^2} \qquad \text{(26) from (24)}$$

c) Poynting-Thomson model:

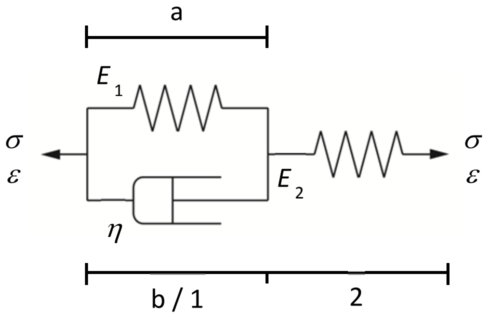

$$\sigma_1 = \sigma_a + \sigma_b \qquad (1)$$

$$\dot{\sigma}_1 = \dot{\sigma}_a + \dot{\sigma}_b \qquad (2)$$

$$\sigma = \sigma_1 = \sigma_2 \qquad (3)$$

$$\dot{\sigma} = \dot{\sigma}_1 = \dot{\sigma}_2 \qquad (4)$$

$$\varepsilon = \varepsilon_1 + \varepsilon_2 \qquad (5)$$

$$\dot{\varepsilon} = \dot{\varepsilon}_1 + \dot{\varepsilon}_2 \qquad (6)$$

$$\varepsilon_1 = \varepsilon_a = \varepsilon_b \qquad (7)$$

$$\dot{\varepsilon}_1 = \dot{\varepsilon}_a = \dot{\varepsilon}_b \qquad (8)$$

$$\sigma_b = \eta\,\dot{\varepsilon}_1 \qquad (9)$$

$$\varepsilon_1 = \frac{\sigma_a}{E_1} \qquad (10)$$

$$\varepsilon_2 = \frac{\sigma}{E_2} \qquad \text{(11)}$$

$$\sigma = E_2\, \varepsilon_2 = E_2\, \varepsilon - E_2\, \varepsilon_1 \qquad \text{(12) by (9) \& (10) in (1)}$$

$$\dot{\sigma} = E_2\, \dot{\varepsilon} - E_2\, \dot{\varepsilon}_1 \qquad \text{(13)}$$

$$\dot{\varepsilon}_1 = \frac{1}{\eta}\, \sigma - \frac{E_1}{\eta}\, \varepsilon - \frac{\frac{E_1}{E_2}}{\eta}\, \sigma \qquad \text{(14) by (9), (10) \& (11) in (6)}$$

$$\dot{\sigma} + \frac{E_1 + E_2}{\eta}\, \sigma = E_2\, \dot{\varepsilon} + \frac{E_1 E_2}{\eta}\, \varepsilon \qquad \text{(15) by (14) in (13)}$$

$$\varepsilon(t) = \varepsilon_0\, \cos(\omega t) \qquad \text{(16)}$$

$$\overline{\varepsilon} = \varepsilon_0\, e^{i\omega t} \qquad \text{(17)}$$

$$\dot{\varepsilon} = \varepsilon_0\, i\, \omega\, e^{i\omega t} \qquad \text{(18)}$$

$$\sigma(t) = \sigma_0\, \cos(\omega t - \delta) \qquad \text{(19)}$$

$$\overline{\sigma}(t) = \sigma_0\, e^{i\delta}\, e^{i\omega t} \qquad \text{(20)}$$

$$\dot{\sigma} = \sigma_0\, i\, \omega\, e^{i\delta} e^{i\omega t} \qquad \text{(21)}$$

$$\sigma_0\, i\, \omega\, e^{i\delta} + \frac{E_1 + E_2}{\eta}\, \sigma_0\, e^{i\delta} = E_2\, \varepsilon_0\, i\, \omega + \frac{E_1 E_2}{\eta}\, \varepsilon_0 \qquad \text{(22)}$$

$$\sigma_0\, e^{i\delta} = \varepsilon_0\, \frac{\frac{E_1 E_2}{\eta} + i\, \omega\, E_2}{\frac{E_1 + E_2}{\eta} + i\, \omega} \qquad \text{(23)}$$

$$\sigma_0\, e^{i\delta} = \varepsilon_0\, \frac{\frac{E_1 E_2 (E_1 + E_2)}{\eta^2} + \omega^2 E_2 + i\, \omega \left(\frac{E_2 (E_1 + E_2)}{\eta} - \frac{E_1 E_2}{\eta} \right)}{\left(\frac{E_1 + E_2}{\eta} \right)^2 + \omega^2} \qquad \text{(23) times } \frac{\frac{E_1 + E_2}{\eta} - i\, \omega}{\frac{E_1 + E_2}{\eta} - i\, \omega}$$

$$\tau = \frac{\eta}{E_1 + E_2} \qquad \text{(25)}$$

$$\sigma_0\, e^{i\delta} = \varepsilon_0\, \frac{\frac{E_1 E_2}{\eta\, \tau} + \omega^2 E_2 + i\, \omega \left(\frac{E_2}{\tau} - \frac{E_1 E_2}{\eta} \right)}{\frac{1}{\tau^2} + \omega^2} \qquad \text{(25 in (24), times } \frac{\tau^2}{\tau^2}$$

$$E = \frac{\sigma}{\varepsilon} \qquad \text{(27)}$$

$$E^* = E' + i\, E'' \qquad \text{(28)}$$

$$E^* = \frac{\sigma_0\, e^{i\delta}}{\varepsilon_0} = \frac{\frac{E_1 E_2}{E_1 + E_2} + E_2 (\omega \tau)^2 + i\, \omega \left(E_2\, \tau - \frac{E_1 E_2\, \tau}{E_1 + E_2} \right)}{1 + (\omega \tau)^2} \qquad \text{(29)}$$

$$E'(\omega) = \frac{\frac{E_1 E_2}{E_1 + E_2} + E_2 (\omega \tau)^2}{1 + (\omega \tau)^2} \qquad \text{(30 from (29)}$$

$$E''(\omega) = \frac{\omega\left(E_2\,\tau - \frac{E_1 E_2\,\tau}{E_1 + E_2}\right)}{1 + (\omega\,\tau)^2} \qquad \text{(31) from (29)}$$

d) Zener model:

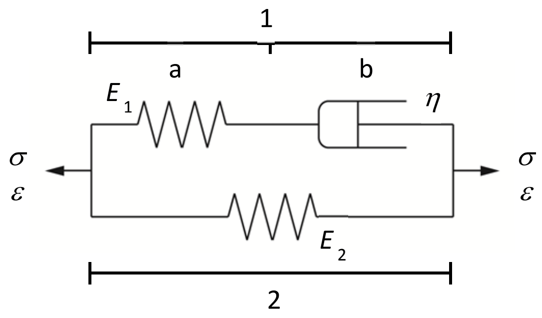

$$\sigma = \sigma_1 + \sigma_2 \qquad (1)$$

$$\dot{\sigma} = \dot{\sigma}_1 + \dot{\sigma}_2 \qquad (2)$$

$$\sigma_1 = \sigma_a = \sigma_b \qquad (3)$$

$$\dot{\sigma}_1 = \dot{\sigma}_a = \dot{\sigma}_b \qquad (4)$$

$$\varepsilon = \varepsilon_1 = \varepsilon_2 \qquad (5)$$

$$\dot{\varepsilon} = \dot{\varepsilon}_1 = \dot{\varepsilon}_2 \qquad (6)$$

$$\varepsilon_1 = \varepsilon_a + \varepsilon_b \qquad (7)$$

$$\dot{\varepsilon}_1 = \dot{\varepsilon}_a + \dot{\varepsilon}_b \qquad (8)$$

$$\varepsilon_a = \frac{\sigma_1}{E_1} \qquad (9)$$

$$\dot{\varepsilon}_b = \frac{\sigma_1}{\eta} \qquad (10)$$

$$\varepsilon = \frac{\sigma_2}{E_2} \qquad (11)$$

$$\sigma = E_2\,\varepsilon + E_1\left(\varepsilon - \varepsilon_b\right) = (E_1 + E_2)\,\varepsilon - E_1\,\varepsilon_b \qquad \text{(12) by (7), (9) \& (1)1 in (1)}$$

$$\dot{\sigma} = (E_1 + E_2)\,\dot{\varepsilon} - E_1\,\dot{\varepsilon}_b \qquad (13)$$

$$\dot{\varepsilon}_b = \frac{1}{\eta}\left(\sigma - \sigma_2\right) = \frac{1}{\eta}\,(\sigma - E_2\,\varepsilon) \qquad \text{(14) by (1) \& (10) in (8)}$$

$$\dot{\sigma} + \frac{E_1}{\eta}\,\sigma = (E_1 + E_2)\,\dot{\varepsilon} + \frac{E_1 E_2}{\eta}\,\varepsilon \qquad \text{(15) by (14) in (13)}$$

$$\varepsilon(t) = \varepsilon_0\,\cos(\omega\,t) \qquad (16)$$

$$\overline{\varepsilon} = \varepsilon_0 \, e^{i\omega t} \qquad (17)$$

$$\dot{\varepsilon} = \varepsilon_0 \, i \, \omega \, e^{i\omega t} \qquad (18)$$

$$\sigma(t) = \sigma_0 \, \cos(\omega t - \delta) \qquad (19)$$

$$\overline{\sigma}(t) = \sigma_0 \, e^{i\delta} e^{i\omega t} \qquad (20)$$

$$\dot{\sigma} = \sigma_0 \, i \, \omega \, e^{i\delta} e^{i\omega t} \qquad (21)$$

$$\sigma_0 \, i \, \omega \, e^{i\delta} + \frac{E_1}{\eta} \, \sigma_0 \, e^{i\delta} = (E_1 + E_2) \, \varepsilon_0 \, i \, \omega + \frac{E_1 E_2}{\eta} \, \varepsilon_0 \qquad \text{(17), (18), (20) \& (21) in (15)}$$

$$\sigma_0 \, e^{i\delta} = \varepsilon_0 \, \frac{\frac{E_1 E_2}{\eta} + i\,\omega\,(E_1 + E_2)}{\frac{E_1}{\eta} + i\,\omega} \qquad (23)$$

$$\sigma_0 \, e^{i\delta} = \varepsilon_0 \, \frac{\frac{E_1^2 E_2}{\eta^2} + \omega^2 \, (E_1 + E_2) + i\,\omega\left((E_1 + E_2)\,\frac{E_1}{\eta} - \frac{E_1 E_2}{\eta}\right)}{\left(\frac{E_1}{\eta}\right)^2 + \omega^2} \qquad \text{(23) times } \frac{\frac{E_1}{\eta} - i\,\omega}{\frac{E_1}{\eta} - i\,\omega}$$

$$\tau = \frac{\eta}{E_1} \qquad (25)$$

$$\sigma_0 \, e^{i\delta} = \varepsilon_0 \, \frac{\frac{E_2}{\tau^2} + \omega^2 \, (E_1 + E_2) + i\,\omega\,\frac{E_1}{\tau}}{\frac{1}{\tau^2} + \omega^2} \qquad \text{(25) in (24), times } \frac{\tau^2}{\tau^2}$$

$$E = \frac{\sigma}{\varepsilon} \qquad (27)$$

$$E^* = E' + i\,E'' \qquad (28)$$

$$E^* = \frac{\sigma_0 \, e^{i\delta}}{\varepsilon_0} = \frac{E_2 + (E_1 + E_2)\,(\omega\tau)^2 + i\,\omega\,\tau E_1}{1 + (\omega\tau)^2} \qquad \text{(29) by (26) in (27) \& (28)}$$

$$E'(\omega) = \frac{E_2 + (E_1 + E_2)\,(\omega\tau)^2}{1 + (\omega\tau)^2} \qquad \text{(30) from (29)}$$

$$E''(\omega) = \frac{E_1 \, \omega \, \tau}{1 + (\omega\tau)^2} \qquad \text{(31) from (29)}$$

e) Conversion of Poynting-Thomson model elements and Zener model $^{(*)}$ elements:

$$E_1 = \frac{E_2^*}{E_1^*} \, (E_1^* + E_2^*) \qquad (1)$$

$$E_2 = E_1^* + E_2^* \qquad (2)$$

$$\eta = \eta^* \left(\frac{E_1^* + E_2^*}{E_1^*}\right)^2 \qquad (3)$$

$$\eta = \frac{\eta}{\left(\frac{E_2}{E_1^*}\right)^2} \qquad (4)$$

$$E_1^{*}= E_2 - E_2^{*} \tag{5}$$

$$E_2^{*}= \frac{1}{E_1} + \frac{1}{E_2} \tag{6}$$